Rapid Neutron-Capture Nucleosynthesis from the Births and Deaths of Neutron Stars

Dhruv Desai

Submitted in partial fulfillment of the
requirements for the degree of
Doctor of Philosophy
under the Executive Committee
of the Graduate School of Arts and Sciences

COLUMBIA UNIVERSITY

2023

© 2023

Dhruv Desai

All Rights Reserved

Abstract

Rapid Neutron-Capture Nucleosynthesis from the Births and Deaths of Neutron Stars

Dhruv K. Desai

The astrophysical origins of the rapid neutron-capture process ($r-$process), which gives rise to roughly half of the elements heavier than iron, has remained a mystery for almost 70 years. The likely violent events, which seed the $r-$process abundances in our solar system and galaxy, remain uncertain to this day. This is in part due to nuclear physics uncertainties associated with the r-process itself, but mainly due to uncertainties in astrophysics modeling. The discovery of the radioactively-powered kilonova emission from the neutron star merger event GW170817 confirmed the violent *deaths* of neutron stars as one key site of the $r-$process in the universe. However, other evidence appears to favor an additional r-process channel that more promptly follows star formation in the universe, such as core-collapse supernovae (CCSNe), i.e. the brilliant *births* of neutron stars.

Chapters 2 and 3 of this dissertation present general relativistic magnetohydrodynamic simulations of one potential $r-$process site associated with CCSNe: the neutrino-driven wind. These outflows are launched from the hot proto-neutron star (PNS) remnant by neutrino-heating above their surfaces, within seconds after the collapse of a massive star. However, previous work has shown that spherically symmetric winds from non-rotating PNS fail to achieve the requisite conditions for a robust r-process. Chapter 2 explores for the first time the combined effects of rapid rotation and strong

gravity of the PNS on the wind properties. Chapter 3 explores the impact of a dynamically strong ordered magnetic field on the properties of non-rotating PNS winds. The wind in both cases is simulated in a controlled environment rather than as a part of a self-consistent global CCSNe simulation, to assess the viability of $r-$process nucleosynthesis as a function of PNS properties (neutrino energies/luminosities, rotation rate, magnetization).
We find that rapid rotation allows for outflows that are $\sim 10\%$ more neutron-rich in the equatorial region, where the mass loss rate is roughly an order of magnitude higher than that of otherwise equivalent non-rotating models. The birth of very rapidly spinning neutron stars may thus be a site for the production of light $r-$process nuclei ($38 < Z < 47$). For PNS with sufficiently strong magnetic fields (such that magnetic pressure exceeds gas pressure above the PNS surface), we find that equatorial outflows are trapped by the magnetic field in a region near the surface, and therefore receive additional neutrino heating relative to a freely-expanding unmagnetized wind. This allows a modest fraction of the wind material to achieves entropies high enough to synthesize 2nd peak $r-$process elements via an alpha-rich freeze-out mechanism.

The final chapter explores the interplay between the $r-$process and the dynamics of compact object merger ejecta. Gravitational wave observatories are expected to detect several additional binary neutron star (BNS) and black hole-neutron star (BHNS) mergers in current and future observing runs, some of which may be accompanied by electromagnetic counterparts such as kilonovae. However, distinguishing more distant BNS from BHNS mergers based on their associated gamma-ray bursts (GRB), has proven tricky. This chapter presents a calculation of the effects of $r-$process heating on the dynamics of tidal ejecta from BNS and BHNS mergers. In particular we explore whether late-time fall-back of weakly bound debris created during the merger to the central black hole remnant, can explain the temporally extended X-ray emission observed following several merger GRB on timescales of several seconds to minutes. As a result of the different impact that r-process heating has depending on the composition of the ejecta and the mass

of the black hole, a method to differentiate BHNS from BNS mergers, based on their extended X-ray emission, is proposed.

Table of Contents

Acknowledgments xiv

Dedication xvii

Chapter 1: Introduction 1

1.0.1 The need for an alternate nucleosynthetic process 2

1.0.2 Challenges to understanding the origin of the $r-$process 4

1.1 Nuclear physics of the $r-$process 5

1.1.1 Mechanism of the $r-$process 5

1.1.2 Requirements for a high ratio of neutrons to seed nuclei 9

1.1.3 Computing nuclear abundance yields given astrophysical conditions . 12

1.1.4 Experimental developments in $r-$process studies 13

1.2 Observational constraints on the $r-$process sites 16

1.2.1 Evidence for universality of the $r-$process 17

1.2.2 Evidence for rare, high-yield r-process sources 19

1.2.3 Evidence for a prompt $r-$process site disfavors compact object mergers 21

1.2.4 Evidence of multiple sites for LEPP elements 23

1.3 Candidate astrophysical sites of the $r-$process 24

1.3.1 Neutron star mergers 24

1.3.2 Core-Collapse Supernovae 31

1.3.3 The neutrino-driven wind 34

1.3.4 This Dissertation: Rapid Rotation and Strong Magnetic Fields 40

Chapter 2: Neutrino-Driven Winds from Rotating Protoneutron Stars 46

2.1 Methodology 49

2.1.1 Numerical Evolution Code 49

2.1.2 Neutron Star Models and Initial Conditions 54

2.1.3 Conditions for *r*-process nucleosynthesis 58

2.2 Results 60

2.2.1 Non-Rotating PNS Wind 60

2.2.2 Rapidly Rotating PNS Winds 68

2.3 Summary and Conclusions 77

Chapter 3: Neutrino-Driven Winds from Magnetized Protoneutron Stars 83

3.1 Methodology 87

3.1.1 Numerical Evolution Code, PNS Initial Data & Grid Setup 87

3.1.2 Addition of a Dipole Magnetic Field 89

3.2 Results 93

3.2.1 Weakly Magnetized Model 94

3.2.2 Strongly Magnetized Model 96

3.2.3 Implications for *r*-process nucleosynthesis 107

3.3 Summary and Conclusions 110

Chapter 4: Imprints of r-process heating on fall-back accretion: distinguishing black hole-neutron star from double neutron star mergers 114

4.1 Model 118

4.1.1 Numerical Simulation Data 118

4.1.2 R-Process Heating 121

4.1.3 Numerical Model 122

4.2 Results for Mass Fall-Back 126

4.2.1 Y_e-dependent spread in fluid element heating 129

4.3 Implications for Extended Emission in SGRBs 131

4.4 Conclusions 134

Conclusion or Epilogue 137

References 141

Appendix A: Appendix 181

A.1 Numerical Tests 181

A.1.1 Spatial Resolution 181

A.1.2 Hemisphere Symmetry Assumption 183

A.1.3 Toroidal Field 185

A.1.4 Landau Level Effects 185

A.1.5 Divergence-free Constraint Violations 186

List of Figures

1.1 Path taken by nuclides in the $r-$process (top panel) and the solar abundance pattern (bottom panel). From Siegel (2022). 7

2.1 Scale height $H = \left|\frac{d\ln\tau_{\bar{\nu}_e}}{dr}\right|^{-1}$ associated with the $\bar{\nu}_e$ optical depth $\tau_{\bar{\nu}_e}$, as a function of radius r from the center of the PNS (*solid lines*), averaged over polar angle ($\theta = 0^\circ - 90^\circ$) and time-averaged from 50 to 100 ms for our three non-rotating PNS solutions with different spatial resolution: `nrot-MR` (black, $\Delta x \simeq 450$ m), `nrot-LR` (*purple*, $\Delta x \simeq 620$ m), and `nrot-HR` (*green*, $\Delta x \simeq 225$ m). None of the simulations resolve the region around the neutrinosphere radius ($\tau_{\bar{\nu}_e} = 1$; *vertical dashed lines*) with several grid points, and hence cannot accurately converge on the neutrino luminosity or mean energy. However, the gain region of net heating and wind zone on larger scales is well resolved by even the lowest resolution runs. 51

2.2 Snapshots of various quantities from our fiducial non-rotating model `nrot-HR` showing a slice through the $y = 0$ plane at $t = 152$ ms, with contours at the neutrinosphere ($\tau_{\bar{\nu}_e} = 1$; *red*), $E_{\rm tot} = 0$ (*white*), the α-particle formation surface (*teal*; $X_{\rm nuc}$ refers to the mass fraction of all nuclei excluding individual nucleons), and the sonic surface (where $v^r = c_s$; *white dotted*). The top left panel shows the density ρ and temperature T. The top right panel shows the specific entropy s and the electron fraction Y_e. The bottom left panel shows $E_{\rm tot}$, the total specific energy of wind matter as measured at infinity ($E_{\rm tot} = -hu_t - 1$, where h is the specific enthalpy and u_t is the time component of the four-velocity), and the net neutrino heating rate $\dot{q}_{\rm net}$. The bottom right panel shows the radial velocity v^r and the isotropic-equivalent mass loss rate $\dot{M}$. Please note the different radial scale on the bottom right sub-panel compared to the other sub-panels. 61

2.3 Radial profiles of angle-averaged quantities for model `nrot-HR` at several times (from dark to light): t =30, 49, 68, 87, 105, 124, and 142 ms. Plotted are (a) temperature, T; (b) mass density, ρ; (c) net specific neutrino heating rate, $\dot{q}_{\rm net}$; (d) electron fraction, Y_e (*solid*), and limited equilibrium electron fraction $Y_{e,eq}^{\rm abs}$ (*dotted*); (e) total specific energy, $E_{\rm tot}$; (f) specific entropy, s; (g) mass outflow rate, $\dot{M}$; (h) radial velocity, v^r. The red vertical dashed line denotes the location of the $\bar{\nu}_e$ neutrinosphere. The $\tau_{\bar{\nu}_e}$=1 and α-formation surface ($X_{\rm nuc}$ = 0.5, where $X_{\rm nuc}$ is the mass fraction of all nuclei excluding individual nucleons) at t = 152 ms (corresponding to the snapshot in Fig. 2.2) are indicated by red dashed and teal dotted lines in panels (a)–(d) and (f), respectively. Red circles denote the sonic surface at which the radial velocity v^r equals the sound speed; there are only three such circles because the sonic surface does not enter the grid until the final three snapshots. Please note the different radial scales for quantities shown in the left and right columns. . . . 62

2.4 Time evolution of angle-averaged wind properties (as measured through a r = 60 km spherical surface) for the non-rotating models of low resolution `nrot-LR` (*purple*), medium resolution `nrot-MR` (*green*), and high resolution `rot-HR` (*black*). Asymptotic wind properties such as the mass-loss rate and specific entropy are not converged with resolution because the neutrino decoupling region which sets the neutrino radiation field is not resolved (Fig. 2.1). However, when the wind properties are scaled following the Qian and Woosley (1996) analytic formulae to results from 1D time-independent models Thompson, Burrows, and Meyer (2001), or to each another, based on their respective neutrino luminosities/energies/neutrinosphere radii, they come into better agreement (Table 2.3). 67

2.5 Similar to Fig. 2.2, except now showing snapshots at t = 100 ms of 2D slices through the rotational axis for model `rot.6-MR`, and including new quantities, such as azimuthal velocity v^ϕ, electron anti-neutrino flux $F_{\bar{\nu}_e}$, and mean energy $E_{\bar{\nu}_e}$. Please note the different radial scales in the top two rows compared to the bottom row. 70

2.6 Temperature (*left*) and electron anti-neutrino mean energy (*right*) close to the PNS surface in the meridional plane for the maximally rotating model `rot.6-MR`. The approximate neutrinosphere surfaces (contours τ_{ν_e}, $\tau_{\bar{\nu}_e}$ = 1) for ν_e and $\bar{\nu}_e$ are shown as blue and red curves, respectively. A bulge due to rapid rotation pushes out the location of the neutrinosphere near the equator, decreasing the τ = 1 temperatures and reducing the mean neutrino energies in the equatorial regions relative to the polar regions. 71

2.7 Wind properties as a function of polar angle θ, measured from the $z-$axis (rotation axis in rotating models), through spherical surfaces at $r = 60$ km (*left*) and $r = 120$ km (*right*) from the non-rotating model `nrot-HR` (non-rotating; *black*) and rotating models `rot.9-MR` (*orange*), `rot.7-MR` (*red*), and `rot.6-MR` (*blue*), time-averaged over the final third of the simulation run (e.g. $100-150$ ms for `nrot-HR`). From top to bottom, the quantities shown include: isotropic mass-loss rate $\dot{M}$, radial velocity v^r, specific entropy s, isotropic electron anti-neutrino luminosity $L_{\bar{\nu}_e}$, mean electron anti-neutrino energy $E_{\bar{\nu}_e}$, and electron fraction Y_e. Dotted lines in the bottom panel show our estimate of the equilibrium electron fraction $Y^{\rm abs}_{e,eq}$ (Eq. (2.12)). 72

2.8 Similar to Fig. 2.4, except now comparing angle-averaged wind properties in the non-rotating model `nrot-HR` (*black*), and rotating models `rot.9-MR` (*orange*), `rot.7-MR` (*red*), and `rot.6-MR` (*blue*) as measured through a spherical surface of radius $r = 60$ km. 73

2.9 R-process figure-of-merit parameter $\eta \equiv s^3_\infty/(Y_e^3\tau_{\rm exp})$ (Eq. (2.8)) as a function of outflow polar angle θ, where the relevant quantities are time-averaged and measured through the $T = 0.5$ MeV surface, shown separately for the models `nrot-HR`, `rot.9-MR`, `rot.7-MR`, `rot.6-MR` as marked. For comparison we show the threshold value $\eta_{\rm thr}$ (Eq. (2.8)) required for neutron captures to reach the 2nd (*purple dotted line*) and 3rd (*green dotted line*) r-process peaks (Hoffman, Woosley, and Qian, 1997). A dotted line-style to the right of the solid triangles in the rapidly rotating models (`rot.6-MR`, `rot.7-MR`) denotes the angles over which Y_e is 10% lower than its average value along the polar angles $0° < \theta < 30°$ (the latter is roughly similar to that obtained from a non-rotating wind for the same neutrino emission properties); the outflow from such regions may be capable of a successful r-process even absent an α-rich freeze-out (i.e., even if $\eta \ll \eta_{\rm thr}$). 76

3.1 Initial magnetic-to-fluid pressure ratio β^{-1} with magnetic field line geometry overlaid. We show models `lo-B` (left) and `hi-B` (right) in a slice through the magnetic dipole axis ($y = 0$ plane), soon after the magnetic field is turned on at $t = 0$ ms. This magnetic field configuration was added onto an unmagnetized PNS wind solution previously evolved for about 176 ms to steady state. For model `hi-B`, magnetic pressure dominates over fluid pressure in the polar regions above the PNS surface out to $\approx$60 km. 91

3.2 Snapshots of the outflow properties as a cross-section through the magnetic dipole axis ($y = 0$ plane) at $t \approx 55\,\mathrm{ms}$ after B-field initialization for models `lo-B` (left) and `hi-B` (right). Colors show the rest-mass density ρ, with the magnetic field line geometry overlaid in white. The neutrinosphere ($\tau_{\bar{\nu}_e} = 1$ surface) is shown with a red contour. The field lines have been nearly completely torn open radially in the weakly magnetized model, while an equatorial belt of closed field lines persists in the strongly magnetized case. 92

3.3 Snapshots showing outflow properties as a cross-section through the magnetic dipole axis ($y = 0$ plane) at $t \approx 55\,\mathrm{ms}$ after B-field initialization for models `no-B` (unmagnetized, left) and `lo-B` (weakly magnetized, right). From top to bottom: specific entropy s, electron fraction Y_e, radial velocity v^r. The green contour represents the alpha-particle formation surface ($X_\alpha = 0.5$), around which r-process seed nuclei begin to form, while the red contour represents the location of the neutrinosphere ($\tau_{\bar{\nu}_e} = 1$ surface). 92

3.4 Radial profiles of the poloidal magnetic field strength $B_{\rm P}$ for models `lo-B` and `hi-B`, taken from a slice through the magnetic dipole axis ($y = 0$), angle-averaged in the polar region from $\theta = 0°$ to $\theta = 45°$. Solid lines show $B_{\rm P}$ time-averaged from $t \approx 0 - 5$ ms after the magnetic field is activated, while dashed lines represent $B_{\rm P}$ time-averaged from $t \approx 25 - 35$ ms. To guide the eye, thick solid lines show power-laws r^{-2} (blue) and r^{-3} (green). Both models approach the split monopole solution ($\propto r^{-2}$) in the polar region. 96

3.5 Mass-loss rate $\dot{M}$ (top), kinetic power $E_K = (W - 1)\dot{M}$ (center), where W is the Lorentz factor, and $\dot{M}$-weighted average specific entropy s (bottom) of outflows through a spherical surface of radius $r = 60$ km, as a function of time since magnetic field initialization. For all models `no-B` (black, ×), `lo-B` (blue circles), and `hi-B` (red triangles) these quantities are shown across the full 4π solid angle. For model `hi-B` (red), we show separately the isotropic equivalent mass-loss rate as well as kinetic power, and average-entropy across a solid angle at high latitudes close to the poles ($\theta = 0° - 45°$ and $\theta = 135° - 180°$; dotted line) and near the equatorial plane ($\theta = 45° - 135°$; solid line). 100

3.6 Snapshots of the magnetic-to-fluid pressure ratio β^{-1} in the $y = 0$ magnetic dipole axis plane for models `lo-B` and `hi-B`. The top panel shows the moment the magnetic field is initialized ($t \approx 0$ ms), while the middle and bottom panels are at $t \approx 31\,\mathrm{ms}$ and $t \approx 55\,\mathrm{ms}$, respectively. A cyan contour represents the alpha particle formation surface ($X_\alpha = 0.5$) around which r-process seed nuclei begin to form, while the red contour represents the neutrinosphere surface ($\tau_{\bar{\nu}_e} = 1$). 101

3.7 Same as Fig. 3.6, but for radial velocity v^r. The lower velocities of matter in the equatorial closed zone region, particularly in the first two snapshots, is apparent. 101

3.8 Same as Fig. 3.6, but for specific entropy s. The effect of the enhanced heating of matter in the equatorial closed zone is apparent. 102

3.9 Same as Fig. 3.6, but for Y_e. 102

3.10 Same as Fig. 3.6, but for temperature T. 103

3.11 Change in the energy contained within the volume extending from $r = 15$ km to an outer radius r between $t \approx 15$ ms and $t \approx 55$ ms following the initialization of the magnetic field for model `hi-B`. Left: Polar component, averaged azimuthally and over polar angles $\theta = 0° - 45°$ and $135° - 180°$. Right: Equatorial component, averaged azimuthally and over polar angles $\theta = 45° - 135°$. The energies are defined as follows: kinetic energy $E_K = \int (W-1)\rho W\sqrt{\gamma}\, d^3x$ (blue); thermal energy $E_{\rm th} = \int \epsilon\rho W\sqrt{\gamma}\, d^3x$ (green); electromagnetic energy $E_{\rm EM} = \int n_\mu n_\nu T^{\mu\nu}_{\rm EM}\sqrt{\gamma}\, d^3x$ (black); net integrated neutrino heating $Q_{\rm net} = \int\int \dot{q}_{\rm net}\rho W\sqrt{\gamma}\, d^3x\, dt$ (red). Here, $T^{\mu\nu}_{\rm EM}$ is the electromagnetic stress-energy tensor, n^μ the 4-velocity of the Eulerian observer, W the Lorentz factor associated with the total 4-velocity, and γ the determinant of the 3-metric. The specific net neutrino heating rate $\dot{q}_{\rm net}$ is integrated over the time interval; all other quantities are evaluated at the final and initial times, with their difference plotted. 103

3.12 Same as Fig. 3.6, but for total specific energy $E_{\rm tot}$, including the effects of magnetic tension (Eq. 3.6). The energy grows in the equatorial belt due to neutrino heating of matter trapped in the closed zone, becoming positive by the final snapshots across a greater region extending to smaller radii approaching the PNS surface. As this high-entropy matter expands through the seed formation region (outside the cyan contour) it can potentially generate the conditions necessary for 2nd or 3rd-peak r-process nucleosynthesis. 104

3.13 Top: Closed-zone ejection timescale $t_{\rm ej}$ (Eq. 3.9) computed just after magnetic field initialization (left) and 30 ms later (right) for model `hi-B` in a slice through the $y = 0$ plane. Bottom: Snapshots from model `hi-B` showing (left) the final entropy $s_{\rm proj}$ of the closed zone material achieved after a time $t_{\rm ej}$ (Eq. 3.9 from Thompson 2003 applied to the initial snapshot) in comparison to (right) the actual entropy s from the simulation at $t \approx 55$ ms after magnetic field initialization. The red contour represents the neutrinosphere surface ($\tau_{\bar{\nu}_e} = 1$). The analytic estimate is roughly consistent with the actual entropy achieved in the trapped zone of the wind. 105

3.14 Histograms of various quantities relevant to r-process nucleosynthesis as measured through a 60 km spherical shell. The left panel shows the unmagnetized (`no-B`, black) and weakly magnetized (`lo-B`, blue) models, while the strongly magnetized model (`hi-B`) is shown on the right, broken down separately into the polar (purple) and equatorial (red) outflows, respectively (defined over the same angular domains as in Fig. 3.5). For the unmagnetized models we show results over the full time interval 25–55 ms, because the outflow is approximately time-stationary, while for the magnetized models we separately bin results for 25–35 ms (thin lines) and 45–55 ms (thick lines). At a given time, quantities are weighted pointwise on the spherical grid by the local mass outflow, they are binned and normalized by the total mass outflow through the entire surface over the time interval. We approximate the outflow expansion time (Eq. 3.4) as $t_{\rm exp} = R/v(R)$, where $v(R)$ is the total wind speed measured at the shell. Threshold values for η (Eq. 3.5) required for neutron captures to reach the 2nd (yellow dashed vertical line) and 3rd (green dotted vertical line) r-process peaks (Hoffman, Woosley, and Qian, 1997) are indicated for comparison. 108

4.1 *Swift* BAT X-ray light curves of two SGRBs, GRB080503 (Perley et al., 2009) and GRB 060614 (Gehrels et al., 2006), which show their temporally-extended prompt emission. Both cases show remarkably similar light curves, which peak on a timescale $\sim$ 30 s after the prompt SGRB spike of duration $\lesssim$ 2 s (gray region; not shown at the chosen time binning). The lull in emission from $t \sim 2-30$ s contrasts with the naive expectation that the X-ray luminosity track the $\propto t^{-5/3}$ mass fall-back accretion (shown for comparison with a pink line). 118

4.2 **Top:** Nuclear heating rate of the unbound debris as a function of time since ejection (blue lines), calculated for ~250 separate fluid elements from the NS-BH merger simulation M7_S8 (Foucart et al., 2014) using the SkyNet nuclear reaction network (Lippuner et al., 2017). We have reduced the heating rate from the rate of nuclear energy by a fraction $(1 - f_\nu) = 0.55$ to account for fraction of the $\beta-$decay energy carried away by neutrinos (eq. 4.3). A black line shows the step-function approximation employed in our fall-back model (eq. 4.4), where in this example $Q_{\rm tot} = 3$ MeV and $t_{\rm heat} = 1$ s. **Bottom:** Total heating rate $Q_{\rm tot}$ for the same fluid elements as a function of their electron fraction Y_e. Shown for comparison is the analytic estimate from equation (4.3), for fixed values of the parameters $\bar{A}/\bar{Z} = 2.4$, $f_\nu = 0.45$, $\left(\frac{B}{A}\right)_s = 8.7$ MeV nuc^{-1} and $\left(\frac{B}{A}\right)_r = 8$ MeV nuc^{-1}. 119

4.3 Mass-weighted distribution of the tidal tail ejecta, extracted from the NS-BH merger simulation data at $t = 15$ ms post-merger, in the space of initial energy, $E_{\rm tot}$, and electron fraction, Y_e. A dashed line at $E_{\rm tot} = 0$ separates the debris which is initially bound versus unbound to the black hole. Fluid elements above the solid blue line could be unbound due to r-process heating along if the ejecta receives the total available heating, $Q_{\rm tot} \sim 3$ MeV (Fig. 4.2, bottom panel). 120

4.4 Schematic illustration of the tidal ejecta from NS-BH or NS-NS mergers, comparing the fluid element trajectories with (dashed lines) and without (solid lines) the effects of r-process heating. The orbital streams are highly elliptical, such that pressure gradients ∇P point almost radially outwards and energy released from the r-process is transferred quickly (on the expansion timescale) into ejecta kinetic energy. The trajectories of tightly bound ($E_{\rm tot} \ll 0$) or strongly unbound ($E_{\rm tot} \gg 0$) matter are not greatly altered. However, marginally bound material with $E_{\rm orb} \gtrsim -Q_{\rm tot}$ and orbital periods comparable to the timescale of the r-process experiences preferential heating relative to more tightly bound debris. This opens a gap in the orbital energy distribution and a temporal gap or late-time cut-off in the mass fall-back rate. 123

4.5 **Top Panel:** Mass fall-back rate, $\dot{M}$, as a function of time, $t_{\rm fb}$, after the NS-BH merger, calculated for different assumptions regarding the total r-process heating experienced $Q_{\rm tot}$ and its characteristic duration $t_{\rm heat}$. Each case is labeled according to the general behavior of the light curve, i.e. whether heating introduces a temporal gap, or a complete cut-off, in the late-time fall-back rate. **Bottom Panel:** Distribution of the debris mass with energy, dM/dE, comparing the initial distribution after the dynamical phase of the merger to that imprinted by r-process heating, shown for the same models and color schemes used in the top panel. r-process heating opens a gap in the energy distribution, which in turn results in either a temporal gap or a complete cut-off in the fall-back rate, depending on whether the energy gap overlaps with $E_{\rm tot} = 0$. 124

4.6 Regimes of the impact of r-process heating on fall-back accretion in the space of the total nuclear released energy, $Q_{\rm tot}$, and the timescale of the heating, $t_{\rm heat}$. The value of $Q_{\rm tot}$ (left vertical axis) is mapped onto the initial electron fraction Y_e (right vertical axis) using eq. (4.3) as shown in the bottom panel of Fig. 4.2. A 2D colored histogram shows the mass distribution of the ejecta in $(Q_{\rm tot}, t_{\rm heat})$, calculated by mapping the ejecta properties of our simulation for a NS-BH merger ($M \simeq 6M_{\odot}$) into the r-process heating trajectories from SkyNet calculations (Fig. 4.2). Symbols show the results of our parameter study in which we assume a BH mass $M \approx 6M_{\odot}$ and that all fluid elements experienced heating characterized by fixed values of $Q_{\rm tot}$ and $t_{\rm heat}$ according to eq. 4.4 (see Fig. 4.5 for a few examples). Crosses denote cases which result in a complete cutoff in the fall-back rate after a given time, while circles show cases in which a temporal gap is opened in the fall-back curve (the duration of the gap is denoted both by the radius and color of the circle using the legend given on the right). Lines represent the critical condition ($\eta = \eta_{\rm c} \approx 0.95$; eq. 4.8) giving rise to a long (~ 30 s) gap for different values of the mass of the central black hole as marked, ranging from $M \approx 2.5M_{\odot}$ relevant to NS-NS mergers to $M \sim 6-20M_{\odot}$ relevant to NS-BH mergers. While the tidal ejecta from NS-NS mergers lies in the cut-off regime ($\eta \gg 1$) for neutron-rich ejecta $Y_e \lesssim 0.2$, the NS-BH merger case resides close to the gap regime ($\eta \sim \eta_{\rm c} \approx 0.95$). 125

4.7 **Top:** Two models from Figure 4.5 showing temporal gaps in the fall-back rate, but now calculated using a realistic spread in the r-process heating experienced by different fluid elements due to variations in their Y_e values (eq. 4.3) (see also Fig. 4.2, bottom panel). The mean values for $Q_{\rm tot}$, around which the spread is centered, are shown in the figure. The previous model with a large temporal gap in the fall-back rate ($t_{\rm heat} = 1.75$ s; *blue*) now shows a complete cut-off, while the case with a shorter gap ($t_{\rm heat} = 1.5$ s; *red*) has been smoothed out to a lull in accretion. **Bottom:** Mass fall-back evolution calculated using r-process heating curves taken directly from the output of SkyNet simulations (Fig. 4.2) mapped into our NS-BH simulation data based on their Y_e values. We see a gap behavior because the ejecta properties lie close to the critical line $\eta = \eta_{\rm c}$ line for the $M = 6M_{\odot}$ black hole (red solid line in Fig. 4.6), but again the gap is partially filled-in due to the spread in heating properties. . . 130

4.8 The critical condition $\eta = \eta_{\rm c}$ (eq. 4.8) in the space of BH mass M and ejecta electron fraction Y_e, which separates a temporal gap, versus a cut-off, in the rate of fall-back accretion. The value of η is calculated by mapping $Q_{\rm tot}$ to Y_e using equation 4.3 for different values of $t_{\rm heat}$ as extracted from the results of our SkyNet calculations for the nuclear heating rate. As long as the ejecta is sufficiently neutron-rich ($Y_e \lesssim 0.2$), the low-mass black hole remnants of NS-NS mergers are predicted to experience a cut-off in the fall-back rate, while the more massive BHs from NS-BH mergers should experience a gap or lull in fall-back, consistent with the extended emission observed after a fraction of SGRBs (Fig. 4.1). 132

A.1 Vertical scale-height as a function of radius of the magnetic field B (black) and neutrino optical depth $\tau_{\bar{\nu}_e}$ (blue) for model `hi-B`, normalized by the grid step size Δx. The radial profiles correspond to the slice through the magnetic dipole axis ($y = 0$ plane), averaged over polar angle between $\theta = 0°$ and $\theta = 45°$, and time-averaged over the first 4 ms after the magnetic field is initialized. Discontinuities at 15 km and 30 km reflect refinement level boundaries. 182

A.2 Comparison of wind properties with and without imposing reflection symmetry across the equatorial plane. Shown are wind cross-sections in the plane of the magnetic dipole axis for specific entropy (left panel) and magnetic-to-fluid pressure ratio (right panel) time-averaged over the interval $t \simeq 30 - 35$ ms after the B-field is initialized. For each panel: the simulation is run across the full $\theta \in [0, \pi]$ domain (left; model `no-sym-B`); reflection symmetry across the $z = 0$ plane is employed (right; model `sym-B`). 182

A.3 Strength of the poloidal (left) and toroidal (right) magnetic field components for model `hi-B` approximately 55 ms after initialization of the magnetic field. The red contour indicates the location of the neutrinosphere. 184

A.4 Cross-section of the $y = 0$ magnetic dipole axis plane for the `lo-B` (left) and `hi-B` run (right) ≈ 55 ms after the magnetic field is initialized, showing the ratio of temperature T (top) and density ρ (bottom) to their respective critical values T_B and ρ_B below which quantizing effects of the magnetic field on the EOS and weak interactions are expected (Eqs. A.1 and A.2). Since $T/T_B > 1$ everywhere, electrons and positrons populate many Landau levels, even in the regime where $\rho < \rho_B$. The magnetic winds are thus in the non-quantizing regime, justifying our negligence of magnetic-field effects onto the EOS and weak interactions. The red contour indicates the $\tau_{\bar{\nu}_e} = 1$ neutrinosphere surface. 186

A.5 Equatorial plane ($z = 0$) cross-section at 3 snapshots in time (≈ 31 ms, 55 ms, 64 ms after dipole magnetic field initialization) for models `lo-B` (shown in the $x < 0$ domain) and `hi-B` (shown in the $x > 0$ domain). The color represents the relative level of $\nabla \cdot \mathbf{B}$ violations, where Δx is the grid spacing, and B is the overall strength of the magnetic field. While the constraint transport scheme maintains $\nabla \cdot \mathbf{B}$ to machine precision interior to refinement level boundaries, spurious violations are introduced at refinement boundaries due to interpolation operations. 188

List of Tables

2.1 Suite of $1.4M_{\odot}$ PNS Simulations 58

2.2 Asymptotic Properties of Rotating and Non-Rotating PNS Winds 69

2.3 Resolution Study of Non-Rotating PNS Wind Properties 69

3.1 **Suite of PNS Wind Simulations: Magnetic Field and Neutrino Properties** (a) Magnetic field strength as measured along the polar axis at the radius of the $\bar{\nu}_e$ neutrinosphere; (b) Initial equatorial radius of the star; (c) Steady-state $\bar{\nu}_e$ neutrinosphere radius; (d) – (g) Luminosities and mean energies of electron neutrinos and anti-neutrinos, averaged over the final factor of three in simulation time. *Fiducial unmagnetized wind model (Fig. 3.3, left panels). †All simulations employ the same grid geometry, but these models are run with three times poorer resolution compared to the models in the first 3 rows (i.e., $\Delta x = 450$ m for the finest grid). 90

3.2 **Time-Averaged Outflow Properties** We report wind properties time-averaged from $t \approx 25 - 55$ ms for models `no-B`, `lo-B`, and `hi-B`, and from $t \approx 0 - 20$ ms for models `sym-B` and `no-sym-B`. Entries of the format ($q \longrightarrow q'$) refer to the same quantity time-averaged from $t \approx 25 - 35$ ms (q) and from $t \approx 45 - 55$ ms (q'). (a) isotropic mass-loss rate; (b) kinetic energy; (c) specific entropy with standard deviation; (d) expansion timescale with standard deviation; (e) electron fraction with standard deviation; (f) $r-$process figure of merit $\eta \equiv s^3/(Y_e^3 t_{\rm exp})$ with standard deviation. *Fiducial unmagnetized wind model shown in Fig. 3.3 (left-hand panels). †All simulations in the table use the same grid geometry, but these models are run with a third of the resolution compared to the models in the first three rows (i.e. $\Delta x = 450$ m for the finest grid). ††Quantities are averaged over different angular sectors in polar angle θ: 'equat.' (45° ≤ θ ≤ 135°), 'pol.' (0° ≤ θ ≤ 45° and 135° ≤ θ ≤ 180°), and 'tot.' (0° ≤ θ ≤ 180°). Isotropic equivalent quantities are reported for $\langle \dot{M} \rangle$ and $\langle \dot{E}_K \rangle$ at a radius $r = 60$ km. 97

Acknowledgements

My PhD experience here in New York City has been incredible. I am indebted to a great number of people over the past 6 years who have made this PhD possible in the first place. They give my work meaning.

First and foremost, I am eternally grateful to Brian who took me on during an uncertain time in my career, post-graduation in 2017. Your constant presence, responsiveness, and patience for even the most trivial questions has meant a lot. As if one supportive advisor weren't enough, I have been blessed with two. Daniel Siegel's enthusiasm is contagious and his humility is inspiring. I feel truly spoiled and I look forward to continuing my work with both of you.

My endeavors in this field began as an undergraduate at UC Berkeley. I am grateful to Dan Kasen who provided me with the initial opportunity, and Francois Foucart who mentored me and introduced me to this vast and rich field. During the PhD itself, I was lucky enough to have the opportunity to visit Perimeter Institute in Canada for several months and to experience pre-pandemic life there. Despite my reservations about Canadian winters, I came to embrace the cold with the help of a wonderful community of friends. Max, I am particularly inspired by your boundless enthusiasm towards life and your persevering attitude (ice skating, baking, running etc.) even as a global pandemic set in.

I will miss my fellow graduate students and the tight-knit Astronomy Department at Columbia. From pizza lunches and colloquia to soccer games and food outings in NYC, the community has felt like home to me. I feel blessed to have been surrounded by incredible

professors from which I've learned so much (Lam Hui, Jeremy Dodd, Andrei Beleborodov, Lorenzo Sironi) through various courses, volunteering activities, THEA group meetings, and teaching events). I am also grateful to former Columbia students who have been exemplary role models. Ben, I admire your work-life balance and dedication to science, and I appreciate your effort to stay in touch even during the busiest times.

To the Relastro group (mostly) based in Greifswald - Daniel, Luciano, Aman, Michael, Javi, Eric, Geoffrey: it has been a joy to work with motivated and kind human beings such as yourselves. Your positive and supportive attitudes are a huge reason for why I am excited to continue onward in science. I look forward to working with you in the coming years.

To the larger Astro community I've learned so much from those I've met at conferences abroad, and at colloquia and seminars here. I feel beyond lucky to have found a research area with such kind, motivated, and enthusiastic human beings.

My time in NYC would not have been the same without the friends I made outside the department. To my newest (but by no means least) set of friends, it's been a joy climbing with you in a space where I can temporarily forget about my research troubles. Ramin, Suki, Jake – I've never laughed harder than I do with you guys. I'm so grateful for the nights we played guitar together and hung around on apartment rooftops. Prad: we've been through a lot, we've grown as friends, and you are one of the most caring people I know. I'll be on messenger. San: it's been incredible getting smoothies and doing wholesome activities with you around the city. Preet: our internet friendship is truly unparalleled and our creative/silly bantering has gotten me through many days. Prasad: your generosity, strength, and light-heartedness is inspiring. Here's to many more Rubirosas and beans and brunches. Su-Ann: you are one of my oldest and most dependable friends. I sense many more adventures to come. Seth, Howard, Kunal, Alison, Adithya, Rahul, and Aditya: Our friendships haven't changed much in 8 years and I love that.

I am lucky enough to have an expansive network of family members all over the

country. To my extended family (in California, NJ, and elsewhere): I very much appreciate your support in even the smallest of ways. Last but not least, I want to highlight my close family: Mom, Dad, Niyati. Thank you for being there and making my journey smoother. No paragraph in an acknowledgment section could sum up how much you matter to me. This would not have been possible without your belief in me and support.

Advisors, family, friends, and colleagues: You continue to inspire me to become a better scientist, and more importantly, a better person.

Thank you.

Dedication

I dedicate this work to my family, friends, and colleagues – all of whom made it possible in the first place. I hope I have been able to share some of the beauty of this subject with you. I do what I do for you.

Chapter 1: Introduction

The Periodic table comprises 118 elements. Of the first 94, 80 have at least one stable isotope, while another 11 (up to atomic number $Z = 94$) are unstable but have sufficiently long half-lives to occur naturally on Earth. How did these elements come to exist? In the minutes following the Big Bang, protons and neutrons combined to create primarily hydrogen (75% by mass), helium (25% by mass) and trace amounts of ^{3}He and ^{7}Li (Cyburt et al., 2016). All other naturally-occurring elements are synthesized in stellar environments (Cameron, 1957; Burbidge et al., 1957). The first stars were formed after about a hundred million years, from massive (typically $\sim 100 M_\odot$) self-gravitating contracting clouds (Abel et al., 1997; Abel et al., 1998). Stars, by definition, contract under the gravitational force until temperatures and pressures at the center are sufficiently high for matter to fuse into heavier elements. Fusion reactions result both in a compositional shift towards heavier elements and energy release, which provides the thermal pressure support to keep a star from collapsing.

Depending on its mass, a star can go through several successive phases of contraction followed by fusion in the core, generating progressively heavier elements along its evolution. Less massive stars ($\lesssim 8 M_\odot$) only reach temperatures in their core high enough to fuse elements up to carbon and oxygen. The lightest of these can live for billions of years and expel their surface layers to form planetary nebulae at the end of their lives (Nomoto, Kobayashi, and Tominaga, 2013). The cores, supported by electron degeneracy pressure, remain mainly as stable carbon-oxygen white dwarfs.

Massive stars (with initial mass $\gtrsim 8 M_\odot$) on the other hand evolve much more rapidly, living for only a few hundred million years or less, and fusing elements up to iron and nickel in the last days of their lives. As the most bound isotope, it is not energetically favorable to form elements heavier than ^{56}Ni due to the large Coulomb barrier with increasing Z and because such reactions would consume energy rather than release it. The result, once the core has converted all lighter elements to Fe and Ni nuclei, is unstable to runaway core collapse under gravity. For stars of initial mass $8M_\odot \lesssim M \lesssim 25M_\odot$, collapse leads to the formation of a dense proto-neutron star (PNS), supported against further collapse by strong nuclear repulsion. Though the precise mechanism is still uncertain, the outer layers of the star are in most cases ejected in a "core-collapse supernova" (CCSN) explosion. The most-promising theory is that neutrinos emitted by the hot PNS are absorbed above its surface, depositing enough energy to reverse the collapse (e.g., Bethe and Wilson 1985; Janka 2012). The unbound ejecta from the explosion, as well as any outflows released by the PNS (such as those explored in this dissertation), enrich the interstellar medium with this processed material.

1.0.1 The need for an alternate nucleosynthetic process

Though they likely cannot form in deep stellar interiors, we nevertheless observe in small abundances elements much heavier than iron on Earth (e.g., gold, uranium), in the Sun, and in neighboring stars and galaxies. How did they get there? i.e., what are the astrophysical mechanism(s) of their production? This remains a longstanding open question in science, which can be traced back to the first complete tabulation of universal abundances by Goldschmidt (1937). Addressing this question requires bringing together knowledge spanning a wide range of research fields – from astrophysical observations and modeling of galactic archaeology/chemical evolution and stellar explosions, to fundamental properties of matter in atomic and theoretical/experimental nuclear physics. Goldschmidt himself attempted to find correlations in his abundances with nuclear structure; though unsuccessful, his compiled elemental abundance data from the atmosphere, the Sun, meteorites, and terrestrial rocks made possible the 1963 Nobel Prize winning work by Maria Mayer and Hans Jensen on the nuclear shell model (Suess, 1988).

Hoyle et al. (1956) first suggested that elements heavier than the iron group (i.e., $Z \gtrsim 26$)

could be generated via neutron capture onto lighter seed nuclei, particularly Fe. This model is attractive simply because neutrons, being neutrally-charged, need not overcome an electric Coulomb barrier to be captured. However, sufficiently neutron-rich nuclei are unstable to $\beta-$decay, in which a neutron n in the nucleus decays to a proton p and emits an electron e^-; it is therefore only through successive neutron captures (which raise mass number A) *followed by* $\beta-$decays ($A \rightarrow A-1$, $Z \rightarrow Z+1$) by which heavy elements can be formed through neutron captures alone.

The competition between $\beta-$decays (timescale τ_β) and neutron captures (timescale τ_n) points to two distinct neutron-capture processes[1]: one where $\tau_\beta \ll \tau_n$ and one where $\tau_\beta \gg \tau_n$. In the first, dubbed the "slow neutron-capture process", or $s-$process, a neutron is captured onto a nucleus of charge Z, which quickly decays into a stable nucleus of charge $Z+1$ much faster than another neutron capture can occur. In this manner the nucleus incrementally grows along a valley of stable nuclei (the 'valley of stability'). In the latter, dubbed the "rapid neutron-capture process", or $r-$process, many neutrons ($\gtrsim 10$) are rapidly captured onto a nucleus before it $\beta-$decays. In this manner the highly neutron-rich nucleus proceeds on a path far from the valley of stability, until available neutrons are exhausted and the nucleus returns to the valley of stability via $\beta-$decays, but now at significantly higher Z than where it started. The details of this theory, predicted abundances, and potential sites were laid out in the seminal 'B^{2}HF' paper (Burbidge et al., 1957).

Of these two dominant processes, the origin of the $r-$process is arguably the most challenging to unravel: many of the properties of nuclei far from stability are poorly understood experimentally and theoretically, while the extreme conditions and transient nature of the most promising astrophysical sites pose a multi-scale physics challenge.

---

[1] Although most heavy element production in the universe occurs either through a $s-$process ($\tau_\beta \gg \tau_n$) or $r-$process ($\tau_n \gg \tau_\beta$), the so-called "intermediate neutron-capture process" ($\tau_n \gg \tau_\beta$), or i-process, has been suggested (Cowan and Rose, 1977; Dardelet et al., 2015) as the origin of some abundance patterns observed on metal-poor stars in the mass range $55 < Z < 75$ (Beers and Christlieb, 2005).

1.0.2 Challenges to understanding the origin of the $r-$process

To fully deduce the origins of the r-process elements requires modeling and expertise which spans a wide range of topics in physics, ranging from the astrophysics of stars, the nuclear physics of neutron-rich nuclei and neutron star interiors, and the fluid dynamics and strong-field gravity. Some of these areas include:

1. the properties of neutron-rich isotopes on the $r-$process nucleosynthesis path far from stability, such as nuclear masses, half-lives, and fission probabilities and fragment distributions

2. nucleosynthesis network calculations which determine the conditions of density, temperature, and neutron-richness required to reproduce the $r-$process abundance patterns observed throughout the cosmos

3. hydrodynamical and magneto-hydrodynamical simulations of explosive astrophysical events, generally under conditions of strong gravity and dynamical spacetime, to determine what astrophysical sites are likely to meet such conditions

4. astrophysical observations of r-process abundances in different environments, ranging from meteoritic abundances on Earth, stellar surface abundances (the Sun, the Milky Way halo, or in nearby dwarf galaxies), or in extragalactic astrophysical transients (supernovae, kilonovae - a direct signature of the production of $r-$process elements: see Sec. 1.3.1) to determine the $r-$process enrichment as a function of galactic evolution

5. radiation transport simulations, which make use of detailed atomic physics properties of r-process nuclei, to transform astrophysical observations of stars or kilonova into accurate abundance information

Although the research presented in this thesis contributes mainly to item 3 of the above, I use the remainder of this introduction to briefly review all of these issues, organized as follows. Section 1.1 describes the physical mechanism of the $r-$process and the requisite astrophysical conditions, as well as currently active areas of experimental nuclear physics research in understanding $r-$process nuclei and how they feed into nuclear reaction network simulations of the $r-$process. Section 1.2 describes observational constraints on $r-$process enrichment sites from the Solar System, nearby stars and galaxies, and evidence for rarity of the $r-$process enrichment events. Finally, Section 1.3 provides a brief historical overview of neutron star mergers and supernovae, which represent the top two candidate astrophysical sites for the $r-$process. I introduce a long-considered $r-$process site: the neutrino-driven wind, which is an outflow of baryonic matter from the surface of the PNS in the seconds following a successful supernova explosion. I conclude this final section with a brief introduction motivating a consideration of the effects of rapid rotation and strong magnetic fields on neutrino-driven PNS winds, which represents the primary topic addressed by this dissertation.

1.1 Nuclear physics of the $r-$process

Significant advancements have been made in experimentally investigating the unstable $r-$process nuclei and in $r-$process nucleosynthesis simulations, which take in experimental data as input. Largely following discussions from Burbidge et al. (1957) and Cowan et al. (2021), the first half of this section explains the physical mechanism of the $r-$process and the conditions required to produce heavy elements ($Z > 26$). The second half briefly reviews the structure of modern $r-$process nuclear reaction network simulations and some of experimental progress made in determining the nuclear ingredients required for such simulations.

1.1.1 Mechanism of the $r-$process

To achieve the high neutron capture rates required for the r-process, extremely high neutron densities $\sim 10^{26}$ cm^{-3} are required; insofar that free neutrons are unstable under ordinary terrestrial or astrophysical conditions (with mean lifetime of about 14 minutes) most viable astrophysical sites are "explosive", in which the high neutron exposure is achieved over a brief period of time during the dynamical expansion of neutron-rich material. For similar reasons, the r-process is likely a "primary process", in which the seed nuclei onto which neutrons are captured are not pre-existing, but are rather formed as a part of the same explosive event responsible for creating the nuclei. In such cases, matter begins in nuclear statistical equilibrium (NSE) at high temperatures $\gtrsim 10^{10}$ K and densities $\gtrsim 10^{12}$ g cm^{-3}, before falling out of it (Meyer, 1994). As densities and temperatures drop in the expanding and cooling matter, quasiequilibrium subgroups of elements form into seed nuclei up to Fe and beyond (atomic mass number $A \approx 50 - 100$) as nuclear reaction timescales become too large to satisfy full NSE. A population of free neutrons and alpha particles also remains (Woosley and Hoffman, 1992).

The $r-$process then takes place in two phases, which can be understood by comparing timescales for three types of nuclear reactions: neutron captures on target nuclei (n, γ) which raise A, photodissociations of target nuclei (γ, n) which lower A, and $\beta-$decays of target nuclei (during which neutrons in the nucleus decay to protons thereby increasing Z). The initial phase is dominated by neutron captures onto and photodissociations of target nuclei, reactions which occur on timescales much shorter than that of $\beta-$decays. As nuclei grow into neutron-rich isotopes far off the valley of stability, $(n, \gamma) \rightleftarrows (\gamma, n)-$equilibrium is reached.

The population of free neutrons will be consumed on a timescale τ_n, which may be expressed as (Cowan et al., 2021)

$$\frac{1}{\tau_n} = \frac{1}{n_s}\left(\frac{1}{\tau_{(n,\gamma)}} - \frac{1}{\tau_{(\gamma,n)}}\right), \tag{1.1}$$

where $\tau_{(n,\gamma)}$ and $\tau_{(\gamma,n)}$ are the (n, γ) and (γ, n) nuclear reaction timescales, respectively and n_s is the ratio of free neutrons to seed nuclei ("neutron-to-seed ratio"). $\beta-$decays (acting

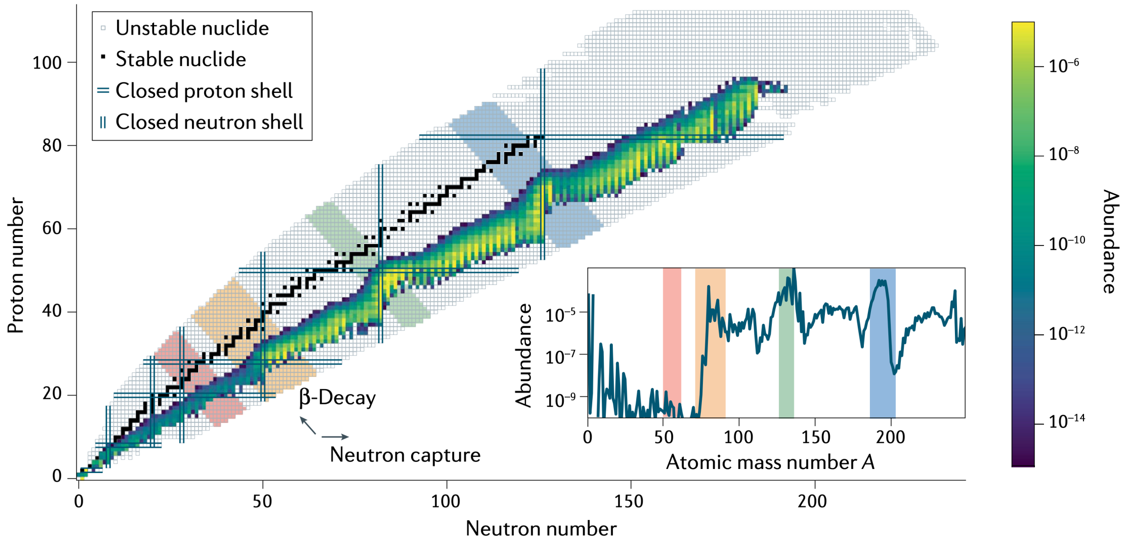

(a) Proton number Z vs. Neutron number N for stable nuclides in the valley of stability (in black) and unstable nuclides (all other squares). Nuclides along the $r-$process path are filled according to colorbar values (with arbitrary normalization), corresponding to the moment all neutrons have been captured by nuclei ($r-$process 'freeze-out') during the $r-$process. Data computed from the nuclear reaction network simulation `SkyNet` (Lippuner and Roberts, 2017). Nuclei typically begin with low $N \lesssim 30, Z \lesssim 26$, and by capturing neutrons evolve far from the valley of stability. Vertical bolded sets of lines represent closed neutron shell locations (at $N = 50, 82, 126$) where $\beta-$decay rates are lower; nuclei accumulate here, resulting in peaks in the abundance pattern shown in the inset on the lower right (corresponding to Fig. 1.1b).

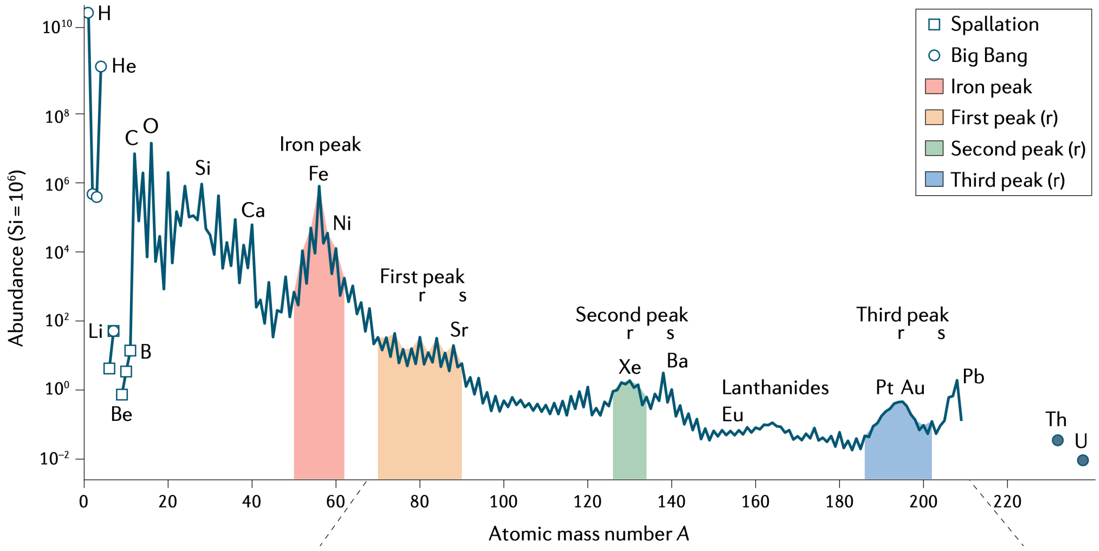

(b) Abundance vs. Atomic mass number A of the Solar $r-$process (Lodders, 2003). 4 sets of elements are highlighted: Fe-peak elements in red; first peak (LEPP) elements in yellow; second and third peak $r-$process elements in green and blue, respectively. The additional peaks in the solar abundance pattern around $A = 140, 210$ correspond to the $s-$process pattern. The shift in peaks are a result of the closed neutron shells lying at higher proton numbers in the valley of stability, as seen in Fig. 1.1a.

Figure 1.1: Path taken by nuclides in the $r-$process (top panel) and the solar abundance pattern (bottom panel). From Siegel (2022).

on timescales τ_β), though much slower with $\tau_\beta \sim 10^5 \tau_{(n,\gamma)}$, manage to push nuclei to higher Z. Thus, τ_n is large for large values of n_s, allowing the $r-$process nuclei to pass through many isotopic chains (each chain at constant Z) via slower $\beta-$decays to high Z nuclei before the population of free neutrons is exhausted. *A large n_s is essential for producing heavy elements.* For example, if a heavy element such as uranium ($A = 238$) is to be produced starting from seed nuclei with $A \approx 50 - 100$, roughly 100 additional neutrons would need to be captured per seed nuclei, requiring $n_s \approx 100$.

The reaction dynamics near so-called neutron 'magic numbers', denoting closed neutron shells with neutron numbers $N = 50, 82, 126$, affect the overall $r-$process abundance pattern (vertical bolded lines in Fig. 1.1a represent neutron magic numbers). As Z rises through $\beta-$decays interspersed throughout the more frequent (γ, n) and (n, γ) reactions, nuclei become increasingly neutron-rich, until reaching a closed neutron shell. At shell closures, the neutron separation energy (energy required to separate the least tightly bound neutron from the nucleus) plummets; any additional neutrons captured are unlikely to remain bound to nuclei. The nuclei then undergo successive $\beta-$decays followed by neutron captures which raise Z at constant N until the separation energy again exceeds some minimum value, typically around 2 MeV. Their beta-decay times τ_β rise as nuclei approach the valley of stability. As a result of their slow migration rate through this region, a population of nuclei accumulate around such shell closures resulting in an $r-$process abundance pattern with so-called 1st, 2nd, and 3rd characteristic peaks near each neutron magic number.

Because the $s-$process involves neutron captures onto stable nuclei within the valley of stability, neutron shell closures are encountered here as well for the same magic numbers $N = 50, 82, 126$. In contrast to the abundance peaks from the $s-$process, those from the $r-$process form far from stability, which shifts peaks leftwards from those of the $s-$process following the $\beta-$decays after freeze-out (note the twin peak structure for $A \sim 135, 195$ in Fig. 1.1b). These different characteristic abundance peaks are in part what allows one to differentiate between $s-$process and $r-$process contributions to the elemental compositions observed on stars, as well as by using the observed abundances of particular elements which are exclusively produced by either the $r-$process or the $s-$process (Goriely, 1999; Sneden, Cowan, and Gallino, 2008; Prantzos et al., 2020).

The abundance pattern in Fig. 1.1a shows a snapshot of $r-$process material at the beginning of its next phase: $r-$process freeze-out. This takes place once n_s drops to $\lesssim 1$, i.e, after the neutron supply is nearly exhausted. Neutron captures therefore now occur over a longer timescale, comparable to that of $\beta-$decay ($\tau_{(n,\gamma)} \sim \tau_\beta$), until nuclei reach the valley of stability. This phase of competing $\beta-$decay and neutron capture rates imprints an $r-$process abundance pattern that is smoothed out as a function of A. Because a similar competition between nuclear rates does not occur in the $s-$process, the s-process pattern shows sharper changes in the abundances between consecutive A (Cowan et al., 2021).

In addition to $\beta-$decays, neutron capture-induced fission of nuclei heavier than uranium can also play an important role in shaping the $r-$process abundance pattern. The lighter daughters of such fissioning nuclei can themselves capture neutrons, building back up to heavier potentially fission-prone nuclei. When the initial neutron abundance is sufficiently high, such a process of successive cycles of fission and neutron captures, known as "fission cycling", can repeat multiple times creating a robust pattern of $r-$process elements between the 2nd and 3rd peaks – from barium to uranium (Beun et al., 2008; Korobkin et al., 2012; Mendoza-Temis et al., 2015).

1.1.2 Requirements for a high ratio of neutrons to seed nuclei

For most astrophysical $r-$process sites of interest, neutron-rich matter begins at high temperatures and densities in the NSE phase, as a fluid composed of nucleons, alpha particles and light seed nuclei up to the Fe-group. As the expanding matter cools, charged-particle reactions freeze-out once $T \lesssim 3 \times 10^9$ K and neutron captures begin. To build elements through neutron captures up to the 2nd r-process peak ($45 \lesssim Z \lesssim 55$) the neutron-to-seed ratio at this point must exceed a critical value $n_s \gtrsim 70$, or $n_s \gtrsim 140$ to reach the 3rd r-

process peak ($65 \lesssim Z \lesssim 75$). This high requisite n_s as matter evolves out of NSE requires an astrophysical site that is either: (1) extremely neutron-rich, i.e. with a low electron fraction $Y_e \ll 0.5$ (being the ratio of protons to total baryons), such that enough free neutrons are present even if all protons end up inside seed nuclei); or (2) is conducive to the suppression of seed formation, resulting in a high neutron-to-seed ratio even without a high abundance of neutrons. Insofar that many astrophysical sites including PNS winds do not satisfy the first criteria, I now briefly review the requirements on the expanding material to fulfill the latter requirement.

During the transition from nucleons and alpha particles to heavy seed nuclei, matter must pass through a bottleneck reaction to first form ^{12}C. For symmetric or proton-rich matter, this reaction is the usual 3-body triple-alpha reaction. For neutron-rich conditions relevant to $r-$process ($Y_e \lesssim 0.5$), it is a faster 4-body "neutron-catalyzed" triple-alpha reaction (Woosley and Hoffman, 1992). For purposes of demonstration, I focus on the triple-alpha reaction case appropriate to proton-rich matter. This 3-body reaction depends strongly on density (with rate $\tau_{3\alpha} \propto \rho^2$), where the intermediate resultant $\alpha + \alpha \rightarrow ^8$Be is highly unstable with a short half-life. Seed formation of heavier nuclei will be dramatically reduced if the third reaction ^{8}Be $+\alpha \rightarrow ^{12}$C in this chain is suppressed. This is known as "alpha-rich freeze-out", where nucleons are trapped in alpha particles and are unable to combine into heavier nuclei. In relevant astrophysical environments, matter is typically radiation-dominated, so entropy is proportional to T^3/ρ (Meyer et al., 1992). It follows then that high specific entropy s in the expanding (i.e., low densities, insofar that the triple-alpha reaction occurs at roughly the same temperature $T \approx 5 \times 10^9$ K, independent of density) favor a strong alpha-rich freeze-out.

For a given value of s (i.e., a given density), an alpha-rich freeze-out is also favored when there is less time available for the reaction to occur, i.e. for a sufficiently rapid expansion rate of the gas through the relevant temperature range (equivalently, a low expansion time $\tau_{\rm exp}$, defined as that required for the the density to drop by a factor of ~ 2). If $\tau_{\rm exp} < \tau_{3\alpha}$, the fluid expands faster than the triple-alpha reactions are allowed to occur, suppressing seed formation.

Hoffman, Woosley, and Qian (1997) performed parameterized calculations of the formation of seed nuclei for initially neutron-rich material (electron fraction $Y_e < 0.5$), where the 4-body bottleneck reaction rate to form ^{12}C is $\propto \rho^3$ (instead of $\propto \rho^2$ for the normal triple-alpha reaction). They delineate the parameter space of specific entropy s, expansion timescale $\tau_{\rm exp}$, and electron fraction Y_e, for which 3rd peak $r-$process elements ($A \gtrsim 195$) can be produced via the α-rich freeze-out process described above. They define an analytic criterion which matches their full numerical results of the form

$$\eta \equiv \frac{s^3}{Y_e^3 \tau_{\rm exp}} \gtrsim \eta_{\rm crit}, \ \text{Condition for } r\text{-process} \qquad (1.2)$$

where $\eta_{\rm crit} \approx 10^{10}$ provided that s is measured in units of k_B per baryon and $\tau_{\rm exp}$ is measured in seconds (see also Lippuner and Roberts 2015). An r-process which reaches just the 2nd peak (light $r-$process) elements is possible for a somewhat lower $\eta_{\rm crit} \approx 3 \times 10^9$, while $\eta_{\rm crit} \approx 10^9$ is sufficient to form neutron-capture elements slightly heavier than Fe (though many of these can be created through charged-particle reactions in NSE under neutron-rich conditions even without an alpha-rich freeze-out).

Indeed, separate from the standard $s-$ and $r-$process, there exists an elemental abundance peak between the Fe and 2nd $r-$process peak for isotopes $38 < Z < 47$ (Johnson and Bolte, 2002; Sneden, Cowan, and Gallino, 2008) whose origin also remains debated. Though updated models of the $s-$process or even alpha captures onto seed nuclei may explain this peak, these so-called “Light Element Primary Process” (LEPP) nuclei may also be created via alpha-rich freeze-out in moderately neutron-rich or proton-rich environments (Arcones and Montes, 2011). This dissertation explores whether the conditions associated with a specific astrophysical site (neutrino-driven winds) are capable of achieving those necessary to synthesize LEPP nuclei versus light r-process element versus the full r-process extending up to the third peak elements.

1.1.3 Computing nuclear abundance yields given astrophysical conditions

In the $r-$process, nuclear reaction timescales vary by large orders of magnitude, and nuclear composition changes occur on much smaller timescales than those relevant for hydrodynamics. Consequently it is only computationally feasible to run such nuclear reaction network calculations (which consider > 7500 nuclides and 140,000 reactions in total) through a post-processing technique, in which Lagrangian densities, compositions, and temperatures extracted from hydrodynamical simulations serve as input (e.g., Hix and Thielemann 1999; Goriely, Hilaire, and Koning 2008; Kelic, Valentina Ricciardi, and Schmidt 2009; Wanajo, Janka, and Kubono 2011; Winteler 2014; Mumpower et al. 2017). One recent example of such a network is the open-source code `SkyNet` (Lippuner et al., 2017), which self-consistently evolves nuclear reactions and thermodynamic functions, given an initial temperature and prescribed density evolution $\rho(t)$. Calculations of the $r-$process require knowledge of myriad properties of unstable neutron-rich nuclei along the $r-$process path, far from the stable or nearly-stable isotopes present on Earth, or even those synthesized in the laboratory. Insofar that many of these properties are thus not experimentally measured, network calculations therefore currently rely largely on theoretical models and extrapolated experimental data.

For example, `SkyNet` uses the following input from nuclear theory and experiment: nuclear masses/partition functions and strong/weak reaction rates distributed in REACLIB (Cyburt et al., 2010), neutron-induced fission reactions (Panov et al., 2010), and spontaneous fission rates computed as in (Frankel and Metropolis, 1947) using fission barriers of (Mamdouh et al., 2001). The details of the final abundance pattern one obtains for a given set of astrophysical conditions is sensitive to the input nuclear physics at their present levels of uncertainty (Mumpower et al., 2016). Work is thus required on the nuclear experiment and theory level, as well as on the astrophysical modeling front, in order to improve our understanding of the $r-$process origin.

1.1.4 Experimental developments in $r-$process studies

Significant advancements are expected in the coming decades with next generation radioactive ion-beam facilities like FAIR and FRIB coming online (Aprahamian et al., 2018). Fig. 13-16 in Mumpower et al. (2016) highlight the range of nuclei which have a significant impact in $r-$process simulation yields. Note the large regions of neutron-rich isotopes that will soon become accessible by FRIB.

The production of rare isotopes for study has not significantly improved in the last few decades due to limitations in ion beam energy, and small cross-sections in nuclear reactions. Once beams collide however, isotopes must be separated from each other in order to be studied individually; on this front there have been considerable advancements.

There are a number of ways in which neutron-rich isotopes can be produced. One method – spallation – is the act of firing particles at and breaking up heavy target nuclei. ISOLDE (Isotope Separator On-Line DEtector) was installed at CERN to separate and analyze the products of spallation, often being neutron-rich nuclei. There have been steady advancements, including the utilization of laser ionization on fission products, which have led to more effective separation (Cowan et al., 2021). These have led to detailed measurements of $^{129-131}$Cd nuclei along the $r-$process path, crucial for reducing uncertainties around 1st peak $r-$process nucleosynthesis (Atanasov et al., 2015). The above techniques however require a minimum amount of time for extracting nuclei, preventing those with shorter half-lives from being studied.

Another technique−fragmentation−involves smashing a high energy heavy-ion beam on light target material and collecting fragments through electromagnetic separator systems. Unlike spallation, this technique allows for even short-lived isotopes to be studied if properly separated. Impressively, the $\beta-$decay half-lives of 110 neutron-rich nuclei near the $N = 82$ closed shell were simultaneously measured at RIKEN (Lorusso et al., 2015) using this technique. It is crucial that $\beta-$decay half-lives at these neutron magic numbers N_{mag} are modeled precisely, due to low separation energies at $N_{\rm mag}+1$ and substantially lower $\beta-$decay rates. $\beta-$decays govern the strength and location of these peaks (see Fig. 14 of Mumpower et al. 2016; see also the discussion in Sec. 1.1.1). When combined with nuclear mass models, the half-lives measured by Lorusso et al. (2015) substantially lowered uncertainties in the abundance pattern around the second $r-$process peak ($A \sim 130$).

Modern isotope mass measurements may be performed using time-of-flight mass spectrometers (Meisel and George, 2013) and storage rings (Litvinov et al., 2004; Sun et al., 2008; Yan et al., 2016); the most precise and accurate mass measurements to date however are those from ion traps (Blaum, 2006; Blaum, Dilling, and Nörtershäuser, 2013). Numerous facilities worldwide (e.g., LEBIT at Michigan State U, TITAN at TRIUMF in Canada, SHIPTRAP at GSI Darmstadt, Germany, ISOLTRAP at CERN, RIKEN trap in Japan) have dedicated studies to measuring nuclei masses by first using radio-frequency confinement (Paul traps) or electromagnetic fields (Penning traps) to trap ions. The phase-imaging ion-cylotron resonance technique introduced by Eliseev et al. (2013) has increased resolving power by a factor of 40, which has informed studies on distinguishing astrophysical $r-$process sites (Mumpower et al., 2016). This breakthrough has led to precision mass measurements of neutron-rich rare earth isotopes at JYFLTRAP (Vilen et al., 2018) and neutron-rich gallium isotopes at TITAN (Reiter et al., 2020).

$\beta-$delayed neutron emission can greatly increase the number of available neutrons to be captured during $r-$process freeze-out. The probabilities P_n with which neutron-rich nuclei emit neutrons have not been experimentally measured for most nuclei. Caballero-Folch et al. (2016) compared experimental results from GSI to theoretical model predictions, and found discrepancies of up to an order of magnitude, highlighting the need for experiments to back models. A recent finding by Yee et al. (2013) using traps demonstrated that one can circumvent challenges of neutron detection by measuring nuclear recoil rather than by measuring energy. Munson et al. (2018) and Siegl et al. (2018) used this technique to obtain measurements of exotic isotopes with half-lives down to 50 ms.

The final compositions obtained from nuclear reaction network simulations are sensitive to neutron capture rates after $r-$process freeze-out (when $(n,\gamma) \rightleftarrows (\gamma,n)$ equilibrium is no longer maintained). Experiments of direct neutron capture onto short-lived neutron-rich nuclei are difficult. With the $\beta-$Oslo method, one can reconstruct neutron capture rates of neutron-rich nuclei on the $r-$process path indirectly using level densities and $\gamma-$ray strength functions of nuclei closer to stability. The uncertainty in neutron-capture rates is within a factor of ~ 3 (Beard et al., 2014). Another approach is to use surrogate reactions. Here, 'surrogate particles' (such as deuterons) which contain neutrons effectively transfer their neutrons onto target nuclei (Escher and Dietrich, 2006). By measuring the surrogate particle's final state, one can infer the neutron-capture cross section. Though some experiments show promise, results indicate that a deeper understanding of such reactions is required for accurate inferences (Potel, Nunes, and Thompson, 2015; Avrigeanu and Avrigeanu, 2016; Manning et al., 2019). A novel method proposed by Reifarth et al. (2017) and supported by their simulations, involves impinging high intensity radioactive beams in a storage ring on a thermalized neutron target gas. Though technically challenging, such a facility if built would allow for measurements of neutron-capture rates on neutron-rich isotopes with half-lives less than a minute.

The density and temperature of the astrophysical environment dictate the $r-$process reaction path under $(n,\gamma) \rightleftarrows (\gamma,n)-$equilibrium, which takes place at constant neutron separation energies S_n. However, nuclei masses (which determine S_n) are not precisely known; this leads to uncertainties in the $r-$process path in nuclear reaction network simulations. There are several different approaches to mass models (Duflo and Zuker, 1995; Sun and Meng, 2008; Möller et al., 2016); all mass models fit certain parameters to known experimental data in order to predict properties of all nuclei. Known masses are reproduced well; yet extrapolating to nuclei in regions far from stability proves challenging, as shown by greater disagreement between new exotic nuclei and mass models (Audi et al., 2012). Overall, the 3-peak structure of the abundance pattern is fairly well-reproduced, independent of the choice of mass model. However discrepancies greater than 10 MeV can arise in S_n especially near the $N = 126$ shell, which can have a noticeable impact on $r-$process abundances (Mendoza-Temis et al., 2015; Mumpower et al., 2016). Differences in the abundance pattern between the 2nd and 3rd peaks is found to be washed out due to fission-cycling, which continuously produces material in this region (Mendoza-Temis et al., 2015).

Fission cycling may be responsible for producing the observed robust $r-$process pattern between 2nd and 3rd peaks (Korobkin et al., 2012; Rosswog et al., 2014; Goriely et al., 2015). Fission rates for $r-$process nuclei are challenging to study, for one because fission barriers (activation energy required for a nucleus to undergo fission) in the first place are uncertain or unknown (See calculations of a few: Howard and Möller 1980; Goriely et al. 2009; Giuliani, Martínez-Pinedo, and Robledo 2018). The dominant fission process in the $r-$process is neutron-induced fission (Panov et al., 2005; Petermann et al., 2012), but few barriers for this type of reaction have been computed (Panov et al., 2010; Giuliani et al., 2020). Fission modeling is particularly important because competition with alpha decays in the last phase of the $r-$process determines abundances of Pb, U and Th—all of which have an important impact on kilonova light curves (Barnes et al., 2016; Rosswog et al., 2017; Wanajo, 2018; Kasen and Barnes, 2019).

1.2 Observational constraints on the $r-$process sites

A variety of observations provide constraints on the sites of the $r-$process in our universe: 1) individual stellar abundance spectra, e.g., of metal-poor stars to elucidate single enrichment events; 2) overall rates and yields of potential r-enrichment sites at different epochs of cosmic time, and 3) probes of the enrichment history which ascertain the environments and timescales of r-process production (e.g., delay times with respect to star formation). From these observations, a few conclusions have been drawn, including: 1) a seemingly universal $r-$process pattern between the 2nd and 3rd abundance peaks; 2) larger event-to-event variations in the production of light $r-$process elements, as well as ultra-heavy elements beyond the 3rd peak (so called “actinide-boost” stars); 3) multiple lines of evidence supporting the dominant $r-$process site being high-yield/low rate enrichment process, both in early and recent Galactic history; 4) a range of delay timescales, spanning values from those which characterize core-collapse and type Ia supernovae, respectively.

1.2.1 Evidence for universality of the $r-$process

Following the Big Bang, the Universe consisted almost entirely of H and He. Such metal-free gas cools inefficiently, suppressing fragmentation as it undergoes gravitational collapse (see Klessen and Glover 2023 for a review). As a consequence, most of the first generation of stars form within the first 100 million years of our Universe are expected to be massive, ranging from $10 - 100 M_{\odot}$ (e.g., Jaura et al. 2022). Metals up to Fe are generated via fusion in the centers of such massive stars. At the end their short lives ($\lesssim$ 10 million years), these stars explode and enrich the surrounding gas with their contents, seeding the chemical composition of the next generation of stars. The now metal-enriched gas fragments into smaller, significantly longer-lived stars. This process gradually increases the cosmic metallicity over time, which can be tracked by the abundance ratio of Fe to H on the surfaces of stars formed in these epochs (for this purpose, we define: [A/B]$\equiv \log(N_A/N_B) - \log(N_A/N_B)_{\odot}$, where N_A (N_B) is the number of atoms of element A (B)). The second or third generation of stars, though not metal-free, are generally still metal-poor with [Fe/H] ~ -2 (Carollo et al., 2007). The field of “stellar archaeology” has produced significant clues about $r-$process enrichment as a function of cosmic time by studying the chemical compositions of metal-poor stellar atmospheres in the halo of the Milky Way and in its nearby satellite galaxies. Having formed so early in the Universe, metal-poor stars have presumably only undergone a single or at most a few $r-$process enrichment events. Any $r-$process pattern found is thus a pristine snapshot of the astrophysical process responsible for it.

The discovery of the strongly $r-$process enhanced metal-poor star CS22892-052 (Sneden et al., 1994) opened the door for studying $r-$process nucleosynthesis in the early universe. Spectra of hundreds of metal-poor red giants were cataloged by the surveys in the 2000s (Christlieb et al., 2004; Barklem et al., 2005; Honda et al., 2006a; Jacobson et al., 2015). Since 2017 the so-called "$R-$Process Alliance" network has carried on this work with telescopes in Northern and Southern hemispheres (Ezzeddine et al., 2020; Holmbeck et al., 2020). While [Fe/H] can be taken as a rough proxy for cosmic time, [Eu/Fe] reveals the level of $r-$process enhancement of a star, insofar that Eu is produced almost exclusively by the $r-$process. To date, 70 of the now 2000 observed candidates exhibit strong $r-$process enhancements with [Eu/Fe]>0.7 (Holmbeck et al., 2020). Metal-poor stars with varying levels of $r-$process enhancement have been found, from factors of 2 to 100 times higher than that found in our Solar System (Holmbeck et al., 2020; Ezzeddine et al., 2020; Cain et al., 2020). The fact that $r-$process enhancement has been seen across all phases of stellar evolution disfavors the possibility that they formed at some point within the star itself (Roederer et al., 2014). Radial velocity measurements of most r-process enriched stars show no evidence of a binary companion, ruling out mass transfer as the origin of $r-$process (Hansen et al., 2015). Indeed, heavy elements must have enriched the clouds that birthed these stars (Roederer et al., 2014).

Perhaps unsurprisingly given that many of these stars were polluted by at most a few $r-$process enrichment events, star-to-star variations are observed across certain segments of the $r-$process abundance pattern (Sneden, Cowan, and Gallino, 2008). However, for those elements between the 2nd and 3rd $r-$process peak ($Z = 56 - 92$), *every observed $r-$process enhanced metal-poor star* exhibits a similar (relative) abundance pattern (e.g., Roederer et al. 2022), which is also remarkably consistent with that measured on the Sun (after subtracting off the $s-$process component; Goriely 1999). It should be noted that solar abundances have been measured down to the isotopic level (Cameron, 1959; Asplund et al., 2009). The fact that such old stars have been enriched with the same relative heavy $r-$process abundance pattern as the Sun despite the vastly different number of events which have contributed to their enrichment, suggests a "universality" of r-process production – abundance patterns are independent of when or where one is in the universe. This set of elements is referred to as the "main" $r-$process.

The observed robustness of the main $r-$process may be attributed to either homogeneous conditions associated with repeatable classes of astrophysical events, or to properties of the nuclear physics such as fission cycling that imprint a robust pattern regardless of the precise astrophysical conditions (Korobkin et al. 2012; Rosswog et al. 2014; Eichler et al. 2015; see Sec. 1.1). One candidate for the former is a self-regulation mechanism that occurs in black hole accretion disks following the mergers of neutron stars or the collapse of massive rotating stars, which results in disk outflows with broadly similar compositions across a wide range of accretion rates (Siegel, Barnes, and Metzger, 2019; Li and Siegel, 2021; De and Siegel, 2021; Just et al., 2022a). Fission cycling can take place in the extremely neutron-rich ejecta from neutron star mergers, particularly the tidal ejecta (Mendoza-Temis et al., 2015).

1.2.2 Evidence for rare, high-yield r-process sources

Assuming the mass fraction of $r-$process elements in our Solar System $X_{\odot,r} \approx 4{\times}10^{-8}$ (Hotokezaka, Beniamini, and Piran, 2018) is roughly representative of those of stars throughout the Milky Way, one can estimate the Galactic production rate of $r-$process elements. If the average star in our Galaxy shares the same $r-$process abundance pattern of the Sun (Arnould, Goriely, and Takahashi, 2007), the total stellar mass of the Milky Way ($\approx 6{\times}10^{10} M_{\odot}$; McMillan 2011) translates into a total quantity of $r-$process material ($A \geq 69$) in our Galaxy $M_r \approx 3 \times 10^4 M_{\odot}$ (Siegel, 2019). Taking the age of the Milky Way to be $\approx 10^{10}$ years, the time-averaged Galactic $r-$process mass production rate is then $\dot{M}_r \approx 3 \times 10^{-6} M_{\odot}$ yr^{-1} (Kappeler, Beer, and Wisshak, 1989).

The r-process production rate $\dot{M}_r$ contributed by a given class of astrophysical events is the product of the event rate and the average r-process mass yield per event. Broadly speaking, the dominant $r-$process sources in the Galaxy can be either rare "high-yield" events or frequent "low-yield" events. As an example of the former, insofar as the Galactic rate of core-collapse supernova is 1/50 yr^{-1}, each supernova would need to produce only $\sim 10^{-5} M_\odot$ of r-process elements to be the dominant source. However, as we now discuss, several lines of evidence support the dominant $r-$process source being much rarer than the average core-collapse supernova.

The Milky Way halo formed by cannibalizing dwarf galaxies disrupted by its tidal field (Frebel and Norris, 2015), such that the birth conditions for most individual halo stars has been lost. Intact dwarf galaxies which still orbit the Milky Way, however, provide pristine environments with galactic histories still intact (star formation history, metal mixing, gas dilution mass). As stars in dwarf galaxies are still in their birth environments, chemical enrichment history can more accurately be reconstructed (Frebel and Ji, 2023). Ultra-faint dwarf (UFD) galaxies in particular have low masses $M_* \lesssim 2\times 10^5 M_\odot$ and are likely no longer star-forming (Simon, 2019). They have so few stars, and have experienced relatively few rare events across their histories (e.g., neutron star mergers or rare core-collapse supernovae), that the stellar abundances on individual stars can be directly linked to the enrichment sites (Frebel and Ji, 2023). High-resolution spectroscopy is available for only 20 out of the 50 known UFDs, and for the vast majority only Sr or Ba can be detected, making it impossible to distinguish $r-$process from $s-$process enrichment sources (Frebel and Norris, 2015; Ji, Drout, and Hansen, 2019).

It is remarkable then that Ji et al. (2016) found 7 out of 9 stars in the UFD Reticulum (Ret) II were highly $r-$process enhanced. Out of 10 similar UFDs for which high resolution spectra was available, Ret II was the only $r-$process enriched galaxy. Assuming an equal likelihood that any of the 10 UFDs could host $r-$process events, the probability that more than one event would occur in the same galaxy (Ret II) is at most $\left(\frac{1}{10}\right)^{\geq 2} \leq 1\%$. They estimated that about 2000 supernovae contributed to the chemical abundances of the 10 UFDs, implying that the $r-$process enrichment event that took place in Ret II must occur at a rate of only ~ 1 per every 1000-2000 supernovae. By estimating the total original H-rich gaseous mass of Ret II ($\sim 10^6 - 10^7 M_\odot$ based on simulations; e.g., Chiaki, Susa, and Hirano 2018; Magg et al. 2020), using the mass ratio of Eu to H ($\approx 10^{-10}$), and taking the mass ratio of total $r-$process material to Eu ($\approx 10^{3.0}$; Sneden, Cowan, and Gallino 2008; Côté et al. 2018), they estimate a per-event yield $r-$process yield of $M_r \gtrsim 10^{-1.8} - 10^{-0.2} M_\odot$ (accounting for uncertainties in the gas mass loss to the intergalactic medium) (Ji et al., 2023). Thus, whatever polluted Ret II with $r-$process elements must have been a rare, high-yield event.

If $r-$process element production events were sufficiently frequent in our Galaxy, the interstellar medium will build-up quasi-steady state abundances of short-lived nuclides. Deep sea sediments preserve the conditions of the interstellar medium, from which solid particles rain down into our Solar System and onto Earth, from within only the last few million years (Hotokezaka, Piran, and Paul, 2015). The radioactive isotope ^{244}Pu was detected (with half-life of ≈80 million years), and is inferred to have been deposited in the last 25 Myr (Wallner et al., 2015), at abundances lower than that expected from continuous production by 2 orders of magnitude. Moreover ^{244}Pu levels in the seabed are much lower than those found in meteoritic data, which reveals elemental abundances of the Solar System preserved from its early formation. This discrepancy points to a rare main $r-$process source enriching our Solar System (Hotokezaka, Piran, and Paul, 2015). On the other hand, significantly higher levels of ^{60}Fe were found in the seabed, which is a product of ordinary CCSN explosions; hence ^{244}Pu could not have been co-produced in significant quantities by CCSNe. This strongly disfavors ordinary core-collapse supernovae as a main $r-$process site (Wallner et al., 2021).

1.2.3 Evidence for a prompt $r-$process site disfavors compact object mergers

The birth rate of binary compact object systems (black holes and/or neutron stars) closely follows in time the star formation rate (as they are formed from short-lived massive stars collapsing), with short delay ($\sim 10 - 100$ Myr) (Eldridge and Stanway, 2022). However, binaries inspiral on significantly longer timescales, slowly radiating away energy due to gravitational wave emission before merging (Peters, 1964). The time delay between star formation and merger takes on a distribution ("delay-time distribution"), with typical delays ranging from 100s to many 1000s of Myrs (Portegies Zwart and Yungelson, 1998; Fryer, Woosley, and Hartmann, 1999; Argast et al., 2004; Matteucci et al., 2014). Observations point to a rare but prodigious event being the major source of $r-$process enrichment (consistent with compact object mergers), but the long delay-time for mergers disfavors them as the dominant enrichment sites in early galactic history, as evidenced by $r-$process enrichment at low metallicities in UFDs (Ji et al., 2016; Hansen et al., 2017). Along the same lines, $r-$process enriched globular clusters in the Milky Way halo with short star formation histories of $\lesssim 10$ Myr require delay-times that are implausible for compact object mergers[2] (Kirby et al., 2020; Zevin et al., 2019). In more recent Galactic history (from observations of higher metallicity stars), [Eu/Fe] abundances exhibit a decreasing trend due to more recent enrichment from iron-producing type Ia supernovae, which have similarly long delay-times as mergers (Freundlich and Maoz, 2021). However, this further provides evidence against mergers as a dominant $r-$process site because similar delay-times should instead result in a flat trend (Côté et al., 2017; Siegel, Barnes, and Metzger, 2019; Hotokezaka, Beniamini, and Piran, 2018).

As an example of evidence pointing to a "prompt" (short delay-time) $r-$process site being dominant in early galactic history, analysis by Ji et al. (2023) found that $\approx 70\%$ of observed stars in Ret II are $r-$process enhanced, implying the $r-$process production event occurred before 70% of the stars had formed. They further found that metals had to have been well-mixed by the time the $r-$process enhanced stars had formed. Insofar that galaxy simulations show that at least 100 Myr are required for metals to homogenize, they conclude that 30% of stars must have formed within the first 100 Myr (during which the $r-$process event occurs) – followed by a gap of at least 100 Myr to allow sufficient metal-mixing as observed – after which the last 70% of $r-$process stars formed. This places a tight upper limit on the time delay < 500 Myr with which the $r-$process event occurred following star formation, suggesting a short-delay time $r-$process site such as a prompt binary neutron star merger or core collapse supernova.

---

[2] It has been argued that a population of binaries could have formed with delay-times < 1 Myr (Belczynski, Kalogera, and Bulik, 2002) via a "common envelope" scenario of a massive star engulfing its binary companion during the expanding red giant phase of stellar evolution. However simulations of this formation channel have not yet confirmed this possibility (See Röpke and De Marco 2023 for a review).

The natal kicks that are expected to occur (from supernovae) upon formation of binary neutron star systems also present a challenge in explaining UFD $r-$process enrichment. If a merger is to enrich a dwarf galaxy (which has a relatively shallow gravitational potential), it must experience a kick less $\lesssim$ 10km s^{-1} to avoid becoming unbound before it can merge. Even with sufficiently short delay-times, galactic $r-$process enrichment is not guaranteed (Beniamini, Hotokezaka, and Piran, 2016; Bonetti et al., 2019).

1.2.4 Evidence of multiple sites for LEPP elements

In contrast to the main r-process, elements below the 2nd $r-$process peak ($38 < Z < 47$) exhibit significantly greater star-to-star scatter (by a factor of ~10) in their relative abundance patterns (Frebel and Ji, 2023). This suggests the presence of either multiple astrophysical sites, or heterogeneity within a given astrophysical site, are responsible for this group of elements (Sneden, Cowan, and Gallino, 2008). Meteoritic data on ^{129}I and ^{182}Hf provided some of the first evidence that multiple nucleosynthetic components may be responsible for the light elements $Z < 47$ (Wasserburg, Busso, and Gallino, 1996). Qian and Wasserburg (2001) and Qian and Wasserburg (2007) extended this to explain metal-poor star abundances, arguing that the lighter elements abundance pattern received different contributions from explosions of low-mass and high-mass progenitor stars. Multiple nucleosynthetic channels have been invoked to produce such elements: the weak $s-$process (Busso, Gallino, and Wasserburg, 1999), alpha captures of seed nuclei (Hoffman, Woosley, and Qian, 1997), or a LEPP (Montes et al., 2007) (See Sec. 1.1.2). This dissertation will support neutrino-driven winds from a subset of CCSNe as an appealing location for the creation of LEPP nuclei.

1.3 Candidate astrophysical sites of the $r-$process

Given the short timescales and large neutron flux required for the $r-$process, explosive phenomena related to neutron stars are the most likely candidate sources. In this section I discuss two promising sites that satisfy these basic requirements: compact object mergers and core-collapse supernovae.

1.3.1 Neutron star mergers

The first binary neutron star (BNS) system was discovered by Hulse and Taylor (1975), who showed the orbit was shrinking at a rate predicted by gravitational wave radiation losses according to General Relativity. Black hole-neutron star (BHNS) and BNS mergers were suggested as a site of $r-$process by Lattimer and Schramm (1974) and Symbalisty and Schramm (1982), who focused on the decompression of cold neutron-rich matter ejected by strong tidal forces of the companion neutron star or black hole. Paczynski (1986) first proposed that mergers could power "gamma ray bursts" (GRBs).

The first numerical simulations of BNS mergers were performed assuming Newtonian gravity (Davies et al., 1994; Ruffert, Janka, and Schaefer, 1996; Rosswog et al., 1999) and predicted mass ejection. Freiburghaus, Rosswog, and Thielemann (1999) performed the first detailed nucleosynthesis calculations based on thermodynamic trajectories extracted from the numerical simulations of Rosswog et al. (1999). Since these pioneering studies, tremendous progress was made in numerical simulations, particularly by self-consistently accounting for the effects of strong gravity by solving Einstein's equations coupled to the fluid equations of hydrodynamics. The first binary black hole and BNS merger simulations in full General Relativity were performed in the first decade of this century (e.g., Pretorius 2005; Shibata and Taniguchi 2006). These advancements in numerical simulations provided input to more extensive nucleosynthesis studies over the subsequent decade (Goriely, Bauswein, and Janka, 2011; Korobkin et al., 2012; Bauswein, Goriely, and Janka, 2013; Wanajo et al., 2014; Hotokezaka, Piran, and Paul, 2015; Radice et al., 2016; Roberts et al., 2017).

As merger simulations were finally reaching the point of making quantitative predictions, a more than 30 year old project (which was first proposed in the 1960s) was itself finally approaching completion – the Laser Interferometer Gravitational Wave Observatory (LIGO), which came online for its first observing run in 2015. Shortly after, the first gravitational waves were detected from the inspiral and coalescence of binary black holes (BBH; Abbott and al. 2016). Only two years later, the first neutron star merger was discovered with gravitational wave event GW170817 (Abbott et al., 2017b,a), accompanied by electromagnetic counterpart emission spanning the frequency spectrum (Abbott et al. 2017c; see Sec. 1.3.1). From the O1-O3 LIGO observing runs, the inferred volumetric rate is $\approx 10-1700$ Gpc^{-3} yr^{-1} for BNS mergers and $\approx 8-140$ Gpc^{-3} yr^{-1} for BHNS mergers (Abbott et al., 2023). The ongoing LIGO O4 observing run is detecting compact binary mergers at the rate of ≈ 2 per week[3]. Although most of these events will be BBH mergers, a handful of BNS or BHNS mergers are also expected; these additional events hold great promise as ways to test the predictions of our theory and simulations of these events.

Neutron star merger theory and simulations

BNS and BHNS mergers give rise to a wide variety of electromagnetic signatures (Metzger and Berger, 2012), as evidenced by observations in $\gamma-$rays, X-rays, UV, optical, infrared, and radio bands associated with GW170817 (Abbott et al., 2017a). In order to understand and place constraints on $r-$process abundances from observations, one must first have a firm grasp on underlying physical mechanisms. Numerical simulations of the merger itself, as well as the post-merger phase, are necessary for understanding the various physical processes at work. Here I briefly review the various sources of ejecta and predicted $r-$process abundance patterns from each.

In both BNS and BHNS systems, mergers can be divided into three phases. In the first, the compact objects inspiral over the course of millions of years due to gravitational waves. As orbits radiate energy, they tend to circularize well before merger (Rosswog, 2015); thus it is only necessary to simulate the latter two phases to determine the properties of ejecta. In the second phase, they merge, which lasts approximately for ~ 1 ms. Lastly, the post-merger phase lasts for ~seconds, during which matter is either accreted onto the central remnant or is ejected from the system.

---

[3] Available on the LIGO website.

Dynamical ejecta is produced during the merger phase. Tidal dynamical ejecta in the equatorial plane is generally cold, fast ($v \sim 0.1-0.3c$), and neutron-rich ($Y_e \lesssim 0.1-0.2$). The $r-$process yields of such highly neutron-rich decompressing matter is found to be independent of precise astrophysical conditions in part due to fission cycling (Korobkin et al., 2012); however, the abundances particularly for lighter elements $110 < A < 140$ (Panov, Korneev, and Thielemann, 2008; Goriely et al., 2013; Eichler et al., 2015) are sensitive to nuclear physics inputs, especially fission models (Bauswein, Goriely, and Janka, 2013; Goriely et al., 2015; Mendoza-Temis et al., 2015) (see Sec. 1.1). Simulations reproduce Solar abundances well for nuclei ($A > 140$). In BNS merger systems, the shearing contact layer between the neutron stars is unstable to the Kelvin-Helmholtz instability, which rapidly amplifies magnetic fields to large values $B \sim 10^{16}$ G (irrelevant for BHNS mergers as matter at the 'contact surface' simply falls into the BH). Simulations of neutron-star mergers recently have shown the growth of a large scale magnetic field from an initially turbulent state, even resulting in the formation of a jet (Combi and Siegel, 2023). Meanwhile, the shock-heated ejecta component attains temperatures high enough for copious pair capture reactions ($e^- + p \to n + \nu_e$, $e^+ + n \to p + \bar{\nu}_e$) which act to increase the electron fraction to moderate values ($Y_e \sim 0.25-0.4$) (Wanajo et al., 2014). Finally, up to $0.1-1\%$ of the dynamical ejecta may be ejected fast enough such that the expansion timescale of the material is shorter than the timescale for neutron captures, resulting in a 'frustrated' $r-$process despite having large neutron densities. These neutrons radioactively decay and may power an early kilonova precursor electromagnetic emission (Metzger et al., 2015; Dean, Fernández, and Metzger, 2021).

BNS mergers typically form a rapid- and differentially-rotating PNS-like remnant after coalescence. Neutrinos emitted at the neutrinosphere of the remnant (defined as the surface where optical depth $\tau_\nu = 1$) can reabsorbed in a 'gain layer' of baryonic material above the surface, driving a neutrino-driven wind (see Sec. 1.3.3 for a more in-depth discussion of the physical model in the context of CCSNe). As with the shock-heated ejecta, the neutron-rich conditions at the remnant surface are erased in the wind, in this case as a result of copious absorption of neutrinos which increase Y_e up to values around ~ 0.5. This results in significant suppression of the formation of 2nd and 3rd peak $r-$process elements in the wind (Martin et al., 2015). Unlike the roughly spherical neutrino-driven winds which follow CCSNe, the winds can be focused in the polar direction as a result of the equatorial regions blocked by the accretion disk which surrounds the remnant (Metzger and Fernández, 2014). The amount of wind ejecta scales with the lifetime of the remnant, since the neutrino-wind terminates once the remnant collapses into a BH (for lifetime $t \sim 100$ ms, typical expected mass: $\sim 10^{-3} M_\odot$). The Y_e of this component is expected to be sensitive to neutrino interactions, which are implemented in numerical simulations with various approximations to the Boltzmann equation for neutrino transport ("leakage scheme" which captures cooling: Ruffert, Janka, and Schaefer 1996; Rosswog and Liebendörfer 2003; Radice et al. 2016; Metzger and Fernández 2014; "M1 scheme" which evolves the first two moments of the Boltzmann equation: Foucart et al. 2015; Fujibayashi et al. 2017). It has been shown that the inclusion of neutrino oscillations (Li and Siegel, 2021; Richers et al., 2021; Just et al., 2022c; Fernández et al., 2022)) can result in flavor conversions of electron neutrinos/antineutrinos to μ and τ neutrinos. This suppresses neutrino absorption in the wind, and the wind retains enough neutron-richness to lead to enhanced $r-$process third-peak production (compared to a simulation that does not account for flavor conversions) (Li and Siegel, 2021). Nucleosynthesis from magnetically-driven winds has only recently begun to be explored (Combi and Siegel, 2023; Curtis et al., 2023). Metzger, Thompson, and Quataert (2018) proposed the neutrino-driven wind to be the source of the blue kilonova from GW170817 (see Section 1.3.1 for further details). Exploring the remnant parameter space (magnetization, neutrino luminosity, rotation rate) is a natural research direction following the work of this dissertation).

The final potential ejecta component from BHNS and BNS mergers, and perhaps the most prodigious in terms of $r-$process material, are the accretion disk outflows that can occur after merger. It should be noted that a disk is not guaranteed to form in the aftermath of BHNS mergers, as the neutron star may not be disrupted before falling into the black hole. Studies show that low mass ratios and/or high spin BHs are the most favorable conditions for neutron star tidal disruption (thus disk formation) and therefore allow post-merger outflows (Foucart et al., 2012; Kyutoku et al., 2015; Capano et al., 2020). Typical disk lifetimes, as set by the timescale for outwards transport of angular momentum due to internal turbulent stresses in the disk, are on the order of $t \sim 1 - 10$ s and may unbind up to $\sim 4 \times 10^{-2} M_{\odot}$ of material. Simulations show that BNS and BHNS accretion disks tend to reach a state independent of initial conditions within ~ 40 ms of formation (Siegel and Metzger, 2017, 2018a). "viscous" heating due to MRI-driven turbulence is balanced by neutrino-cooling at a state of mild electron degeneracy as a result of a self-regulatory process (Chen and Beloborodov, 2007). As a result of these mildly degenerate conditions, general relativistic magnetohydrodynamic (GRMHD) simulations by Siegel and Metzger (2018a) shows that the disk settles into a state of low $Y_e \sim 0.1$, such that outflows from the disk can reproduce solar system $r-$process abundances from the 1st to 3rd peak. Disk winds similar to those simulated are thought to be responsible for the observed red kilonova associated with GW170817 (see Sec. 1.3.1).

BHNS and BNS mergers may also form tightly collimated relativistic jets powered by accretion onto the merger remnant (Eichler et al., 1989; Narayan, Paczynski, and Piran, 1992; Metzger and Berger, 2012; Combi and Siegel, 2023). These jets, which last several seconds, are the likely central engines of short-duration class of gamma-ray bursts (sGRBs), i.e. those which last less than about 2 seconds (Berger, 2014). The sGRB that occurred within ≈ 2 s following the end of the binary inspiral in GW170817 showed that at least some sGRBs arise from BNS mergers (Eichler et al., 1989; Abbott et al., 2017a).

Effects of $r-$process heating on dynamical ejecta from mergers

How to distinguish between BHNS from BNS mergers based on their gamma-ray (Sarin et al., 2022), or−in some cases−even their gravitational wave emission (Chen and Chatziioannou, 2020), remains an open question. A significant fraction of sGRBs are accompanied by temporally extended X-ray emission which emits a comparable energy to the initial burst itself, but lasts for several seconds to minutes (Gehrels and others, 2006; Perley et al., 2009). Several models have been proposed to explain the extended emission, a spinning-down millisecond magnetar remnant created during the merger (Metzger, Thompson, and Quataert, 2008; Bucciantini et al., 2012; Rowlinson et al., 2013; Ciolfi and Siegel, 2015; Siegel and Ciolfi, 2016).

Rosswog (2007) suggested that the fall-back of debris ejected from a BHNS or BNS merger can lead to late-time accretion onto the BH, offering a mechanism to power the temporally-extended X-rays observed following some sGRBs. Because the r-process occurs on a timescale of seconds after the merger ejecta begins to decompress, heat released by the r-process can in principle impact the orbital trajectories of the debris, affecting what matter is unbound entirely and what reaches the BH on similar timescales of seconds to minutes after the merger (Metzger et al., 2010b). For example, suppression of matter with energy such that it falls back to the BH on intermediate timescales of a few seconds could lead to a lull in X-ray emission immediately after the sGRB that rises again and falls over timescales $\gtrsim 10$ s. Rosswog et al. (2014) found evidence of dynamic acceleration of material due to $r-$process heating. I explore the dynamics of this process by means of a semi-analytic model in Chapter 4. Due to the dependence of the r-process heating effects on the ejecta composition and the mass of the central remnant, I argue that this process could help observationally distinguish BNS from BHNS mergers based on the presence or absence, respectively, of late X-ray emission.

Theory and discovery of the kilonova: first confirmation of an $r-$process site

In August 2017 during the tail end of LIGO's 2nd observing run, the first neutron star merger was detected, in conjunction with electromagnetic follow up in every band from gamma rays to radio waves. I delve into a brief history and background of kilonova theory, and how this discovery provided the first smoking gun evidence of an $r-$process site in the universe.

The idea of a radioactive transient from BNS or BHNS merger ejecta was first suggested by Li and Paczyński (1998). They employed a simple semi-analytic model which assumed the radioactive decay of isotopes with logarithmically distributed half-lives. This yielded a power law radioactive heating t^{-1} with a largely unconstrained normalization, that precluded predicting the transient's luminosity. Metzger et al. (2010a) presented the first calculations of the radioactive heating rate of freshly created $r-$process nuclei (using a nuclear reaction network) and the first radiative-transfer simulations which determined the timescale and luminosity of the transient; they dubbed neutron star merger optical transients "kilonovae" based on their finding that the peak luminosity was approximately 1000 times higher than classical novae typically observed in our own Galaxy. However, lacking appropriate atomic data, Metzger et al. (2010a) assumed an opacity corresponding to that of Fe nuclei; though a good approximation for ejecta containing exclusively light r-process nuclei (which generates so-called "blue" kilonova emission), this treatment was not self-consistent. Kasen, Badnell, and Barnes (2013) showed the transient would be redder and peak over longer timescales (so-called "red" kilonova emission) than predicted by Metzger et al. (2010a) by estimating lines from lanthanide elements which, owing to the many levels of their f-shell valence electron shell, exhibit a high density of line transitions and therefore increase the opacity compared to Fe-rich ejecta from Type Ia supernovae (lanthanide nucleosynthesis requires $Y_e \lesssim 0.25$ for typical NS merger ejecta conditions; see Lippuner and Roberts 2015). Fernández and Metzger (2013) performed the first 2D simulations of the post-merger accretion torus under the simplifying parameterization of angular momentum transport as occurring by means of an

α-viscosity, finding that neutron-rich matter is ejected from the disk. Metzger and Fernández (2014) extended this work to consider the impact of a long-lived neutron star remnant on the disk outflows, showing that a sufficiently long-lived remnant can produce a blue kilonova counterpart peaking at earlier times (~ 1 day) from neutrino driven winds creating mainly light r-process nuclei. Siegel and Metzger (2017) performed the first GRMHD simulations of the post-merger BH accretion disk system, demonstrating that a self-regulating mechanism in the neutrino-cooled disks preserves neutron-rich material, and generates $\approx 6 \times 10^{-3} M_{\odot}$ of lanthanide-rich (thus high-opacity) material ejected in disk winds.

On August 17, 2017, the first neutron star merger detection was confirmed with the gravitational wave event GW170817 (Abbott et al., 2017b), followed shortly thereafter by the discovery of electromagnetic emission. A short burst of gamma-rays was detected by the *Fermi* and *Integral* satellites, with a delay of $\approx$1.7 s following the end of the binary inspiral (Abbott et al., 2017a). On timescales starting 11 hours after the burst and lasting for weeks, a blue and then red kilonova were observed−the entire thermal transient being dubbed AT2017gfo (Villar et al., 2017). The total mass and velocities of the merger ejecta inferred from the red kilonova counterpart was consistent with lanthanide-rich wind ejecta found in disk simulations by Siegel and Metzger (2017). However the velocities and mass of the blue component were much higher than expected. Metzger, Thompson, and Quataert (2018) later theorized the formation of a magnetar remnant in the aftermath of the neutron star merger, from which neutrino-driven outflows could produce the high-velocity, high-mass ejecta blue component.

1.3.2 Core-Collapse Supernovae

Core collapse supernovae were in fact the first proposed site of $r-$process nucleosynthesis (Burbidge et al., 1956; Burbidge et al., 1957; Truran et al., 1968); however theory and simulations of the supernova explosion and its aftermath have faced challenges in synthesizing $r-$process elements (Witti, Janka, and Takahashi, 1994; Martínez-Pinedo et al., 2012; Curtis et al., 2019). Moreover, the relatively high rate of CCSN (and corresponding low $r-$process yields) are in tension with several astrophysical observations (discussed in Sec. 1.2). However, a rare subclass of CCSN with a high $r-$process -yield $\gtrsim 10^{-2} - 10^{-1} M_{\odot}$ (representing at most a few percent of all stellar explosions) would be consistent with observations. Two candidates for this rare supernova class are MHD supernovae and collapsars; I now briefly review the arguments for both.

MHD supernovae

A massive star whose core is rapidly rotating at the time of its death may collapse to form a highly magnetized neutron star with an ultra-strong surface magnetic field $\sim 10^{15}$ G, a so-called "magnetar" (Duncan and Thompson, 1992; Kaspi and Beloborodov, 2017; Beniamini et al., 2019). The CCSN associated with the hypothesized birth of such rapidly spinning magnetars, known as "MHD supernovae" (LeBlanc and Wilson, 1970; Kasen and Bildsten, 2010; Nicholl et al., 2017), provide a potential site for the $r-$process (Symbalisty, 1984). Early axisymmetric simulations of magnetized core collapse Nishimura et al. (2006) and Winteler et al. (2012) found the formstion of jet-like structures giving rise to neutron-rich ejecta, the conditions needed for the successful creation of heavy $r-$process nuclei. Later 3D GRMHD simulations (Mösta et al., 2014; Mösta et al., 2015) also found jet formation and sufficient magnetic field amplification to explain the origin of the majority of magnetars (Beniamini et al., 2019). However, as a result of MHD instabilities that develop in 3D simulations (but which are suppressed in 2D), the outflow material expanded more slowly, allowing the ejecta to be irradiated with neutrinos enhancing Y_e and reducing the prospects for successful $r-$process (Mösta et al., 2018; Obergaulinger, Just, and Aloy, 2018; Reichert et al., 2020). Prompt explosions, combined with aligned magnetic dipole and rotational axes (within 30 degrees) yield strongest $r-$process (Halevi and Mösta, 2018). Weaker MHD supernovae yield less neutron-rich ejecta, and therefore a weaker $r-$process. Further, observations of energetic engine-driven supernovae do not show signs of high-opacity $r-$process material in the outer layers of the explosion ejecta, despite the prediction that matter from the explosion may be mixed to the surface (Winteler et al., 2012). Though the possibility for variation in this site may explain variations for $r-$process abundances past the 3rd peak (Wehmeyer, Pignatari, and Thielemann, 2015; Thielemann et al., 2017), it does not appear to be robust astrophysical site for the $r-$process.

Collapsars

Another rare type of CCSN and promising $r-$process site are 'collapsars', first proposed by Woosley (1993) as a model for the long-duration class of GRBs (lGRBs: GRBs lasting $\gtrsim 2$ seconds) (Kouveliotou et al., 1993). The model considers the fate of a massive rotating star ($M \sim 40 M_{\odot}$) with a large Fe core that fails to explode at the end of its life (Wilson et al., 1986). Instead, the core collapses into a BH, with outer in-falling layers of the rotating star forming a centrifugally-supported accretion disk which powers the observable lGRB. This model received support after Galama and others (1998) detected a highly energetic supernova (so-called "hypernova") 1998bw with kinetic energy $> 10^{52}$ erg, following the long GRB 980425. This discovery motivated additional global simulations of the collapse of rotating massive stars and the disk/jet formation process (MacFadyen and Woosley, 1999; MacFadyen, Woosley, and Heger, 2001; Fujimoto et al., 2006; Nagataki et al., 2007; Sekiguchi et al., 2011; McKinney, Tchekhovskoy, and Blandford, 2013).

Owing to large spatial/temporal scale separation and wide range of physical processes involved, it is difficult to self-consistently model the collapsar from core-collapse, to BH+disk formation, and finally to the launching of the jet. Instead, several studies have focused on specific aspects of the model (e.g., Pruet, Thompson, and Hoffman 2004; McLaughlin and Surman 2005; Fujimoto et al. 2007; Janiuk 2014; Nakamura et al. 2015). Disk wind outflows under the same arguments given in Sec. 1.3.1 are likely to be neutron-rich for sufficiently high accretion rates (Beloborodov, 2003; Siegel and Metzger, 2018a; De and Siegel, 2021) – a promising sign for collapsars as an $r-$process site. Siegel, Barnes, and

Metzger (2019) argue from their disk simulations that $r-$process yields per collapsar event may be as high as $\sim 1M_{\odot}$ – much greater than ejecta from the MHD supernova scenario. The authors further demonstrate that due to their 'prompt' nature (short delay time $\sim$ 10 Myr between massive star formation and collapsar event, compared to that of NS - see Sec. 1.2), collapsars as the dominant galactic source of $r-$process best explain [Eu/Fe] trends among stars in the Milky Way disk and halo. Other groups have since run large-scale simulations of collapsars/collapsar disks finding less neutron-rich outflows, though with simplifying assumptions (Fujibayashi et al., 2022; Just et al., 2022b) or very high disk masses (which enhance neutrino emission) (Miller et al., 2019). Questions still remain, a few of which include: the nature of the stellar progenitor, conditions leading to a successful vs. failed hypernova, conditions for the emergence of the jet, and whether the ejection of $r-$process material is necessarily concomitant with the hypernova.

1.3.3 The neutrino-driven wind

In the seconds following a successful CCSN, in which the outer layers of the massive star are ejected by an outward propagation shock, the remaining bound core is a hot PNS, which cools via neutrino emission (due to extremely high densities $\rho \gtrsim 10^{12}$ g cm^{-3}, which prevent the escape of photons during this phase). Duncan, Shapiro, and Wasserman (1986) found that copious neutrino emission is responsible for producing a thermally-driven outflow of matter known as the the neutrino-driven wind. As the wind expands and cools below $T \simeq 0.5$ MeV, free nucleons fall out of NSE and assemble into alpha particles and heavier seed nuclei. This occurs typically at radii $r \sim 50 - 100$ km, outside of which $r-$process nucleosynthesis begins. The next section provides a historical overview of the developments in assessing the viability of the $r-$process in neutrino-driven PNS winds.

Simulations of neutrino-driven winds assessing $r-$process viability

Woosley and Hoffman (1992) found neutrino-driven winds to be a promising site for $r-$process nucleosynthesis. Although the winds are only moderately neutron-rich ($0.4 \lesssim Y_e \lesssim 0.46$), they found sufficiently high entropies were achieved ($s > 100k_b$ bar^{-1}) for the alpha-rich freeze-out mechanism discussed in Sec. 1.1.2. However, later supernova simulations found lower entropies $s < 100k_B$ nuc^{-1} (Witti, Janka, and Takahashi, 1994). Qian and Woosley (1996) obtained analytical expressions for the $r-$process -relevant wind properties s, τ_{exp}, and Y_e as a function of the PNS properties in the context of Newtonian gravity. They concluded that high entropies necessary for an alpha-rich freeze-out are not robustly obtained by neutrino-heating along, leading them to consider potential additional heating sources in the wind. Cardall and Fuller (1997) showed that including general relativistic (GR) effects leads to higher wind entropies and lower expansion timescales, thus increasing the neutron-to-seed ratio for higher PNS compactness (M/R).

Otsuki et al. (2000) and Thompson, Burrows, and Meyer (2001) developed steady-state 1D parameterized models of the neutrino-driven wind phase, performed as a function of the PNS mass and neutrino properties (independent of a global core-collapse simulation). Even including GR effects, they found wind entropies/expansion timescales were not sufficient to achieve the main r-process. Nevertheless, the neutrino-driven wind is still considered as a potential site of weak $r-$process or LEPP nuclei, provided the wind is neutron rich, $Y_e < 0.5$ (Roberts, Woosley, and Hoffman, 2010; Arcones and Montes, 2011; Akram et al., 2020).

Efforts since then have been directed towards incorporating increasingly detailed neutrino physics into hydrodynamic simulations with the aim of determining wind properties more precisely. Some studies focus on the long-term cooling evolution of the PNS (Fischer et al., 2010; Hüdepohl et al., 2010; Roberts et al., 2012) starting self-consistently from core-collapse initial conditions. With the inclusion of convection, Roberts et al. (2012a) find a proton-rich wind which undergoes the $\nu p-$process (Fröhlich et al., 2006) and can produce $p-$process nuclei such as ^{92}Mo (Martínez-Pinedo, Fischer, and Huther, 2014; Wanajo, 2018). More recently, Wang and Burrows (2023) performed 3D core-collapse simulations for a variety of initial mass progenitors, resulting in self-consistently generated neutrino-driven winds. They found wind entropies $< 50k_b$ bar^{-1} for all progenitor masses, and for some models, relatively small portions of the wind with electron fraction < 0.5. Given the sensitivity to neutrino physics, work is ongoing to incorporate neutrino processes to better understand the nucleosynthetic yields of neutrino-driven winds from the birth of ordinary (slowly rotating, weakly magnetized) neutron stars.

The next section details the events of a core-collapse supernova that lead to the formation of the neutrino-driven wind.

Core-collapse supernova, proto-neutron star formation and cooling

In the last few moments of a massive star's life, temperatures at the center of the Fe core become high enough such that the Fe nuclei photodisocciate and matter neutronizes, reducing the degeneracy pressure provided by electrons. Unstable gravitational collapse ensues. This increase in density leads to further neutronization and thermal emission, both which generate large quantities of neutrinos that remain trapped due to the extreme nuclear densities attained. In less than a second, the gravitational potential energy of the Fe core ($E_{\rm bind} \sim \frac{3GM_{\rm PNS}^2}{5R}$) is transformed into the internal energy of a now neutron-rich remnant. Given a supernova successfully explodes (which is not guaranteed), outer layers initially free-fall and then 'bounce' off the now compressed, neutronized core, becoming unbound and being ejected from the system. Considerable progress has been made in the last few decades in precisely understanding the supernova ejection mechanism, though is not yet entirely understood. This is however outside the scope of this dissertation.

The core is now a hot PNS which undergoes Kelvin-Helmholtz contraction in two phases. The first is deleptonization, where on the order of $N \sim M_{\rm PNS}/m_p \approx 1{\times}10^{57}\left(\frac{M_{\rm PNS}}{1.4M_\odot}\right)$ neutrinos (due to the fact that neutrinos are produced by converting protons in the core to neutrons) heat the PNS core as they diffuse out. This is followed by a cooling stage where the entropy gradually declines. At such interior temperatures and nuclear densities ($\rho \sim 10^{14}$ g cm^{-3}), the energy of the PNS is primarily radiated away via neutrinos, each with energy $E_\nu \sim E_{\rm bind}/N_L \approx 60$ MeV. The neutrino cross section σ_ν is given by

$$\sigma_\nu = \frac{4G_F^2 E_\nu^2}{\pi} \approx 3 \times 10^{-40} {\rm cm}^2 \left(\frac{E_\nu}{60{\rm MeV}}\right)^2, \tag{1.3}$$

where G_F is the Fermi coupling constant and E_ν is the characteristic neutrino energy. The neutrino mean free path λ_ν may then be estimated as

$$\lambda_\nu \sim \frac{1}{\bar{n}_b \sigma_\nu} \approx 14{\rm cm} \left(\frac{E_\nu}{60{\rm MeV}}\right)^{-2} \left(\frac{R_{\rm pns}}{12{\rm km}}\right)^3 \left(\frac{M_{\rm pns}}{M_\odot}\right)^{-1}, \tag{1.4}$$

where $\bar{n_b}$ is the average baryonic number density, $M_{\rm pns}$ & $R_{\rm pns}$ are the mass and radius of the PNS respectively. The neutrino mean free path is much smaller than the radius $R_{\rm PNS}$ of the PNS (≈ 10 km), so the diffusion approximation holds with the diffusion timescale being $t_{\rm diff} \sim R_{\rm PNS}^2/(\lambda_\nu c) \sim 1 - 10$ s. Thus, neutrinos diffuse out on timescales of $t \sim 1$ minute (Burrows and Lattimer, 1986), until they reach the radius – defined as the neutrinosphere – with optical depth $\tau \sim 1$ and are able to escape freely. The detection of about 30 neutrinos over a period of 15 seconds from supernova 1987A confirmed this picture (Bionta et al., 1987; Hirata et al., 1987).

The neutrino luminosity of the PNS may be estimated as:

$$L_\nu \sim E_{\rm bind}/t_{\rm diff} \sim 10^{52} \text{ erg s}^{-1}. \tag{1.5}$$

Numerous codes have been developed to simulate the long-term PNS cooling evolution over the last ~35 years (Burrows and Lattimer, 1986; Pons et al., 1999; Fischer et al., 2010; Hüdepohl et al., 2010; Roberts et al., 2012; Nakazato et al., 2013).

This dissertation focuses on a single snapshot of the PNS in its cooling stage, at approximately ~ 1s post-bounce (see Fig. 2 of Roberts and Reddy 2017). The aim is to achieve steady-state neutrino properties during the $\simeq$ 100 milliseconds-long evolution of the simulation, in order to study the effects of neutrino properties on wind properties relevant for nucleosynthesis.

Physics of the neutrino-driven wind

The dominant weak interactions responsible for neutrino absorption and are

$$\nu_e + n \rightleftarrows e^- + p \quad \text{and} \quad \bar{\nu}_e + p \rightleftarrows e^+ + n, \tag{1.6}$$

where ν_e, $\bar{\nu}_e$ are the electron neutrino and anti-neutrino, e^-, e^+ are the electron and positron, and n, p are the neutron and proton.

The forward direction represents neutrino absorption, which heats up baryonic material, while the backwards direction represents neutrino emission, which cools material. ν_τ and ν_μ neutrinos are also included, usually grouped together as ν_x in simulation codes.

The PNS mass $M_{\rm PNS}$ and radius $R_{\rm PNS}$ as well as neutrino luminosities L_ν and energies E_ν decay on timescales longer than the sound crossing time and time for matter to be accelerated to supersonic speeds from the gain region (Thompson, Burrows, and Meyer, 2001). Thus the wind may be assumed to be in steady-state, governed by the following conservation equations for mass, momentum, and energy, respectively:

$$\begin{aligned} \dot{M} &= 4\pi r^2 \rho v && (1.7)\\ v\frac{dv}{dr} &= -\frac{1}{\rho}\frac{dP}{dr} - \frac{GM_{\rm PNS}}{r^2} && (1.8)\\ \dot{q} &= v\left(\frac{d\varepsilon}{dr} - \frac{P}{\rho^2}\frac{d\rho}{dr}\right), && (1.9) \end{aligned}$$

where $\dot{M}$ is the mass loss rate, v is the velocity, $\dot{q}$ is the net specific heating rate, ρ is the density, r is the radius, ε is the specific internal energy, and G is the gravtitational constant.

Heating is most prominent near the surface of the PNS – in a so-called 'gain layer' at $\sim R_{\rm PNS}$. The neutrino specific heating rate $\dot{q}^+$ is given by

$$\dot{q}^{+} \propto \frac{E_\nu^2 L_\nu}{r^2} \tag{1.10}$$

while the specific cooling rate $\dot{q}^{-}$ is proportional to

$$\dot{q}^{-} \propto T^6, \tag{1.11}$$

where T is the temperature of the gain layer (Qian and Woosley, 1996).

To see that a gain layer with net positive neutrino heating must exist, note that the region near the vicinity of the PNS is in near hydrostatic equilibrium ($v \ll \sqrt{GM_{\rm PNS}/R_{\rm PNS}}$), so Eq. 1.8 implies $\frac{dP}{dr} \approx -\rho \frac{GM_{\rm PNS}}{r^2}$. Further note that temperatures are high enough such that the fluid is radiation pressure-dominated, so $P \propto T^4$ and $s \propto T^3/\rho$. This implies $T \propto r^{-1}$, or $\dot{q}^{-} \propto r^{-6}$ from Eq. 1.11. Net specific neutrino heating then takes the functional form $\dot{q}_{\rm net} = \frac{A}{r^2} - \frac{B}{r^6}$, where A, B are constants. It follows that an intermediate region of net positive heating lies between $r = R_{\rm PNS}$ (where $\dot{q}^{-} \approx \dot{q}^{+}$) and $r \to \infty$ (where $\dot{q}^{-} = \dot{q}^{+} \to 0$).

Setting $\dot{q}^{+} = \dot{q}^{-}$ gives an approximation for the temperature in the gain layer $T_{\rm gain}$. The baryonic wind must climb out of the gravitational potential well in order to unbind from the PNS. To do so matter must gain specific energy $\Delta u \sim \frac{GM_{\rm PNS}}{R_{\rm PNS}}$ via neutrino absorption, which corresponds to a gain in specific entropy $\Delta s \approx GM_{\rm PNS}/(R_{\rm PNS} T_{\rm gain})$. In terms of neutrino and wind properties, the entropy of the wind is therefore

$$s \propto L_\nu^{-1/6}\ E_\nu^{-1/3}\ R_{\rm PNS}^{-2/3}\ M_{\rm PNS}. \tag{1.12}$$

$\dot{M}$ and the expansion timescale of the wind $\tau_{\rm exp}$ may be derived following similar arguments (Qian and Woosley, 1996). The results are shown below:

$$\dot{M} \propto L_\nu^{5/3}\ E_\nu^{10/3}\ R_{\rm PNS}^{5/3}\ M_{\rm PNS}^{-2} \tag{1.13}$$

$$\tau \propto L_\nu^{-1}\ E_\nu^{-2}\ R_{\rm PNS}\ M_{\rm PNS} \tag{1.14}$$

Variations on the neutrino-driven wind

It has been shown that ordinary neutrino-driven winds likely do not achieve the necessary conditions for the main $r-$process (e.g., Qian and Woosley 1996; Thompson, Burrows, and Meyer 2001). Several studies have since then incorporated alternative mechanisms to achieve conditions more amenable to the $r-$process in the form of additional heating (Suzuki and Nagataki, 2005; Metzger, Thompson, and Quataert, 2007; Gossan, Fuller, and Roberts, 2020; Nagakura, Burrows, and Vartanyan, 2021).

One such example is a study on the effects of convection inside the PNS (Nevins and Roberts, 2023). Specifically in this model, the effects of gravito-acoustic waves generated by convection are incorporated into the wind energy and momentum conservation equations. Physically, these waves are generated within the PNS in a layer of convection, attentuated in a layer near the surface, and continue to propagate radially outwards until shock formation and dissipation in the wind region ($r \sim$ tens of km). The region of shock dissipation overlaps with the $\alpha-$forming region, i.e., where seed nuclei are formed. If heating occurs at a radius within the $\alpha-$formation surface, seed nuclei formation is inhibited, making conditions favorable for a strong $r-$process.

A range of wave luminosities and frequencies are sampled, and results are compared to wind simulations without wave heating. They find that even for wave luminosities 10^{-5} times that of neutrino luminosities, impact on wind dynamics is appreciable and has two effects: (1) the wind is accelerated, which lowers τ_{exp} and raises s; and (2) shock heating in the wind region can generate conditions for strong $r-$process even when moderately neutron-rich and for waves with only 10^{-4} times neutrino energy flux.

1.3.4 This Dissertation: Rapid Rotation and Strong Magnetic Fields

I study variations of the ordinary spherical neutrino-driven wind addressed by Qian and Woosley (1996) and Thompson, Burrows, and Meyer (2001). In Chapters 2-3 of this dissertation, I use a GRMHD code to self-consistently evolve a hot PNS and wind with neutrino absorption and emission. With these simulations I study the wind at what should be considered a single snapshot in the course of the entire cooling stage of the PNS, meant to capture the response of key $r-$process parameters s, Y_e, and $\tau_{\rm exp}$ from various wind properties. In Chapter 2, I reproduce the spherical neutrino-driven wind as a control, and all else being the same, simulate winds from rapidly rotating PNSs with a range of rotation periods. In this manner I isolate the effects of rotation to ascertain its effects on neutrino and wind properties, and to assess the viability of $r-$process by measuring effects on the three key parameters s, Y_e, and $\tau_{\rm exp}$. In Chapter 3, I run a similarly controlled experiment, except with strong magnetic fields, without rotation.

Tolman–Oppenheimer–Volkoff Equations

The Tolman–Oppenheimer–Volkoff (TOV) equations are the relativistic equations of hydrostatic equilibrium derived for non-vacuum solutions to Einstein's Equations, which describe a static non-rotating, unmagnetized neutron star. They are as follows:

$$\frac{dP}{dr} = -\frac{G(M_g + 4\pi r^3 P)(\rho c^2 + \rho\varepsilon + P)}{r^2\Gamma^2} \tag{1.15}$$

and

$$\frac{dM_g}{dr} = 4\pi r^2(\rho c^2 + \rho\varepsilon), \tag{1.16}$$

where M_g is the gravitational mass, P is the pressure, ρ is the mass density, ε is the specific internal energy, r is the radius, and $\Gamma = \sqrt{1 - 2GM_g/r}$. Additionally, an equation of state $P = P(\rho, T, Y_e)$ is required. We employ a tabulated nuclear equation of state which governs matter at high densities. Exact properties of matter at and above nuclear densities are unknown; we use the SFHo equation of state (EOS) (Steiner, Hempel, and Fischer, 2013) which is constructed to be consistent with both nuclear experimental data and neutron star mass observations (Hebeler et al., 2010; Tsang et al., 2012; Lattimer and Lim, 2013). The pressure and internal energy density of the fluid is determined by the EOS.

Neutrino absorption

Previous studies such as (Thompson, Burrows, and Meyer, 2001) have input neutrino luminosities by hand as a boundary condition at the surface of the PNS. We choose to adapt a more self-consistent approach, where we include the effects of neutrino absorption and emission on composition and energy of matter in the PNS and wind. Neutrino luminosities are thereby a result of the ad hoc initial PNS density, temperature and composition profile from (Kaplan et al., 2014).

Using the neutrino scheme from (Radice et al., 2016), we evolve the first moment of the Boltzmann transport equation for neutrinos, evolving average energies and number densities separately for species $\nu_e, \bar{\nu}_e$ and ν_x (which includes both $\mu-$ and $\tau-$ neutrinos). The neutrino evolution is coupled to fluid evolution; neutrinos deposit energy to matter and alter the composition based on interactions in Bruenn (1985) and Ruffert, Janka, and Schaefer (1996). Electron fraction evolution is governed primarily by the reactions in Eq. 1.6 giving

$$\frac{dY_e}{dt} = (\lambda_{e^+} + \lambda_{\nu_e})Y_n - (\lambda_{e^-} + \lambda_{\bar{\nu}_e})Y_p, \tag{1.17}$$

where λ_x is the absorption/capture rate of particle x from the reactions in Eq. 1.6, and Y_n, $Y_p = Y_e = 1 - Y_n$ are the neutron and proton mass fractions (the latter being equal to Y_e due to charge conservation).

We are concerned with the limiting case where neutrino absorption dominates emission, as it does in the gain layer of the neutrino-driven wind:

$$Y_{e,\mathrm{eq}}^{\mathrm{abs}} = \frac{\lambda_{\nu_e}}{\lambda_{\nu_e} + \lambda_{\bar{\nu}_e}} \tag{1.18}$$

In terms of neutrino energies and luminosities, the neutrino absorption rate using Eq. 1.10 is $\lambda_\nu \propto \langle \dot{E}_\nu^2 \rangle \approx (L_\nu / \langle E_\nu \rangle) \langle E_\nu^2 \rangle$.

The asymptotic electron fraction $Y_e^{\rm eq}$ of the neutrino-driven wind is thus (Qian and Woosley, 1996)

$$Y_{e,\rm eq}^{\rm abs} \approx \left[1 + \frac{L_{\bar{\nu}_e}(\epsilon_{\bar{\nu}_e} - 2\Delta + 1.2\Delta^2/\epsilon_{\bar{\nu}_e})}{L_{\nu_e}(\epsilon_{\nu_e} + 2\Delta + 1.2\Delta^2/\epsilon_{\nu_e})}\right]^{-1}, \tag{1.19}$$

where $\Delta \equiv m_n - m_p \simeq 1.293$ MeV and $\langle\epsilon_\nu\rangle \equiv \langle E_\nu^2\rangle/\langle E_\nu\rangle$ is the corresponding ratio of mean neutrino energy moments (additional terms Δ terms are corrections from weak magnetism). Baryons have gravitational binding energy per nucleon of ~ 200 MeV, which greatly exceeds mean neutrino energies ~ 20 MeV; thus by the time the wind is unbound it will have absorbed $\gtrsim 10$ neutrinos. The initially neutron-rich history of the wind is erased and Y_e of the wind rapidly approaches $Y_{e,\rm eq}^{\rm abs}$.

It is evident from Eq. 1.19 then that in order to obtain a neutron-rich (low-Y_e) wind, electron anti-neutrino energies/luminosities must deviate sufficiently from electron neutrino energies/luminosities.

Rapid rotation

The neutrinosphere is at the base of an approximately isothermal gain layer such that the sound speed is $c_s \simeq (kT/m_p)^{1/2}$. One can approximate the neutrino luminosity as that of a blackbody $L_\nu \simeq 4\pi 7/8 R_\nu^2 \sigma T^4$. Then PNS rotation becomes dynamically important only for spin periods $P = 2\pi/\Omega$ less than

$$P_c \approx 2\pi\frac{R_\nu}{c_s} \approx 3.4 \text{ ms}\left(\frac{R_\nu}{12 \text{ km}}\right)^{5/4}\left(\frac{L_\nu}{10^{52} \text{ erg s}^{-1}}\right)^{-1/8} \tag{1.20}$$

Chapter 2 investigates the effects of rapid rotation of a PNS, i.e. for spin periods $P < P_c$, on the wind properties.

Magnetars

Magnetars, highly magnetized neutron stars with surface dipole strength $10^{14} - 10^{15}$ G, make up at least 10% of the young neutron star population, though they may represent a much larger fraction (Kaspi and Beloborodov, 2017). About 30 have been discovered (Olausen and Kaspi, 2014). Most are slowly spinning with relatively long $\sim 2 - 10$ s rotation periods (Igoshev, Popov, and Hollerbach, 2021). Observations of supernova remnants associated with magnetars all have ordinary explosion energy (Martin et al., 2014; Zhou et al., 2019), suggesting that most magnetars are formed in the aftermath of standard supernovae. Indeed, magnetars are too common ($> 10\%$ of NSs) to be associated with only rare SNe (1% of all SNe) (Kouveliotou et al., 1994; Gill and Heyl, 2007; Beniamini et al., 2019). Vink and Kuiper (2006) constrain the initial rotation period of new-born, or proto-magnetars, to $\gtrsim 5$ ms by asserting the rotational energy must not exceed the supernova explosion energy.

How can magnetic fields be amplified to magnetar-strength fields? With flux-freezing (Woltjer, 1964; Ferrario and Wickramasinghe, 2006), magnetic fields in the cores of massive stars can amplify during core-collapse under magnetic flux conservation. However Spruit (2008b) argue that fields would not amplify sufficiently to match observations of magnetic field strengths in magnetars and pulsars. More recently thanks to new astroseismic techniques (Fuller et al., 2015), Cantiello, Fuller, and Bildsten (2016) found that the cores of some massive stars indeed have sufficiently high magnetic field strengths to form magnetars via flux-freezing during core-collapse. High initial magnetic fields would couple the massive star core to the outer envelope, reducing angular momentum thereby resulting in a more slowly rotating proto-magnetar (Spruit, 2008a).

The magnetic field may be amplified within ~seconds after core-collapse instead, e.g., via convective dynamos in the PNS (Duncan and Thompson, 1992). In a recent study, White et al. (2022) analyze the core collapse-simulations from Burrows et al. (2020) which include advanced treatments of microphysics (neutrino transport, equation of state, neutrino-matter coupling) and attain vigorous convection in the formed PNS. Though these simulations do not include magnetic field evolution, White et al. (2022) analyze the possibility of magnetic field amplification via the convective dynamo. They compute the Rossby number (Ro), which is the ratio of the rotation period to eddy turnover timescale. Previous studies (Christensen and Aubert, 2006; Olson and Christensen, 2006) found a low (modified) Ro ($\lesssim 0.12$; i.e., rotation rate is high relative to turnover rate) enables the convective dynamo to generate strong magnetic fields. White et al. (2022) find in their models that even rotation periods as large as ~ 2 s have sufficiently low Ro sustained for a long enough time for predicted magnetic fields to reach $> 10^{15}$ G.

Such evidence motivates our study in Chapter 3, in which we endow a non-rotating neutron star with a strong dipole magnetic field. Though proto-magnetars are likely born with mild rotation period (e.g., $\boldsymbol{P} > 100$ ms), this would have the effect of opening a larger fraction of field lines in the polar regions (Metzger, Thompson, and Quataert, 2008). Field lines in the equatorial region may still exhibit a dipole-like structure where results from our study might apply.

Chapter 2: Neutrino-Driven Winds from Rotating Protoneutron Stars

This work has published and may be found ***here.***

The aftermath of a successful core-collapse supernova explosion is the formation of a hot, proto-neutron star (PNS) that cools via the emission of thermal neutrinos over the ensuing seconds, radiating the gravitational binding energy of the star (e.g., Burrows and Lattimer 1986; Pons et al. 1999; Roberts 2012; see Roberts and Reddy 2017 for a recent review). These neutrinos deposit energy into the atmosphere of the PNS, driving an outflow of mass known as the *neutrino-driven wind* (e.g., Duncan, Shapiro, and Wasserman 1986; Qian and Woosley 1996; Thompson, Burrows, and Meyer 2001). A similar PNS cooling phase, and concomitant neutrino-driven wind, accompanies the cooling evolution of the remnant of a neutron star merger (e.g., Dessart et al. 2009; Metzger and Fernández 2014; Perego et al. 2014; Kaplan et al. 2014; Metzger, Thompson, and Quataert 2018), in cases when the remnant does not promptly collapse into a black hole.

The neutrino wind has long been considered a potential site for the nucleosynthesis of heavy neutron-rich isotopes through the rapid neutron capture process (r-process; e.g., Meyer et al. 1992; Takahashi, Witti, and Janka 1994; Woosley et al. 1994). The many past studies of neutrino-driven winds have primarily been focused on spherically symmetric, non-rotating PNS winds accelerated by thermal pressure (e.g., Kajino et al. 2000; Sumiyoshi et al. 2000; Otsuki et al. 2000; Thompson, Burrows, and Meyer 2001; Arcones, Janka, and Scheck 2007; Fischer et al. 2010; Roberts, Woosley, and Hoffman 2010; Arcones and Montes 2011; Roberts et al. 2012b; Martínez-Pinedo et al. 2012; Fischer et al. 2012). This body of work has led to the conclusion that normal PNS winds fail to achieve the conditions necessary for nucleosynthesis to reach the third r-process peak around an atomic mass number $A \sim 195$. The latter requires an outflow with a combination of high specific entropy s_∞, short expansion timescale $\tau_{\rm exp}$, and low electron fraction Y_e (Hoffman, Woosley, and Qian, 1997; Meyer and Brown, 1997) as it passes through the radii where seed nuclei form. In particular, even for only moderately neutron-rich conditions (e.g., $0.4 \lesssim Y_e \lesssim 0.5$) a sufficiently large value of $s_\infty^3/(Y_e^3\tau_{\rm exp})$ results in a high ratio of neutrons to seed nuclei−and hence a successful heavy r-process−by trapping protons into α-particles as a result of the freeze-out of the neutron-modified triple-α reaction ^{4}He(αn,γ)^{9}Be(α,n)^{12}C (e.g., Meyer et al. 1992; Woosley and Hoffman 1992).

Several ideas have been proposed beyond the standard scenario in order to achieve a high neutron-to-seed ratio, and a successful second- or third-peak r-process. These include postulating the existence of additional sources of heating (e.g., damping of convectively-excited waves; Suzuki and Nagataki 2005; Metzger, Thompson, and Quataert 2007; Gossan, Fuller, and Roberts 2020) or by resorting to extreme parameters, such as massive $\gtrsim 2.2M_\odot$ neutron stars (Wanajo, 2013) or those with extremely strong magnetic fields ("magnetars"; Thompson 2003; Thompson, Chang, and Quataert 2004; Metzger, Thompson, and Quataert 2007; Metzger, Thompson, and Quataert 2008; Vlasov, Metzger, and Thompson 2014; Vlasov et al. 2017).

Insofar as rapidly spinning magnetars are contenders for the central engines of gamma-ray bursts (e.g., Thompson, Chang, and Quataert 2004; Bucciantini et al. 2007; Metzger et al. 2011), the nuclear composition of their outflows may have important implications for the gamma-ray emission mechanism (e.g., Beloborodov 2010) and the composition of cosmic rays accelerated in the relativistic jet (e.g., Metzger, Giannios, and Horiuchi 2011; Bhattacharya, Horiuchi, and Murase 2021). Nevertheless, the physical processes responsible for the creation of an ordered large-scale magnetic field during the PNS phase remain uncertain and subject to active research (e.g., Raynaud et al. 2020).

Two of the potentially important ingredients in neutrino-driven winds, which we explore in this work, are the effects of general relativity (GR) and rapid rotation. The deeper gravitational potential well of the PNS present in GR tends to increase the entropy of the outflows relative to an otherwise equivalent model with Newtonian gravity by around 50% (e.g., Cardall and Fuller 1997; Otsuki et al. 2000; Thompson, Burrows, and Meyer 2001). Rotation, on the other hand, will generally act to decrease the entropy of the outflows, by reducing the effective gravitational potential due to centrifugal effects (e.g., Metzger, Thompson, and Quataert 2007). Extremely rapid rotation could in principle also reduce the wind electron fraction, in part because fewer neutrino absorptions per nucleon are necessary to unbind the wind material near the rotational equator, allowing the outflow's composition to remain closer to that of the highly neutron-rich PNS surface (e.g., Metzger, Thompson, and Quataert 2008).

Beyond parametrized one-dimensional models (e.g. Duncan, Shapiro, and Wasserman 1986; Qian and Woosley 1996; Thompson, Burrows, and Meyer 2001), numerical work on neutrino-driven winds has focused on 1D and 2D Newtonian hydrodynamical simulations with approximate neutrino transport (e.g., Arcones, Janka, and Scheck 2007; Hüdepohl et al. 2010; Fischer et al. 2010; Roberts, Woosley, and Hoffman 2010; Nakazato et al. 2013; Dessart et al. 2009; Arcones and Janka 2011). Three-dimensional simulations have so far concentrated on the neutron star merger case, including the Newtonian simulations by Perego et al. (2014). Three-dimensional simulations in the context of core-collapse supernovae have so far focused on the early post-bounce evolution and the explosion mechanism itself, rather than on the long-term cooling evolution of the PNS (e.g., Burrows et al. 2020).

In this paper, we explore the effects of rapid rotation on neutrino-heated PNS winds by means of general-relativistic hydrodynamical simulations with approximate neutrino transport. Rather than employing initial conditions for the PNS motivated by self-consistent supernova or merger simulations, we instead follow previous work (Kaplan et al., 2014) in constructing parameterized models for the thermodynamic and compositional structure of the PNS that result in neutrino luminosities and energies consistent with those predicted by successful supernova and neutron star merger simulations to occur a few seconds after the birth of the star (the epoch over which most of the integrated wind mass-loss occurs). By first isolating the effects of rapid rotation in the purely hydrodynamical context, our work here also paves the way for future simulations which will include additional effects, such as the presence of a strong ordered magnetic field.

This paper is organized as follows. In Section 2.1, we describe the physical set-up, initial conditions, and numerical code used to perform our neutrino-wind simulations. In Section 2.2, we describe our results, starting with non-rotating PNS wind solutions and then moving on to the rotating cases. As we shall discuss, rapid (~ millisecond period) rotation can have large effects on essentially all of the key wind properties. In Section 2.3 we summarize our conclusions and speculate on the potential role of rapidly spinning PNS birth as sources of heavy neutron-rich nuclei.

2.1 Methodology

2.1.1 Numerical Evolution Code

Our simulations of PNS winds are performed in three-dimensional general-relativistic hydrodynamics (GRHD) using a modified version of `GRHydro` (Mösta et al., 2014) as described in Siegel and Metzger (2018b), which is built on the open-source `Einstein Toolkit`[1](Goodale et al., 2003; Schnetter, Hawley, and Hawke, 2004; Thornburg, 2004; Löffler et al., 2012; Babiuc-Hamilton et al., 2019). This code implements the equations of ideal general-relativistic magnetohydrodynamics with a finite-volume scheme using piecewise parabolic reconstruction (Colella and Woodward, 1984) and the approximate HLLE Riemann solver (Harten, Lax, and Leer, 1983). Recovery of primitive variables is implemented using the framework presented in Siegel et al. (2018) and Siegel and Mösta (2018), which provides support for any composition-dependent, three-parameter equation of state (EOS). The magnetic field is evolved using a variant of constrained transport (the "flux-CT" method; Tóth 2000) in order to maintain the solenoidal constraint. In the present study of purely hydrodynamical winds, however, the magnetic field is ignored. Its initial field strength is set to a very small number and monitored throughout the evolution to ensure that it does not impact the dynamics of the simulation.

---

[1] http://einsteintoolkit.org

Although the code is capable of evolving spacetime, the present set of simulations employs a fixed metric for computational efficiency, determined self-consistently from the matter distribution of the initial conditions (Sec. 2.1.2). A fixed spacetime is a good approximation here, because the star's structure remains nearly constant in time and less than a fraction of $\sim 10^{-5}$ of the star's mass is removed by winds over the duration of the simulation. We also performed a test simulation including the full metric evolution, which exhibited only small differences from the fixed-metric case.

We consider both non-rotating and rotating PNS models (Sec. 2.1.2). The computational domain is set-up as a Cartesian grid hierarchy consisting of one base grid and six nested refinement levels for our non-rotating PNS model. In our fiducial non-rotating PNS model `nrot-HR`, the finest and smallest grid is a $30 \times 30 \times 30\,\mathrm{km}$ box centered at the origin and the center of the star, with a resolution of $\Delta x \simeq 225$ m. The size of the largest box is $960\,\mathrm{km} \times 960\,\mathrm{km} \times 960\,\mathrm{km}$, which allows us to capture the wind zone and to determine the asymptotic properties of the wind. In comparison, the grid setup for our most rapidly rotating PNS models (`rot.7-MR`, `rot.6-MR`) has one less refinement level, with the finest and smallest grid being a $60 \times 60 \times 60$ km box; this is necessary to resolve the high-velocity outflows from the PNS surface out to larger radii. All of our rotating models employ a spatial resolution on the finest grid of $\Delta x \simeq 450$ m.

We find that our adopted resolution is not sufficient to resolve the neutrino decoupling region near the PNS surface, which we quantify in Fig. 2.1 using the optical depth scale-height near the neutrinosphere obtained once our wind solutions have reached a steady state. This would require a resolution that is approximately a factor of 10 higher than the highest

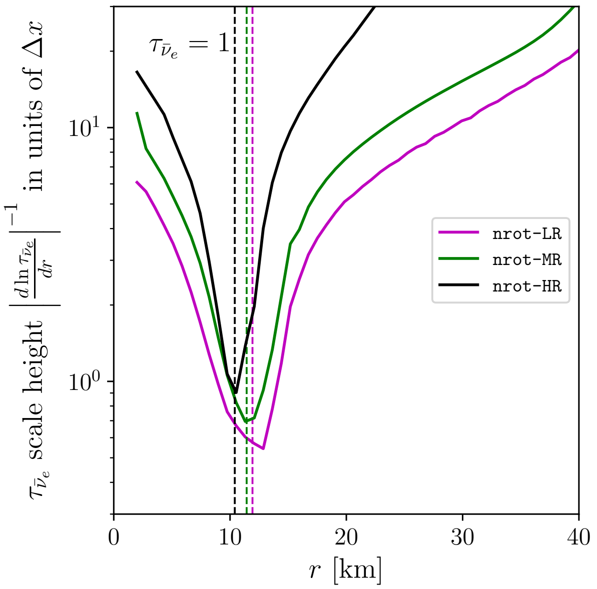

Figure 2.1: Scale height $H = \left|\frac{d \ln \tau_{\bar{\nu}_e}}{dr}\right|^{-1}$ associated with the $\bar{\nu}_e$ optical depth $\tau_{\bar{\nu}_e}$, as a function of radius r from the center of the PNS (*solid lines*), averaged over polar angle ($\theta = 0° - 90°$) and time-averaged from 50 to 100 ms for our three non-rotating PNS solutions with different spatial resolution: `nrot-MR` (black, $\Delta x \simeq 450$ m), `nrot-LR` (*purple*, $\Delta x \simeq 620$ m), and `nrot-HR` (*green*, $\Delta x \simeq 225$ m). None of the simulations resolve the region around the neutrinosphere radius ($\tau_{\bar{\nu}_e} = 1$; *vertical dashed lines*) with several grid points, and hence cannot accurately converge on the neutrino luminosity or mean energy. However, the gain region of net heating and wind zone on larger scales is well resolved by even the lowest resolution runs.

resolution run we have explored (`nrot-HR`, with $\Delta x \simeq 225$ m), which is computationally infeasible for this study. As discussed below, we therefore do not (nor would we expect to) obtain convergent values for the steady-state neutrino luminosities or mean energies (Figs. 2.4 and 2.8), as these are determined near the decoupling surface. However, this deficiency is not critical for the purposes of this study, because the neutrino radiation field serves primarily as a boundary condition controlling the wind heating and compositional changes at larger radii above the neutrinosphere−regions which are properly resolved. For example, our fiducial simulation `nrot-HR` resolves the temperature scale-height in the decoupling region with at least 4-5 points while obtaining reasonably convergent hydrodynamic wind properties. Furthermore, as discussed in Section 2.2, the key wind properties (e.g., mass loss rate, entropy) obtained by our non-rotating PNS simulations performed at lower spatial resolution than the fiducial model (`nrot-MR` and `nrot-LR`, respectively) do agree with one another to $\lesssim 10\%$, once the impact of their different neutrino luminosities and energies are accounted for as predicted by analytic scaling relations (Qian and Woosley, 1996).

In order to reduce computational costs, we make use of appropriate symmetries and limit the computational domain to one quadrant of the full 4π–3D domain. For our rotating models, the z-axis corresponds to the rotational axis; thus for all models we employ 180° rotational symmetry around the z-axis (simulating only the $x > 0$ domain), as well as reflection symmetry across the xy-plane.

On physical grounds, we do not expect these symmetries to have an appreciable impact. For example, the wind entropy gradient in the gain layer is positive (cf. Fig. 2.3f) and thus large-scale convective instabilities do not arise. Furthermore, our stellar models are not differentially rotating and have sufficiently low ratios of rotational energy to gravitational binding energy ($T/|W|$; see Tab. 2.1), so that they do not develop non-axisymmetric instabilities. To ensure that indeed our results do not depend on the choice of symmetry, we performed one of our rotating simulations with and without imposing symmetry (simulating the full 4π-$3D$ domain for about 10 ms), finding indistinguishable results in the two cases.

Weak interactions and approximate neutrino transport are included via a leakage scheme (Bruenn, 1985; Ruffert, Janka, and Schaefer, 1996) following the implementation of Galeazzi et al. (2013) and Radice et al. (2016) as described in Siegel and Metzger (2018b), together with a 'ray-by-ray' transport scheme ('M0' scheme; Radice et al. 2016, 2018). The M0 scheme represents an approximation to neutrino transport derived by taking the first moment of the Boltzmann equation and using a closure relation that assumes neutrinos stream along radial rays at the speed of light. Neutrino mean energies and number densities are evolved according to radial evolution equations (Eqs. (A11) and (A15) of Radice et al. 2016). This ray-by-ray transport scheme does not account for potential neutrino interactions between different rays (i.e. lateral transport). The M0 transport scheme will be least accurate in regions of high optical depth, i.e. within the PNS for our study. As a result, the neutrino properties within the PNS may not be fully consistent with the temperature profile. However, in this region we initiate a somewhat *ad hoc* radial temperature profile (Sect. 2.1.2), rather than one based on a self-consistent evolution (e.g., from the stellar core collapse or neutron star merger). In the spirit of previous work (e.g., Thompson, Burrows, and Meyer 2001) our primary goal is instead to characterize the properties of the resulting wind at a given neutrino luminosity and mean energy. Thus, the radial approximation should be sufficient because the wind is launched above the surface of the PNS where the optical depth is low, and is furthermore roughly spherically symmetric, even in the fastest rotating models.

The leakage scheme includes charged-current β-processes, electron-positron pair annihilation, and plasmon decay (plasma wave packets that create neutrino pairs) (Ruffert, Janka, and Schaefer, 1996). Neutrino opacities include neutrino absorption by nucleons and coherent scattering on free nucleons and heavy nuclei. We neglect the effects of magnetic fields on the neutrino opacities, which is a good approximation except unless the PNS is extremely highly magnetized (e.g., Beloborodov 2003; Duan and Qian 2004). Optical depths are calculated using the quasi-local scheme presented by Neilsen et al. (2014).

The neutrino evolution is coupled to the equations of GRHD in an operator-split fashion, leading to electron fraction changes as well as neutrino energy and momentum deposition to matter. The dominant weak reactions for heating the wind and changing the electron fraction are

$$\nu_e + n \longleftrightarrow e^- + p \quad \text{and} \quad \bar{\nu}_e + p \longleftrightarrow e^+ + n, \tag{2.1}$$

where ν_e and $\bar{\nu}_e$ are the electron neutrino and anti-neutrino, p is the proton, n is the neutron, and e^- and e^+ are the electron and positron, respectively.

Neutrino energies and number densities are evolved on radial rays that represent a uniform spherical 'M0 grid' extending radially to 200 km, with $n_r \times n_\theta \times n_\phi = 600 \times 20 \times 40$ grid points. As neutrino transport quantities only slowly change in time with respect to the hydro time step, and for computational efficiency, effective neutrino absorption is updated via M0 only every 16 time steps of the hydro evolution. Neutrino transport includes three neutrino species: electron neutrinos and anti-neutrinos ($\nu_e, \bar{\nu}_e$), as well as all μ and τ neutrinos and anti-neutrinos grouped into one additional category (ν_x). The grid covers the neutrinosphere (for all species), defined by the surface above which the neutrino optical depth to infinity lies between 0.7 and 1, and the gain layer, where net neutrino heating unbinds matter from the PNS surface. The grid also extends to large enough radii to cover all densities for which weak interactions are expected to be appreciable ($\rho \gtrsim 10^4$ g cm^{-3}).

2.1.2 Neutron Star Models and Initial Conditions

For initial conditions, we construct axisymmetric hydrostatic profiles of non-rotating and solid-body rotating neutron stars of gravitational mass $1.4 M_\odot$ with the `RNS` code (Stergioulas and Friedman, 1995). Our grid of simulations, and the key properties of the PNS for each model, are summarized in Table 2.1.

For the equation of state (EOS), we adopt the SFHo[2] model (Steiner, Hempel, and Fischer, 2013), which covers particle densities from 10^{27} to 10^{40} cm^{-3} and temperatures from 0.1 to 160 MeV. The EOS parameters are calibrated to nuclear binding energies as well as to other observational and experimental constraints. For densities below saturation density, the model accounts for light and heavy nuclei formation, and smoothly transitions from nuclei to uniform nuclear matter with a thermodynamically consistent excluded volume description (Hempel and Schaffner-Bielich, 2010). A distribution of different nuclear species are assumed, rather than just the single nuclei approximation. Results for light nuclei are in agreement with quantum many-body models. The presence of nuclei ensures that nuclear binding energy released as individual nucleons recombine into light nuclei is captured by the flow; conversion of this energy into kinetic energy can significantly affect the unbinding of winds (cf. Sec. 2.2). For this EOS, the radius of a $1.4 M_\odot$ non-rotating cold neutron star is 11.88 km and the maximum stable mass is 2.059 $M_\odot$.

---

[2] Available in tabulated form on stellarcollapse.org.

The initial temperature profile of the star as a function of density, $T(\rho)$, must be specified as an initial condition. Although our goal is to study PNS winds generated following a core-collapse supernova (or, potentially, a neutron star merger), we do not obtain the initial temperature profiles directly from supernova or merger simulations. Rather, we specify $T(\rho)$ as an *ad hoc* functional form following Kaplan et al. (2014), the parameters of which are so chosen to generate steady-state neutrino emission properties from the star similar to those predicted a few seconds after a successful core collapse explosion (e.g., Pons et al. 1999) or neutron star merger event (e.g., Dessart et al. 2009). Specifically, we adopt a temperature profile that smoothly transitions from the hot PNS core temperature $T_{\max}$ to a colder atmosphere temperature $T_{\min}$ (Eq. (A1) of Kaplan et al. 2014):

$$T(\rho) = T_{\min} + \frac{T_{\max}}{2}\left(\tanh\frac{(\log_{10}(\rho) - \bar{m})}{\bar{s}} + 1\right), \tag{2.2}$$

where $\bar{m}$ is the midpoint of the logarithmic density roll-off and $\bar{s}$ is the e-folding scale. We use the temperature profile denoted `C20p0` in Kaplan et al. (2014), with parameters set as follows: $\bar{m} = 14.2$, $\bar{s} = 0.3$, $T_{\min} = 0.015$ MeV, and $T_{\max} = 20$ MeV. These parameter values were chosen to give rise to approximate target values of the neutrino luminosities and mean energies, once a steady wind has been established.

As with the temperature profile, the initial electron fraction profile $Y_e(\rho, T)$ must be specified. Given the EOS and temperature profile, we again follow Kaplan et al. (2014) and set

$$\begin{aligned} Y_e(\rho, T[\rho]) &= Y_{e,\nu-\mathrm{free}\beta}(\rho)(1 - e^{-\rho_{\mathrm{trap}}/\rho}) \\ &+ Y_{e,\nu-\mathrm{trap}\beta}(\rho, T[\rho])e^{-\rho_{\mathrm{trap}}/\rho}, \end{aligned} \tag{2.3}$$

where $Y_{e,\nu-\mathrm{free}\beta}$ denotes the electron fraction for cold matter in β-equilibrium without neutrinos (computed at T_{min}) and $Y_{e,\nu-\mathrm{trap}\beta}$ refers to the electron fraction for hot and dense matter in β-equilibrium with neutrinos present. For densities $\rho \ll \rho_{\mathrm{trap}} \sim 10^{12.5}$ g cm^{-3}, neutrinos decouple from matter. To account for free streaming neutrinos near the PNS surface ($\rho \lesssim \rho_{\mathrm{trap}}$), the attenuation factor $e^{-\rho_{\mathrm{trap}}/\rho}$ serves to smoothly connect the hot and cold matter solutions.

The function $Y_{e,\nu-\mathrm{free}\beta}$ in Eq. (2.3) is obtained from the EOS according to the condition

$$\mu_\nu = 0 = \mu_p - \mu_n + \mu_e, \tag{2.4}$$

at T_{min}, where μ_ν, μ_n, μ_p, μ_e are the chemical potentials of the neutrinos, neutrons, protons, and electrons, respectively. As the neutrino density n_ν is negligible in the free-streaming regions, the lepton fraction (ratio of lepton to baryon number) obeys $Y_{\mathrm{lep}} = Y_{e,\nu-\mathrm{free}\beta}$.

We calculate $Y_{e,\nu-\mathrm{trap}\beta}$ by treating neutrinos as a relativistic Fermi gas in equilibrium, computing the neutrino fraction Y_ν according to

$$Y_\nu = \frac{n_\nu}{\rho N_A}, \tag{2.5}$$

where n_ν is obtained from Fermi integral relations (Eq. (B5) of Kaplan et al. 2014). We then iteratively solve the relation

$$0 = Y_{\rm lep} - (Y_{e,\nu-{\rm trap}\beta} + Y_\nu), \tag{2.6}$$

where $Y_{\rm lep}$ is computed from Eq. (2.4), used here as a fixed input. The value of Y_e dictated by this prescription is roughly constant for $\rho \lesssim 10^7$ g cm^{-3} (corresponding to the "atmosphere" on the simulation grid), so we initialize $Y_e(\rho \lesssim 3 \times 10^6$ g cm$^{-3})$ to $Y_{\rm atm} \approx 0.46$. Likewise, we set the density and temperature of the initial atmosphere to $\rho_{\rm atm} = 340$ g cm^{-3} and $T_{\rm atm} = 0.015$ MeV, respectively.

Stellar models are computed using `RNS`, which solves the general-relativistic Euler equations for a uniformly rotating star in axisymmetric spacetime (Stergioulas and Friedman, 1995). In specifying the EOS, `RNS` requires a table of the energy density as a function of pressure. We generate this table over the relevant range of densities using the EOS with the temperature and Y_e prescriptions from above. A stellar model is constructed by specifying a central density ρ_c and a polar to equatorial radius axis ratio R_p/R_e. For solutions with arbitrary rotation frequency, `RNS` first integrates the TOV equations and finds a nearest solution. The code then estimates solutions through an iterative procedure until the desired ratio R_p/R_e is achieved. For the non-rotating models, the radius of the neutron star is found to be $R_e = R_p = 12.70$ km, larger than the equivalent cold radius of 11.88 km and consistent with the temperature-dependent PNS radius found by Kaplan et al. (2014).

For our most rapidly rotating model `rot.6-MR`, we adopt a PNS rotating near-break up, with $\Omega/\Omega_K \approx 0.944$, where Ω_K is the Keplerian orbital frequency, corresponding to an axis ratio $R_p/R_e = 0.6$ ($R_{\rm e} \simeq 17.6$ km) and spin period $P \approx 1.11$ ms. We also run two cases of intermediate rotation, $R_p/R_e = 0.7$ (`rot.7-MR`; $P = 1.15$ ms) and $R_p/R_e = 0.9$ (`rot.9-MR`; $P = 1.78$ ms). Further details on the models are given in Table 2.1.

Table 2.1: Suite of $1.4 M_\odot$ PNS Simulations

Model -	$R_e^{(a)}$ (km)	$P^{(b)}$ (ms)	$R_p/R_e^{(c)}$ -	$T/\lvert W\rvert^{(d)}$ -	$\Omega/\Omega_{\rm K}^{(e)}$ -	$R_{\bar{\nu}_e}^{(f)}$ (km)	$\langle L_{\nu_e}\rangle^{(g)}$ (erg s^{-1})	$\langle L_{\bar{\nu}_e}\rangle^{(h)}$ (erg s^{-1})	$\langle E_{\nu_e}\rangle^{(i)}$ (MeV)	$\langle E_{\bar{\nu}_e}\rangle^{(j)}$ (MeV)
`nrot-LR`	12.7	n/a	1	0	0	12.1	5.3e51	8.5e51	12.5	18.0
`nrot-MR`	12.7	n/a	1	0	0	11.4	4.1e51	6.7e51	13.3	17.8
`nrot-HR`*	12.7	n/a	1	0	0	10.5	2.5e51	4.2e51	12.8	18.3
`rot.9-MR`	13.4	1.78	0.9	2.6e-2	0.40	10.5–11.7	2.9e51	4.4e51	12.5	18.4
`rot.7-MR`	15.7	1.15	0.7	7.8e-2	0.75	9.8–16.4	3.3e51	5.2e51	12.0	17.1
`rot.6-MR`	17.6	1.11	0.6	9.4e-2	0.94	10.0–17.5	3.0e51	4.9e51	11.7	17.0

(a) Initial equatorial radius. (b) Spin period. (c) Initial ratio of polar to equatorial radius. (d) Ratio of total rotational energy to gravitational binding energy. (e) Ratio of rotational frequency to Keplerian frequency at stellar equator, $\Omega_{\rm K} = \sqrt{GM/R_e^3}$. (f) Steady-state radius of the anti-electron neutrinosphere (or range of radii, in rotating cases). $(g) - (j)$ Luminosities and mean energies of electron neutrinos and anti-neutrinos, averaged over the final factor of three in simulation time. Model names ending in `HR, MR, LR` have smallest box resolutions of $225, 450, 620$m, respectively.

*Fiducial non-rotating wind model shown in Figs. 2.2, 2.3.

2.1.3 Conditions for r-process nucleosynthesis

Before describing the results of our simulations, we briefly review the physical processes in the PNS wind that determine whether a successful r-process can take place. The surface of the PNS and the inner regions of the wind are sufficiently hot that protons and neutrons exist as free nucleons. Free nuclei recombine into α-particles at radii in the wind where the temperature decreases to $T \lesssim 5 \times 10^9$ K, as typically occurs $\sim 50 - 100$ km above the PNS surface in our models (cf. Figs. 2.2 and 2.5). Heavier elements then begin to form as the temperature decreases further, starting with the reaction ^{4}He(αn,γ)^{9}Be(α,n)^{12}C for $Y_e \lesssim 0.5$. After ^{12}C forms, additional α particle captures produce heavy seed nuclei with characteristic mass $\bar{A} \approx 90 - 120$ and charge $\bar{Z}$ (“alpha-process”; e.g., Woosley and Hoffman 1992). Finally, the r-process itself occurs, as the remaining free neutrons (if any) capture onto these seed nuclei.

The maximum atomic mass $A_{\rm max}$ to which the r-process can proceed depends on the ratio of free neutrons to seed nuclei following the completion of the α-process. Because ^{12}C-formation is the rate-limiting step to forming the seeds, the neutron to seed ratio (and hence $A_{\rm max}$) depends on the electron fraction Y_e, asymptotic wind entropy s_∞, and expansion time $\tau_{\rm exp}$ through the seed formation region (Meyer and Brown, 1997; Hoffman, Woosley, and Qian, 1997). We follow Hoffman, Woosley, and Qian (1997) in defining the latter as[3]

$$\tau_{\rm exp} \equiv \frac{1}{v^r}\left|\frac{d{\rm ln}T}{dr}\right|^{-1}_{\rm T=0.5MeV}. \tag{2.7}$$

For $\bar{Z}/\bar{A} \approx 0.35 - 0.4 \lesssim Y_e \lesssim 0.5$, the condition for the r-process to reach the second or third peak can be expressed as[4]

$$\begin{aligned} \eta &\equiv \frac{s_\infty^3}{Y_e^3\tau_{\rm exp}} \\ &\gtrsim \eta_{\rm thr} \approx \begin{cases} 4\times10^9 & \text{if } A_{\rm max}\sim 135 \text{ (2nd peak)} \\ 9\times10^9 & \text{if } A_{\rm max}\sim 195 \text{ (3rd peak)} \end{cases}, \end{aligned} \tag{2.8}$$

where s_∞ is expressed[5] in k_b baryon^{-1} and $\tau_{\rm exp}$ in seconds. Thus, the ratio $\eta/\eta_{\rm thr}$ serves as a "figure of merit" for the potential success of a given r-process site in the $0.4 \lesssim Y_e \lesssim 0.5$ regime.

Previous studies of the r-process in spherical non-rotating PNS winds typically find $\eta \ll \eta_{\rm thr}$, thus disfavoring these events as sources of heavy r-process nuclei unless $Y_e \ll 0.4$. Furthermore, if $Y_e > 0.5$, as suggested by some recent cooling calculations of non-rotating PNS (e.g., Pascal, Novak, and Oertel 2022), then an r-process will not be achieved for any value of η (however, see Meyer 2002 for an exception).

---

[3] Thompson, Burrows, and Meyer (2001) define a similar quantity, but in terms of the gradient of the density profile rather than the temperature ($\tau_{{\rm exp},\rho}$). Given that entropy obeys $s \propto T^3/\rho$ for a radiation-dominated plasma and that s is roughly constant in the wind outside the gain region, it follows that $\tau_{\rm exp} \approx 3\ \tau_{{\rm exp},\rho}$.

[4] The combination $s^3/\tau_{\rm exp}$ enters because the abundance of ^{12}C nuclei (and hence the number of seed nuclei) created in the wind is equal to an integral of the effective 4-body ^{4}He(αn,γ)^{9}Be(α,n)^{12}C reaction rate $\propto \rho^3$ times the timescale available for formation $\propto \tau_{\rm dyn}$; for radiation-dominated conditions $s \propto T^3/\rho$ and so $\rho \propto s^{-1}$ given that seed nuclei form at roughly a fixed temperature.

[5] Throughout the remainder of the paper, specific entropy is expressed in units of k_B baryon^{-1} for notational brevity.

On the other hand, if $Y_e < \bar{Z}/\bar{A} \sim 0.35 - 0.4$, then an r-process is possible for $\eta \ll \eta_{\rm thr}$, with third-peak element production occurring for $Y_e \lesssim 0.25$ (Lippuner and Roberts, 2015). The latter is the regime encountered in the dynamical and disk-wind ejecta of neutron star mergers (e.g., Freiburghaus, Rosswog, and Thielemann 1999; Siegel and Metzger 2017) and, potentially, the winds from rapidly spinning proto-magnetars (e.g., Metzger, Thompson, and Quataert 2007; Metzger, Thompson, and Quataert 2018).

2.2 Results

2.2.1 Non-Rotating PNS Wind

Figures 2.2–2.4 illustrate our results for the fiducial non-rotating model `nrot-HR`. Figure 2.2 shows snapshots through the meridional ($y = 0$) plane of various quantities near the end of the simulation at $t = 152$ ms, once the wind has achieved an approximate steady-state (defined such that the asymptotic wind properties have reached a state of being approximately radially and temporally constant). Figure 2.3 shows angle-averaged radial profiles of the density ρ, temperature T, radial velocity v^r, net specific heating rate $\dot{q}_{\rm net}$, mass-loss rate $\dot{M}$, specific entropy s, and electron fraction Y_e at different snapshots in time, starting from $t \approx 30$ ms and going through to the end of the simulation at $t \approx 142$ ms. The net specific heating rate is given by

$$\dot{q}_{\rm net} = \dot{q}^{+} - \dot{q}^{-} = \sum_{\nu_e, \bar{\nu}_e} \kappa_{\nu_i} (n_{\nu_i}/\rho) E_{\nu_i} - \sum_{\nu_i} \dot{q}^{\rm eff}_{\nu_i}, \tag{2.9}$$

where κ_{ν_i}, n_{ν_i}, and E_{ν_i} denote the neutrino opacities, number densities, and mean energies, respectively, and $\dot{q}^{\rm eff}_{\nu_i}$ are the total specific cooling rates for each neutrino species $\nu_i = \{\nu_e, \bar{\nu}_e, \nu_X\}$. Here, ν_X collectively labels the heavy-lepton neutrinos and antineutrinos. The time evolution of the outflowing wind properties, angle-averaged across a spherical surface of radius 60 km, are shown in Figure 2.4.

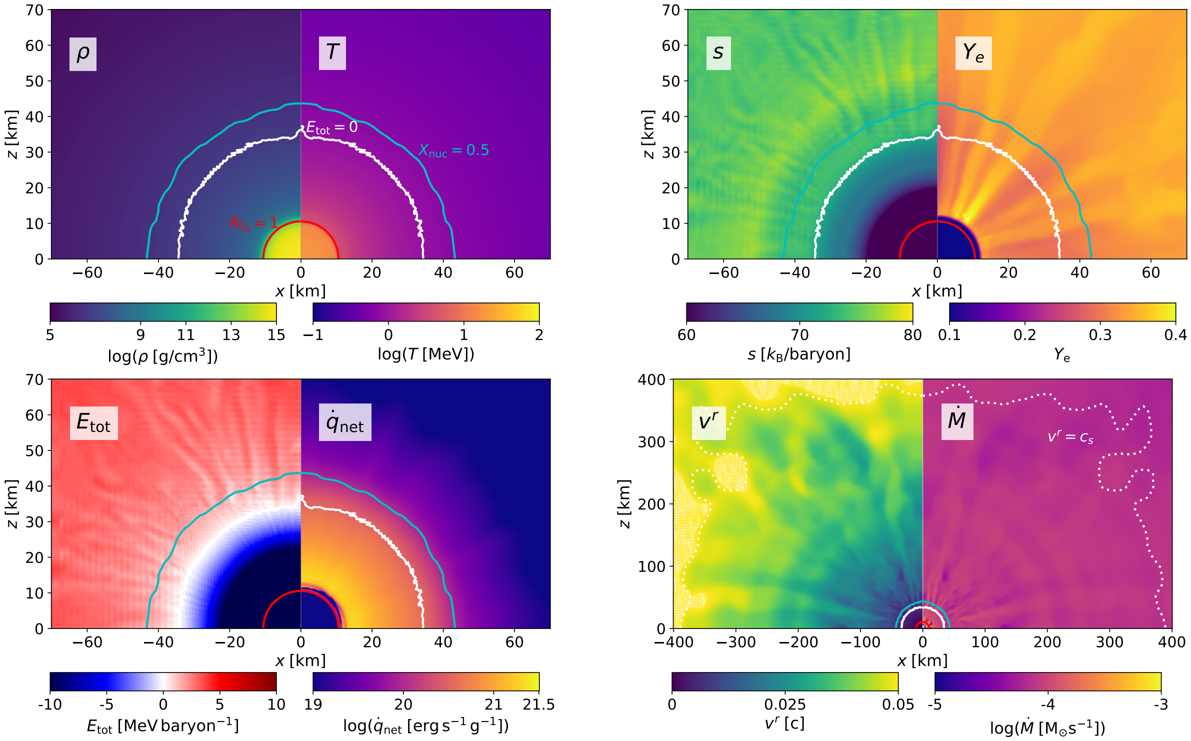

Figure 2.2: Snapshots of various quantities from our fiducial non-rotating model `nrot-HR` showing a slice through the $y = 0$ plane at $t = 152$ ms, with contours at the neutrinosphere ($\tau_{\bar{\nu}_e} = 1$; *red*), $E_{\rm tot} = 0$ (*white*), the α-particle formation surface (*teal*; $X_{\rm nuc}$ refers to the mass fraction of all nuclei excluding individual nucleons), and the sonic surface (where $v^r = c_s$; *white dotted*). The top left panel shows the density ρ and temperature T. The top right panel shows the specific entropy s and the electron fraction Y_e. The bottom left panel shows $E_{\rm tot}$, the total specific energy of wind matter as measured at infinity ($E_{\rm tot} = -hu_t - 1$, where h is the specific enthalpy and u_t is the time component of the four-velocity), and the net neutrino heating rate $\dot{q}_{\rm net}$. The bottom right panel shows the radial velocity v^r and the isotropic-equivalent mass loss rate $\dot{M}$. Please note the different radial scale on the bottom right sub-panel compared to the other sub-panels.

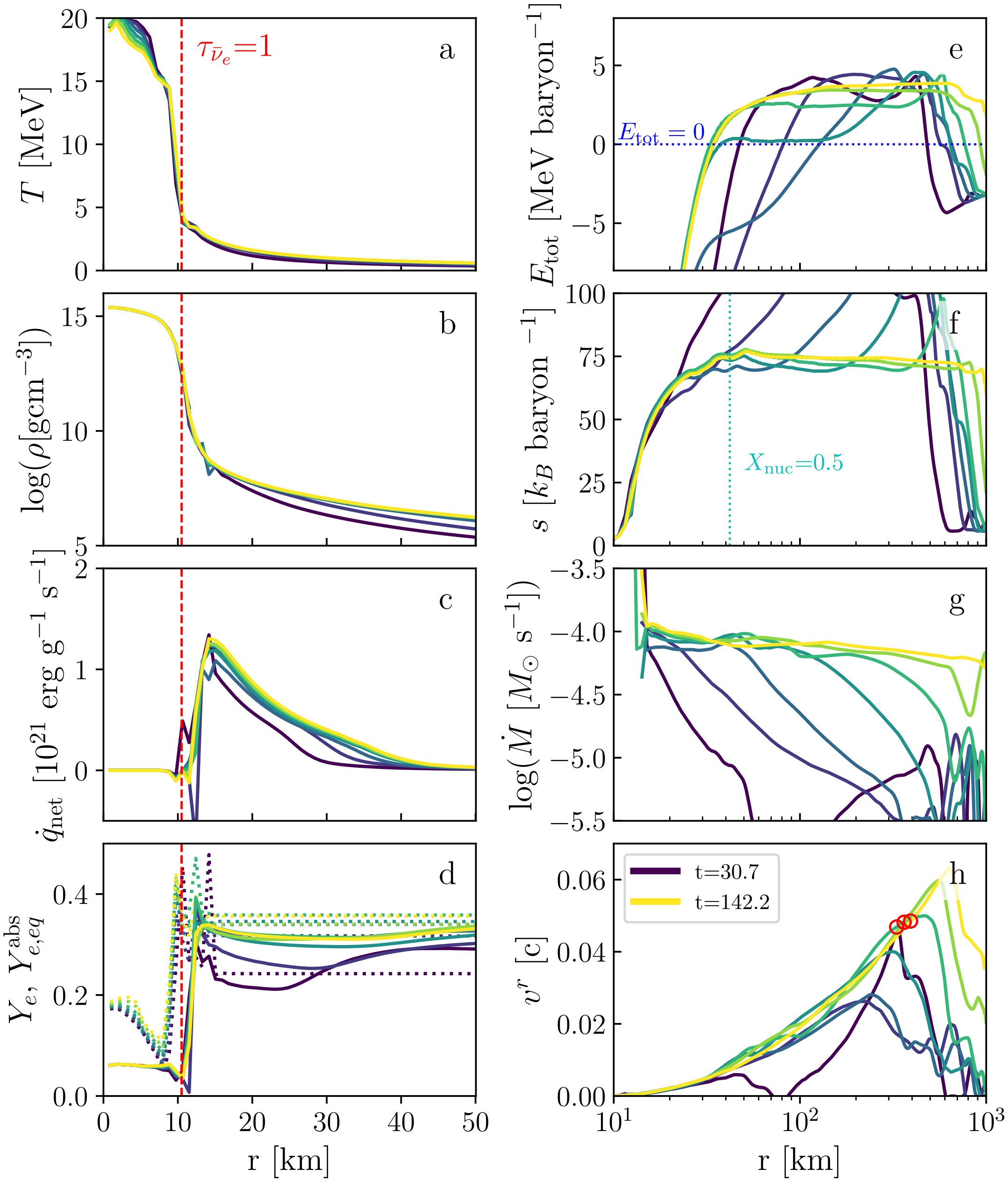

Figure 2.3: Radial profiles of angle-averaged quantities for model `nrot-HR` at several times (from dark to light): t =30, 49, 68, 87, 105, 124, and 142 ms. Plotted are (a) temperature, T; (b) mass density, ρ; (c) net specific neutrino heating rate, $\dot{q}_{\rm net}$; (d) electron fraction, Y_e (*solid*), and limited equilibrium electron fraction $Y_{e,eq}^{\rm abs}$ (*dotted*); (e) total specific energy, $E_{\rm tot}$; (f) specific entropy, s; (g) mass outflow rate, $\dot{M}$; (h) radial velocity, v^r. The red vertical dashed line denotes the location of the $\bar{\nu}_e$ neutrinosphere. The $\tau_{\bar{\nu}_e}$=1 and α-formation surface ($X_{\rm nuc}$ = 0.5, where $X_{\rm nuc}$ is the mass fraction of all nuclei excluding individual nucleons) at t = 152 ms (corresponding to the snapshot in Fig. 2.2) are indicated by red dashed and teal dotted lines in panels (a)–(d) and (f), respectively. Red circles denote the sonic surface at which the radial velocity v^r equals the sound speed; there are only three such circles because the sonic surface does not enter the grid until the final three snapshots. Please note the different radial scales for quantities shown in the left and right columns.

After a transient phase, the density profile close to the PNS surface settles into an exponentially declining profile of a hydrostatic atmosphere, which then transitions at larger radii to a more gradual power-law decline characteristic of a wind (Figs. 2.2, 2.3). The $\bar{\nu}_e$ neutrinosphere is indicated by a red line and a red dashed vertical line in Figs. 2.2 and 2.3, respectively.

The radial profiles of the matter density, temperature, and net specific neutrino heating rate ($\dot{q}_{\rm net} = \dot{q}^+ - \dot{q}^-$; heating minus cooling) settle into an approximate steady state by $t \approx 68$ ms (Figs. 2.2, 2.3 a–c). By this time, the neutrino luminosities and energies also stabilize (Fig. 2.4, middle row), with $L_{\nu_e} \approx 2.5 \times 10^{51}$ erg s^{-1}, $L_{\bar{\nu}_e} \approx 4.2 \times 10^{51}$ erg s^{-1}, $E_{\nu_e} \approx 13$ MeV, and $E_{\bar{\nu}_e} \approx 18$ MeV (Table 2.1). Over this same period, the radius of the neutrinosphere (taken to be that of $\bar{\nu}_e$) grows from ≈ 10 km to 10.5 km. These PNS luminosities and radii correspond to those achieved on timescales of a few seconds after a successful core collapse supernovae (e.g., Pons et al. 1999; Scheck et al. 2006; Roberts et al. 2012b), the same epoch over which the bulk of the total PNS mass-loss occurs.

Close to the PNS surface, heating from neutrino captures balance cooling from pair captures (Eq. 2.1). Moving above the surface, the temperature drops (Figs. 2.2, 2.3 a) and neutrino cooling from pair captures on nuclei ($\dot{q}^- \propto T^6$) plummets, while the heating rate $\dot{q}^+$ remains roughly constant with radius. Consequently, a “gain layer" of net neutrino heating $\dot{q}_{\rm net} = \dot{q}^+ - \dot{q}^- > 0$ forms at radii $r \sim 10 - 50$ km (Fig. 2.2, 2.3 c). This heating causes the entropy of the outflowing material to rise, $s = \int dq/T$, in the gain layer and then plateau at larger radii to $s \simeq 74$ (Fig.2.2, 2.3 f).

The α-particle formation surface lies at $r \approx 45$ km, where the temperature has dropped to $\approx 0.5 - 0.7$ MeV. We define this surface here as that beyond which the mass fraction $X_{\rm nuc}$ of all nuclei excluding individual nucleons becomes larger than 50%. Heat released during α recombination reactions introduces an increase in the wind entropy, which can be seen as the bright ring in the top right panel of Fig. 2.2, or the fluctuations at $r = 30 - 60$ km in the entropy radial profiles of Figs. 2.2, 2.3 f.

Radiation pressure dominates over gas pressure in the high-entropy outflow near and above the gain layer, and the resulting radial pressure gradient causes material to accelerate outwards. The radial velocity, plotted in Figs. 2.2, 2.3 h, increases with radius. Material becomes unbound from the PNS around $r \approx 30 - 40\,\mathrm{km}$, as indicated by a positive total specific energy $E_{\mathrm{tot}} = -hu_t - 1$ (Figs. 2.2 and 2.3 e).

By $t \approx 105$ ms, a sonic surface, at which the radial velocity equals the sound speed, has been established around $r = 300\,\mathrm{km}$ (denoted by red circles in Fig. 2.3 h). By the end of the simulation the sonic surface is approaching $\approx 400\,\mathrm{km}$ (see also Fig. 2.2) and the wind has attained a velocity $v \gtrsim 0.06c$. The sonic radius agrees with those found by Thompson, Burrows, and Meyer (2001) for similar wind parameters. Though the wind is still accelerating, its total energy E_{tot} has plateaued to a value ≈ 3 MeV per baryon, which will translate (once the enthalpy is converted into bulk kinetic energy) into an asymptotic speed $v_\infty \equiv \sqrt{2E_{\mathrm{tot}}} \approx 0.09$ c. By the final snapshot, the mass loss rate approaches the radially constant profile expected of a steady-state wind (Figs. 2.2, 2.3 g), reaching an asymptotic value $\dot{M} \approx 3.2 \times 10^{-4} M_\odot\ \mathrm{s}^{-1}$.

Absorption of neutrinos by the wind material also causes the electron fraction Y_e to rise with radius from its low value near the neutrinosphere (Fig. 2.4, bottom row). Neglecting relativistic effects, the electron fraction in an outflowing fluid element evolves according to the reactions in Eq. (2.1),

$$\frac{dY_e}{dt} = \left(\lambda_{e^+} + \lambda_{\nu_e}\right)(1 - Y_e) - \left(\lambda_{e^-} + \lambda_{\bar{\nu}_e}\right) Y_e, \tag{2.10}$$

where λ_{e^+} and λ_{ν_e} are the positron and electron neutrino capture rates on neutrons, and λ_{e^-} and $\lambda_{\bar{\nu}_e}$ are the electron and electron anti-neutrino capture rates on protons, respectively. The equilibrium electron fraction at any location can be defined as the value $Y_e = Y_e^{\mathrm{eq}}$ for which $dY_e/dt = 0$. This equilibrium is approached on the characteristic timescale,

$$\tau_\beta = \frac{1}{\left(\lambda_{e^+} + \lambda_{\nu_e}\right)(1 - Y_e) + \left(\lambda_{e^-} + \lambda_{\bar{\nu}_e}\right) Y_e}. \tag{2.11}$$

Near the PNS surface, where the radial velocity is low, τ_β is much shorter than the expansion time of the outflow ($\tau_{\rm exp} \sim \rho/\dot{\rho}$) and hence $Y_e \simeq Y_e^{\rm eq}$ is well-satisfied. However, as the wind accelerates at larger radii, $\tau_{\rm exp}$ decreases, until eventually $\tau_\beta \gtrsim \tau_{\rm exp}$, causing Y_e to freeze out.

In PNS winds, the temperatures are sufficiently low by the radii at which Y_e freeze-out occurs that the pair capture reactions (λ_{e^+}, λ_{e^-}) are negligible compared to the neutrino absorption reactions (λ_{ν_e}, $\lambda_{\bar{\nu}_e}$). Thus, around the point of freeze-out, a limited equilibrium has been achieved, in which ν_e absorption reactions on protons balance $\bar{\nu}_e$ absorption reactions on neutrons.[6] The electron fraction corresponding to this limited equilibrium, $Y_{e,eq}^{\rm abs}$, depends exclusively on the $\nu_e/\bar{\nu}_e$ neutrino radiation fields (Qian et al. 1993, Qian and Woosley 1996), viz.

$$\begin{aligned} Y_{e,eq}^{\rm abs} &\simeq \frac{\lambda_{\nu_e}}{\lambda_{\nu_e} + \lambda_{\bar{\nu}_e}} \\ &\approx \left(1 + \frac{L_{\bar{\nu}_e}}{L_{\nu_e}} \frac{\langle\epsilon_{\bar{\nu}_e}\rangle - 2\Delta + 1.2\Delta^2/\langle\epsilon_{\bar{\nu}_e}\rangle}{\langle\epsilon_{\nu_e}\rangle - 2\Delta + 1.2\Delta^2/\langle\epsilon_{\nu_e}\rangle}\right)^{-1}, \end{aligned} \tag{2.12}$$

where $\Delta \equiv m_n - m_p \simeq 1.293$ MeV is the proton-neutron mass-difference and $\langle\epsilon_\nu\rangle = \langle E_\nu^2\rangle/\langle E_\nu\rangle$ is the corresponding ratio of mean neutrino energy moments.

Figure 2.3 d shows that the non-rotating PNS wind achieves $Y_e < Y_{e,eq}^{\rm abs}$ near the PNS surface at early times, but that Y_e approaches $Y_{e,eq}^{\rm abs}$ at large radii and late times. At larger radii $r \gtrsim 15$ km, both $Y_{e,eq}^{\rm abs}$ and Y_e are roughly constant with radius, as expected since the neutrino radiation field is fixed well above the neutrinosphere and weak interactions have frozen out, respectively.

---

[6] The fact that $Y_e \simeq Y_{e,eq}^{\rm abs}$ in PNS winds can also be understood from an energetic argument (e.g., Metzger, Thompson, and Quataert 2008): (1) the wind is unbound from the gravitational potential well of the PNS by neutrino heating; (2) because the gravitational binding energy per nucleon ~ 200 MeV greatly exceeds the mean energy of the neutrinos absorbed by the wind material $\lesssim 20$ MeV, each nucleon must absorb several neutrinos on average to become unbound; (3) from these multiple absorptions per nucleon, the wind necessarily "forgets" about the initial ratio of protons to neutrons on the PNS surface in favor of $Y_e^{\rm eq}$.

Figure 2.4 (bottom row) shows that by $t \sim 100$ ms, $Y_{e,eq}^{\rm abs}$ has settled close to a value of ~0.35, with Y_e approaching this value as well, from below. These Y_e values are lower than predicted by detailed PNS cooling calculations at epochs of comparable neutrino luminosities to those of our solutions (e.g., Roberts, Reddy, and Shen 2012; Martínez-Pinedo et al. 2012; Pascal, Novak, and Oertel 2022); this is not surprising because our initial conditions are not based on the self-consistent outcome of a successful supernova and because the decoupling region which determines the neutrino luminosities and energies is not well-resolved (Fig. 2.1).

The black lines in Fig. 2.7 show the time-averaged wind properties through two different spherical surfaces ($r = 60, 120$ km) as a function of polar angle θ with respect to the z-axis. With the exception of the isotropic neutrino luminosity right along the pole ($\theta = 0$, where luminosity is is suppressed due to the M0 spherical grid boundary conditions), most of the wind quantities are roughly spherically symmetric and show no major effects of the grid boundaries, with $\dot{M}$ and v^r varying by factors $\lesssim 2$ across all θ and the other quantities varying by $\lesssim 10\%$.

Table 2.2 summarizes the asymptotic wind properties, including $\dot{M}$, s_∞, Y_e, and v_∞. These are usefully compared to time-independent 1D wind solutions available in the literature (e.g., Thompson, Burrows, and Meyer 2001). The model of Thompson, Burrows, and Meyer (2001) which has neutrino and PNS properties closest to those from our non-rotating models is their $M = 1.4 M_\odot$ model with $L_{\nu_e} = 3.1 \times 10^{51}$erg s^{-1}, $L_{\bar{\nu}_e} = 4 \times 10^{51}$ erg s^{-1}, for which they obtain: $\dot{M} \approx 1.63 \times 10^{-5} M_\odot$ s^{-1}, $s_\infty \approx 98$, and $v_\infty \approx 0.08c$ (their Table 1; hereafter model `Thompson`). As summarized in Table 2.2, other than the value of Y_e (which is not expected to agree given the different $L_{\nu_e}/L_{\bar{\nu}_e}/E_{\nu_e}/E_{\bar{\nu}_e}$ values), the Thompson, Burrows, and Meyer (2001) wind properties broadly agree with those of our non-rotating PNS wind solutions. This agreement is further improved if the wind properties are scaled to ours using the analytic formulae of Qian and Woosley (1996) given our solutions' respective neutrino luminosities and energies.

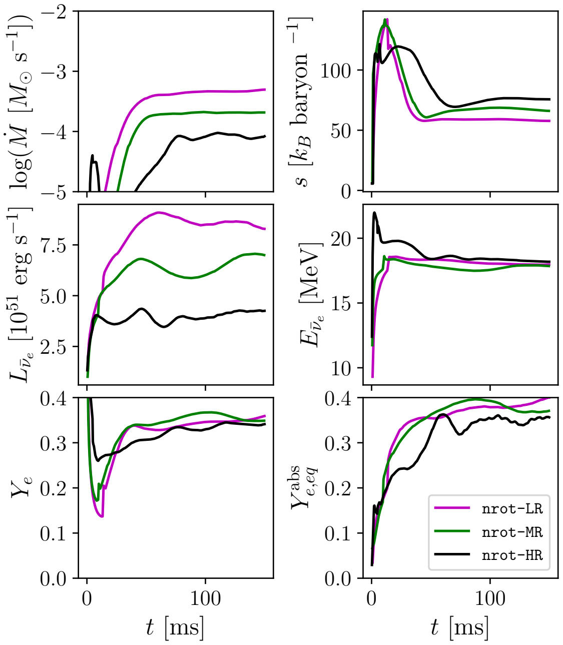

Figure 2.4: Time evolution of angle-averaged wind properties (as measured through a $r = 60$ km spherical surface) for the non-rotating models of low resolution `nrot-LR` (*purple*), medium resolution `nrot-MR` (*green*), and high resolution `rot-HR` (*black*). Asymptotic wind properties such as the mass-loss rate and specific entropy are not converged with resolution because the neutrino decoupling region which sets the neutrino radiation field is not resolved (Fig. 2.1). However, when the wind properties are scaled following the Qian and Woosley (1996) analytic formulae to results from 1D time-independent models Thompson, Burrows, and Meyer (2001), or to each another, based on their respective neutrino luminosities/energies/neutrinosphere radii, they come into better agreement (Table 2.3).

To verify that our wind properties converge, we compare results from three otherwise similar non-rotating wind simulations with different resolutions in Fig 2.4. Figure 2.1 shows that we do not resolve the neutrino decoupling region in any of the models, as this would require a tenfold increase in spatial resolution. As such, the predicted properties of the neutrino radiation field $\{L_{\bar{\nu}_e}, L_{\nu_e}, E_{\bar{\nu}_e}, E_{\nu_e}\}$ and the neutrinosphere radii $\{R_{\bar{\nu}_e}, R_{\nu_e}\}$ vary significantly between the models in Fig 2.4. However, after scaling the steady-state wind quantities $\dot{M}$ and s_∞ to the closest equivalent model of Thompson, Burrows, and Meyer (2001) and to each other based on their respective neutrino properties following the analytic formulae from Qian and Woosley (1996), the wind quantities come into approximate agreement (within tens of percent; Table 2.3).

The parameter $\eta = s_\infty^3/(Y_e^3\tau_{\rm exp})$ (Eq. (2.8)) quantifies the potential to form heavy r-process elements at large radii in the wind via the α-rich freeze-out mechanism (Sec. 2.1.3). Given the asymptotic wind entropy ($s_\infty \approx 74$) and expansion time through the seed-formation region ($\tau_{\rm exp} \approx 21.5$ ms) of our non-rotating model, this yields a value $\eta \approx 4.5 \times 10^8$ (Table 2.2), well below the threshold value $\eta_{\rm thr} \approx 9\times10^9$ to achieve even a second-peak r-process (Eq. (2.8)) for values of the electron fraction $Y_e \gtrsim \bar{Z}/\bar{A} \sim 0.4$ regime. The inability of spherically symmetric non-rotating purely-neutrino-driven winds to yield a successful heavy r-process is consistent with previous findings (see discussion and references in Sec. 3). The next subsection addresses whether these conclusions change in the presence of rapid rotation.

2.2.2 Rapidly Rotating PNS Winds

Rotation is expected to have a significant impact on the dynamics of the wind, at least in the equatorial regions of the flow, if the rotational velocity $v^\phi \sim R_\nu\Omega$ near the neutrinosphere radius R_ν exceeds the sound speed, $c_{\rm s}$, in the gain region (which has the effect of increasing the pressure scale height; see the discussion on $\dot{M}$ later in this section). Gas pressure dominates radiation pressure near the neutrinosphere at the base of the approximately isothermal gain layer ($s \sim P_{\rm rad}/P_{\rm gas} \gtrsim 1$; Figs. 2.2, 2.3f), such that $c_{\rm s} \simeq (kT/m_p)^{1/2}$. Approximating the

Table 2.2: Asymptotic Properties of Rotating and Non-Rotating PNS Winds

Model -	s_∞ $[k_B$ baryon$^{-1}]$	Y_e -	$\eta/\eta_{\rm crit}$ (Eq. 2.8) -	$\tau_{\rm exp}$ [ms]	$\dot{M}$ $[M_\odot$ s$^{-1}]$	$v_\infty^{(c)}$ $[c]$
`nrot-HR`	73.9	0.34	4.9×10^{-2}	21.5	7.40×10^{-5}	$\gtrsim 0.09$
`Thompson`[†]	98.4	0.47	3.9×10^{-2}	23.79	1.63×10^{-5}	≈ 0.08
`nrot-HR` scaled[‡] to `Thompson`	85.1	0.47	1.9×10^{-2}	32.5	1.80×10^{-5}	-
`rot.6-MR` ($0 \leq \theta \leq 180°$)	28.6	0.33	2.2×10^{-3}	31.1	1.19×10^{-3}	0.037
`rot.6-MR` (Polar[a])	56.9	0.35	1.4×10^{-2}	15.2	1.37×10^{-4}	0.096
`rot.6-MR` (Equatorial[b])	19.2	0.30	1.0×10^{-3}	49.3	6.09×10^{-4}	0.019

All quantities are averaged over the final third of the simulation run (e.g., $100-150$ ms for `nrot-HR`). [a] Averaged over $\theta \in [0, 30°]$ and $\theta \in [150°, 180°]$; [b] Averaged over $\theta \in [60°, 120°]$; [c] Asymptotic wind velocity, calculated from the total energy of the wind at large radii according to $v_\infty \equiv \sqrt{2E_{\rm tot}}$; [†] From the $M = 1.4M_\odot$, $L_{\bar{\nu}_e} = 4 \times 10^{51}$ erg s^{-1} model of Thompson, Burrows, and Meyer (2001) (Row 6 of their Table 1); [‡] Expressions for entropy, mass-loss rate, and dynamical time obtained by rescaling the results of model `nrot-HR` to the neutrino luminosities, energies, and neutrinosphere radii of model `Thompson` following analytic expressions from Qian and Woosley (1996), e.g. $\dot{M} \propto \sum_{\nu=\nu_e,\bar{\nu}_e} L_\nu^{5/3} E_\nu^{10/3} R_\nu^{5/3}$; $s_\infty \propto \sum_{\nu=\nu_e,\bar{\nu}_e} L_\nu^{-1/6} E_\nu^{-1/3} R_\nu^{-2/3}$; $\tau_{\rm exp} \propto \sum_{\nu=\nu_e,\bar{\nu}_e} L_\nu^{-1} E_\nu^{-2} R_\nu$.

Table 2.3: Resolution Study of Non-Rotating PNS Wind Properties

Model -	s_∞ $[k_B$ baryon$^{-1}]$	s_∞ (scaled)‡ $[k_B$ baryon$^{-1}]$	$\dot{M}$ $[M_\odot$ s$^{-1}]$	$\dot{M}$ (scaled)‡ $[M_\odot$ s$^{-1}]$
`Thompson`[†]	98.4	-	1.63×10^{-5}	-
`nrot-HR`	73.9	85.1	7.40×10^{-5}	1.80×10^{-5}
`nrot-MR`	67.6	90.2	2.02×10^{-4}	2.00×10^{-5}
`nrot-LR`	58.7	85.0	3.71×10^{-4}	1.89×10^{-5}

Quantities are averaged over polar angle $\theta \in [0, 180°]$, and in time from $t = 100$ to 150 ms. [†] From the $M = 1.4M_\odot$, $L_{\bar{\nu}_e} = 4 \times 10^{51}$ erg s^{-1} model of Thompson, Burrows, and Meyer (2001) (Row 6 of their Table 1).

‡Entropy and mass-loss rate scaled to the `Thompson` model in the same way as described in Table 2.2.

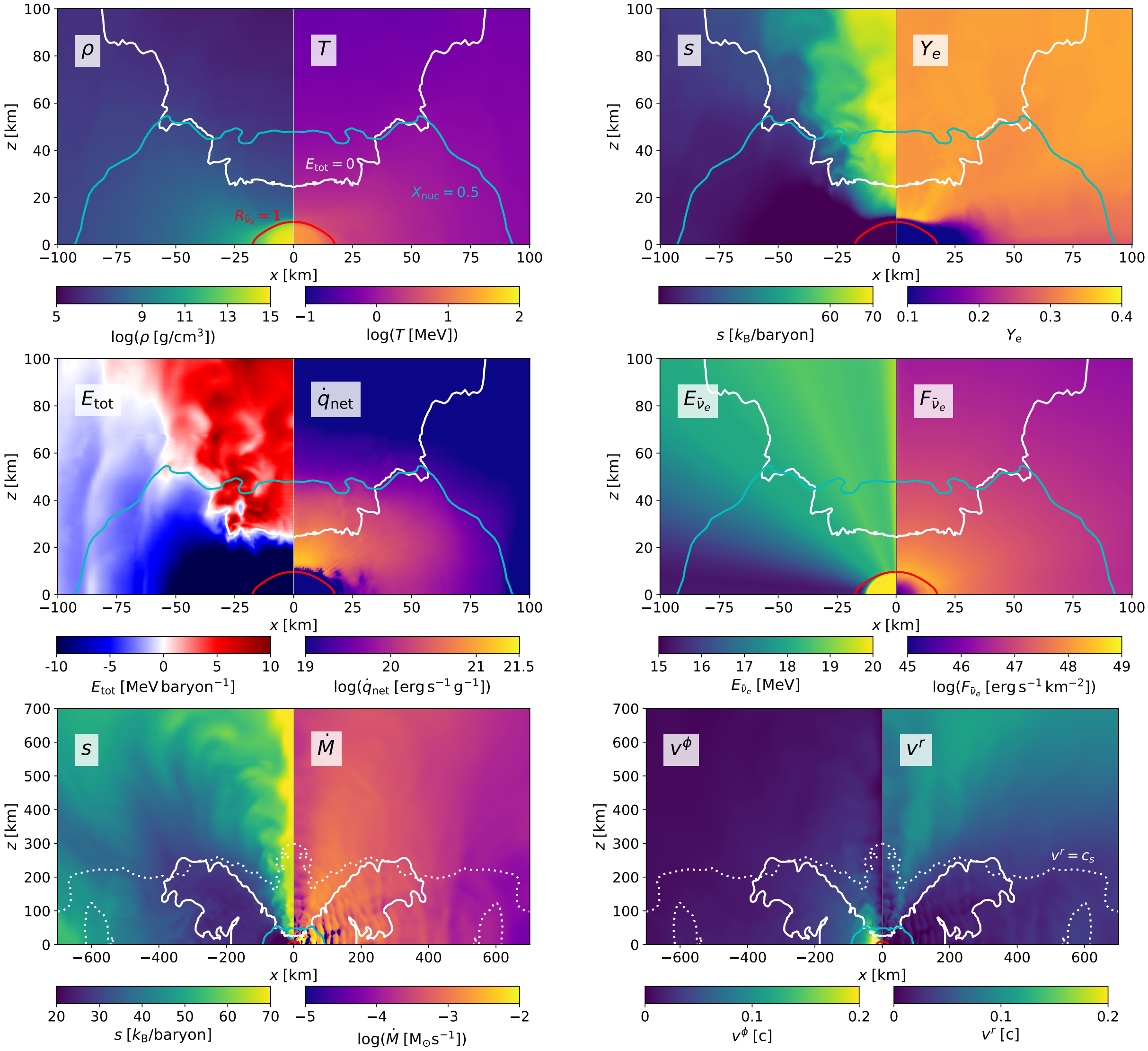

Figure 2.5: Similar to Fig. 2.2, except now showing snapshots at t = 100 ms of 2D slices through the rotational axis for model `rot.6-MR`, and including new quantities, such as azimuthal velocity v^ϕ, electron anti-neutrino flux $F_{\bar{\nu}_e}$, and mean energy $E_{\bar{\nu}_e}$. Please note the different radial scales in the top two rows compared to the bottom row.

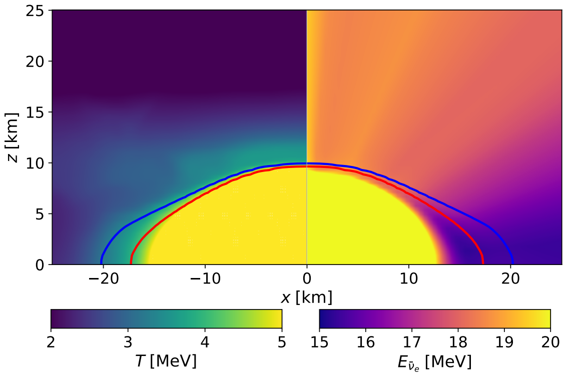

Figure 2.6: Temperature (*left*) and electron anti-neutrino mean energy (*right*) close to the PNS surface in the meridional plane for the maximally rotating model `rot.6-MR`. The approximate neutrinosphere surfaces (contours τ_{ν_e}, $\tau_{\bar{\nu}_e} = 1$) for ν_e and $\bar{\nu}_e$ are shown as blue and red curves, respectively. A bulge due to rapid rotation pushes out the location of the neutrinosphere near the equator, decreasing the $\tau = 1$ temperatures and reducing the mean neutrino energies in the equatorial regions relative to the polar regions.

single-species neutrino luminosity $L_\nu \simeq 4\pi(7/8)R_\nu^2\sigma T^4$ as that of a Fermi-Dirac blackbody, rotation will become dynamically important in the PNS atmosphere for spin periods $P = 2\pi/\Omega$ below a critical value (e.g., Thompson, Chang, and Quataert 2004),

$$P_{\rm c} \approx 2\pi\frac{R_\nu}{c_s} \approx 3.4\,{\rm ms}\left(\frac{R_\nu}{12\,{\rm km}}\right)^{5/4}\left(\frac{L_\nu}{10^{52}\,{\rm erg\,s^{-1}}}\right)^{-1/8}. \tag{2.13}$$

We focus our discussion on the most rapidly-rotating model, `rot.6-MR`, with axis ratio $R_p/R_e = 0.6$ and spin period of $P = 1.11$ ms $\ll P_{\rm c}$ (Table 2.1). Figure 2.5 shows 2D snapshots of various kinematic and thermodynamic quantities in the meridional (x-z) plane for model `rot.6-MR` near the end of the simulation at $t = 100$ ms. Angular profiles (where θ is measured from the axis of rotation) of wind quantities through spherical surfaces of radius $r = 60$ km and $r = 120$ km are shown in Fig. 2.7, comparing the results of `rot.6-MR` to those of the non-rotating model `nrot-HR` (for which the wind properties are expected and seen to be approximately uniform with angle).

Broadly speaking, our simulations reveal that the rotating wind can be divided into two angular regions with qualitatively distinct properties: (1) a fast polar outflow that develops quickly with properties across this region qualitatively similar to those of a non-rotating

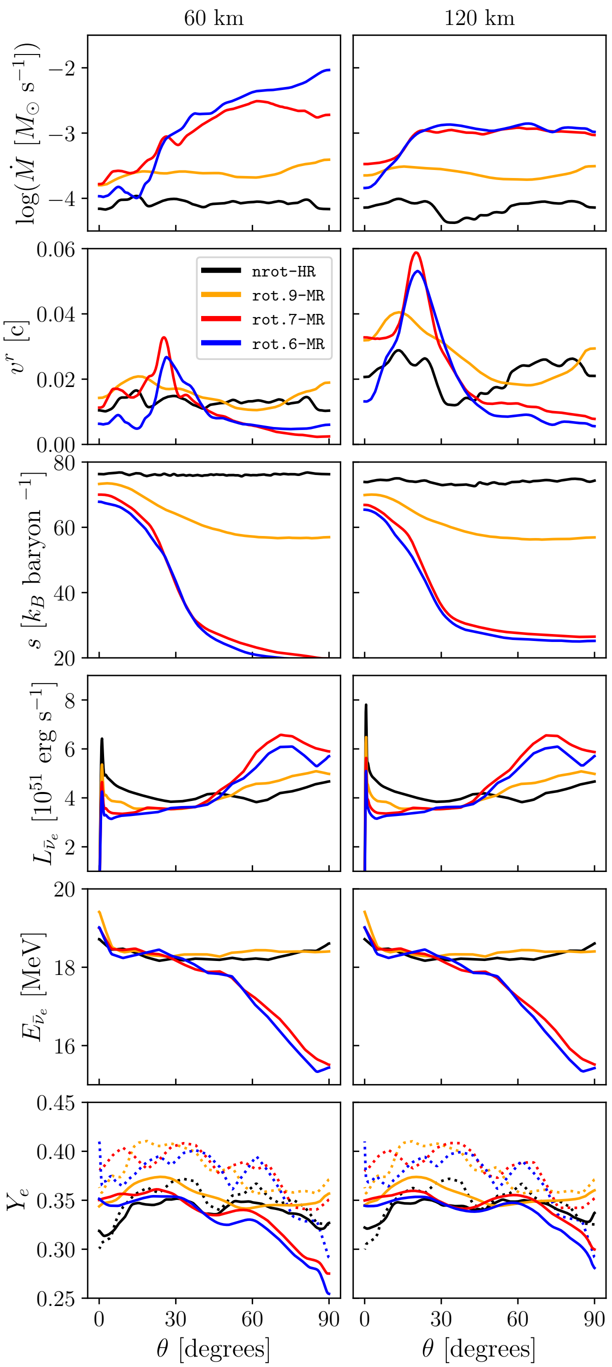

Figure 2.7: Wind properties as a function of polar angle θ, measured from the $z-$axis (rotation axis in rotating models), through spherical surfaces at r = 60 km (*left*) and r = 120 km (*right*) from the non-rotating model `nrot-HR` (non-rotating; *black*) and rotating models `rot.9-MR` (*orange*), `rot.7-MR` (*red*), and `rot.6-MR` (*blue*), time-averaged over the final third of the simulation run (e.g. 100 – 150 ms for `nrot-HR`). From top to bottom, the quantities shown include: isotropic mass-loss rate $\dot{M}$, radial velocity v^r, specific entropy s, isotropic electron anti-neutrino luminosity $L_{\bar{\nu}_e}$, mean electron anti-neutrino energy $E_{\bar{\nu}_e}$, and electron fraction Y_e. Dotted lines in the bottom panel show our estimate of the equilibrium electron fraction $Y^{\mathrm{abs}}_{e,eq}$ (Eq. (2.12)).

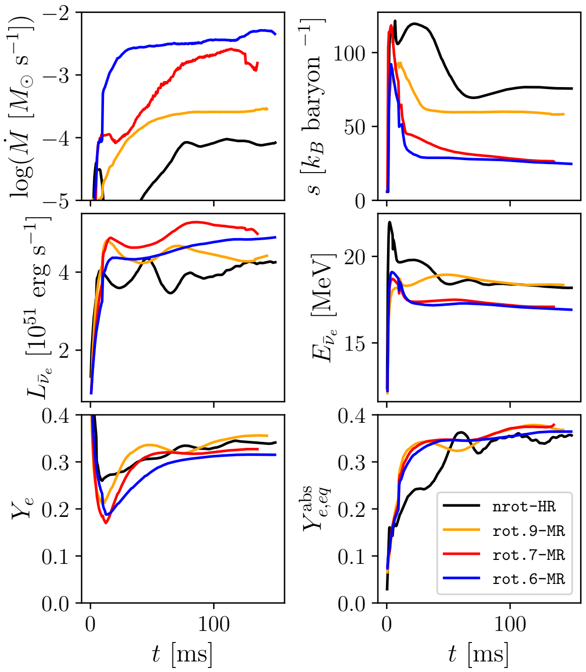

Figure 2.8: Similar to Fig. 2.4, except now comparing angle-averaged wind properties in the non-rotating model `nrot-HR` (*black*), and rotating models `rot.9-MR` (*orange*), `rot.7-MR` (*red*), and `rot.6-MR` (*blue*) as measured through a spherical surface of radius r = 60 km.

PNS; (2) a slower, denser equatorial outflow whose properties differ markedly from the non-rotating case, and which dominates the total mass-loss rate from the star.

After an initial transient phase, the density settles into an approximate steady state with an equatorial bulge of density $\rho \sim 10^{12}$ g cm^{-3} extending out to a cylindrical radius $\varrho \approx 30$ km (Fig. 2.5), compared to the steeper density profile along the polar axis, which falls to $\rho \lesssim 10^8$ g cm^{-3} by $z \gtrsim 15$ km. The neutrinosphere surface is likewise oblate in shape, bulging out to $\varrho \approx 17$ km in the equatorial plane compared to $z \approx 10$ km along the polar axis (Fig. 2.6), the latter being similar to the spherical neutrinosphere radius in the non-rotating model `nrot-HR`. The time- and angle-averaged ν_e and $\bar{\nu}_e$ luminosities of model `rot.6-MR` are similar to those of `nrot-HR` (Table 2.1). These differences are small enough that comparing these models allows us to roughly isolate the effects of rotation on the wind properties at a fixed epoch in the PNS cooling evolution (i.e., at approximately fixed neutrino luminosity).

Matter near the PNS surface in the rotational equator has high azimuthal velocity $v^\phi \gtrsim$

$0.2c$ due to the rapid rotation. Moving above the stellar surface, $v^{\phi} \propto 1/\varrho$, consistent with conservation of specific angular momentum in the wind, $\ell = \varrho v^{\phi} = \text{const.}$ (Fig. 2.5).

The isothermal surfaces are also oblate in shape, with a slightly higher neutrinosphere temperature (and hence mean neutrino energy) along the polar axis than in the equator (Fig. 2.6). This difference may in part be attributable to the Zeipel (1924) effect, whereby the effective temperature scales with the effective surface gravity $T_{\rm eff} \propto g_{\rm eff}^{1/4}$. Given that $g_{\rm eff}(R_{\rm eq})/g_{\rm eff}(R_{\rm p}) \sim \left[1 - \Omega^2/\Omega_{\rm K}^2\right] \sim 0.1$ for model `rot.6-MR`, this would predict $T_{\rm eff}(R_{\rm eq}) \lesssim 0.6 T_{\rm p}(R_{\rm eq})$, close to the ratio of polar and equatorial mean neutrino energies (Fig. 2.7).

The gain region around where $\dot{q}_{\rm net}$ peaks is also more radially extended in the equatorial region, but the peak heating rate $\dot{q}_{\rm net}$ is noticeably higher in the polar region, where it again resembles that seen of the non-rotating case. This enhancement of the polar heating rate results from the greater neutrino flux in this region and the higher mean neutrino energy (Fig. 2.5). The neutrino heating rate drops off abruptly outside of the α-particle formation surface (see below), because the neutrino absorption cross section of α-particles is much smaller than that of free nucleons.

The isotropic mass-loss rate $\dot{M} \sim 10^{-4} M_{\odot}\ {\rm s}^{-1}$ along the polar direction in model `rot.6-MR`, is similar to that of the non-rotating model `nrot-HR` (Fig. 2.7). By contrast, the values of $\dot{M}$ in the equatorial plane are larger than those in the non-rotating case by $1 - 2$ orders of magnitude, $\sim 10^{-3} - 10^{-2} M_{\odot}\ {\rm s}^{-1}$. Rotational enhancement of the mass-loss rate is a well known-effect in thermally-driven winds (e.g., Lamers and Cassinelli 1999, and references therein). Rotation has the effect of expanding the density scale-height of the atmosphere $H \approx c_{\rm s}^2/g_{\rm eff}$, where $g_{\rm eff} = g - a_c$, and g and a_c are the gravitational and centripetal acceleration experienced by material in the equator, respectively. A larger scale height exponentially increases the mass in the gain region (since $\rho \propto e^{-H/r}$), thus boosting $\dot{M}$ at the equator relative to the pole, despite the lower specific neutrino heating rate in the equatorial regions. Latitudinal mixing of the wind material occurs moving outwards with radius; however, an order of magnitude pole-to-equator difference in $\dot{M}$ is preserved to large radii $\gtrsim 120$ km

(Fig. 2.7), outside the sonic surface where further mixing is unlikely to occur.

Another consequence of the lower specific heating rate in the equatorial plane is a suppression of the wind entropy with increasing polar angle. The entropy along the polar direction, $s \approx 70$, is similar to that of the non-rotating PNS wind solution, compared to $s \approx 20$ in the equatorial plane (Fig. 2.7).

Since material in the rotational equator starts out more weakly bound to the star and receives less heating, the radial velocity v^r is lower there ($\lesssim 0.05c$) and matter is slower to become unbound. In the polar region, where the net neutrino heating is maximal, matter accelerates to supersonic velocities $v \approx 0.1c$ within a few hundred km (Fig. 2.5), significantly closer to the PNS than in the non-rotating case (Fig. 2.2). This higher polar acceleration may result from "focusing" of the polar flow by the denser equatorial outflow (somewhat akin to the 'de Laval nozzle' effect; Blandford and Rees 1974), which causes the areal function of the polar flow-lines to decrease with radius differently than the $\propto 1/r^2$ spherical outflow case.

Matter attains $E_{\rm tot} > 0$ and becomes unbound from the PNS along the polar directions by radii $z \approx 20$ km, while in the equatorial regions this is only achieved outside the α-formation surface at radii $\gtrsim 90$ km (Fig. 2.5). The significant heating due to α-particle formation (≈ 7 MeV per nucleon) helps unbind still-marginally bound material, similar to as found in simulations of viscously spreading accretion disks in neutron star mergers (e.g., Fernández and Metzger 2013; Siegel and Metzger 2018b). Given the low entropy of the outflow, just outside this surface, the α-particles rapidly assemble into seed nuclei, releasing further energy.

The asymptotic value of the wind electron fraction Y_e along the polar directions is ≈ 0.35, similar or moderately lower than that achieved in the non-rotating model (Fig. 2.7). However, outflows from the equator regions are significantly more neutron-rich, with $0.25 \lesssim Y_e \lesssim 0.3$. In both the polar and equatorial outflow regions, the wind composition still approaches equilibrium with the neutrino radiation field, as evidenced by $Y_e \approx Y_{e,eq}^{\rm abs}$. The

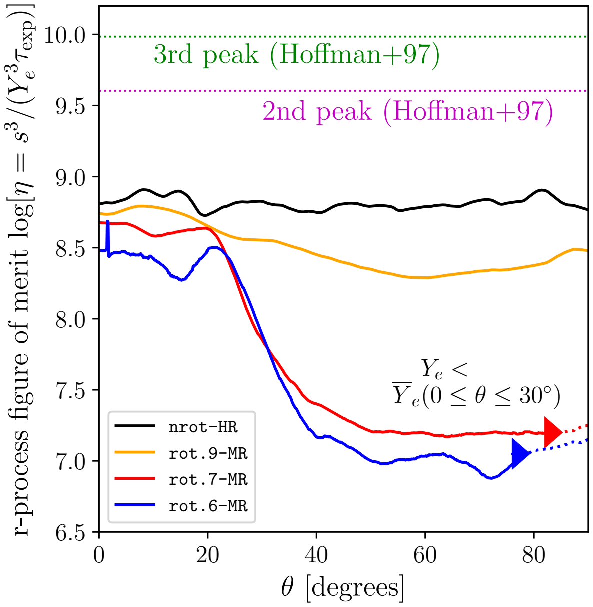

Figure 2.9: R-process figure-of-merit parameter $\eta \equiv s_{\infty}^3/(Y_e^3\tau_{\rm exp})$ (Eq. (2.8)) as a function of outflow polar angle θ, where the relevant quantities are time-averaged and measured through the $T = 0.5$ MeV surface, shown separately for the models `nrot-HR`, `rot.9-MR`, `rot.7-MR`, `rot.6-MR` as marked. For comparison we show the threshold value $\eta_{\rm thr}$ (Eq. (2.8)) required for neutron captures to reach the 2nd (*purple dotted line*) and 3rd (*green dotted line*) r-process peaks (Hoffman, Woosley, and Qian, 1997). A dotted line-style to the right of the solid triangles in the rapidly rotating models (`rot.6-MR`, `rot.7-MR`) denotes the angles over which Y_e is 10% lower than its average value along the polar angles $0° < \theta < 30°$ (the latter is roughly similar to that obtained from a non-rotating wind for the same neutrino emission properties); the outflow from such regions may be capable of a successful r-process even absent an α-rich freeze-out (i.e., even if $\eta \ll \eta_{\rm thr}$).

lower value of $Y_{e,eq}^{\rm abs}$ (Eq. (2.12)) and hence Y_e in the equatorial outflow results from the suppression of L_{ν_e} relative to $L_{\bar{\nu}_e}$ in this region, due to greater ν_e optical depth through the neutron-rich equatorial bulge. The large contrast between the temperatures at the ν_e and $\bar{\nu}_e$ neutrinospheres in the equatorial plane (Fig. 2.6) gives rise to the distinct average neutrino energies of ν_e and $\bar{\nu}_e$ along these directions.

The strong angular dependence of several wind quantities also impacts the angular averaged wind properties as illustrated in Fig. 2.8 (see also Tab. 2.2). Notably, the overall mass-loss rate is enhanced by 1-2 orders of magnitude for the most rapidly rotating model relative to the non-rotating model, while the overall entropy of the wind decreases to less than half of the value of the non-rotating model. As expected from the angular trends in Fig. 2.7, Fig. 2.8 also shows somewhat larger electron anti-neutrino luminosities, smaller electron anti-neutrino mean energies, and a smaller overall Y_e.

As a result of the strong angular dependence of $\{Y_e, v^r, s, T\}$ in the rotating models, the r-process figure of merit η also varies as a function of polar angle θ. Figure 2.9 compares the angular profile of η from the rotating star simulations to the non-rotating model. In the polar region, the rotating and non-rotating models achieve a similar value $\eta \approx 3 - 6 \times 10^8$. However, in the equatorial region, η is significantly suppressed for the rotating models, with η being $\approx$ 2 orders of magnitude lower for `rot.7-MR` and `rot.6-MR`. Taken together, the value of η lies well below the minimum threshold for 2nd or 3rd peak r-process element production for all outflow angles and all models. This disfavors rapidly spinning PNS as r-process sources via the α-rich freeze-out mechanism.

At face value, rotation appears to be detrimental to the r-process in PNS winds. However, this does not account for the effect of a lower Y_e alone, absent an α-rich freeze-out. The value of Y_e in our most rapidly rotating models is $\approx 10\%$ smaller in the equatorial direction than along the pole (we denote the Y_e-suppressed region with a dashed linestyle in Fig. 2.9) or in the non-rotating wind model with otherwise similar neutrino luminosities and energies. Thus, for example, if the "true" wind electron fraction at a given point in the cooling evolution of a non-rotating PNS were $Y_{e,0} \approx 0.45 - 0.5$, (e.g., Roberts et al. 2012b; their Fig. 5), rotation could act to reduce Y_e to $\approx 0.9 Y_{e,0} \approx 0.4 - 0.45$, sufficient to produce neutron-rich light element primary-process (LEPP) nuclei with $38 < Z < 47$ (e.g., Arcones and Montes 2011), even absent an α-rich freeze-out (i.e., even for arbitrarily low values of η).

2.3 Summary and Conclusions

We have explored the effects of rapid rotation on the properties of neutrino-heated PNS winds by means of three-dimensional GRHD simulations with M0 neutrino transport.

We calculate a suite of $1.4M_\odot$ PNS models corresponding to different solid-body rotation rates (Tab. 2.1), ranging from the non-rotating case studied in most previous works ($\Omega = 0$) to stars rotating near break-up ($\Omega/\Omega_\mathrm{K} \simeq 0.94$; $P \simeq 1.11$ ms). We initialize the axisymmetric PNS structure using the `RNS` code integrated via a novel procedure with the SFHo tabulated EOS. Rather than following the self-consistent cooling evolution of the PNS from an initial post-explosion or post-merger state, we initialize the PNS temperature and Y_e radial profiles in β-equilibrium following Kaplan et al. (2014). The chosen temperature normalization generates steady-state neutrino luminosities and energies close to those achieved on a timescale of seconds after a supernova explosion, and over which the bulk of the integrated wind mass-loss will occur.

Our focus is on studying the wind properties in the gain layer above the PNS surface and out to large radii (~ 1000 km); however, we are not able to fully resolve the neutrinosphere decoupling region (Fig. 2.1). As a consequence of this, as well as of our idealized initial temperature/Y_e structure, the partitioning between ν_e and $\bar{\nu}_e$ luminosities and their energies in our simulations do not match those predicted by supernova simulations, nor the resulting wind electron fractions $Y_e \simeq Y_{e,eq}^{\mathrm{abs}}(L_{\nu_e,\bar{\nu}_e}, E_{\nu_e,\bar{\nu}_e})$. Specifically, our non-rotating wind solutions achieve values $Y_e \simeq 0.34$ (Fig. 2.4) significantly lower than those found by detailed PNS cooling calculations, $Y_e \approx 0.45 - 0.55$ (e.g., Roberts and Reddy 2017; Pascal, Novak, and Oertel 2022). Nevertheless, our simulations can still be used to explore the relative effects of rotation on Y_e through a comparison to otherwise equivalent non-rotating models with similar neutrino emission properties.

Our main conclusions can be summarized as follows.

- After an initial transient phase, all of our models reach approximately steady outflow solutions with positive energies $E_\mathrm{tot} > 0$ and sonic surfaces captured on the computational grid, on timescales ~ 100 ms (Fig. 2.2, 2.3). We validate our non-rotating solutions by comparing them to time-independent spherical wind calculations (Tab. 2.3). Scaling our wind properties ($\dot{M}$, s_∞, τ_exp, v_∞) based on analytic expressions from Qian and Woosley (1996) given the relative neutrino properties (L_ν, E_ν, R_ν), we obtain good agreement (to within $\lesssim 10\%$) with Thompson, Burrows, and Meyer (2001).

- Our non-rotating and slower rotating models (`rot.9-MR`; $\Omega/\Omega_{\rm K} \simeq 0.4$) exhibit approximately spherical outflow properties. In contrast, the fastest rotating models (`rot.7-MR`, `rot.6-MR`; $\Omega/\Omega_{\rm K} \gtrsim 0.75$) generate outflows with distinct properties near the equatorial plane versus higher latitudes closer to the rotational axis (Fig. 2.5, Table 2.2). The outflow properties along the rotational axis ($\theta \lesssim 30^\circ$) are qualitatively similar to those of the slowly rotating models in their key properties (e.g., $\dot{M}$, Y_e, s_∞, L_ν, E_ν; Fig. 2.7), as would be expected because centrifugal effects are weak along these directions. However, outflows from intermediate latitudes accelerate faster to higher speeds compared to a spherical wind (Fig. 2.7); these features may result from 'de Laval'-like focusing of polar streamlines by the denser equatorial outflow.

- The equatorial outflows from rapidly rotating PNS exhibit qualitative differences from the non-rotating case (Fig. 2.7), as expected because centrifugal forces have a large effect on the hydrostatic structure of the atmosphere for spin periods $P \ll P_{\rm c} \approx 3$ ms (Eq. (2.13)). Relative to slowly rotating models, the equatorial outflows from rapid rotators possess: higher mass-loss rates $\dot{M}$ by over an order of magnitude in the fastest spinning case; slower acceleration and lower asymptotic radial velocities; and lower entropy s_∞ by a factor up to ≈ 4. These features may be understood as a consequence of the rotation-induced reduction in the effective gravitational mass, when applied to analytic predictions for the M-dependence of the wind properties (Qian and Woosley, 1996).

  The equatorial outflows of the rapidly rotating solutions are also characterized by lower neutrino energies and a larger contrast between the ν_e and $\bar{\nu}_e$ neutrinospheres and their respective temperatures/luminosities; these features result from the presence of a dense neutron-rich equatorial bulge/decretion disk near the surface of the star (Fig. 2.6).

These changes in the $\nu_e/\bar{\nu}_e$ properties reduce the equilibrium electron fraction $Y_{e,eq}^{\rm abs}$ (Eq. (2.12); and hence $Y_e \lesssim 0.3$) of the equatorial outflows relative to the slowly rotating case.

- Rapid rotation tends to reduce s_∞ and to increase $\tau_{\rm exp}$ as a result of the slower expansion speed in the dense equatorial outflow; both effects act to reduce the key parameter $\eta = s_\infty^3/(\tau_{\rm exp}Y_e^3)$ (Eq. (2.8)) by over an order of magnitude in the rotating wind case (Fig. 2.9). We conclude that rotation (at least absent a strong magnetic field) does not facilitate a successful 2nd or 3rd r-process via the α-rich freeze-out mechanism.

  On the other hand, outflows near the equatorial plane in our fastest rotating models possess Y_e smaller by $\approx 10-15\%$ compared to the otherwise equivalent non-rotating case. The winds from very rapidly spinning PNS could therefore generate nucleosynthetic abundance patters which are quantitatively distinct from those of slowly rotating PNS, even neglecting potential rotation-induced changes to the PNS cooling evolution. For example, if slowly rotating PNS winds achieve $Y_e \gtrsim 0.5-0.55$ (e.g., Pascal, Novak, and Oertel 2022) and generate mostly iron group elements and p-nuclei via the rp-process and νp-process (e.g., Fröhlich et al. 2006; Roberts, Woosley, and Hoffman 2010; Fischer et al. 2010), rotating PNS winds could obtain $Y_e \lesssim 0.5$ and would instead synthesize neutron-rich LEPP or light r-process nuclei (e.g., Qian and Wasserburg 2007; Arcones and Montes 2011).

- The neutrino luminosities achieved by our models ~few ×10^{51} erg s^{-1} will last for a timescale $\tau_{\rm c} \approx 3$ seconds after a successful supernova explosion (Roberts and Reddy 2017; their Fig. 3). Although our simulations are not run this long, our most rapidly spinning PNS solutions therefore predict a total wind-ejecta mass $\sim \dot{M}\tau_{\rm c} \approx 3\times10^{-3}M_\odot$ comprised of more neutron-rich nuclei than would accompany the birth of a slowly rotating PNS of otherwise similar properties (which produce only $\approx 10^{-4}M_\odot$ in total wind-ejecta; e.g., Thompson, Burrows, and Meyer 2001).

Several strains of observational (e.g., Faucher-Giguère and Kaspi 2006; Vink and Kuiper 2006; Perna et al. 2008) and theoretical (e.g., Ma and Fuller 2019) evidence indicate that the birth of neutron stars with rapid spin periods $P \approx 1$ ms are rare in nature among the core collapse population. However, given their larger wind ejecta mass-yields (by a factor $\gtrsim 10$), even if such rapidly spinning PNS are formed in only $\sim 10\%$ of all core collapse supernovae, their total nucleosynthetic contribution may be competitive with "ordinary" supernovae birthing slowly spinning PNS. Broad-lined supernovae with atypically large ejecta kinetic energies (hinting at an important role of rotation in facilitating the explosion) indeed represent $\sim 10\%$ of core collapse explosions (e.g., Perley et al. 2020). The contributions of rapidly spinning PNS on individual "pollution events" observed in the surface abundances of halo stars (e.g., Honda et al. 2006b; Spite et al. 2018) will be further enhanced if stellar cores retain greater angular momentum at core collapse at lower metallicity (e.g., Yoon and Langer 2005).

Hot, rapidly spinning PNS-like stars are also generated from the merger of binary neutron stars (e.g., Dessart et al. 2009), albeit with higher masses $\gtrsim 2M_{\odot}$ than assumed in our models. However, the limited lifetimes of most such objects before they lose rotational support and collapse into a black hole, may limit the contribution of their neutrino-driven winds relative to other sources of mass ejection during the merger and its aftermath (though strong magnetic fields may change this picture; e.g., Siegel, Ciolfi, and Rezzolla 2014; Metzger, Thompson, and Quataert 2018; Curtis et al. 2021).

Our present set-up incorporates neutrino transport using an M0 scheme, which neglects the effects of lateral transport. This is likely a good approximation in our case because deviations from spherical symmetry are fairly modest and (compared, e.g. to simulations of the supernova explosion; Skinner, Burrows, and Dolence 2016) we are mainly interested in the properties of the outflows above the neutrino decoupling region. However, future work should aim to explore the impact of more accurate neutrino transport in the rapidly rotating cases.

In this paper, we have focused on an idealized numerical experiment to explore the effects of rotation on PNS winds in a controlled and general way. However, with the results now benchmarked, we can explore more realistic (albeit specific) PNS configurations from core-collapse SNe or NS mergers with the same code infrastructure. In the context of a self-consistent core-collapse SN or NS merger, the specifics of the neutrino luminosities and energies, Y_e profile near the PNS surface, and the large-scale environment, will differ from those we have assumed. As an example of the latter, in a NS merger the PNS will be surrounded by an accretion torus, which generates its own outflow that may interact with the PNS wind (e.g., Metzger and Fernández 2014; Perego et al. 2014); likewise, at early times after a SN explosion, the PNS wind may catch up to the SN shock (e.g., Arcones, Janka, and Scheck 2007). Although quantitative features of the wind, particularly the asymptotic Y_e values, may differ substantially due to these effects, the qualitative features (and the quantitative results for other properties set near the PNS surface such as $\dot{M}$ and the outflow entropy) are likely to be robust.

The study presented here also lays the groundwork for future 3D simulation work including additional physical effects. One of the most important are those arising from strong, ordered magnetic field, which may accompany the birth of rapidly spinning PNS as a result of dynamo processes which tap into the energy available in rotation or convection (e.g., Thompson and Duncan 1993; Siegel et al. 2013; Mösta et al. 2014; Raynaud et al. 2020). Magnetic fields of strength $\gtrsim 10^{14} - 10^{15}$ G comparable to those of Galactic magnetars have been shown to have major effects on the PNS wind properties and their efficacy in generating r-process elements, both with (e.g., Thompson, Chang, and Quataert 2004; Metzger, Thompson, and Quataert 2007; Winteler et al. 2012; Vlasov, Metzger, and Thompson 2014; Vlasov et al. 2017) and without (e.g., Thompson 2003; Thompson and ud-Doula 2018) rapid rotation.

Chapter 3: Neutrino-Driven Winds from Magnetized Protoneutron Stars

*This work has published and may be found **here.***

Magnetars are neutron stars with exceptionally high surface magnetic field strengths $\sim 10^{14} - 10^{15}$ G (e.g., Kouveliotou et al. 1998; Kaspi and Beloborodov 2017), which comprise $\gtrsim 30\%$ of the young neutron star population (Woods and Thompson, 2006; Beniamini et al., 2019). These strong magnetic fields affect the appearance of magnetars throughout their active lifetimes, for example by providing an additional source of heating due to magnetic dissipation and by powering transient outbursts and flares (e.g., Coti Zelati et al. 2018; Beniamini et al. 2019; CHIME/FRB Collaboration et al. 2020). In this paper we shall explore one way in which such strong magnetic fields also affect the very first moments in a magnetar's life.

Whether formed from the core-collapse of a massive star (e.g., Burrows, Hayes, and Fryxell 1995; Janka et al. 2007), the accretion-induced collapse of a white dwarf (e.g., Dessart et al. 2006), or the merger of two neutron stars (e.g., Dessart et al. 2009; Giacomazzo and Perna 2013; Perego et al. 2014; Kaplan et al. 2014; Metzger, Thompson, and Quataert 2018), all neutron stars begin as hot "proto-neutron stars" (PNS; e.g., Burrows and Lattimer 1986; Pons et al. 1999), which cool and contract via optically-thick neutrino emission for the first tens of seconds following their creation. As neutrinos stream outwards from the neutrinosphere through the atmosphere of the PNS, the heat they deposit in the surface layers drives a thermally-driven outflow of baryons, known as the "neutrino-driven" wind (e.g., Duncan, Shapiro, and Wasserman 1986; Qian and Woosley 1996; Thompson, Burrows, and Meyer 2001). Neutrino-driven winds have received extensive interest as potential sites for the nucleosynthesis of rare heavy isotopes, particularly via the rapid neutron capture process (r-process; e.g., Meyer et al. 1992; Takahashi, Witti, and Janka 1994; Woosley et al. 1994). However, previous studies have shown that the roughly spherically symmetric winds from (slowly-rotating, unmagnetized) PNS fail to achieve the requisite combination of high entropy and short outflow expansion time through the seed nucleus formation region (Hoffman, Woosley, and Qian 1997; Meyer and Brown 1997; Meyer et al. 1992) to enable the high ratio of neutrons to seeds necessary to achieve a successful 2nd or 3rd peak r-process (e.g., Kajino et al. 2000; Sumiyoshi et al. 2000; Otsuki et al. 2000; Thompson, Burrows, and Meyer 2001; Arcones, Janka, and Scheck 2007; Fischer et al. 2010; Roberts, Woosley, and Hoffman 2010; Arcones and Montes 2011; Roberts et al. 2012b; Martínez-Pinedo et al. 2012; Fischer et al. 2012). Waves driven by convection, which steepen above the PNS surface and deposit additional entropy in the outflow, offer one possible mechanism to boost their r-process potential (e.g., Suzuki and Nagataki 2005; Metzger, Thompson, and Quataert 2007; Gossan, Fuller, and Roberts 2020; Nevins and Roberts 2023).

As prefaced above, most previous studies of PNS winds also neglect the impact of two other neutron star properties: rotation and magnetic fields. In recent work (Desai, Siegel, and Metzger 2022 – hereafter Paper I) we explored the effects of rapid rotation on the wind properties by means of three-dimensional general-relativistic (GR) hydrodynamic simulations. These simulations revealed that, while rapid rotation (spin periods $P \lesssim$ few ms) acts to increase the mass-loss rate of the PNS near the rotational equator, the entropy and velocity of such outflows are suppressed compared to an otherwise equivalent non-rotating star, precluding r-process production via an alpha-rich freeze-out. On the other hand, extremely rapid rotation approaching centrifugal break-out ($P \sim 1$ ms), was found to reduce the outflow electron fraction compared to the equivalent non-rotating wind model, thus potentially enabling the production of light r-process or light elementary primary process (LEPP) nuclei even absent an alpha-rich freeze-out.

The prevalence of such very rapidly spinning PNS in nature is not clear, however. Helioseismology observations and theoretical modeling suggest that angular momentum may be transferred out of the core of a massive star prior to core collapse with higher efficiency than had been previously assumed (e.g., Cantiello, Fuller, and Bildsten 2016; Fuller, Piro, and Jermyn 2019). Another potential consequence of rapid birth rotation, which may limit its prevalence in nature, is to endow the PNS with a strong magnetic field $\gtrsim 10^{15}$ G via a dynamo process (e.g., Thompson and Duncan 1993; Price and Rosswog 2006; Siegel et al. 2013; Mösta et al. 2015; Raynaud et al. 2020; Reboul-Salze et al. 2022; White et al. 2022). While such "millisecond magnetars", formed in magnetorotational core-collapse supernovae (e.g., Obergaulinger and Aloy 2021; Bugli, Guilet, and Obergaulinger 2021; Bugli et al. 2023 for recent work) or neutron star mergers (e.g., Kiuchi et al. 2018; Mösta et al. 2020; Combi and Siegel 2023), are a contender for the central engines behind energetic transients such as engine-powered supernovae and gamma-ray bursts (e.g., Usov 1992a; Wang et al. 2001; Thompson, Chang, and Quataert 2004; Bucciantini et al. 2007; Metzger, Thompson, and Quataert 2007; Bucciantini et al. 2009; Metzger et al. 2011; Prasanna et al. 2023), these explosions are so rare as to represent at most only a tiny fraction of all magnetar births (e.g., Vink and Kuiper 2006; Fuller and Lu 2022). Nevertheless, if such objects exist, recent works studying the dynamics and nucleosynthesis of magnetorotational supernovae, find that the combination of rapid rotation and magnetic fields can indeed give rise to conditions that would allow for 2nd and potentially 3rd peak $r-$process element production (e.g., (Winteler et al., 2012; Kuroda et al., 2020; Reichert et al., 2023)).

On the other hand, rapid rotation may not be the only mechanism to generate magnetar-strength fields, which in principle could originate from flux freezing from the pre-collapse stellar core (Woltjer, 1964; Ruderman, 1972; Ferrario and Wickramasinghe, 2006; Cantiello, Fuller, and Bildsten, 2016) or dynamos during the PNS phase which require less extreme core angular momentum (White et al., 2022; Barrère et al., 2022). This motivates considering the effects of a strong magnetic field on PNS birth even in the absence of rapid rotation.

In this work (Paper II) we perform general-relativistic magnetohydrodynamical (GRMHD) simulations which explore the impact of strong ($B \gtrsim 10^{14} - 10^{15}$ G) dipole magnetic fields on the properties of neutrino-heated outflows from non-rotating PNS winds. We are motivated by the work of Thompson (2003), who showed that a magnetar-strength field can initially trap plasma close to the PNS surface, where it can be heated by neutrinos to a higher entropy than achieved in an otherwise equivalent freely outflowing wind. Thompson and ud-Doula (2018) studied this problem numerically by means of 2D axisymmetric MHD simulations with Newtonian gravity, using an approximate inner boundary condition near the PNS neutrinosphere and a prescribed free-streaming neutrino radiation field above. They found that a moderate fraction $\sim 1-10\%$ of the wind material may be ejected in high-entropy outflows capable of r-process via an alpha-rich freezeout. Likewise, Prasanna et al. (2022) performed similar simulations but covering a wider parameter space of the neutrino-driven winds from slowly rotating magnetars, focusing on the effects that neutrino-driven mass-loss has in opening magnetic field lines and enhancing the star's spin-down rate relative to the magnetic dipole rate. Our goal here is to explore a similar setup using 3D GRMHD simulations including neutrino transport via an M0 scheme, thus paving the way for future simulations within this numerical setup that include both magnetic fields and rapid rotation together.

This paper is organized as follows. In Section 3.1 we introduce the numerical code and models run. In Section 3.2, we compare outflows from magnetars of various magnetic field strengths. In Section 3.3 we summarize and compare our results to outflows from un-magnetized winds, and further discuss viability of r-process nucleosynthesis in magnetar winds.

3.1 Methodology

3.1.1 Numerical Evolution Code, PNS Initial Data & Grid Setup

We perform GRMHD simulations of magnetized PNS winds using a modified version of `GRHydro` (Mösta et al., 2014) as described in Siegel and Metzger (2018b), built on the open-source `Einstein Toolkit`[1](Goodale et al., 2003; Schnetter, Hawley, and Hawke, 2004; Thornburg, 2004; Löffler et al., 2012; Babiuc-Hamilton et al., 2019). The initial conditions reflect the state of a PNS in its cooling phase (~ 1 s post-bounce, e.g. Fig. 3 of Roberts and Reddy (2017)), following the end of the dynamical accretion phase responsible for forming the PNS. As in Paper I, we do not evolve spacetime for the current models. Instead, we evolve the GRMHD equations on a fixed background metric, determined at the start of the simulation by our initial data solver, for computational efficiency. This assumption is justified by the fact that only a tiny fraction $\sim 10^{-5}$ of the star's mass is removed over the course of the simulation and the total energy in the magnetic field is $\lesssim 10^{-7}$ of the star's gravitational energy.

We include weak interactions via a leakage scheme based on the formalism of Bruenn (1985) and Ruffert, Janka, and Schaefer (1996), following the implementation in Galeazzi et al. (2013) and Radice et al. (2016) (see also Siegel and Metzger 2018b). In the presence of strong magnetic fields, the neutrino heating and cooling rates will be altered with respect to a non-magnetized setup, due to the impact of Landau quantization on the available electron/positron states (e.g., Lai and Qian 1998; Duan and Qian 2004). However, as we show in Appendix A.1.4, these effects are small, even for the strongest magnetic field strength cases explored in this work. We are thus justified in neglecting these corrections.

As in Paper I, we employ a one-moment approximation to the general-relativistic Boltzmann equation ('M0') to describe neutrino transport. It is implemented as a ray-by-ray scheme (Radice et al., 2016) in our enhanced version of `GRHydro`, in which neutrino mean energies and number densities are evolved along null radial coordinate rays (see also Combi and Siegel 2022). The M0 radiation transport grid is separate from that of the GRMHD variables. It uses spherical coordinates centered on the PNS, uniformly spaced in $\{r, \theta, \phi\}$ extending out to radii of 200 km, with the number of grid points $(n_r, n_\theta, n_\phi) = (600, 20, 40)$. It thus covers the density range $\rho \gtrsim 10^4$ g cm^{-3}, for which weak interactions are relevant, to ensure accuracy of the model (see Paper I for more details).

---

[1] http://einsteintoolkit.org

Our magnetized PNS models use as initial conditions unmagnetized PNS wind solutions similar to those presented in Paper I, run sufficiently long for the wind to achieve a quasi-steady-state, but short compared to the Kelvin-Helmholtz cooling timescale of the PNS. These unmagnetized wind solutions are then endowed with a large-scale dipolar magnetic field (see Sec. 3.1.2 for more details). Here, we briefly review the setup of the unmagnetized models.

The initial conditions for the PNS structure are determined by the Tolman-Oppenheimer-Volkoff equations, employing a density-dependent initial temperature and Y_e profile (computed by imposing β-equilibrium), following the approach by Kaplan et al. (2014). We use the SFHo equation of state (Steiner, Hempel, and Fischer 2013) in tabular form as provided by O'Connor and Ott (2010)[2]. We do not self-consistently follow PNS cooling evolution to arrive at initial conditions for our models; thus the final electron fraction Y_e in the outflows, which depends sensitively on the neutrinosphere properties, will not be physically accurate. Nevertheless, we can draw conclusions regarding the effects (if any) of strong magnetic fields on the wind composition by comparing Y_e from our magnetized models to those obtained from otherwise equivalent unmagnetized models.

Our fiducial model employs a grid hierarchy consisting of a base Cartesian grid and six fixed nested refinement levels. We improve upon the resolution used in the models from Paper I. The smallest and finest grid is a $30 \times 30 \times 30$ km box centered at the origin now with a resolution of 150 m, while the size of the base grid is 960 × 960 × 960 km. As discussed in Paper I, this grid setup allows us to simultaneously capture the wind zone on scales of ~100 − 1000 km, while providing enough resolution from the finest grid to capture the details of outflows from the PNS surface. For this resolution, the magnetic pressure scale height $H_{p_B} = |d \ln p_B/dr|^{-1}$ is resolved by at least 10 grid points throughout the entire domain of the simulation (see Appendix A.1.1, Fig. A.1). As in Paper I, the neutrinosphere is only marginally resolved, with the grid resolution approximately equal to the optical depth scale height (see Appendix A.1.1, Fig. A.1). This issue is not critical for the purposes of this study, as the neutrino energies and luminosities determined at the neutrinosphere serve as a boundary condition for heating that occurs at larger radii, a region that by comparison is well resolved. Most of our calculations employ reflection symmetry across the equatorial ($z = 0$) plane for computational efficiency. We have checked that our results for the time-averaged wind properties are not appreciably affected by this assumption, by performing a full-domain simulation and a side-by-side comparison to the half-domain case (see Appendix A.1.2).

---

[2] https://stellarcollapse.org/equationofstate.html

3.1.2 Addition of a Dipole Magnetic Field

We evolve the unmagnetized PNS and its wind for ~150 ms, the last ~50 ms over which the wind has achieved a quasi-steady state. At this point, we superimpose a large scale magnetic field onto the stationary wind solution. As in Siegel, Ciolfi, and Rezzolla (2014) and similar to the configurations in Shibata et al. (2011) and Kiuchi, Kyutoku, and Shibata (2012), we define this large-scale, dipole-like magnetic field by initializing the components of the vector potential as $A_r = A_\theta = 0$, and

$$A^\phi = A_{0,d} \frac{\varpi_{0,d}/\sqrt{2}}{(r^2 + \varpi_{0,d}^2/2)^{3/2}}, \tag{3.1}$$

where $A_{0,d}$ tunes the overall field strength, ϖ is the cylindrical radius, $r^2 = \varpi^2 + z^2$, and $\varpi_{0,d} \simeq 8$ km is the ‘neutral point’. The neutral point corresponds to a ring-like current in

Model -	$B_{\mathrm{S}}^{(a)}$ (10^{15} G)	$R_e^{(b)}$ (km)	$R_{\bar{\nu}_e}^{(c)}$ (km)	$\langle L_{\nu_e} \rangle^{(d)}$ (erg s^{-1})	$\langle L_{\bar{\nu}_e} \rangle^{(e)}$ (erg s^{-1})	$\langle E_{\nu_e} \rangle^{(f)}$ (MeV)	$\langle E_{\bar{\nu}_e} \rangle^{(g)}$ (MeV)
`no-B`*	0.0	13	10	2.2e51	3.9e51	13	18
`lo-B`	0.61	13	10	2.2e51	3.9e51	13	18
`hi-B`	2.5	13	10	2.3e51	3.8e51	13	18
`sym-B`†	2.1	13	11	4.3e51	6.0e51	13	17
`no-sym-B`†	2.2	13	11	4.1e51	6.8e51	13	18

Table 3.1: **Suite of PNS Wind Simulations: Magnetic Field and Neutrino Properties**
(a) Magnetic field strength as measured along the polar axis at the radius of the $\bar{\nu}_e$ neutrinosphere; (b) Initial equatorial radius of the star; (c) Steady-state $\bar{\nu}_e$ neutrinosphere radius; $(d)-(g)$ Luminosities and mean energies of electron neutrinos and anti-neutrinos, averaged over the final factor of three in simulation time.
*Fiducial unmagnetized wind model (Fig. 3.3, left panels). †All simulations employ the same grid geometry, but these models are run with three times poorer resolution compared to the models in the first 3 rows (i.e., $\Delta x = 450$ m for the finest grid).

the equatorial ($z = 0$) plane centered at the origin. We require this neutral point to lie within the star (of radius $R_{\mathrm{PNS}} \simeq 12$ km) so as to yield a plausible, nearly point-like dipole field that is non-singular everywhere. The magnetic field is then obtained via $\boldsymbol{B} = \nabla \times \boldsymbol{A}$, yielding the initial configuration shown in Fig. 3.1. The dipole geometry is symmetric across the $z = 0$ plane at initialization. Although the current sheet that forms in this plane can "wobble", we find that when averaged over time, these wobbles smooth out (Fig. A.2 of Appendix A.1.2). Hence, the time-averaged wind outflow properties should also be roughly symmetric across the $z = 0$ plane, justifying our use of equatorial symmetry for computational efficiency.

We activate the magnetic field after running the non-magnetized PNS wind evolution for roughly $\approx 176\,$ms, at which point we "reset" the clock and hereafter refer to this time as $t = 0$. In order to explore different physical regimes of magnetized winds, we consider models which span two different initial surface magnetic field strengths but are otherwise identical. We distinguish these models by their polar magnetic field strength B_{S} at the neutrinosphere, with $B_{\mathrm{S}} \simeq [6.1\times10^{14}\,\mathrm{G}, 2.5\times10^{15}\,\mathrm{G}]$, referred to as `lo-B` and `hi-B`, respectively (see Tab. 3.1 and Fig. 3.1 for further details). In addition to the magnetized models, we run in parallel a non-magnetized model ($B_{\mathrm{S}} = 0$, referred to as `no-B`), which provides a set of comparison wind

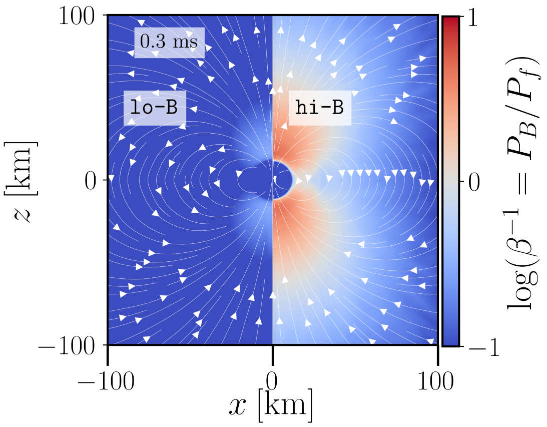

Figure 3.1: Initial magnetic-to-fluid pressure ratio β^{-1} with magnetic field line geometry overlaid. We show models `lo-B` (left) and `hi-B` (right) in a slice through the magnetic dipole axis ($y = 0$ plane), soon after the magnetic field is turned on at $t = 0$ ms. This magnetic field configuration was added onto an unmagnetized PNS wind solution previously evolved for about 176 ms to steady state. For model `hi-B`, magnetic pressure dominates over fluid pressure in the polar regions above the PNS surface out to ≈60 km.

properties over the same time interval (i.e., for the same PNS neutrino cooling evolution).

The magnetic field does not significantly impact the hydrostatic structure of the PNS. At the time the field is initialized, the magnetic-to-fluid pressure ratio $\beta^{-1} \equiv P_B/P_f$ obeys $< 10^{-2}$ for all the models we consider (see Fig. 3.1). This ratio similarly shows that the gradient of the magnetic field is negligible with respect to the fluid pressure gradient. The magnetic field is not dynamically relevant; only the wind region is potentially impacted by its presence.

The toroidal component of the magnetic field remains subdominant compared to the poloidal component at all epochs and for all models (see Appendix A.1.3). This is expected because the initial magnetic field configuration is purely poloidal and there is no significant active mechanism, such as rotation, winding up magnetic fields on large scales.

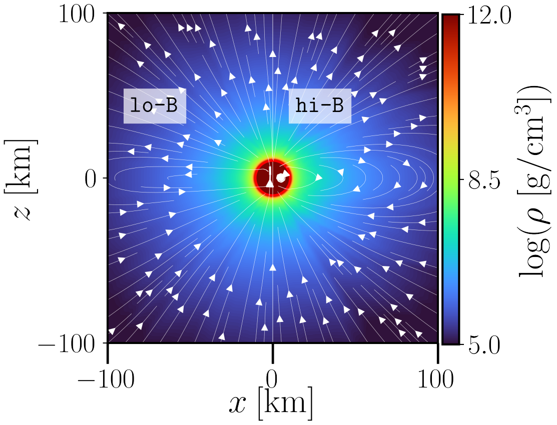

Figure 3.2: Snapshots of the outflow properties as a cross-section through the magnetic dipole axis ($y = 0$ plane) at $t \approx 55\,\mathrm{ms}$ after B-field initialization for models `lo-B` (left) and `hi-B` (right). Colors show the rest-mass density ρ, with the magnetic field line geometry overlaid in white. The neutrinosphere ($\tau_{\bar{\nu}_e} = 1$ surface) is shown with a red contour. The field lines have been nearly completely torn open radially in the weakly magnetized model, while an equatorial belt of closed field lines persists in the strongly magnetized case.

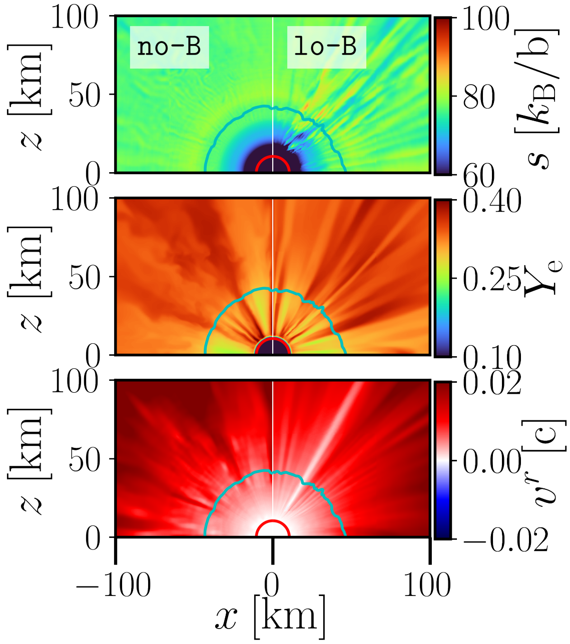

Figure 3.3: Snapshots showing outflow properties as a cross-section through the magnetic dipole axis ($y = 0$ plane) at $t \approx 55\,\mathrm{ms}$ after B-field initialization for models `no-B` (unmagnetized, left) and `lo-B` (weakly magnetized, right). From top to bottom: specific entropy s, electron fraction Y_e, radial velocity v^r. The green contour represents the alpha-particle formation surface ($X_\alpha = 0.5$), around which r-process seed nuclei begin to form, while the red contour represents the location of the neutrinosphere ($\tau_{\bar{\nu}_e} = 1$ surface).

3.2 Results

The presence of a magnetic field can significantly impact the dynamics of the PNS wind in regions where the magnetic pressure $P_{\rm B} = B^2/8\pi$ greatly exceeds the fluid pressure P_f (Thompson 2003; Thompson and ud-Doula 2018; Prasanna et al. 2022). In the gain region just above the PNS surface, where neutrino heating begins to exceed neutrino cooling, radiation pressure of photons and electron/positrons dominates over gas pressure and hence $P_f \simeq P_{\rm rad} = (11/12)aT^4$, where a is the radiation constant. Just below this point closer to the star, the specific neutrino heating rate $\propto L_\nu \epsilon_\nu^2/r^2$ and neutrino cooling rate $\propto T^6$ (due to pair capture reactions on free nucleons) balance, resulting in a roughly isothermal atmosphere of temperature (e.g., Qian and Woosley 1996)

$$T_{\rm eq} \approx 1\, L_{\bar{\nu}_e,51}^{1/6} \langle E_{\bar{\nu}_e,{\rm MeV}}\rangle^{1/3} R_{\bar{\nu}_e,6}^{-1/3}\ {\rm MeV}, \tag{3.2}$$

where $R_{\bar{\nu}_e} = R_{\bar{\nu}_e,6} \times 10^6$ cm , $L_{\bar{\nu}_e} = L_{\bar{\nu}_e,51} \times 10^{51}$ erg s^{-1}, and $\langle E_{\bar{\nu}_e}\rangle = \langle E_{\bar{\nu}_e,{\rm MeV}}\rangle \times$ MeV are the PNS radius, electron antineutrino luminosity, and mean electron antineutrino energy, respectively.

Equation 3.2 reveals that $P_{\rm B} > P_{\rm rad}$ for magnetic field strengths above a critical value

$$B_{\rm crit} \approx 7 \times 10^{14}\,{\rm G} \left(\frac{L_{\bar{\nu}_e,51}}{4}\right)^{\frac{1}{3}} \left(\frac{E_{\bar{\nu}_e}}{18\,{\rm MeV}}\right)^{\frac{2}{3}} \left(\frac{R_{\bar{\nu}_e}}{10\,{\rm km}}\right)^{-\frac{2}{3}}. \tag{3.3}$$

Thus, for surface dipole fields $B_{\rm S} \gg B_{\rm crit}$ we expect the wind dynamics to be significantly altered by the presence of the magnetic field.

We begin in Sec. 3.2.1 by presenting results for a relatively weakly magnetized model (`lo-B`), for which $B_{\rm S} < B_{\rm crit}$ and hence the wind dynamics are expected to be similar to the unmagnetized wind. In Sec. 3.2.2, we move onto describing a strongly magnetized model (`hi-B`) for which $B_{\rm S} > B_{\rm crit}$ and discuss prospects for r-process nucleosynthesis in Sec. 3.2.3.

3.2.1 Weakly Magnetized Model

The left panel of Fig. 3.1 shows the magnetic-to-fluid pressure ratio $\beta^{-1} = P_{\rm B}/P_{\rm f}$ and magnetic field line geometry for the weakly magnetized model `lo-B` at the moment of magnetic field initialization. Figure 3.3 shows a comparison of key quantities from the magnetized and unmagnetized models (`lo-B` and `no-B`, respectively) 55 ms after a weak magnetic field is turned on.

Before the magnetic field is activated, the PNS wind has achieved an approximately steady state, as detailed in Paper I. At the moment the magnetic field is initialized, magnetic field lines reflect a dipole geometry and $\beta^{-1} = P_{\rm B}/P_{\rm f}$ of the wind is $\lesssim 1$, indicating that fluid pressure dominates over magnetic pressure from the start (Fig. 3.1). As the wind subsequently evolves, the dipole magnetic field structure is disrupted, as evidenced by the field line geometry at late times (Fig. 3.2, left panel). The magnetic field is 'frozen in' within the radial fluid flow (see the velocity field in Fig. 3.3, bottom panel). By $\sim$ 55 ms after magnetic field initialization, outflows in models `lo-B` ($B_{\rm S} = 6.1 \times 10^{14}$ G) and `no-B` ($B_{\rm S} = 0$) are nearly indistinguishable (Fig. 3.3).

Because fluid pressure exceeds magnetic pressure upon magnetic field initialization nearly everywhere ($\beta^{-1} < 1$ in Fig. 3.1, left), and since magnetic fields are frozen into the fluid flow, magnetic field lines follow the mostly radial outflow of the neutrino-driven wind. The magnetic field thus tears open from its initial dipole configuration within milliseconds, approaching a split monopole configuration (see left panel of Fig. 3.2). For such a split-monopole solution, $B(r) \propto r^{-2}$, rather than $B(r) \propto r^{-3}$, as for the dipole geometry (e.g., Weber and Davis 1967). This is illustrated in Fig. 3.4, which shows angle-averaged radial profiles of the poloidal magnetic field strength in the polar region for models `lo-B` and `hi-B` at the time the magnetic field is initialized (solid lines, for which $B(r) \propto r^{-3}$) as well as ~30 ms later (dashed lines, for which $B(r) \propto r^{-2}$). A thin 'current sheet' region forms in the equatorial plane with a low magnetic-to-fluid pressure ratio β^{-1} as the wind evolves to $t \approx 55$ ms (Fig. 3.2, left panel). Here, magnetic field lines of opposite polarities from the northern and southern hemispheres reconnect and heat the fluid (however, note that the physical thickness of the current sheet is not resolved by the simulation because the resistivity is numerical in this ideal MHD setup).

Aside from the magnetic field properties, all of the asymptotic wind properties remain largely unaffected compared to the prior unmagnetized state. The PNS hydrostatic structure and neutrino energies as well as luminosities are essentially unchanged with respect to the unmagnetized model (see Tab. 3.1). Consequently, the net specific heating rate $\dot{q}_{\rm net}$, which depends on neutrino properties and temperature, retains a similar radial profile. After an initial transient phase, the outflow properties of model `lo-B` such as the specific entropy s, electron fraction Y_e, and radial velocity v^r, and the asymptotic wind properties are also very similar to the `no-B` model (Fig. 3.3, Tab. 3.2).

Because the temperature and density profiles change little after the magnetic field is activated, the surface at which α-particles form (roughly where $T \lesssim 5 \times 10^9$ K) remains at $r \approx 45$ km, close to the outer edge of the gain region (Fig. 3.3). As outlined by Qian and Woosley (1996) and reviewed in Paper I, the ability of the PNS wind to generate r-process nuclei yields depends on s, Y_e, and the expansion timescale $t_{\rm exp}$, which we define as

$$t_{\rm exp} = \left(v^r \frac{\ln dT}{dr} \right)^{-1} \Bigg|_{X_{\rm nuc}=0.5}, \tag{3.4}$$

where we have defined $X_{\rm nuc} = 0.5$ as the α-particle surface ($X_{\rm nuc}$ is the mass fraction of all nuclei excluding protons and neutrons), as typically located $50 - 100$ km above the PNS surface. In particular, the r-process figure of merit defined by (Hoffman, Woosley, and Qian, 1997)

$$\eta \equiv \frac{s^3}{Y_e^3 t_{\rm exp}} \tag{3.5}$$

is a rough measure of success for heavy element nucleosynthesis due to alpha-rich freeze-out, where here and hereafter $t_{\rm exp}$ is measured in seconds and s is meausred in $k_{\rm B}$ per baryon.

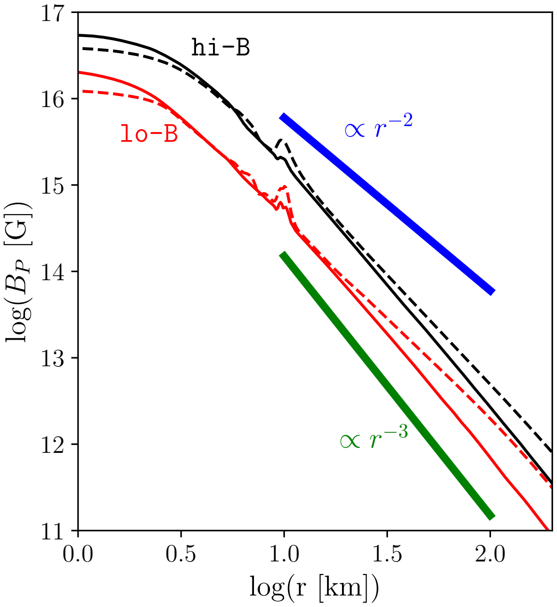

Figure 3.4: Radial profiles of the poloidal magnetic field strength B_P for models `lo-B` and `hi-B`, taken from a slice through the magnetic dipole axis ($y = 0$), angle-averaged in the polar region from $\theta = 0°$ to $\theta = 45°$. Solid lines show B_P time-averaged from $t \approx 0 - 5$ ms after the magnetic field is activated, while dashed lines represent B_P time-averaged from $t \approx 25 - 35$ ms. To guide the eye, thick solid lines show power-laws r^{-2} (blue) and r^{-3} (green). Both models approach the split monopole solution ($\propto r^{-2}$) in the polar region.

Threshold values of $\eta \gtrsim 4 \times 10^9$ and $\eta \gtrsim 9 \times 10^9$ are required for neutron capture to proceed to the 2nd and 3rd r-process peak, respectively. As found in Paper I, and consistent with past findings (e.g., Qian and Woosley 1996; Hoffman, Woosley, and Qian 1997; Thompson, Burrows, and Meyer 2001), unmagnetized PNS winds (model `no-B`) generally have $\eta \ll 1 \times 10^9$, insufficient for an r-process. Not surprisingly then, our weakly magnetized model `lo-B` is also not capable of an r-process (Tab. 3.2).

3.2.2 Strongly Magnetized Model

We now consider results for the strongly magnetized model (`hi-B`) with $B_\mathrm{S} = 2.5 \times 10^{15}\,\mathrm{G} > B_\mathrm{crit}$. Immediately after the magnetic field is activated, its dipole geometry is identical to that of model `lo-B`, with the poloidal field strength following the expected r^{-3} radial profile (Fig. 3.4). The magnetic-to-fluid pressure ratio, however, is much larger

Model -	Sector†† -	$\langle \dot{M} \rangle^{(a)}_{60\ \mathrm{km}}$ ($M_\odot$ s^{-1})	$\langle \dot{E}_K \rangle^{(b)}_{60\ \mathrm{km}}$ (erg s^{-1})	$\langle s \rangle^{(c)}_{60\ \mathrm{km}} \pm \sigma_s$ k_B baryon^{-1}	$\langle t_{\mathrm{exp}} \rangle^{(d)}_{60\ \mathrm{km}} \pm \sigma_{t_{\mathrm{exp}}}$ (ms)	$\langle Y_e \rangle^{(e)}_{60\ \mathrm{km}} \pm \sigma_{Y_e}$ -	$\langle \eta \rangle^{(f)}_{60\ \mathrm{km}} \pm \sigma_\eta$ [10^8]
`no-B`*	tot.	5.5e-5	5.4e45	78±0.9	20±9	0.40±0.003	5.6±2
`lo-B`	tot.	5.6e-5	5.1e45	78±1.9, (78→78)	21±6	0.36±0.003	5.3±2 (5.2→5.3)
`hi-B`	tot.	3.8e-5	3.1e45	82±5	29±20	0.37±0.002	5.1±4
`hi-B`	pol.	2.9e-5	2.3e45	80±4 (80→80)	32±10	0.37±0.002	3.8±2 (3.5→3.9)
`hi-B`	equat.	4.3e-5	3.6e45	84±6 (83→85)	25±20	0.37±0.02	6.5±4 (5.7→7.8)
`sym-B`†	tot.	1.6e-4	3.6e46	67±3	16±10	0.38±0.02	4.6±2
`no-sym-B`†	tot.	1.8e-4	5.4e46	68±3	21±40	0.38±0.03	4.6±3

Table 3.2: **Time-Averaged Outflow Properties**
We report wind properties time-averaged from $t \approx 25-55$ ms for models `no-B`, `lo-B`, and `hi-B`, and from $t \approx 0-20$ ms for models `sym-B` and `no-sym-B`. Entries of the format $(q \rightarrow q')$ refer to the same quantity time-averaged from $t \approx 25-35$ ms (q) and from $t \approx 45-55$ ms (q').
(a) isotropic mass-loss rate; (b) kinetic energy; (c) specific entropy with standard deviation; (d) expansion timescale with standard deviation; (e) electron fraction with standard deviation; (f) $r-$process figure of merit $\eta \equiv s^3/(Y_e^3 t_{\mathrm{exp}})$ with standard deviation.
*Fiducial unmagnetized wind model shown in Fig. 3.3 (left-hand panels). †All simulations in the table use the same grid geometry, but these models are run with a third of the resolution compared to the models in the first three rows (i.e. $\Delta x = 450$ m for the finest grid). ††Quantities are averaged over different angular sectors in polar angle θ: 'equat.' ($45° \leq \theta \leq 135°$), 'pol.' ($0° \leq \theta \leq 45°$ and $135° \leq \theta \leq 180°$), and 'tot.' ($0° \leq \theta \leq 180°$). Isotropic equivalent quantities are reported for $\langle \dot{M} \rangle$ and $\langle \dot{E}_K \rangle$ at a radius $r = 60$ km.

compared to the weakly magnetized model, reaching $\beta^{-1} \sim 10$ near the polar regions for model `hi-B` (Fig. 3.1). Right after the magnetic field is initialized, the radial velocity v^r is negative in a region extending from slightly above the neutrinosphere at $r \approx 15$ km to $r \approx 50$ km, as a result of the previously outflowing wind plasma being trapped by the strong magnetic field.

The mass-loss rate $\dot{M}$ through a fixed surface of radius ≈ 60 km is also suppressed after the magnetic field is initialized ($t \approx 0$) by almost a factor of 2 from its original value, from $\dot{M} \approx 5.6 \times 10^{-5} M_{\odot}$ s^{-1} to $\dot{M} \approx 3.2 \times 10^{-5} M_{\odot}$ s^{-1} (top panel of Fig. 3.5). Dividing the outflow into separate polar ($\theta = 0 - 45°$, $135 - 180°$) and equatorial ($\theta = 45° - 135°$) angular sectors, we see that the isotropic-equivalent mass-loss rate $\dot{M}_{\rm iso}$ along the equatorial direction has returned to its original value by $t \approx 35$ ms and continues to increase, approaching $\dot{M}_{\rm iso} \approx 10^{-4} M_{\odot}$ s^{-1} by $t \approx 55$ ms. By contrast, $\dot{M}_{\rm iso}$ in the polar region remains significantly suppressed for the entirety of the simulation. As we describe below, this suppression is the result of the extra work the polar outflows must perform to open field lines in this region and escape to infinity.

As shown in Fig. 3.7, the radial velocity remains small or negative $|v^r| \ll 0.01c$ in the equatorial region between $r \approx 15$ km and $r \approx 100$ km, indicating the presence of a sustained 'trapped zone' at low latitudes. The magnetic-to-fluid pressure ratio β^{-1} begins to rise in the polar region and to drop in the equatorial region (Fig. 3.6). At the same time, the specific entropy in the $\theta = 60° - 120°$ equatorial trapped belt between $r = 15$ km and $r = 100$ km rises from $s \approx 75$ to $s \approx 100$ by $t \approx 55$ ms (Fig. 3.8).

Since magnetic fields do not strongly impact the hydrostatic structure of the PNS atmosphere near the neutrinosphere, neither the neutrino luminosities/energies nor the neutrinosphere radii are altered significantly by the magnetic field (Tab. 3.1). Insofar as the neutrino fluxes and energies determine the relative rate of ν_e and $\bar{\nu}_e$ absorption by the wind material, the wind's electron fraction is not altered considerably compared to the unmagnetized model (Fig. 3.9). The density and temperature profile, particularly of the inner hydrostatic atmosphere, also remain only mildly affected by the presence of the magnetic field (Fig. 3.10).

As discussed at the beginning of Sec. 3.2, the impact of the magnetic field on the wind dynamics can be understood in terms of the high magnetic-to-fluid pressure ratio in model `hi-B` (Fig. 3.1, right panel). Outflowing matter in the polar regions tear open originally closed magnetic field lines, resulting in a split-monopole geometry at high latitudes (similar to that achieved across all outflow directions in model `lo-B`). Given that the surface magnetic field strength is fixed, the transformation from $B \propto r^{-3}$ to $\propto r^{-2}$ by ≈ 30 ms (Fig. 3.4) causes the magnetic to fluid pressure ratio above the surface at high latitudes to increase with time.

In addition, matter that would otherwise have traveled radially in the polar region is partially redirected along magnetic field lines, which bend towards lower latitudes. This suppresses $\dot{M}_{\rm iso}$ in the polar region (Fig. 3.5, top panel, dashed line). Field lines at mid-latitudes ($\theta \approx 30^\circ - 60^\circ$ and $120^\circ - 150^\circ$) are gradually opened ('peeled off' from originally closed field lines at low latitudes) and the pressure ratio there similarly increases (Fig. 3.6). In the equatorial region ($\theta \approx 60^\circ - 120^\circ$), however, magnetic tension remains high enough to oppose radial fluid motion, which is orthogonal to magnetic field lines in this region as a result of the dipole geometry. The resulting 'trapped zone' extends to $r \approx 50\,\mathrm{km}$.

To better understand the wind dynamics, Fig. 3.11 shows the cumulative change of various energies interior to a given radius above the PNS surface, over the ≈ 55 ms duration of the simulation, again broken down separately into polar (left panel) and equatorial angular sectors (right panel). In both latitude ranges, the increase in the magnetic energy (black lines) exceeds the increases in the wind thermal (green lines) or kinetic (blue lines) energies. This illustrates that most of the energy deposited by neutrino heating (red lines) is used to open magnetic field lines, rather than powering the wind. The energy being expended to open field lines is not available to unbind matter from the gravitational potential well of the PNS and hence contributes to the initial suppression of the wind mass-loss rate and kinetic power shown in Fig. 3.5. Indeed, the magnetic energy rises with a greater delay in the equatorial

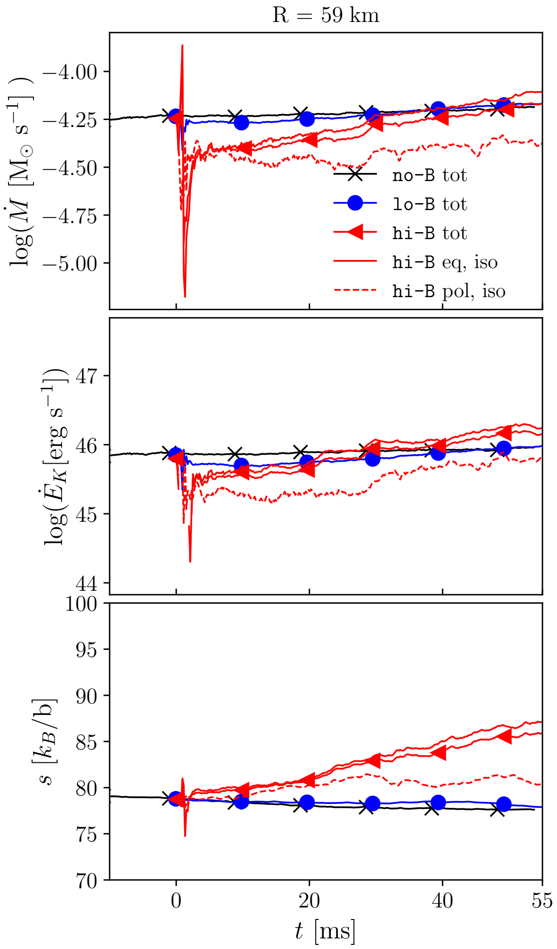

Figure 3.5: Mass-loss rate $\dot{M}$ (top), kinetic power $E_K = (W - 1)\dot{M}$ (center), where W is the Lorentz factor, and $\dot{M}$-weighted average specific entropy s (bottom) of outflows through a spherical surface of radius $r = 60$ km, as a function of time since magnetic field initialization. For all models `no-B` (black, ×), `lo-B` (blue circles), and `hi-B` (red triangles) these quantities are shown across the full 4π solid angle. For model `hi-B` (red), we show separately the isotropic equivalent mass-loss rate as well as kinetic power, and average-entropy across a solid angle at high latitudes close to the poles ($\theta = 0° - 45°$ and $\theta = 135° - 180°$; dotted line) and near the equatorial plane ($\theta = 45° - 135°$; solid line).

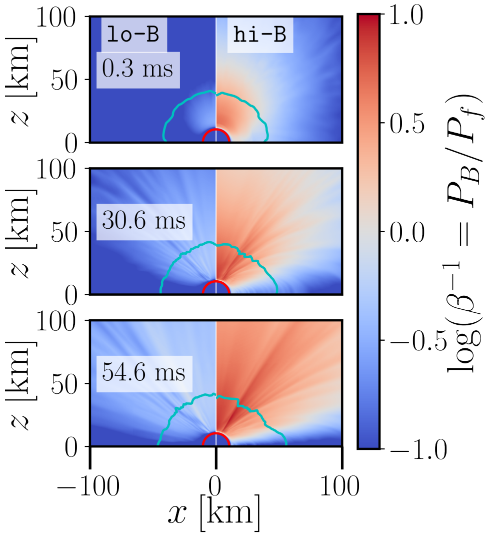

Figure 3.6: Snapshots of the magnetic-to-fluid pressure ratio β^{-1} in the $y = 0$ magnetic dipole axis plane for models `lo-B` and `hi-B`. The top panel shows the moment the magnetic field is initialized ($t \approx 0$ ms), while the middle and bottom panels are at $t \approx 31$ ms and $t \approx 55$ ms, respectively. A cyan contour represents the alpha particle formation surface ($X_\alpha = 0.5$) around which r-process seed nuclei begin to form, while the red contour represents the neutrinosphere surface ($\tau_{\bar{\nu}_e} = 1$).

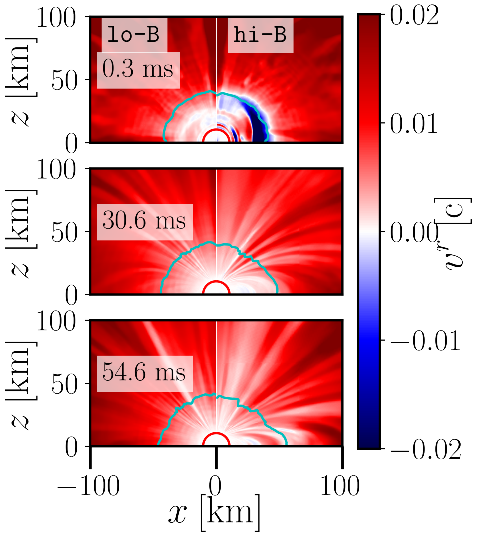

Figure 3.7: Same as Fig. 3.6, but for radial velocity v^r. The lower velocities of matter in the equatorial closed zone region, particularly in the first two snapshots, is apparent.

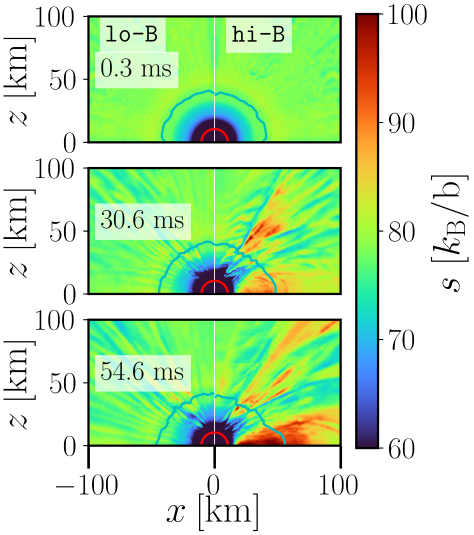

Figure 3.8: Same as Fig. 3.6, but for specific entropy s. The effect of the enhanced heating of matter in the equatorial closed zone is apparent.

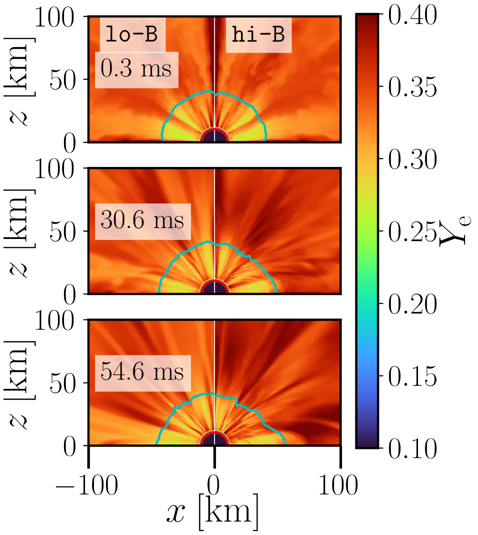

Figure 3.9: Same as Fig. 3.6, but for Y_e.

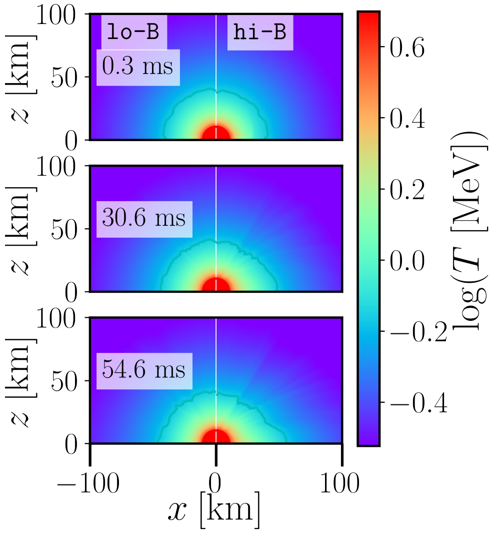

Figure 3.10: Same as Fig. 3.6, but for temperature T.

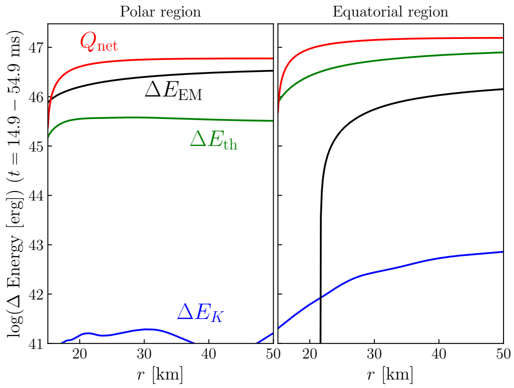

Figure 3.11: Change in the energy contained within the volume extending from $r = 15$ km to an outer radius r between $t \approx 15$ ms and $t \approx 55$ ms following the initialization of the magnetic field for model `hi-B`. Left: Polar component, averaged azimuthally and over polar angles $\theta = 0° - 45°$ and $135° - 180°$. Right: Equatorial component, averaged azimuthally and over polar angles $\theta = 45° - 135°$. The energies are defined as follows: kinetic energy $E_K = \int (W-1)\rho W \sqrt{\gamma}\, d^3x$ (blue); thermal energy $E_{\rm th} = \int \epsilon \rho W \sqrt{\gamma}\, d^3x$ (green); electromagnetic energy $E_{\rm EM} = \int n_\mu n_\nu T^{\mu\nu}_{\rm EM} \sqrt{\gamma}\, d^3x$ (black); net integrated neutrino heating $Q_{\rm net} = \int\int \dot{q}_{\rm net} \rho W \sqrt{\gamma}\, d^3x\, dt$ (red). Here, $T^{\mu\nu}_{\rm EM}$ is the electromagnetic stress-energy tensor, n^μ the 4-velocity of the Eulerian observer, W the Lorentz factor associated with the total 4-velocity, and γ the determinant of the 3-metric. The specific net neutrino heating rate $\dot{q}_{\rm net}$ is integrated over the time interval; all other quantities are evaluated at the final and initial times, with their difference plotted.

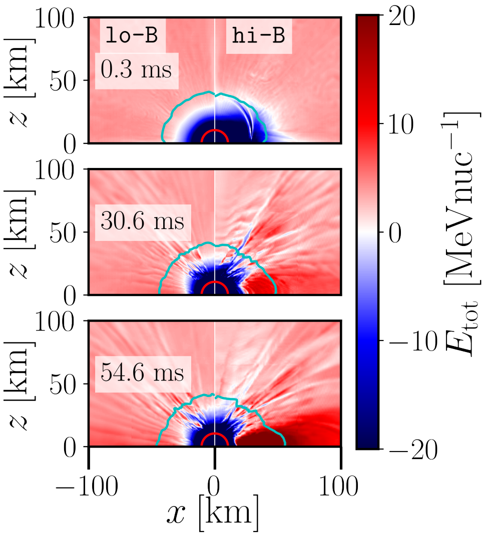

Figure 3.12: Same as Fig. 3.6, but for total specific energy $E_{\rm tot}$, including the effects of magnetic tension (Eq. 3.6). The energy grows in the equatorial belt due to neutrino heating of matter trapped in the closed zone, becoming positive by the final snapshots across a greater region extending to smaller radii approaching the PNS surface. As this high-entropy matter expands through the seed formation region (outside the cyan contour) it can potentially generate the conditions necessary for 2nd or 3rd-peak r-process nucleosynthesis.

belt relative to the polar regions, because it takes longer to open the closed magnetic field lines at lower latitudes (which are initially oriented perpendicular to fluid flow) through neutrino heating. This is counterbalanced by a greater fraction of the neutrino heating rate being deposited into thermal energy in the equatorial region (the ratio of the black to red lines in Fig. 3.5) compared to the polar region, because of the longer residence time of the matter trapped in the closed portion of the magnetosphere compared to the expansion time of a continuous outflow. Moreover, the 'equatorial' region corresponding to Fig. 3.5 is defined as the broad angular sector with polar angle $\theta = 45° - 90°$; polar outflowing material is diverted by field lines to the equatorial angular sector, which contributes to the steady rise in equatorial $\dot{M}_{\rm iso}$.

The trapped zone is further illustrated by Fig. 3.12, which shows the total specific energy of the fluid,

$$E_{\rm tot} = -h' u_t - 1, \tag{3.6}$$

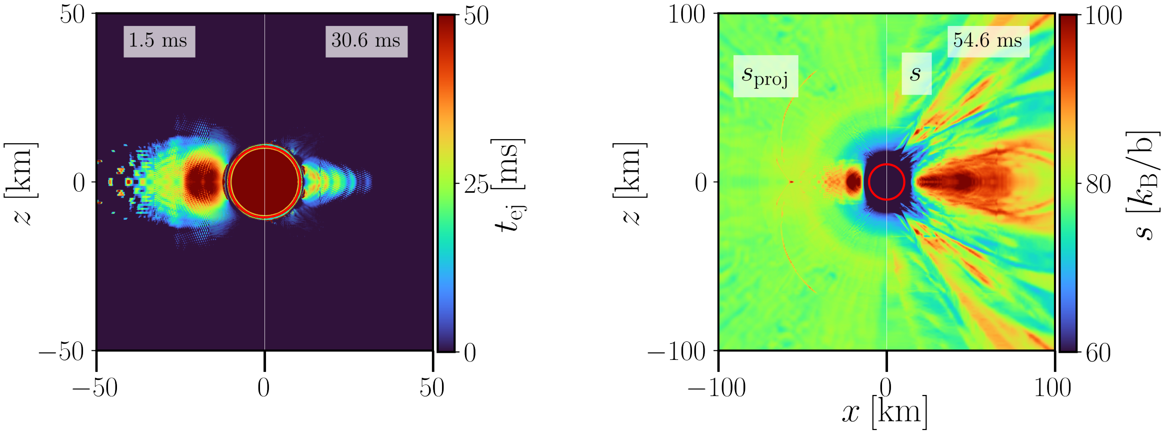

Figure 3.13: Top: Closed-zone ejection timescale $t_{\rm ej}$ (Eq. 3.9) computed just after magnetic field initialization (left) and 30 ms later (right) for model `hi-B` in a slice through the $y = 0$ plane. Bottom: Snapshots from model `hi-B` showing (left) the final entropy $s_{\rm proj}$ of the closed zone material achieved after a time $t_{\rm ej}$ (Eq. 3.9 from Thompson 2003 applied to the initial snapshot) in comparison to (right) the actual entropy s from the simulation at $t \approx 55$ ms after magnetic field initialization. The red contour represents the neutrinosphere surface ($\tau_{\bar{\nu}_e} = 1$). The analytic estimate is roughly consistent with the actual entropy achieved in the trapped zone of the wind.

where we have now modified the specific enthalpy h to include the effects of magnetic tension according to

$$h' = 1 + \epsilon + \frac{P_f - P_{B,\rm T}}{\rho}. \tag{3.7}$$

Here, u_t is the 0-component of the four-velocity, ϵ is the specific internal energy, and

$$P_{B,\rm T} \equiv \sin\alpha \frac{B^2}{4\pi}\left(\frac{R_\nu}{R_c(r,\theta)}\right), \tag{3.8}$$

is the effective confining pressure of magnetic tension, where α is the local angle between the radial direction and the magnetic field line direction and R_c is the radius of curvature. The bound region $E_{\rm tot} < 0$ under this definition extends to 50 km in equatorial regions for model `hi-B`, consistent with the geometry of a trapped zone evident in the velocity field as discussed above (Fig. 3.7).

Since the neutrino properties are not significantly altered by the strong magnetic field, the gain region remains almost identical to that in models `no-B` and `lo-B`, starting at the PNS surface and extending out to ≈50 km. As a result, the trapped zone experiences additional neutrino heating, increasing the ratio of fluid pressure to magnetic tension pressure (Fig. 3.6). Unlike for the quasi steady-wind solutions achieved in models `no-B` and `lo-B`, the specific entropy in the trapped magnetosphere, $\Delta s = \int \dot{q}_{\rm net}/T dt$, thus rises monotonically with time (Fig. 3.8).

Eventually, once the trapped zone is heated sufficiently for the fluid pressure to exceed the magnetic pressure, the field lines should open and the high-entropy matter will be ejected. The timescale over which this occurs, $t_{\rm ej}$, can be estimated by (e.g. Thompson 2003; Thompson and Doula 2018)

$$t_{\rm ej} = \frac{P_{B,{\rm T}} - P_f}{\dot{q}_{\rm net}\rho}. \tag{3.9}$$

The top panel of Fig. 3.13 shows the ejection time $t_{\rm ej}$ (Eq. 3.9) computed for model `hi-B` at two times: just after the magnetic field is initialized (left panel) and at a snapshot taken ≈31 ms later (right panel). Initially, $t_{\rm ej}$ peaks in the equatorial belt above the PNS surface at a value $\simeq$ 50 ms. By $\approx$ 31 ms the trapped region has shrunk in size, and the maximum ejection time has dropped to $t_{\rm ej} \simeq 20$ ms, roughly as expected given the amount of time elapsed. The entropy of the trapped zone material at the time of ejection $t = t_{\rm ej}$ can be estimated as (e.g. Thompson 2003)

$$s_{\rm proj} \approx s + t_{\rm ej}\dot{q}_{\rm net}/T, \tag{3.10}$$

where $t_{\rm ej}\dot{q}_{\rm net}/T$ is the projected entropy gain at the approximate time of ejection (Eq. 3.9). The bottom panel of Fig. 3.13 compares this future-projected final entropy $s_{\rm proj}$ at the time of magnetic field initialization (left panel) to the actual entropy achieved $t_{\rm ej} \approx 55$ ms later (right panel), around when trapped zone material is expected to be ejected. The fact that the maximum value of the entropy achieved in the equatorial region roughly agrees with the projected entropy $s_{\rm proj}$ in this region, suggests that complete ejection of the closed zone is imminent by the end of our simulation.

Unlike the equatorial region, the polar region is not trapped by the magnetic field; thus the material there does not experience additional heating and the entropy of the outflowing material is similar to that obtained in the weakly magnetized models `lo-B` and `no-B` (Fig. 3.8). The bottom panel of Fig. 3.5 shows for model `hi-B` how the entropy in the equatorial region at radius ≈ 60 km grows in time (solid red line, bottom panel) in comparison to the roughly constant entropy of `lo-B` and `no-B` (blue and black lines) and for polar outflows in model `hi-B`. Given the neutrino luminosities/energies and the strength of the magnetic field of our simulations, the entropy gain we find agrees with that found by Thompson and Doula (2018) (see their Fig. 5).

Figure 3.8 shows that the alpha-particle formation surface (cyan contour) passes through the equatorial trapped zone region. Thompson and ud-Doula (2018) found that neutrino heating of material in the trapped zone increases the ratio of gas to magnetic pressure until a minimum β^{-1} is reached, after which the closed zone is ejected as a single coherent structure. In our `hi-B` model we find that material from the trapped zone already has begun to leak out by $t \gtrsim 35$ ms. We speculate that the energy released by alpha-particle recombination, neglected by Thompson and ud-Doula 2018, contributes to unbinding matter from the edge of the closed zone in our simulation, in addition to neutrino heating.

3.2.3 Implications for r-process nucleosynthesis

Figure 3.14 shows angle- and time-sampled histograms of the outflow properties relevant to r-process nucleosynthesis as measured through a spherical surface of radius ≈ 60 km for models `no-B` and `lo-B` (left column). We also show results for model `hi-B` (right column), in this case broken down separately into polar and equatorial outflows and (since the highly magnetized case has not reached a steady state) shown in separate time intervals $25-35$ ms and $45-55$ ms after activation of the magnetic field, respectively. Some of these time-averaged wind properties are also summarized in Tab. 3.2.

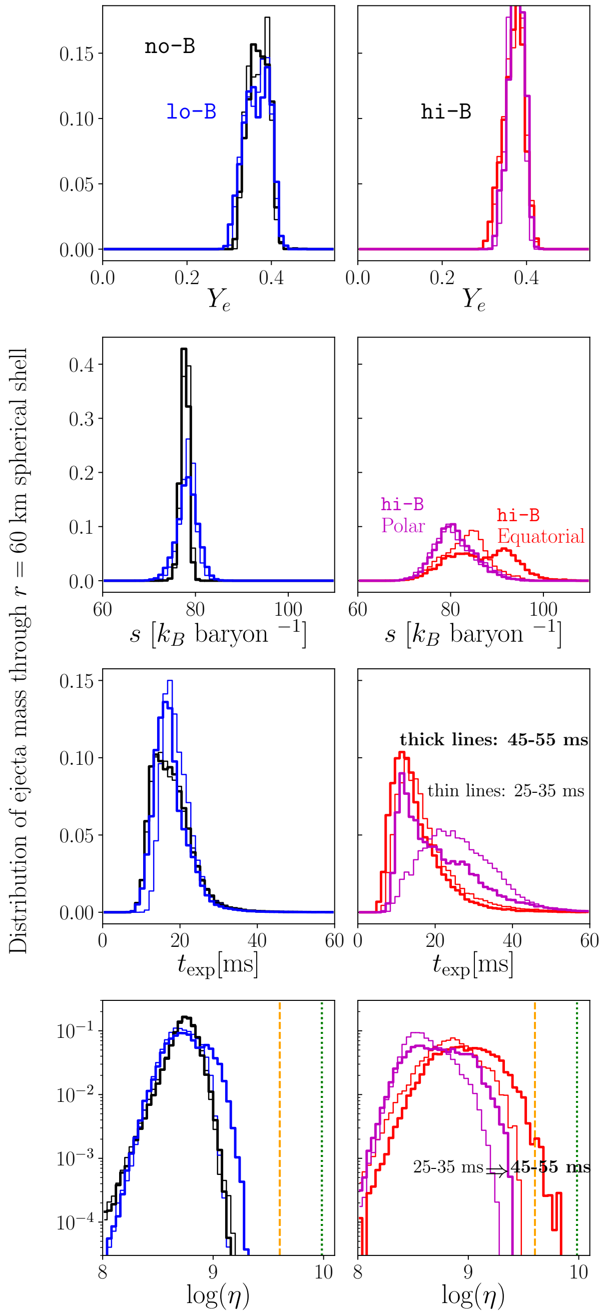

Figure 3.14: Histograms of various quantities relevant to r-process nucleosynthesis as measured through a 60 km spherical shell. The left panel shows the unmagnetized (`no-B`, black) and weakly magnetized (`lo-B`, blue) models, while the strongly magnetized model (`hi-B`) is shown on the right, broken down separately into the polar (purple) and equatorial (red) outflows, respectively (defined over the same angular domains as in Fig. 3.5). For the unmagnetized models we show results over the full time interval 25–55 ms, because the outflow is approximately time-stationary, while for the magnetized models we separately bin results for 25–35 ms (thin lines) and 45–55 ms (thick lines). At a given time, quantities are weighted pointwise on the spherical grid by the local mass outflow, they are binned and normalized by the total mass outflow through the entire surface over the time interval. We approximate the outflow expansion time (Eq. 3.4) as $t_{\rm exp} \equiv R/v(R)$, where $v(R)$ is the total wind speed measured at the shell. Threshold values for η (Eq. 3.5) required for neutron captures to reach the 2nd (yellow dashed vertical line) and 3rd (green dotted vertical line) r-process peaks (Hoffman, Woosley, and Qian, 1997) are indicated for comparison.

The Y_e distributions for all models are isotropic and nearly identical to one another (see also Fig. 3.9); this is as expected because the outflow speeds are sufficiently low that neutrino absorptions have time to bring Y_e into equilibrium, and as already mentioned, the properties of the neutrino radiation are similar between the magnetized and unmagnetized models (Tab. 3.1). The entropy distributions for the weakly magnetized models `lo-B` and `no-B` are nearly identical to each other, centered around $s \approx 78$ with a relatively narrow spread of $\Delta s \approx \pm 1$ (Tab. 3.2). This is also as expected given the previously noted similarities between the unmagnetized and weakly magnetized models, for both of which the outflow reaches an approximate steady-state (Sec. 3.2.1).

In the strongly magnetized model `hi-B`, the entropy distribution of the polar outflows overlaps that of the weakly magnetized case, though with a significantly larger spread $\Delta s \approx \pm 3.6$. By contrast, the mean entropy of the equatorial `hi-B` outflows is shifted to a higher value $s \gtrsim 80$, with an even greater spread $\Delta s \approx \pm 6$ in the distribution. Furthermore, the mean entropy rises significantly in time (compare the 25–35 ms vs. 45–55 ms samples in Fig. 3.14), such that by the end of the simulation values as high as $s \gtrsim 100$ are achieved (see also Fig. 3.8).

The expansion timescale distribution for models `lo-B` and `no-B` are again nearly identical, centered around ~ 20 ms. For both polar and equatorial ejecta in model `hi-B` the distribution extends to larger expansion times than the weakly magnetized cases, due to the significant trapping effect of the magnetic field. The nearly indistinguishable $\{Y_e, s, t_{\rm exp}\}$ distributions between models `lo-B` and `no-B` imply that the distribution of η (Eq. 3.5) should also agree; this is seen in the bottom panel of Fig. 3.14. As already noted (Sec. 3.2.1), both models remain well below the required threshold η for 2nd-peak r-process production.

By contrast, for the strongly magnetized model `hi-B`, the η distribution of the equatorial outflows extend to higher values due to the higher entropy ($\eta \propto s^3$). Over the course of the simulation, η increases from a mean value of $\approx 4 \times 10^8$ to $\approx 1 \times 10^9$, with the high-η tail (about 0.4% of equatorial material) achieving values $\gtrsim 4 \times 10^9$ necessary for 2nd peak

r-process production $\approx 45-55$ ms after the magnetic field is initialized. We conclude that−all else being equal (e.g., in terms of their neutrino emission properties)−strongly magnetized PNS are more promising r-process sources than weakly magnetized PNS.

The outflow entropies for our model `hi-B` are broadly consistent with those found by Thompson and ud-Doula (2018) using 2D axisymmetric MHD simulations, for roughly the same surface magnetic field strength. These authors also found that a small fraction of the ejecta reaches large values of $\eta \gtrsim 10^{10}$, sufficient for a 2nd or even 3rd peak r-process, due to the transient ejection of high-entropy matter from the closed zone. Although the evolution of our `hi-B` model indeed resembles a single episode of closed-zone inflation and eruption, our simulations unfortunately cannot be run as long as those by Thompson and ud-Doula (2018) and Prasanna et al. (2022) due to the higher computational cost of our 3D GRMHD simulations that aim to marginally resolve the neutrinosphere, versus axisymmetric 2D simulations.

Beyond their computational cost, the duration of our simulations are also limited by numerical issues: at late times $t \gtrsim 60$ ms, spurious violations of $\nabla \cdot \mathbf{B} = 0$ at refinement level boundaries of our fixed Cartesian grid hierarchy of concentric boxes at a level of $\sim 1\%$ have accumulated due to interpolation operations over a total of $\gtrsim 210$ ms of evolution and residual violations introduced by initializing a large-scale dipole magnetic field. At this level, we do not entirely trust subsequent results and choose not to consider those data in our analyses, even though the conditions for heavy r-process nucleosynthesis are seen to be improving with time as higher entropy material expands through the seed formation region. We refer to Appendix A.1.5 for a more detailed discussion of the issue of $\nabla \cdot \mathbf{B} = 0$ violation.

3.3 Summary and Conclusions

We have performed 3D GRMHD simulations including M0 neutrino transport of magnetized PNS winds to explore the impact that magnetar-strength dipole surface magnetic fields have on the outflow properties, with a particular focus on the conditions necessary for a successful r-process via the α-rich freeze-out mechanism in mildly neutron-rich winds. Our results can be summarized as follows.

- For even the strongest magnetic fields that we consider ($B_{\rm S} = 2.5\times10^{15}$ G; model `hi-B`), magnetic forces do not appreciably impact the hydrostatic structure of the wind near the neutrinosphere radii. As a result, the properties of the neutrino radiation (L_ν, E_ν, R_ν) which dictate the equilibrium electron fraction and specific heating rate in the gain region, are similar between the magnetized and unmagnetized models.

- In the case of a relatively weak magnetic field ($B_{\rm S} \simeq 6.1\times10^{14}$ G; $B_{\rm S} < B_{\rm crit}$; model `lo-B`) for which $\beta^{-1} = P_{\rm B}/P_{\rm f} \lesssim 1$, the dipole field structure is torn open by neutrino-driven outflows within $\sim$ 10 ms, and the magnetic field takes on a split-monopole configuration by ≈40 ms (Figs. 3.2, 3.4). Outflow properties such as the mass-loss rate and entropy are approximately spherical and quantitatively similar to those from the otherwise similar unmagnetized PNS model `no-B` (e.g., Figs. 3.3, 3.14).

- In stark contrast, the wind structure of the highly magnetized model ($B_{\rm S} \simeq 2.5\times10^{15}$ G $B_{\rm S} > B_{\rm crit}$; model `hi-B`) differs qualitatively from the weakly magnetized cases. Outflows that emerge along the polar axis of the dipole follow open magnetic field lines and are broadly similar in their isotropic-equivalent properties to the spherical unmagnetized and weakly magnetized winds. One exception is the isotropic mass-loss rate, which is initially suppressed compared to a weakly magnetized wind, because a significant portion of the energy deposition from neutrino heating goes into opening polar magnetic field lines rather than lifting matter out of the gravitational potential of the star (Fig. 3.11). Furthermore, as a result of opening-up field lines, a fraction of the polar outflows are diverted toward intermediate latitudes in the equatorial region, which enhances the equatorial isotropic equivalent mass flux.

  By contrast, outflowing material in the equatorial regions of the wind are initially trapped by the non-radial magnetic field at lower latitudes (Figs. 3.5, 3.7, 3.13), with the magnetosphere in this region maintaining a dipole field structure well above the PNS surface (Fig. 3.2). Neutrino heating raises the thermal pressure of the trapped fluid in the equatorial region until it obeys $P_f > P_B$ (Thompson, 2003; Prasanna et al., 2022), at which point fluid begins to escape and the closed zone begins to shrink from the outside inwards. Energy input from α-particle formation appears to aid the ejection of matter from the equatorial regions, and by the end of the simulation the isotropic-equivalent mass-loss rate even slightly overshoots that of the otherwise equivalent unmagnetized wind (Fig. 3.5).

- The weakly magnetized wind model achieves a rough steady-state and does not show significant entropy growth relative to the unmagnetized model, because matter is not trapped by the magnetic field (Fig. 3.3, top panel; Fig. 3.5, bottom panel). By contrast, plasma trapped in the strongly magnetized model causes the mean entropy of the trapped and eventually outflowing material from the equatorial region to rise, its standard deviation grows concurrently (Fig. 3.14, second row, right panel), over the course of $\sim 50 - 60$ ms. The mean expansion time of the equatorial outflows through the seed formation region is also moderately larger compared to the weakly magnetized cases because of the suppressed outflow speed.

- For the strongly magnetized model, the heating profile and magnetic field strength in the trapped equatorial belt imply an ejection timescale of the trapped plasma of ~ 50 ms, following the analytic estimates of Thompson and Doula (2018) (Fig. 3.13); although we do not see a discrete ejection event, a continuous slow but accelerating "peeling" of the trapped zone is observed to occur on this timescale. The projected entropy gain (Thompson, 2003) broadly agrees with the rise in entropy we observe in the simulation.

- The r-process figure-of-merit parameter η for unmagnetized and weakly magnetized models are similar ($\lesssim 10^9$), remaining well below the required threshold ($\approx 4 \times 10^9$) to produce 2nd peak r-process elements (Fig. 3.14). By contrast in the strongly magnetized model, due to the monotonic rise in the mean entropy of the equatorial outflows (particularly a "tail" of matter extending to high entropy $s \gtrsim 100$), sufficiently high η may be achieved for a small subset ($\approx 0.4\%$) of equatorial material, within ∼50 ms of magnetic field initialization. Following this trend to later times than the duration of our simulation, we conclude that a moderate fraction of the time-averaged wind material could well attain values of η that surpass the 2nd and potentially also 3rd r-process peaks. Though due to numerical limitations we cannot follow the multiple cycles of trapped-zone inflation and mass ejection seen by Thompson and ud-Doula (2018) and Prasanna et al. (2022), our results are in broad agreement with the findings of these authors.

Paper I demonstrated that rapid rotation in unmagnetized PNS winds tends to reduce the entropy of neutrino-driven outflows, while in the present paper we have shown that a strong magnetic field tends to increase the wind entropy. Although some aspects of the phenomena we have studied will be "additive" (i.e., neutrino-heating driven ejections from a rotating magnetosphere), qualitatively new features of the wind properties, such as magneto-centrifugal acceleration, are expected to emerge through the combined impact of rapid rotation and strong magnetic fields (e.g., Thompson, Chang, and Quataert 2004; Metzger, Thompson, and Quataert 2007; Vlasov et al. 2017; Prasanna et al. 2022; Combi and Siegel 2023; Raives, Coleman, and Thompson 2023; Prasanna et al. 2023). Rotating proto-magnetar winds will be the focus of future work.

Chapter 4: Imprints of r-process heating on fall-back accretion: distinguishing black hole-neutron star from double neutron star mergers

This work has published and may be found ***here.***

Short-duration gamma ray bursts (SGRBs) are commonly believed to be powered by rapid accretion onto a rapidly-spinning black hole, following the coalescence of a compact binary system (e.g. Narayan, Paczynski, and Piran 1992). The latter may be comprised either of two neutron stars (NS-NS) or a neutron star and a stellar-mass black hole (NS-BH). The recent discovery of an SGRB (**LIGO+17Fermi**) coincident with the gravitational wave event GW170817 (Abbott et al., 2017b), as well as non-thermal emission from the off-axis afterglow of a relativistic jet (e.g. Hallinan, Corsi, et al. 2017; Alexander et al. 2017; Margutti et al. 2017; Troja, Piro, van Eerten, et al. 2017; Haggard et al. 2017), provided compelling evidence that at least some SGRBs arise from NS-NS mergers (Blinnikov et al., 1984; Paczynski, 1986; Goodman, 1986; Eichler et al., 1989). Although no NS-BH binaries are currently known, they are theoretically predicted to exist and may also give rise to SGRB emission in cases where the merger results in the creation of an accretion disk (e.g. Rosswog 2005; Kyutoku et al. 2011; Foucart et al. 2013; Foucart et al. 2014; Foucart et al. 2016; Paschalidis, Ruiz, and Shapiro 2015; Bhattacharya, Kumar, and Smoot 2018). This latter condition requires that the BH be of sufficiently low mass and/or rapidly spinning in the prograde direction with respect to the binary orbit, such that the NS will be tidally disrupted before falling into the BH horizon (e.g. Foucart 2012).

At least $\sim 20\%$ of SGRBs are followed by temporally-extended X-ray emission, which lasts $\sim 10-1000$ s or longer after the initial prompt gamma-ray burst (Norris and Bonnell

2006; Gehrels et al. 2006; Perley et al. 2009; Norris, Gehrels, and Scargle 2010; Minaev, Pozanenko, and Loznikov 2010; Kaneko et al. 2015; Kisaka, Ioka, and Sakamoto 2017; Burns et al. 2018); Fig. 4.1 shows the light curves in two clear cases. This "extended emission" is too luminous and time variable to be synchrotron afterglow emission generated as the GRB jet interacts with the interstellar medium. Instead, it likely results from ongoing activity (e.g. prompt energy release in the form of a relativistic jet) from the central compact object remnant left by the merger (however, see Eichler, Guetta, and Manis 2009; Eichler 2017 for an alternative interpretation).

Several models have been proposed for the engine behind the extended emission. These include the electromagnetic spin-down of a long-lived millisecond magnetar generated from a NS-NS merger (e.g. Metzger, Thompson, and Quataert 2008; Bucciantini et al. 2012; Rowlinson et al. 2013; Gao et al. 2013; Gompertz, O'Brien, and Wynn 2014; Gibson et al. 2017). While this model remains in contention, the lack of late-time radio detections of short GRBs is beginning to place constraints on the amount of rotational energy released from such magnetar remnants (Metzger and Bower, 2014; Horesh et al., 2016; Fong et al., 2016). A stable magnetar is also disfavored in GW170817 by the relatively weak afterglow (Margutti et al., 2018; Pooley et al., 2018) and the red colors of the late kilonova emission indicative of black hole formation (Metzger and Fernández, 2014); however, no extended prompt emission was observed in this event (**LIGO+17Fermi**).

Another possibility is that the extended emission is powered by late-time accretion ("fall-back") onto the black hole of tidal matter which is marginally bound to the system after the merger event (Rosswog, 2007). However, a glaring issue with this model are the observed evolution of the extended emission light curves. The rate of mass fall-back after the merger, which is generally taken as a proxy for engine activity, is usually predicted to follow an uninterrupted power law, $\dot{M} \propto t^{-5/3}$, starting from very early times $\lesssim 0.1$ s after the merger. This result follows from a distribution of ejecta mass with energy, $dM/dE \propto E^{\alpha}$ that is relatively flat ($\alpha \approx 0$) around $E = 0$ (Rees 1988). Fig. 4.1 shows that a single power-law decay is incompatible with observed extended emission light curves, which generally show a lull and delay until peak of a few to tens of seconds after the initial gamma-ray burst. Explanations proposed for this behavior include a transition in the jet launching mechanism from neutrino-driven to MHD-powered (Barkov and Pozanenko, 2011), or differences in the rate of accretion of mass versus magnetic flux (Tchekhovskoy and Giannios, 2015; Kisaka and Ioka, 2015), as the latter controls the jet power in the Blanford-Znajek process (however, Parfrey, Giannios, and Beloborodov 2015 argue that a jet may be produced even in the absence of net magnetic flux).

Studies of fall-back accretion in neutron star mergers also generally neglect a robust physical process: the dynamical influence of radioactive heating by heavy nuclei synthesized by rapid neutron captures (r-process) in the decompressing material (Metzger et al., 2010a). This same heating within the unbound debris is responsible for powering the "kilonova" emission (Li and Paczyński, 1998; Metzger et al., 2010b) days to weeks after the merger, as was observed following GW170817 (e.g. Coulter et al. 2017; Soares-Santos et al. 2017; Cowperthwaite et al. 2017; Drout et al. 2017). However, at earlier times, less than a few seconds following mass ejection from the merger, the r-process heating rate is orders of magnitude higher. Energy released by the r-process does not qualitatively alter the dynamics of the bulk of the *unbound* ejecta (Rosswog et al., 2014). However, it can increase the quantity of ejecta and critically shape the dynamics of the *marginally bound* ejecta responsible for fall-back accretion, particularly on the second to minute timescales of relevance to the observed extended emission (Metzger et al., 2010a).

Depending on the electron fraction of the ejecta, $Y_e \sim 0.02 - 0.3$, the r-process releases a total energy of $Q_{\rm tot} \sim 1 - 3$ MeV per nucleon, mostly through beta-decays, at an approximately constant rate over a characteristic heating timescale $t_{\rm heat} \sim 1$ s following ejection (see Fig. 4.2). Then, at times $t \gg t_{\rm heat}$ (e.g. relevant to the kilonova), the heating rate approaches an asymptotic power-law decay $\dot{q} \propto t^{-1.3}$ (Metzger et al., 2010b). A nucleon (mass m_n) which is marginally gravitationally bound to the black hole of mass M, on an orbit of energy per nucleon $|E_{\rm tot}| = GMm_n/2a$ and semi-major axis a (under the approximation of Newtonian gravity), returns to the hole and circularizes into the accretion disk on a timescale given by its orbital period,

$$t_{\rm orb} = 2\pi \left(\frac{a^3}{GM}\right)^{1/2} \approx 1.6\,{\rm s}\left(\frac{|E_{\rm tot}|}{1\,{\rm MeV}}\right)^{-3/2}\left(\frac{M}{5M_\odot}\right) \tag{4.1}$$

This expression reveals several important facts. First, the total energy available from the r-process, $Q_{\rm tot}$, exceeds the binding energy of orbits with fall-back times comparable to observed extended emission after SGRBs ($\gtrsim$ 10 s; Fig. 4.1); including the effects of r-process heating is thus crucial to determining the late-time fall-back rate (Metzger et al., 2010a). Also of interest is the apparent coincidence that the fall-back time of matter with energy $|E_{\rm tot}| \sim Q_{\rm tot}$ is comparable to the timescale $t_{\rm heat} \sim 1$ s over which the bulk of the heating occurs. This means that different parts of the debris could receive different amounts of the total available heating, depending on their fall-back time. Metzger et al. (2010a) show that this can imprint a more complex mass fall-back evolution than the standard $\propto t^{-5/3}$ decay, instead generating either temporal gaps of several seconds or sharp cut-offs in the fall-back rate after a certain time, depending on the ratio of $t_{\rm orb}(|E_{\rm tot}| = Q_{\rm tot})$ and $t_{\rm heat}$.

In this paper we apply the model of Metzger et al. (2010a) in order to estimate the effects of r-process heating on the energy distribution of the merger ejecta and its resulting mass fall-back rate, using for the first time initial conditions for the debris properties taken directly from a numerical relativity simulation of a NS-BH merger (Foucart et al., 2016). We also explore what effects the Y_e-dependent nuclear heating rate has, given a realistic spread in the debris properties, on the predicted range of fall-back behavior. In § 4.1 we describe the problem setup, our treatment of the nuclear heating, and the numerical technique. In § 4.2, we present our results for the mass fall-back rate. Finally, in § 4.3 we map our findings onto mergers leaving BHs of different mass scales to demonstrate how NS-NS and NS-BH mergers might in principle be distinguished based on the properties of their late-time X-ray

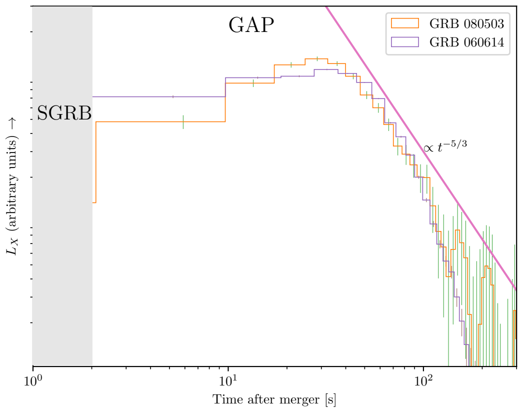

Figure 4.1: *Swift* BAT X-ray light curves of two SGRBs, GRB080503 (Perley et al., 2009) and GRB 060614 (Gehrels et al., 2006), which show their temporally-extended prompt emission. Both cases show remarkably similar light curves, which peak on a timescale ~ 30 s after the prompt SGRB spike of duration $\lesssim 2$ s (gray region; not shown at the chosen time binning). The lull in emission from $t \sim 2-30$ s contrasts with the naive expectation that the X-ray luminosity track the $\propto t^{-5/3}$ mass fall-back accretion (shown for comparison with a pink line).

light curves.

4.1 Model

4.1.1 Numerical Simulation Data

We use 3D position/velocity data taken from the grid points of the NS-BH merger simulation “M5-S7-I60” performed by Foucart et al. (2016) using the numerical code SpEC[1] (Kidder et al., 2000). This simulation implemented the DD2 Equation of State (Hempel et al., 2012) for a 1.4 $M_\odot$ NS, and included a neutrino leakage scheme, as implemented in Deaton et al. (2013). The initial mass of the BH is $M_i \simeq 5\ M_\odot$. This is a precessing system, with a dimensionless spin of $\chi = 0.7$ on the BH, prograde but misaligned by 60° with respect to the orbital angular momentum. The final mass of the BH after the merger is $M = 6.11 M_\odot$.

---

[1] The Spectral Einstein Code: `http://www.black-holes.org/SpEC.html`

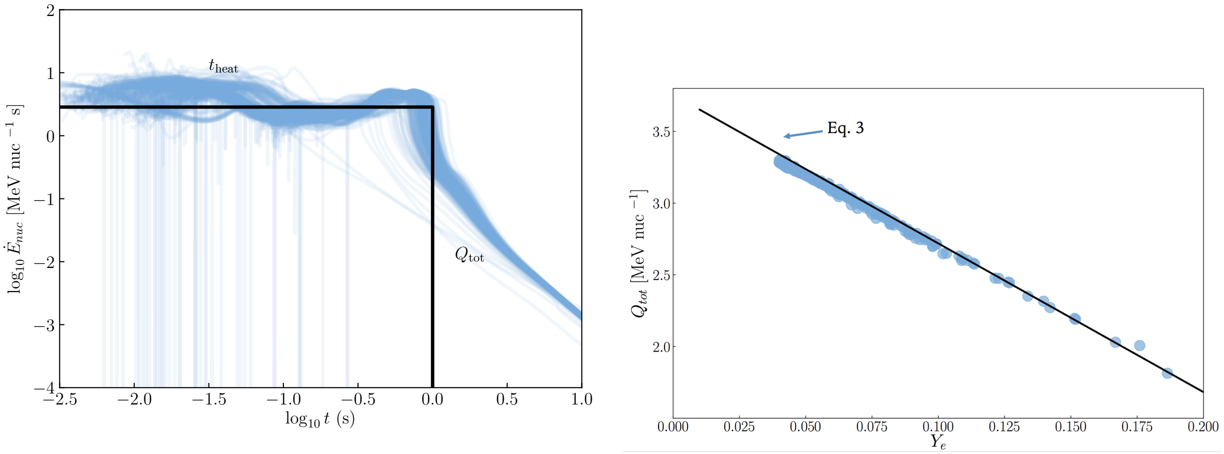

Figure 4.2: **Top:** Nuclear heating rate of the unbound debris as a function of time since ejection (blue lines), calculated for ~250 separate fluid elements from the NS-BH merger simulation M7_S8 (Foucart et al., 2014) using the SkyNet nuclear reaction network (Lippuner et al., 2017). We have reduced the heating rate from the rate of nuclear energy by a fraction $(1 - f_\nu) = 0.55$ to account for fraction of the $\beta-$decay energy carried away by neutrinos (eq. 4.3). A black line shows the step-function approximation employed in our fall-back model (eq. 4.4), where in this example $Q_{\rm tot} = 3$ MeV and $t_{\rm heat} = 1$ s. **Bottom:** Total heating rate $Q_{\rm tot}$ for the same fluid elements as a function of their electron fraction Y_e. Shown for comparison is the analytic estimate from equation (4.3), for fixed values of the parameters $\bar{A}/\bar{Z} = 2.4$, $f_\nu = 0.45$, $\left(\frac{B}{A}\right)_s = 8.7$ MeV nuc^{-1} and $\left(\frac{B}{A}\right)_r = 8$ MeV nuc^{-1}.

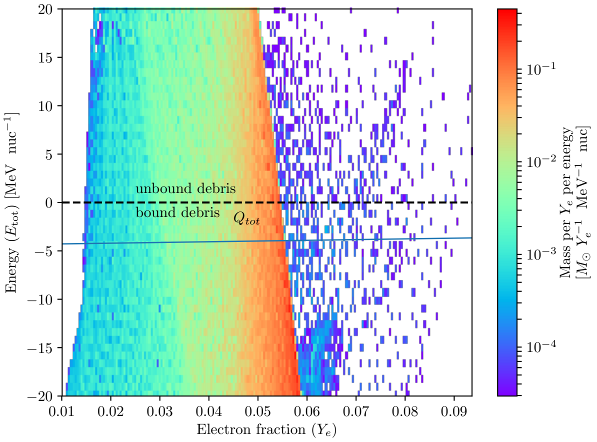

Figure 4.3: Mass-weighted distribution of the tidal tail ejecta, extracted from the NS-BH merger simulation data at t = 15 ms post-merger, in the space of initial energy, $E_{\rm tot}$, and electron fraction, Y_e. A dashed line at $E_{\rm tot} = 0$ separates the debris which is initially bound versus unbound to the black hole. Fluid elements above the solid blue line could be unbound due to r-process heating along if the ejecta receives the total available heating, $Q_{\rm tot} \sim 3$ MeV (Fig. 4.2, bottom panel).

We extract data on the ejecta tidal tail at a time t =15 ms after merger. These are then used as initial conditions in post-processing analysis, in which we evolve the fluid elements further as non-interacting Lagrangian particles. Because initial energies, positions and velocities used in our analysis were derived from a general relativistic simulation, they are inconsistent with the Newtonian expression for total energy. We therefore rescale the initial velocities from the simulations ($\vec{v}_{\rm GR}$) to their Newtonian equivalent according to $\vec{v}_{\rm N} = \frac{\vec{v}_{\rm GR}}{|\vec{v}_{\rm GR}|}|\vec{v}_{\rm N}|$, where

$$\frac{1}{2}m_n|\vec{v}_{\rm N}|^2 - \frac{GMm_n}{r} = E_{\rm tot}, \tag{4.2}$$

and $E_{\rm tot} = -m_n(u_t + 1)$ is an estimate of the specific binding energy (per nucleon) of the test particle, assuming geodesic motion in a time-independent spacetime, and r is the distance from the BH.

Fig. 4.3 shows the distribution of initial ejecta properties as a function of $E_{\rm tot}$ and electron fraction Y_e, weighted by mass. Most of the debris is neutron-rich, with an electron fraction $Y_e \lesssim 0.05$. A dashed line separates ejecta which is initially gravitationally bound

($E_{\rm tot} \geq 0$) from unbound material ($E_{\rm tot} \leq 0$). Of the total mass $0.116 M_\odot$ of the tidal ejecta, approximately $1.23 \times 10^{-2} M_\odot$ is unbound. Even if they are initially bound to the black hole, fluid elements above the solid blue line could in principle gain sufficient heating from the r-process (Fig. 4.2, bottom panel) during their orbit to become unbound. As we discuss later, depending on the timescale over which the r-process heating is released, matter near this line can also remain bound but fall back to the black hole at a later time than had it experienced zero heating.

4.1.2 R-Process Heating

We include the effects of r-process heating on the trajectories of the fall-back debris in a post-processing step, similar to the model employed by Metzger et al. (2010a). The total nuclear energy released as neutrons are captured onto seed nuclei during the r-process is approximately given by the difference between the initial and final nuclear binding energies,

$$Q_{\rm tot} \simeq (1 - f_\nu) \left[\left(\frac{B}{A}\right)_r - X_s \left(\frac{B}{A}\right)_s - X_n \Delta_n \right], \tag{4.3}$$

minus the fraction f_ν of energy lost to neutrino emission ($f_\nu \approx 1/2$ at early times of interest). Here $X_s = \bar{A} Y_e / \bar{Z}$ is the mass fraction of seed nuclei of average atomic mass number $\bar{A}$ and charge $\bar{Z}$; $\left(\frac{B}{A}\right)_s = 8.7$ MeV nuc^{-1} and $\left(\frac{B}{A}\right)_r = 8$ MeV nuc^{-1} are the average binding energies of seed and final r-process nuclei, respectively; $X_n = 1 - X_s$ is the neutron mass fraction; and $\Delta_n = (m_n - m_p)c^2 = 1.293$ MeV is the neutron-proton mass difference. For typical values $Y_e \approx 0.05$ (Fig. 4.3), $\bar{A} \approx 90$, $\bar{Z} = 38$, $f_\nu = 0.45$, we find $Q_{\rm tot} \approx 3$ MeV, consistent with the results of SkyNet nuclear reaction calculations (bottom panel of Fig. 4.2).

As shown in the top panel Fig. 4.2, the r-process heating in freely-expanding unbound debris is approximately constant for a timescale of $t_{\rm heat} \sim 1$ s, when most of the total energy is released, before rapidly entering a power-law decline. We approximate this behavior by a function of the simple form,

$$\dot{q} = \begin{cases} Q_{\rm tot}/t_{\rm heat}, & \text{if } t \le t_{\rm heat} \text{ and } v_r > 0 \\ 0, & \text{if } t > t_{\rm heat} \text{ or } v_r < 0, \end{cases} \tag{4.4}$$

where v_r is the radial velocity of the fluid element and the values of $Q_{\rm tot} \sim 3$ MeV and $t_{\rm heat} \sim 1$ s are parameters which we allow to vary modestly about these fiducial values.

The r-process heating, as described by equation (4.4), is assumed to terminate if and once matter starts to return to the black hole ($v_r < 0$), for reasons we now discuss. Although the heating rate evolution shown in Fig. 4.2 was calculated for unbound debris, this behavior is a good approximation also for bound debris during its initial outwards motion. However, the heating is abruptly suppressed once matter reaches apocenter and begins to return to the black hole (Metzger et al., 2010a). As matter undergoes re-compression, its temperature rises adiabatically and the r-process path (which is determined at fixed Z by the equilibrium between neutron capture (n,γ) and photodissociation (γ,n) processes) is driven closer to the stable valley, where the $\beta-$decay timescales, and thus neutron consumption and energy release timescale, becomes much longer. Metzger et al. (2010a) show that to good approximation the heating rate effectively shuts off once $v_r < 0$, motivating us to neglect heating entirely during re-compression.

4.1.3 Numerical Model

At early times after the merger, the ejecta is dense and highly opaque to photons, such that all of the r-process heating (other than that which escapes as neutrinos) goes into internal thermal energy. The fluid element orbits of interest possess high eccentricities e, where

$$1 - e = \frac{r_{\rm p}}{a} \approx 0.03 \left(\frac{r_{\rm p}}{5r_{\rm g}}\right)\left(\frac{|E_{\rm tot}|}{3{\rm MeV}}\right). \tag{4.5}$$

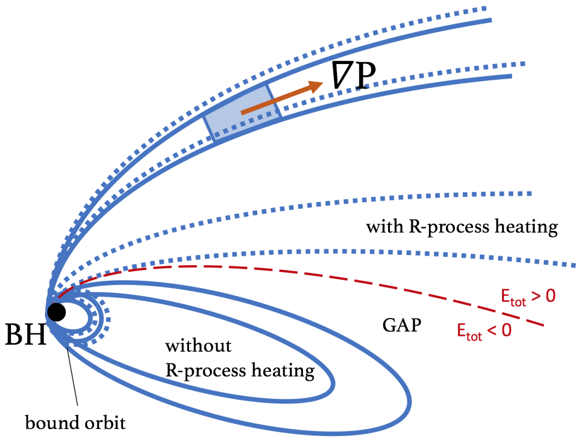

Figure 4.4: Schematic illustration of the tidal ejecta from NS-BH or NS-NS mergers, comparing the fluid element trajectories with (dashed lines) and without (solid lines) the effects of r-process heating. The orbital streams are highly elliptical, such that pressure gradients ∇P point almost radially outwards and energy released from the r-process is transferred quickly (on the expansion timescale) into ejecta kinetic energy. The trajectories of tightly bound ($E_{\rm tot} \ll 0$) or strongly unbound ($E_{\rm tot} \gg 0$) matter are not greatly altered. However, marginally bound material with $E_{\rm orb} \gtrsim -Q_{\rm tot}$ and orbital periods comparable to the timescale of the r-process experiences preferential heating relative to more tightly bound debris. This opens a gap in the orbital energy distribution and a temporal gap or late-time cut-off in the mass fall-back rate.

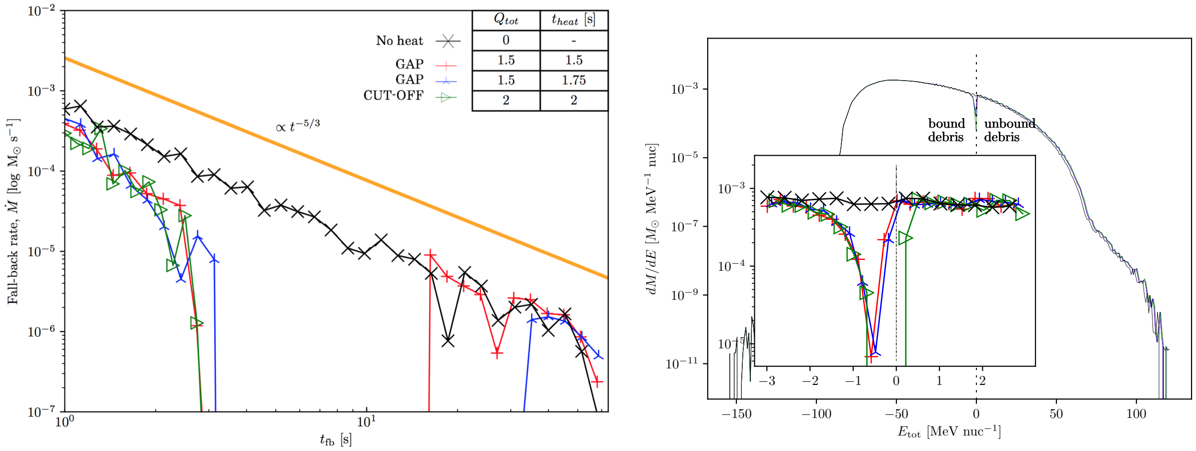

Figure 4.5: **Top Panel:** Mass fall-back rate, $\dot{M}$, as a function of time, $t_{\rm fb}$, after the NS-BH merger, calculated for different assumptions regarding the total r-process heating experienced $Q_{\rm tot}$ and its characteristic duration $t_{\rm heat}$. Each case is labeled according to the general behavior of the light curve, i.e. whether heating introduces a temporal gap, or a complete cut-off, in the late-time fall-back rate. **Bottom Panel:** Distribution of the debris mass with energy, dM/dE, comparing the initial distribution after the dynamical phase of the merger to that imprinted by r-process heating, shown for the same models and color schemes used in the top panel. r-process heating opens a gap in the energy distribution, which in turn results in either a temporal gap or a complete cut-off in the fall-back rate, depending on whether the energy gap overlaps with $E_{\rm tot} = 0$.

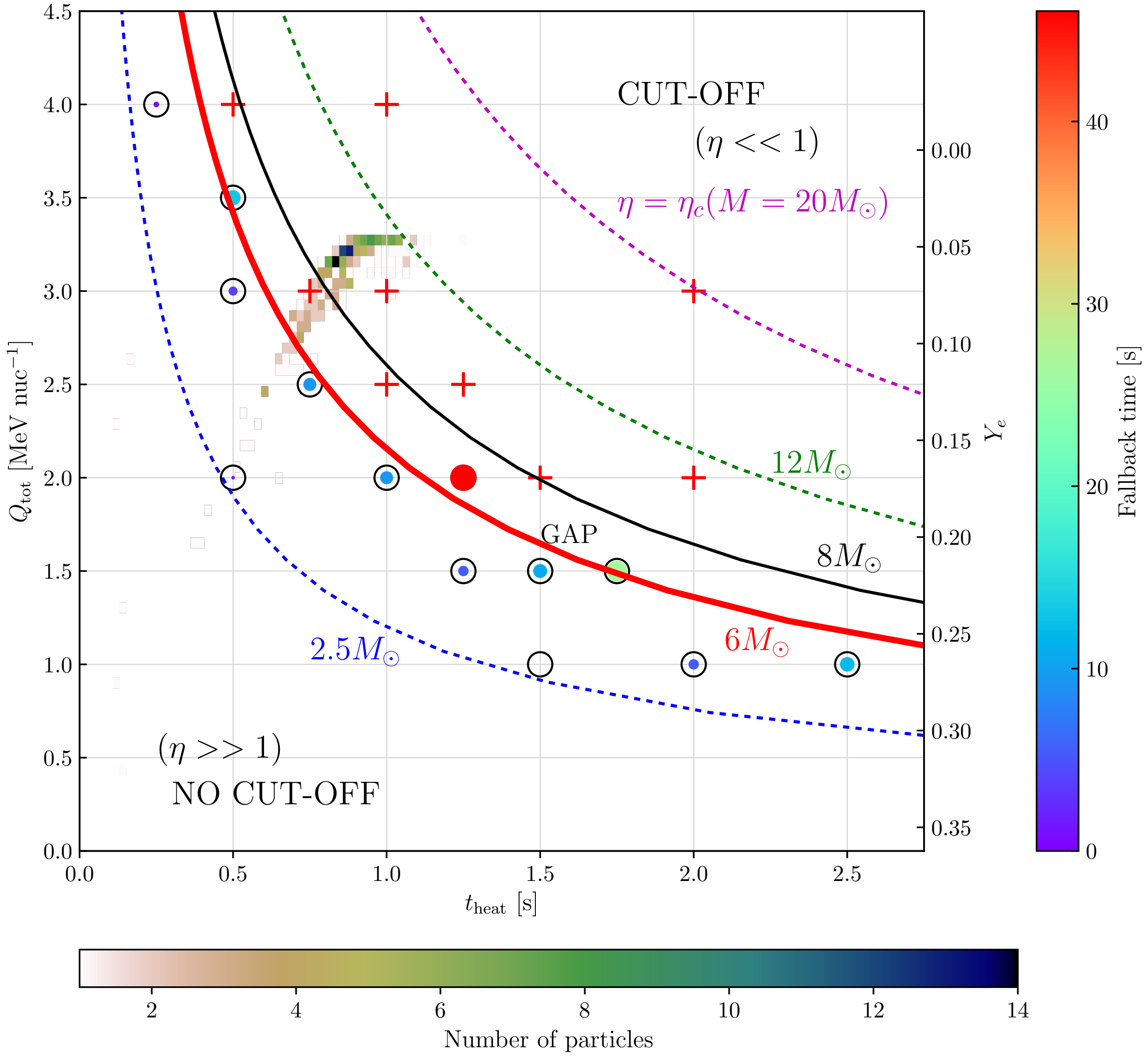

Figure 4.6: Regimes of the impact of r-process heating on fall-back accretion in the space of the total nuclear released energy, $Q_{\rm tot}$, and the timescale of the heating, $t_{\rm heat}$. The value of $Q_{\rm tot}$ (left vertical axis) is mapped onto the initial electron fraction Y_e (right vertical axis) using eq. (4.3) as shown in the bottom panel of Fig. 4.2. A 2D colored histogram shows the mass distribution of the ejecta in $(Q_{\rm tot}, t_{\rm heat})$, calculated by mapping the ejecta properties of our simulation for a NS-BH merger ($M \simeq 6M_\odot$) into the r-process heating trajectories from SkyNet calculations (Fig. 4.2). Symbols show the results of our parameter study in which we assume a BH mass $M \approx 6M_\odot$ and that all fluid elements experienced heating characterized by fixed values of $Q_{\rm tot}$ and $t_{\rm heat}$ according to eq. 4.4 (see Fig. 4.5 for a few examples). Crosses denote cases which result in a complete cutoff in the fall-back rate after a given time, while circles show cases in which a temporal gap is opened in the fall-back curve (the duration of the gap is denoted both by the radius and color of the circle using the legend given on the right). Lines represent the critical condition ($\eta = \eta_{\rm c} \approx 0.95$; eq. 4.8) giving rise to a long (~ 30 s) gap for different values of the mass of the central black hole as marked, ranging from $M \approx 2.5M_\odot$ relevant to NS-NS mergers to $M \sim 6-20M_\odot$ relevant to NS-BH mergers. While the tidal ejecta from NS-NS mergers lies in the cut-off regime ($\eta \gg 1$) for neutron-rich ejecta $Y_e \lesssim 0.2$, the NS-BH merger case resides close to the gap regime ($\eta \sim \eta_{\rm c} \approx 0.95$).

Here we have normalized the pericenter radius of the debris, r_p, to the gravitational radius of the BH, $r_g = GM/c^2$. Temperature and density gradients in the ejecta are thus directed nearly radially outwards, such that the r-process energy will be transferred through PdV work into ejecta kinetic energy on the local expansion timescale. Fig. 4.4 shows a schematic illustration of the influence of r-process heating on the trajectories of different fluid elements.

Following explicitly the effects of r-process heating on the debris dynamics would require a three-dimensional hydrodynamical simulation across a large dynamical range in radius. However, given the highly supersonic expansion velocities of the ejecta, such a treatment is not necessary, as the main effect of the heating is a local slow acceleration of the ejecta along the local pressure gradient radial direction and thus the adiabatic conversion of the injected thermal energy to kinetic energy. Starting with fluid element velocities rescaled from the simulation data (eq. 4.2), we directly increase the kinetic energy of the ith element according to

$$\frac{d}{dt}\left(\frac{1}{2}m_n v_{r,i}^2\right) = \dot{q}_i, \tag{4.6}$$

where $\dot{q}_i$ follows equation (4.4). For each fluid element, we follow its 3D trajectory until either it reaches periapse, which we define as the fall-back time $t_{\rm fb}$, or once the simulation terminates. We then record $t_{\rm fb}$ for all bound material and use the total mass in different bins of $t_{\rm fb}$ to calculate the fall-back accretion rate.

4.2 Results for Mass Fall-Back

The top panel of Figure 4.5 shows examples of the fall-back accretion rate as a function of time after the merger. In this initial analysis, for each model we assume that all fluid elements experience r-process heating rate (according to eq. 4.4) characterized by the same total amount $Q_{\rm tot}$ and characteristic duration, $t_{\rm heat}$. The bottom panel of the figure shows the final energy distribution of the ejecta mass for the same models as compared to the initial energy distribution.

When r-process heating is neglected ($Q_{\rm tot} = 0$), the roughly flat energy distribution $dM/dE \approx constant$ around $E_{\rm tot} = 0$, as imparted by the dynamical phase of the merger, is unaltered and the fall-back rate follows the canonical prediction of an uninterrupted $\dot{M} \propto t^{-5/3}$ decay. By contrast, including the effects of r-process heating for values of $Q_{\rm tot} \sim 1-3$ MeV and $t_{\rm heat} \sim 1$ s drastically changes the energy distribution around $E_{\rm tot} \approx 0$ and results in a more complex fall-back history. In particular, there are two possible outcomes in shape of the fall-back curve: either an absolute cut-off after some time (e.g. as in the $Q_{\rm tot} = 2$ MeV, $t_{\rm heat} = 2$ s case), or a cut-off followed by re-emergence of fall-back, i.e. a "gap" (e.g. as in the $Q_{\rm tot} = 1.5$ MeV and $t_{\rm heat} = 1.5$ s case). As we now discuss, these qualitatively different behaviors can be understood by comparing the timescale over which the ejecta is heated to its orbital timescale (eq. 4.1; see also Metzger et al. 2010a).

First consider the existence of a *critical* orbital period $t_{\rm orb,c}$, which corresponds to matter bound to the BH by an energy equal to the energy $\approx (Q_{\rm tot}/t_{\rm heat})t_{\rm orb}$ it receives from the r-process over the orbital period $t_{\rm orb}$ (when $t_{\rm orb} \lesssim t_{\rm heat}$). Using equation (4.1) for $t_{\rm orb}$, this gives

$$t_{\rm orb,c} \approx 0.62\,{\rm s}\left(\frac{Q_{\rm tot}}{3\,{\rm MeV}}\right)^{-3/5}\left(\frac{M}{5M_{\odot}}\right)^{2/5}\left(\frac{t_{\rm heat}}{1{\rm s}}\right)^{3/5}, \tag{4.7}$$

Ejecta which starts on an orbit of period $t_{\rm orb} \gg t_{\rm orb,c}$ always receives the full r-process heating before reaching apocenter (at which point the matter starts to re-compress and heating shuts off for reasons discussed earlier), while matter which starts very tightly bound ($t_{\rm orb} \ll t_{\rm orb,c}$) may receive only a fraction $t_{\rm orb}/t_{\rm heat}$ of the total heating (if $t_{\rm heat} \gtrsim t_{\rm orb,c}$).

Crucially, however, if $t_{\rm heat} \gtrsim t_{\rm orb,c}$ even matter with an initial $t_{\rm orb}$ which is slightly less than $t_{\rm orb,c}$ can *also receive the full heating* because, as the energy of a fluid element increases, its orbital period also grows, giving it more time to receive the full allotment of nuclear energy (in other words, the final value of $t_{\rm orb}$ diverges in a runaway process due to the r-process heating). This preferential heating opens a gap in the energy distribution of the debris, which can result in an absolute cut-off in the accretion rate, or a temporal gap, depending on the location of the gap.

Whether such behavior is possible depends on whether the r-process heating indeed acts uniformly over the orbit, i.e. on a critical ratio:

$$\eta \equiv \frac{t_{\rm heat}}{t_{\rm orb,c}} \approx 1.6 \left(\frac{M}{5M_{\odot}}\right)^{-2/5} \left(\frac{Q_{\rm tot}}{3\,{\rm MeV}}\right)^{3/5} \left(\frac{t_{\rm heat}}{1{\rm s}}\right)^{2/5} \tag{4.8}$$

If $t_{\rm heat} \ll t_{\rm orb,c}$ ($\eta \gg 1$), then the heating is applied in a short burst uniformly to all fluid elements and there is no runaway (preferential heating) of fluid elements as discussed above. In this case no significant energy gap is opened; $\dot{M}_{\rm fb}$ shows a slight dip around the time at which $t_{\rm orb} \sim t_{\rm heat} \sim 1$ s, but otherwise experiences no significant interruption of fall-back activity and $\dot{M}$ still approaches a power-law $\propto t^{-5/3}$ decay at later times.

If $t_{\rm heat} \gtrsim t_{\rm orb,c}$ ($\eta \gtrsim 1$) then an energy gap is opened in the debris. If $t_{\rm heat} \gg t_{\rm orb,c}$ ($\eta \gg 1$), then only the most marginally-bound matter will receive enough heat to unbind before arriving at apocenter and the energy gap extends to $E > 0$. This case produces an absolute cut-off in $dM/d|E|$ (and hence $\dot{M}_{\rm fb}$) for $|E_{\rm tot}| \lesssim E_{\rm c}$, where $E_{\rm c}$ is the energy of orbits of period $t_{\rm orb} = t_{\rm orb,c}$.

In intermediate cases for which $t_{\rm heat} \sim t_{\rm orb,c}$ ($\eta \sim 1$), a large gap is opened in the energy distribution of the debris, but now material with initial orbital periods $t_{\rm orb} \lesssim t_{\rm orb,c}$ remains marginally bound despite the extra energy it receives, thus opening up a large temporal gap in $\dot{M}_{\rm fb}$ (see Fig. 4.4 for an illustration). Specifically, we find that a critical value of $\eta = \eta_{\rm c} \approx 0.95$ is needed to generate a long cutoff of ~ 30 s, similar to the observed lulls in the SGRB extended emission light curves (Fig. 4.1). As we discuss later, the black hole mass-dependence of $\eta_{\rm c}$ may have implications for distinct fall-back behavior in NS-BH versus NS-NS mergers.

Fig. 4.6 shows the results of a broader study of the outcomes of fall-back across the parameter space of r-process heating parameters $1 \leq Q_{\rm tot} \leq 4$ MeV and $0 \leq t_{\rm heat} \leq 3$ s. Crosses denote runs resulting in cut-off behavior, while circles denote cases with gaps (with the duration of gap indicated by the size of the circle and its color, based on the key given on the right of the diagram). To highlight the relevant region of parameter space we overlay with a colored histogram the mass-weighted distribution of $(Q_{\rm tot}, t_{\rm heat})$, obtained by mapping the ejecta properties from our NS-BH simulation data into the parameters extracted from the SkyNet heating trajectories based on their Y_e values (Fig. 4.2), where we define $t_{\rm heat}$ as the time at which the heating rate curve first decreases below half of its maximum value. We also overlay with lines the condition $\eta = \eta_{\rm c}$ (eq. 4.8) for different assumptions about the BH masses, ranging from low values $M \approx 2.5 M_{\odot}$ relevant to the remnants of NS-NS mergers to higher values $M \sim 6 - 20 M_{\odot}$ appropriate to NS-BH mergers. This location of the crosses and circles relative to the $\eta = \eta_{\rm c}$ line for the BH mass $M \simeq 6 M_{\odot}$ corresponding to our simulation verifies the validity of this criterion as that responsible for separating cut-off from gaps in fall-back behavior.

4.2.1 Y_e-dependent spread in fluid element heating

Our calculations shown in Fig. 4.5 were performed under the assumption that all fluid elements experienced heating characterized by single values of $Q_{\rm tot}$ and $t_{\rm heat}$. While reasonable as a first-order approximation (Fig. 4.2), in detail these parameters will vary between fluid elements as a result of a finite spread in their initial electron fraction Y_e and precise thermodynamic conditions (e.g. entropy and expansion rate, which affect the properties of the seed nuclei). It is thus important to address whether the different fall-back outcomes discussed above, particularly the presence of long temporal gaps in accretion, are preserved in the face of such realistic heating variations.

In order to explore the impact of a physical heating spread on our results, we vary the value of $Q_{\rm tot}$ between fluid elements based on their Y_e value (as taken from the simulation data) using equation (4.3; see also Fig. 4.2, bottom panel). The other free parameters in the equation (e.g. $\bar{A}/\bar{Z}$) are chosen to match the *mean* values of $Q_{\rm tot}$ and $t_{\rm heat}$ to the comparison cases in which these values are fixed for all fluid elements (e.g., as in the cases shown in Fig. 4.5)

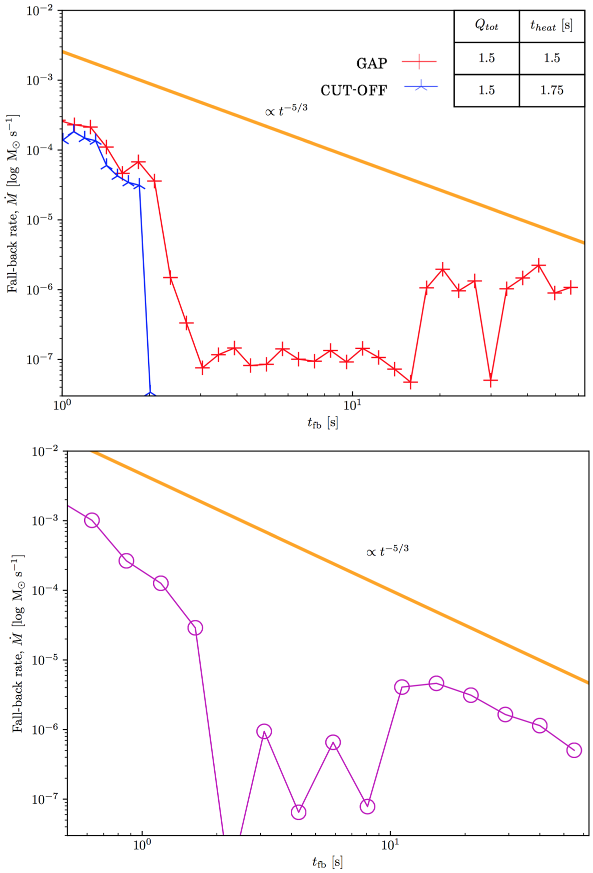

Figure 4.7: **Top:** Two models from Figure 4.5 showing temporal gaps in the fall-back rate, but now calculated using a realistic spread in the r-process heating experienced by different fluid elements due to variations in their Y_e values (eq. 4.3) (see also Fig. 4.2, bottom panel). The mean values for $Q_{\rm tot}$, around which the spread is centered, are shown in the figure. The previous model with a large temporal gap in the fall-back rate ($t_{\rm heat}$ = 1.75 s; *blue*) now shows a complete cut-off, while the case with a shorter gap ($t_{\rm heat}$ = 1.5 s; *red*) has been smoothed out to a lull in accretion. **Bottom:** Mass fall-back evolution calculated using r-process heating curves taken directly from the output of SkyNet simulations (Fig. 4.2) mapped into our NS-BH simulation data based on their Y_e values. We see a gap behavior because the ejecta properties lie close to the critical line $\eta = \eta_{\rm c}$ line for the $M = 6M_{\odot}$ black hole (red solid line in Fig. 4.6), but again the gap is partially filled-in due to the spread in heating properties.

Figure 4.7 shows the effect of Y_e-dependent heating on $\dot{M}(t_{\rm fb})$ compared to the two previous models from Figure 4.5 which showed gaps in the fall-back rate. The case with an initially long gap of $\gtrsim 30$ s was transformed into a complete cut-off by the heating spread. However, in the case with a shorter gap of ~ 20 s the effect of the finite heating spread is to smooth out, but not eliminate, the gap in mass fall-back, in other words turning the "gap" into a "lull". Our initial conclusion that r-process heating can lead to at least partial gaps in the fall-back when the critical condition $\eta \approx \eta_{\rm c}$ is satisfied (where now η is defined using the mass averaged values of $Q_{\rm tot}$ and $t_{\rm heat}$) thus appears to be robust.

Our calculations thus far have employed a step-function heating profile as given by eq. 4.4. To explore the sensitivity of our conclusions to this assumption, we perform an identical calculation where we directly using the direct heating curves from SkyNet (Fig. 4.2, top panel), which have been mapped onto the ejecta from our simulation data according to their closest Y_e value (e.g. 4.3). We still assume that heating for a given fluid element goes to zero when re-compressing ($v_r < 0$). The results of this simulation, as shown in the bottom panel of Fig 4.7, is fall-back with a gap of about 10 seconds. This is because the heating parameters for our fiducial simulation of a NS merging with a $\approx 6M_{\odot}$ BH overlaps with the gap condition $\eta \approx \eta_{\rm c}$ (red solid line in Fig. 4.6).

4.3 Implications for Extended Emission in SGRBs

As described in §4.2, the condition $\eta = \eta_{\rm c} \approx 0.95$ separates two distinct regions in the space of $Q_{\rm tot} - t_{\rm heat}$ shown in Fig. 4.6: the lower left corner ($\eta \ll \eta_{\rm c}$), where fall-back has a gap or is uninterrupted, and the upper right ($\eta \gg \eta_{\rm c}$), where fall-back exhibits a complete cutoff.

The heating properties of the ejecta from our NS-BH simulation, which left a black hole

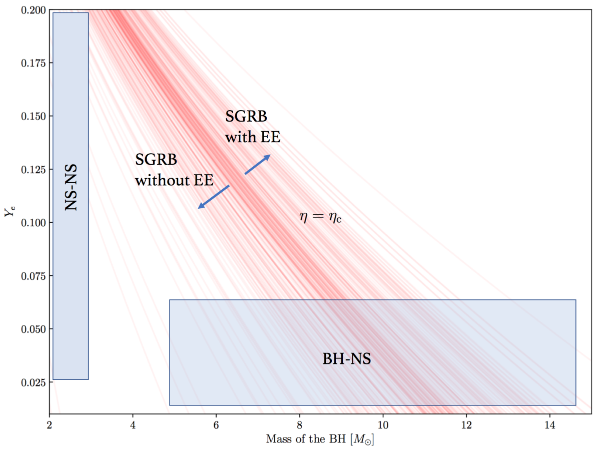

Figure 4.8: The critical condition $\eta = \eta_c$ (eq. 4.8) in the space of BH mass M and ejecta electron fraction Y_e, which separates a temporal gap, versus a cut-off, in the rate of fall-back accretion. The value of η is calculated by mapping $Q_{\rm tot}$ to Y_e using equation 4.3 for different values of $t_{\rm heat}$ as extracted from the results of our SkyNet calculations for the nuclear heating rate. As long as the ejecta is sufficiently neutron-rich ($Y_e \lesssim 0.2$), the low-mass black hole remnants of NS-NS mergers are predicted to experience a cut-off in the fall-back rate, while the more massive BHs from NS-BH mergers should experience a gap or lull in fall-back, consistent with the extended emission observed after a fraction of SGRBs (Fig. 4.1).

of mass $M \simeq 6M_\odot$, lies in the gap region close to the solid red line. We have confirmed this behavior by calculating the fall-back rate directly using SkyNet heating trajectories (Fig. 4.7, bottom panel). However, because $\eta \propto M^{-2/5}$ (eq. 4.8), otherwise similar ejecta from a merger that resulted in central black hole of lower or greater mass would instead result in $\eta \gg \eta_c$ or $\eta \ll \eta_c$, respectively, and thus would exhibit qualitatively different fall-back behavior. Figure 4.8 shows the condition $\eta = \eta_c$, now in the space of black hole mass M and electron fraction Y_e, where we have used the relationship $Q_{\rm tot}(Y_e)$ from eq. (4.3) (see bottom panel of Fig. 4.2).

If the X-ray luminosity of the extended prompt emission following a short GRB is proportional to the mass fall-back rate, $L_X \propto \dot{M}$, then this reasoning would suggest that NS-NS mergers ($M \approx 2.5M_\odot$) with similar ejecta properties would lie in the regime $\eta \gg \eta_c$ and thus should generate little or no late-time fall-back and hence would not be accompanied by luminous extended X-ray emission. By contrast, NS-BH mergers, given their more massive

BHs $\gtrsim 5M_\odot$, lie in the regime $\eta \sim \eta_c$ or $\eta \lesssim \eta_c$ and thus could produce fall-back with temporal gaps extending up to tens of seconds, in agreement with those short GRBs showing extended emission (Fig. 4.1).

One caveat is that, while these conclusions hold for highly neutron-rich ejecta ($Y_e \lesssim 0.2$), as characterizes the equatorial tidal tails in NS-NS and NS-BH mergers, it would not necessarily apply to the most polar-concentrated shock-heated dynamical ejecta, which experiences stronger weak interactions. At least in the case of NS-NS mergers, this has been shown to give rise to a wider range of Y_e (Wanajo et al., 2014; Goriely et al., 2015; Sekiguchi et al., 2016), potentially extending to values $Y_e \gtrsim 0.2$ that would place even NS-NS mergers into the $\eta \sim \eta_c$ regime and result in some fall-back. However, because in many cases the quantity of high Y_e matter is likely to be much less than the total, the amount of fall-back from this component would be significantly smaller and the presence of a cut-off in the fall-back rate might be preserved.

Our results suggest the possibility that the two apparent classes of SGRBs−those with and those without extended emission−may be associated with NS-BH and NS-NS mergers, respectively. Such a dichotomy of origin was previously suggested on the completely different basis of the observed distribution of spatial offsets of short GRBs from their host galaxies (Troja et al., 2008); however, the statistical significance of this difference was subsequently challenged (Fong and Berger, 2013).

Is such a model consistent with current event rate constraints? A fraction $f_{\rm EE} \gtrsim 0.2 - 0.4$ of SGRBs are accompanied by extended emission (Norris and Bonnell 2006). For our progenitor dichotomy scenario to hold, the ratio of the volumetric rate of NS-BH mergers to that NS-NS mergers must be at least as high as $f_{\rm EE}/f_{\rm SGRB}$, where we have assumed that all NS-NS mergers are accompanied by a SGRB but only a fraction $f_{\rm SGRB} < 1$ of NS-BH mergers do the same (as the latter requires rapid BH spin in the prograde direction relative to the orbit for the NS to be tidally disrupted outside the BH horizon).

From the O1-O3 LIGO observing runs, the inferred volumetric rate is $\approx 10 - 1700$ Gpc^{-3}

yr^{-1} for BNS mergers and $\approx 8-140$ Gpc^{-3} yr^{-1} for BHNS mergers (Abbott et al., 2023). The ratio of these rates is thus only weakly constrained at present, such that as long as a moderate fraction of NS-BH mergers produce GRBs,

$$f_{\mathrm{SGRB}} \gtrsim f_{\mathrm{EE}}\left(\frac{\mathcal{R}_{\mathrm{NSNS}}}{\mathcal{R}_{\mathrm{NSBH}}}\right) \gtrsim 0.02\left(\frac{f_{\mathrm{EE}}}{0.3}\right), \tag{4.9}$$

one cannot yet rule out the possibility that NS-BH mergers are sufficiently common to account for the population of SGRBs with extended emission ($f_{\mathrm{EE}} \gtrsim 0.2-0.4$). Thus far only two NS-NS mergers and two NS-BH mergers have been discovered; as such, the statistics of the current sample are obviously very small. If all extended emission is attributed to fall-back accretion in NS-BH mergers, then our model implies that the steady-state discovery rate of of NS-BH mergers will be significantly higher than that of NS-NS mergers (and that a sizable fraction of the BHs in these systems are spinning in the prograde orbital direction).

4.4 Conclusions

Despite the recent discovery of a short burst of gamma-rays in association with the gravitational waves from a NS-NS merger, the origin of the temporally-extended X-ray emission which is observed following a significant fraction of short GRBs remains a mystery. Late-time activity from the black hole accretion disk powered by fall-back of marginally bound debris, as would naively be expected in both NS-NS and NS-BH mergers, has been proposed as a source of this behavior (e.g. Rosswog 2007). Following Metzger et al. (2010a), we have employed a simple model to explore the impact of $\beta-$decay heating due to r-process nucleosynthesis on the time-dependence of the mass fall-back rate, using initial data on the ejecta fluid elements (Fig. 4.3), and the properties of the r-process heating received (Fig. 4.2), extracted directly from NS-BH merger simulations.

We confirm that this r-process heating significantly alters the fall-back rate from the canonical $\dot{M} \propto t^{-5/3}$ behavior, generating instead either an abrupt cut-off, or temporal gap, in the fall-back rate on a timescale of $\sim 10-100$ s (Fig. 4.5, 4.6). This behavior is robust to the presence of a realistic spread in the heating properties of the fluid elements imparted by a realistic range in the electron fraction and thermodynamic history (Fig. 4.7). Whether a cut-off or gap behavior is obtained depends on the value of a critical dimensionless parameter η (eq. 4.8). The dependence of η on black hole mass suggests a possible distinction between cut-off behavior in NS-NS mergers (low black hole mass) and delayed fall-back in NS-BH mergers (high black hole mass), as illustrated in Fig. 4.8. The presence or absence, respectively, of extended emission thus provides a possible way to distinguish NS-BH from NS-NS mergers.

Our model could be improved or extended along several fronts in future work. In addition to the BH mass, the critical parameter η depends on the total energy $Q_{\rm tot}$ and heating timescale $t_{\rm heat}$ of the r-process. These properties are related to the Q values and $\beta-$decay rates of neutron-rich isotopes whose masses and other properties have yet to be measured by laboratory experiments (e.g. Horowitz et al. 2018 and references therein). A more thorough parameter study of the range of $t_{\rm heat}$ and $Q_{\rm tot}$, e.g. assuming different theoretical models for the nuclear masses, would provide an additional check on the robustness of our conclusions.

More ambitiously, multidimensional hydrodynamical simulations of the fall-back process, accounting for the effects of r-process heating, are needed for a more robust assessment of the gap or cut-off formation process. Our treatment of directly placing the r-process thermal energy into debris kinetic energy neglects the transfer of thermal energy between adjacent fluid elements, though the highly-supersonic and nearly radial motion of the debris should mitigate these effects (Fig. 4.4). Models that do not self-consistently include the back-reaction of the thermodynamics of the fluid elements on the r-process path (Rosswog et al. 2014) may be inadequate, because once matter starts to recompress and adiabatically heat, the rate of $\beta-$decay heating will be substantially suppressed as the r-process path moves back towards the stable valley due to the higher temperatures (Metzger et al., 2010a). This complex "feed-back" process may ultimately necessitate coupling at least a simplified r-process network (e.g., a one-zone model such as that of Lattimer et al. 1977) directly into the hydrodynamical simulations.

Conclusion

Summary of key results

The results of this thesis can be summarized as follows:

- We explore the effects of rapid rotation on the properties of neutrino-heated winds from proto-neutron stars (PNS) formed in core-collapse supernovae or neutron-star mergers by means of three-dimensional general-relativistic hydrodynamical simulations with M0 neutrino transport. We focus on conditions characteristic of a few seconds into the PNS cooling evolution when the neutrino luminosities obey $L_{\nu_e} + L_{\bar{\nu}_e} \approx 7 \times 10^{51}$ erg s^{-1}, and over which most of the wind mass-loss will occur. After an initial transient phase, all of our models reach approximately steady-state outflow solutions with positive energies and sonic surfaces captured on the computational grid. Our non-rotating and slower-rotating models (angular velocity relative to Keplerian $\Omega/\Omega_{\rm K} \lesssim 0.4$; spin period $P \gtrsim 2$ ms) generate approximately spherically symmetric outflows with properties in good agreement with previous PNS wind studies. By contrast, our most rapidly spinning PNS solutions ($\Omega/\Omega_{\rm K} \gtrsim 0.75$; $P \approx 1$ ms) generate outflows focused in the rotational equatorial plane with much higher mass-loss rates (by over an order of magnitude), lower velocities, lower entropy, and lower asymptotic electron fractions, than otherwise similar non-rotating wind solutions. Although such rapidly spinning PNS are likely rare in nature, their atypical nucleosynthetic composition and outsized mass yields could render them important contributors of light neutron-rich nuclei compared to more common slowly rotating PNS birth. Our calculations pave the way to including the combined effects of rotation and a dynamically-important large-scale magnetic field on the wind properties within a 3D GRMHD framework.

- Formed in the aftermath of a core-collapse supernova or neutron star merger, a hot proto-neutron star (PNS) launches an outflow driven by neutrino heating lasting for up to tens of seconds. Though such winds are considered potential sites for the nucleosynthesis of heavy elements via the rapid neutron capture process (r-process), previous work has shown that unmagnetized PNS winds fail to achieve the necessary combination of high entropy and/or short dynamical timescale in the seed nucleus formation region. We present three-dimensional general-relativistic magnetohydrodynamical (GRMHD) simulations of PNS winds which include the effects of a dynamically strong ($B \gtrsim 10^{15}$ G) dipole magnetic field. After initializing the magnetic field, the wind quickly develops a helmet-streamer configuration, characterized by outflows along open polar magnetic field lines and a "closed" zone of trapped plasma at lower latitudes. Neutrino heating within the closed zone causes the thermal pressure of the trapped material to rise in time compared to the polar outflow regions, ultimately leading to the expulsion of this matter from the closed zone on a timescale of ~60 ms, consistent with the predictions of Thompson (2003). The high entropies of these transient ejecta are still growing at the end of our simulations and are sufficient to enable a successful 2nd-peak r-process in at least a modest $\gtrsim 1\%$ of the equatorial wind ejecta.

- Mergers of compact binaries containing two neutron stars (NS-NS), or a neutron star and a stellar-mass black hole (NS-BH), are likely progenitors of short-duration gamma ray bursts (SGRBs). A fraction $\gtrsim 20\%$ of SGRBs are followed by temporally-extended ($\gtrsim$ minute-long), variable X-ray emission, attributed to ongoing activity of the central engine. One source of late-time engine activity is fall-back

> accretion of bound tidal ejecta; however, observed extended emission light curves do not track the naively-anticipated, uninterrupted $t^{-5/3}$ power-law decay, instead showing a lull or gap in emission typically lasting tens of seconds after the burst. Here, we re-examine the impact of heating due to rapid neutron capture (r-process) nucleosynthesis on the rate of the fall-back accretion, using ejecta properties extracted from numerical relativity simulations of NS-BH mergers. Depending on the electron fraction of the ejecta and the mass of the remnant black hole, r-process heating can imprint a range of fall-back behavior, ranging from temporal lulls of up to tens of seconds to complete late-time cut-off in the accretion rate. This behavior is robust to realistic variations in the nuclear heating experienced by different parts of the ejecta. Central black holes with masses $\lesssim 3M_{\odot}$ typically experience absolute cut-offs in the fall-back rate, while more massive $\gtrsim 6-8M_{\odot}$ black holes instead show temporal gaps. We thus propose that SGRBs showing extended X-ray emission arise from NS-BH, rather than NS-NS, mergers. Our model implies a NS-BH merger detection rate by LIGO which, in steady-state, is comparable to or greater than that of NS-NS mergers.

Future directions: rotation + magnetic fields

Given the findings of this dissertation that separately rapid rotation and magnetic fields can have important effects on the conditions in PNS winds and their ability to synthesize r-process elements, a natural next step is to perform simulations of PNS winds under the combined effects of rotation and magnetic fields. Thompson, Chang, and Quataert (2004) performed analytic estimates of the effects of magnetic fields and rotation on neutrino-driven winds, with a focus on whether such winds could provide central engines for powering gamma-ray bursts. Metzger, Thompson, and Quataert (2007) performed 1D MHD simulations of such winds (along open magnetic field lines in the equatorial plane), exploring the parameter space of neutrino luminosities, magnetic field strengths, and PNS rotation rates. 2D Special relativistic MHD simulations by Bucciantini et al. (2009) have shown close agreement with results from (Metzger, Thompson, and

Quataert, 2007) and explored the interaction of the wind with the surrounding envelope of the exploding star; however, they did not include the effects of neutrino heating explicitly (rather, they specified an inner boundary temperature consistent with that expected in the gain region), and did not study the prospects for nucleosynthesis in the wind. By using physically realistic and more self-consistent conditions (tabulated nuclear equation of state, strong magnetic fields, neutrino absorption/emission), we are in a position to self-consistently address the viability of the $r-$process. Prasanna et al. (2022, 2023) perform ~seconds-long 2D magnetar wind simulations, varying rotation period, mass outflow rate and PNS radius in order to study effects on dynamics and magnetar spin down. Our simulations with more realistic gravity (GR versus Newtonian) and neutrino transport would complement these results.

Rapidly rotating magnetars may form in the aftermath of energetic supernovae (Usov, 1992b; Wang et al., 2001; Thompson, Chang, and Quataert, 2004) or neutron star mergers (Metzger, Thompson, and Quataert, 2018). In the model developed by the latter, Metzger, Thompson, and Quataert (2018) inferred that the high mass/high-velocity blue component of kilonova AT2017gfo can be explained by a rapidly rotating magnetar driving a relativistic wind. NS mergers are often accompanied by disks; using disk models from (Siegel and Metzger, 2018a) we can thus investigate the interaction between wind and disk in our simulations.

References

Abbott, B. P. and et al. (2016). “Observation of Gravitational Waves from a Binary Black Hole Merger”. *Phys. Rev. Lett.* 116, p. 061102. DOI: `10.1103/PhysRevLett.116.061102`. arXiv: `1602.03837 [gr-qc]`.

Abbott, B. P. et al. (2017b). “GW170817: Observation of Gravitational Waves from a Binary Neutron Star Inspiral”. *Physical Review Letters* 119, p. 161101. DOI: `10.1103/PhysRevLett.119.161101`. arXiv: `1710.05832 [gr-qc]`.

Abbott, B. P. et al. (2017a). “Gravitational Waves and Gamma-Rays from a Binary Neutron Star Merger: GW170817 and GRB 170817A”. *ApJL* 848, p. L13. DOI: `10.3847/2041-8213/aa920c`. arXiv: `1710.05834 [astro-ph.HE]`.

Abbott, B. P. et al. (2017c). “Multi-messenger Observations of a Binary Neutron Star Merger”. *ApJL* 848, p. L12. DOI: `10.3847/2041-8213/aa91c9`. arXiv: `1710.05833 [astro-ph.HE]`.

Abbott, R. et al. (2023). “Population of Merging Compact Binaries Inferred Using Gravitational Waves through GWTC-3”. *Physical Review X* 13, p. 011048. DOI: `10.1103/PhysRevX.13.011048`. arXiv: `2111.03634 [astro-ph.HE]`.

Abel, T. et al. (1997). “Modeling Primordial Gas in Numerical Cosmology”. *New Astronomy* 2, p. 181.

Abel, T. et al. (1998). “First Structure Formation: I. Primordial Star Forming Regions in Hierarchical Models”. *Astrophys. J.* 508, pp. 518–529.

Akram, W. et al. (2020). “Nucleosynthesis of light trans-Fe isotopes in ccSNe: Implications from presolar SiC-X grains”. In: *European Physical Journal Web of Conferences.* Vol. 227. European Physical Journal Web of Conferences, p. 01009. DOI: `10.1051/epjconf/202022701009`.

Alexander, K. D. et al. (2017). “The Electromagnetic Counterpart of the Binary Neutron Star Merger LIGO/Virgo GW170817. VI. Radio Constraints on a Relativistic Jet and Predictions for Late-time Emission from the Kilonova Ejecta”. *ApJL* 848, p. L21. DOI: `10.3847/2041-8213/aa905d`. arXiv: `1710.05457 [astro-ph.HE]`.

Aprahamian, A. et al. (2018). “FRIB and the GW170817 Kilonova”. *arXiv:1809.00703.* arXiv: 1809.00703.

Arcones, A., H.-T. Janka, and L. Scheck (2007). "Nucleosynthesis-relevant conditions in neutrino-driven supernova outflows. I. Spherically symmetric hydrodynamic simulations". *Astron. Astrophys.* 467, pp. 1227–1248. DOI: 10.1051/0004-6361:20066983.

Arcones, A. and H. T. Janka (2011). "Nucleosynthesis-relevant conditions in neutrino-driven supernova outflows. II. The reverse shock in two-dimensional simulations". *A&A* 526, A160. DOI: 10.1051/0004-6361/201015530. arXiv: 1008.0882 [astro-ph.SR].

Arcones, A., H. T. Janka, and L. Scheck (2007). "Nucleosynthesis-relevant conditions in neutrino-driven supernova outflows. I. Spherically symmetric hydrodynamic simulations". *A&A* 467, pp. 1227–1248. DOI: 10.1051/0004-6361:20066983. arXiv: astro-ph/0612582 [astro-ph].

Arcones, A. and F. Montes (2011). "Production of Light-element Primary Process Nuclei in Neutrino-driven Winds". *ApJ* 731, p. 5. DOI: 10.1088/0004-637X/731/1/5. arXiv: 1007.1275 [astro-ph.GA].

Argast, D. et al. (2004). "Neutron star mergers versus core-collapse supernovae as dominant r-process sites in the early Galaxy". *Astron. Astrophys.* 416, pp. 997–1011. DOI: 10.1051/0004-6361:20034265.

Arnould, M., S. Goriely, and K. Takahashi (2007). "The r-process of stellar nucleosynthesis: Astrophysics and nuclear physics achievements and mysteries". *Phys. Rep.* 450, pp. 97–213. DOI: 10.1016/j.physrep.2007.06.002.

Asplund, M. et al. (2009). "The Chemical Composition of the Sun". *Annual Review of Astronomy and Astrophysics* 47, pp. 481–522. DOI: 10.1146/annurev.astro.46.060407.145222. eprint: https://doi.org/10.1146/annurev.astro.46.060407.145222.

Atanasov, D. et al. (2015). "Precision Mass Measurements of ^{Cd}-131$_{129}$ and Their Impact on Stellar Nucleosynthesis via the Rapid Neutron Capture Process". *PRL* 115, p. 232501. DOI: 10.1103/PhysRevLett.115.232501. arXiv: 1512.05676 [nucl-ex].

Audi, G. et al. (2012). "The Ame2012 atomic mass evaluation". *Chinese Physics C* 36, p. 002. DOI: 10.1088/1674-1137/36/12/002.

Avrigeanu, M. and V. Avrigeanu (2016). "On deuteron interactions within surrogate reactions and nuclear level density studies". In: *Journal of Physics Conference Series.* Vol. 724. Journal of Physics Conference Series, p. 012003. DOI: 10.1088/1742-6596/724/1/012003.

Babiuc-Hamilton, M. et al. (2019). *The Einstein Toolkit (The "Mayer" release, ET_2019_10)*. DOI: `10.5281/zenodo.3522086`.

Barklem, P. S. et al. (2005). “The Hamburg/ESO R-process enhanced star survey (HERES). II. Spectroscopic analysis of the survey sample”. *A&A* 439, pp. 129–151. DOI: `10.1051/0004-6361:20052967`. arXiv: `astro-ph/0505050 [astro-ph]`.

Barkov, M. V. and A. S. Pozanenko (2011). “Model of the extended emission of short gamma-ray bursts”. *MNRAS* 417, pp. 2161–2165. DOI: `10.1111/j.1365-2966.2011.19398.x`. arXiv: `1103.4246 [astro-ph.HE]`.

Barnes, J. et al. (2016). “Radioactivity and Thermalization in the Ejecta of Compact Object Mergers and Their Impact on Kilonova Light Curves”. *Astrophys. J.* 829, p. 110. DOI: `10.3847/0004-637X/829/2/110`. arXiv: `1605.07218 [astro-ph.HE]`.

Barrère, P. et al. (2022). “A new scenario for magnetar formation: Tayler-Spruit dynamo in a proto-neutron star spun up by fallback”. *arXiv e-prints*, arXiv:2206.01269. arXiv: `2206.01269 [astro-ph.HE]`.

Bauswein, A., S. Goriely, and H.-T. Janka (2013). “Systematics of dynamical mass ejection, nucleosynthesis, and radioactively powered electromagnetic signals from neutron-star mergers”. *ApJ, submitted, arXiv:1302.6530*.

Beard, M. et al. (2014). “Comparison of statistical model calculations for stable isotope neutron capture”. *Phys. Rev. C* 90 (3), p. 034619. DOI: `10.1103/PhysRevC.90.034619`.

Beers, T. C. and N. Christlieb (2005). “The Discovery and Analysis of Very Metal-Poor Stars in the Galaxy”. *ARA&A* 43, pp. 531–580. DOI: `10.1146/annurev.astro.42.053102.134057`.

Belczynski, K., V. Kalogera, and T. Bulik (2002). “A Comprehensive Study of Binary Compact Objects as Gravitational Wave Sources: Evolutionary Channels, Rates, and Physical Properties”. *Astrophys. J.* 572, pp. 407–431. DOI: `10.1086/340304`.

Beloborodov, A. M. (2010). “Collisional mechanism for gamma-ray burst emission”. *MNRAS* 407, pp. 1033–1047. DOI: `10.1111/j.1365-2966.2010.16770.x`.

Beloborodov, A. M. (2003). “Nuclear Composition of Gamma-Ray Burst Fireballs”. *ApJ* 588, pp. 931–944. DOI: `10.1086/374217`.

Beniamini, P., K. Hotokezaka, and T. Piran (2016). “Natal Kicks and Time Delays in Merging Neutron Star Binaries: Implications for r-process Nucleosynthesis in Ultra-faint Dwarfs and in the Milky Way”. *ApJL* 829, p. L13. DOI: `10.3847/2041-8205/829/1/L13`.

Beniamini, P. et al. (2019). “Formation rates and evolution histories of magnetars”. *MNRAS* 487, pp. 1426–1438. DOI: `10.1093/mnras/stz1391`. arXiv: `1903.06718 [astro-ph.HE]`.

Berger, E. (2014). “Short-Duration Gamma-Ray Bursts”. *Annu. Rev. Astron. Astrophys.* 52, pp. 43–105. DOI: `10.1146/annurev-astro-081913-035926`.

Bethe, H. A. and J. R. Wilson (1985). “Revival of a stalled supernova shock by neutrino heating”. *ApJ* 295, pp. 14–23. DOI: `10.1086/163343`.

Beun, J. et al. (2008). “Fission cycling in a supernova r process”. *PRC* 77, p. 035804. DOI: `10.1103/PhysRevC.77.035804`. arXiv: `0707.4498 [astro-ph]`.

Bhattacharya, M., P. Kumar, and G. Smoot (2018). “Mergers of black hole–neutron star binaries and rates of associated electromagnetic counterparts”. *ArXiv e-prints*. arXiv: `1809.00006 [astro-ph.HE]`.

Bhattacharya, M., S. Horiuchi, and K. Murase (2021). “On the synthesis of heavy nuclei in protomagnetar outflows and implications for ultra-high energy cosmic rays”. *arXiv e-prints*, arXiv:2111.05863. arXiv: `2111.05863 [astro-ph.HE]`.

Bionta, R. M. et al. (1987). “Observation of a neutrino burst in coincidence with supernova 1987A in the Large Magellanic Cloud”. *PRL* 58, pp. 1494–1496. DOI: `10.1103/PhysRevLett.58.1494`.

Blandford, R. D. and M. J. Rees (1974). “A “twin-exhaust” model for double radio sources.” *MNRAS* 169, pp. 395–415. DOI: `10.1093/mnras/169.3.395`.

Blaum, K. (2006). “High-accuracy mass spectrometry with stored ions”. 425, pp. 1–78. DOI: `10.1016/j.physrep.2005.10.011`.

Blaum, K., J. Dilling, and W. Nörtershäuser (2013). “Precision atomic physics techniques for nuclear physics with radioactive beams”. *Physica Scripta Volume T* 152, p. 014017. DOI: `10.1088/0031-8949/2013/T152/014017`. arXiv: `1210.4045 [physics.atom-ph]`.

Blinnikov, S. I. et al. (1984). “Exploding Neutron Stars in Close Binaries”. *Sov. Astro. Lett.* 10, pp. 177–179.

Bonetti, M. et al. (2019). “Neutron star binary orbits in their host potential: effect on early r-process enrichment”. *MNRAS* 490, pp. 296–311. DOI: `10.1093/mnras/stz2554`.

Bruenn, S. W. (1985). “Stellar core collapse - Numerical model and infall epoch”. *ApJ Supplements* 58, p. 771. DOI: `10.1086/191056`.

Bucciantini, N. et al. (2007). “Magnetar-driven bubbles and the origin of collimated outflows in gamma-ray bursts”. *MNRAS* 380, pp. 1541–1553. DOI: `10.1111/j.1365-2966.2007.12164.x`.

Bucciantini, N. et al. (2009). “Magnetized relativistic jets and long-duration GRBs from magnetar spin-down during core-collapse supernovae”. *MNRAS* 396, pp. 2038–2050. DOI: `10.1111/j.1365-2966.2009.14940.x`.

Bucciantini, N. et al. (2012). “Short gamma-ray bursts with extended emission from magnetar birth: jet formation and collimation”. *MNRAS* 419, pp. 1537–1545. DOI: `10.1111/j.1365-2966.2011.19810.x`.

Bucciantini, N. et al. (2012). “Short gamma-ray bursts with extended emission from magnetar birth: jet formation and collimation”. *Mon. Not. R. Astron. Soc.* 419, pp. 1537–1545. DOI: `10.1111/j.1365-2966.2011.19810.x`. arXiv: `1106.4668 [astro-ph.HE]`.

Bugli, M., J. Guilet, and M. Obergaulinger (2021). “Three-dimensional core-collapse supernovae with complex magnetic structures - I. Explosion dynamics”. *MNRAS* 507, pp. 443–454. DOI: `10.1093/mnras/stab2161`. arXiv: `2105.00665 [astro-ph.HE]`.

Bugli, M. et al. (2023). “Three-dimensional core-collapse supernovae with complex magnetic structures - II. Rotational instabilities and multimessenger signatures”. *MNRAS* 520, pp. 5622–5634. DOI: `10.1093/mnras/stad496`. arXiv: `2210.05012 [astro-ph.HE]`.

Burbidge, E. M. et al. (1957). “Synthesis of the Elements in Stars”. 29, pp. 547–650. DOI: `10.1103/RevModPhys.29.547`.

Burbidge, G. R. et al. (1956). “Californium-254 and Supernovae”. *Phys. Rev.* 103, pp. 1145–1149. DOI: `10.1103/PhysRev.103.1145`.

Burns, E. et al. (2018). “Fermi GBM Observations of GRB 150101B: A Second Nearby Event with a Short Hard Spike and a Soft Tail”. *ApJL* 863, p. L34. DOI: `10.3847/2041-8213/aad813`. arXiv: `1807.02866 [astro-ph.HE]`.

Burrows, A., J. Hayes, and B. A. Fryxell (1995). “On the Nature of Core-Collapse Supernova Explosions”. *ApJ* 450, pp. 830–+. DOI: `10.1086/176188`.

Burrows, A. and J. M. Lattimer (1986). “The birth of neutron stars”. *ApJ* 307, pp. 178–196. DOI: `10.1086/164405`.

Burrows, A. and J. M. Lattimer (1986). “The birth of neutron stars”. *ApJ* 307, pp. 178–196. DOI: `10.1086/164405`.

Burrows, A. et al. (2020). “The overarching framework of core-collapse supernova explosions as revealed by 3D FORNAX simulations”. *MNRAS* 491, pp. 2715–2735. DOI: `10.1093/mnras/stz3223`. arXiv: `1909.04152 [astro-ph.HE]`.

Busso, M., R. Gallino, and G. J. Wasserburg (1999). “Nucleosynthesis in Asymptotic Giant Branch Stars: Relevance for Galactic Enrichment and Solar System Formation”. *ARA&A* 37, pp. 239–309. DOI: `10.1146/annurev.astro.37.1.239`.

Caballero-Folch, R. et al. (2016). “First Measurement of Several β -Delayed Neutron Emitting Isotopes Beyond N = 126”. *PRL* 117, p. 012501. DOI: `10.1103/PhysRevLett.117.012501`.

Cain, M. et al. (2020). “The R-Process Alliance: A Very Metal-poor, Extremely r-process-enhanced Star with [Eu/Fe] = + 2.2, and the Class of r-III Stars”. *ApJ* 898, p. 40. DOI: `10.3847/1538-4357/ab97ba`. arXiv: `2006.08080 [astro-ph.SR]`.

Cameron, A. G. W. (1957). “On the origin of the heavy elements.” *AJ* 62, pp. 9–10. DOI: `10.1086/107435`.

Cameron, A. G. W. (1959). “A Revised Table of Abundances of the Elements.” *ApJ* 129, p. 676. DOI: `10.1086/146667`.

Cantiello, M., J. Fuller, and L. Bildsten (2016). “Asteroseismic Signatures of Evolving Internal Stellar Magnetic Fields”. *ApJ* 824, p. 14. DOI: `10.3847/0004-637X/824/1/14`. arXiv: `1602.03056 [astro-ph.SR]`.

Capano, C. D. et al. (2020). “Stringent constraints on neutron-star radii from multimessenger observations and nuclear theory”. *Nature Astronomy* 4, p. 8.

Cardall, C. Y. and G. M. Fuller (1997). “General Relativistic Effects in the Neutrino-driven Wind and r-Process Nucleosynthesis”. *ApJL* 486, pp. L111–L114. DOI: `10.1086/310838`. eprint: `astro-ph/9701178`.

Carollo, D. et al. (2007). “Two stellar components in the halo of the Milky Way”. *Nature* 450, pp. 1020–1025. DOI: `10.1038/nature06460`. arXiv: `0706.3005 [astro-ph]`.

Chen, H.-Y. and K. Chatziioannou (2020). “Distinguishing Binary Neutron Star from Neutron Star-Black Hole Mergers with Gravitational Waves”. *ApJL* 893, p. L41. DOI: `10.3847/2041-8213/ab86bc`. arXiv: `1903.11197 [astro-ph.HE]`.

Chen, W.-X. and A. M. Beloborodov (2007). “Neutrino-cooled Accretion Disks around Spinning Black Holes”. *ApJ* 657, pp. 383–399. DOI: `10.1086/508923`. eprint: `astro-ph/0607145`.

Chiaki, G., H. Susa, and S. Hirano (2018). "Metal-poor star formation triggered by the feedback effects from Pop III stars". *MNRAS* 475, pp. 4378–4395. DOI: `10.1093/mnras/sty040`. arXiv: `1801.01583 [astro-ph.GA]`.

CHIME/FRB Collaboration et al. (2020). "A bright millisecond-duration radio burst from a Galactic magnetar". *Nature* 587, pp. 54–58. DOI: `10.1038/s41586-020-2863-y`. arXiv: `2005.10324 [astro-ph.HE]`.

Christensen, U. R. and J. Aubert (2006). "Scaling properties of convection-driven dynamos in rotating spherical shells and application to planetary magnetic fields". *Geophysical Journal International* 166, pp. 97–114. DOI: `10.1111/j.1365-246X.2006.03009.x`.

Christlieb, N. et al. (2004). "The Hamburg/ESO R-process Enhanced Star survey (HERES). I. Project description, and discovery of two stars with strong enhancements of neutron-capture elements". *A&A* 428, pp. 1027–1037. DOI: `10.1051/0004-6361:20041536`. arXiv: `astro-ph/0408389 [astro-ph]`.

Ciolfi, R. and D. M. Siegel (2015). "Short Gamma-Ray Bursts in the "Time-Reversal" Scenario". *ApJL* 798, p. L36. DOI: `10.1088/2041-8205/798/2/L36`.

Colella, P. and P. R. Woodward (1984). "The Piecewise Parabolic Method (PPM) for gas-dynamical simulations". *Journal of Computational Physics* 54, pp. 174–201. DOI: `10.1016/0021-9991(84)90143-8`.

Combi, L. and D. Siegel (2022). "GRMHD simulations of neutron-star mergers with weak interactions: r-process nucleosynthesis and electromagnetic signatures of dynamical ejecta". *ApJ, accepted*, arXiv:2206.03618. arXiv: `2206.03618 [astro-ph.HE]`.

Combi, L. and D. M. Siegel (2023). "Jets from neutron-star merger remnants and massive blue kilonovae". *arXiv e-prints*, arXiv:2303.12284. DOI: `10.48550/arXiv.2303.12284`. arXiv: `2303.12284 [astro-ph.HE]`.

Côté, B. et al. (2017). "Advanced LIGO Constraints on Neutron Star Mergers and r-process Sites". *ApJ* 836, p. 230. DOI: `10.3847/1538-4357/aa5c8d`.

Côté, B. et al. (2018). "The Origin of r-process Elements in the Milky Way". *ApJ* 855, p. 99. DOI: `10.3847/1538-4357/aaad67`.

Coti Zelati, F. et al. (2018). "Systematic study of magnetar outbursts". *MNRAS* 474, pp. 961–1017. DOI: `10.1093/mnras/stx2679`. arXiv: `1710.04671 [astro-ph.HE]`.

Coulter, D. A. et al. (2017). "Swope Supernova Survey 2017a (SSS17a), the Optical Counterpart to a Gravitational Wave Source". *ArXiv e-prints*. arXiv: `1710.05452 [astro-ph.HE]`.

Cowan, J. J. and W. K. Rose (1977). “Production of ^{14}C and neutrons in red giants.” *ApJ* 212, pp. 149–158. DOI: `10.1086/155030`.

Cowan, J. J. et al. (2021). “Origin of the heaviest elements: The rapid neutron-capture process”. 93, p. 015002. DOI: `10.1103/RevModPhys.93.015002`.

Cowperthwaite, P. S. et al. (2017). “The Electromagnetic Counterpart of the Binary Neutron Star Merger LIGO/Virgo GW170817. II. UV, Optical, and Near-infrared Light Curves and Comparison to Kilonova Models”. *ApJL* 848, p. L17. DOI: `10.3847/2041-8213/aa8fc7`. arXiv: `1710.05840 [astro-ph.HE]`.

Curtis, S. et al. (2019). “PUSHing Core-collapse Supernovae to Explosions in Spherical Symmetry. III. Nucleosynthesis Yields”. *ApJ* 870, p. 2. DOI: `10.3847/1538-4357/aae7d2`. arXiv: `1805.00498 [astro-ph.SR]`.

Curtis, S. et al. (2021). “*r*-process Nucleosynthesis and Kilonovae from Hypermassive Neutron Star Remnants”. *arXiv e-prints*, arXiv:2112.00772. arXiv: `2112.00772 [astro-ph.HE]`.

Curtis, S. et al. (2023). “r-process nucleosynthesis and kilonovae from hypermassive neutron star post-merger remnants”. *MNRAS* 518, pp. 5313–5322. DOI: `10.1093/mnras/stac3128`. arXiv: `2112.00772 [astro-ph.HE]`.

Cyburt, R. H. et al. (2010). “The JINA REACLIB Database: Its Recent Updates and Impact on Type-I X-ray Bursts”. *ApJ Supplements* 189. REACLIB is available at `https://groups.nscl.msu.edu/jina/reaclib/db/`, p. 240. DOI: `10.1088/0067-0049/189/1/240`.

Cyburt, R. H. et al. (2016). “Big bang nucleosynthesis: Present status”. 88, p. 015004. DOI: `10.1103/RevModPhys.88.015004`.

Dardelet, L. et al. (2015). “The i-process and CEMP-r/s stars”. *arXiv e-prints*, arXiv:1505.05500. DOI: `10.48550/arXiv.1505.05500`. arXiv: `1505.05500 [astro-ph.SR]`.

Davies, M. B. et al. (1994). “Merging neutron stars. I. Initial results for coalescence of noncorotating systems”. *Astrophys. J.* 431, pp. 742–753. DOI: `10.1086/174525`.

De, S. and D. M. Siegel (2021). “Igniting Weak Interactions in Neutron Star Postmerger Accretion Disks”. *ApJ* 921, p. 94. DOI: `10.3847/1538-4357/ac110b`.

Dean, C., R. Fernández, and B. D. Metzger (2021). “Resolving the fastest ejecta from binary Neutron Star mergers: implications for electromagnetic counterparts”. *arXiv:2108.08311 [astro-ph, physics:gr-qc, physics:nucl-th]*. arXiv: 2108.08311.

Deaton, M. B. et al. (2013). “Black Hole-Neutron Star Mergers with a Hot Nuclear Equation of State: Outflow and Neutrino-cooled Disk for a Low-mass, High-spin Case”. *ApJ* 776, p. 47. DOI: 10.1088/0004-637X/776/1/47. arXiv: 1304.3384 [astro-ph.HE].

Desai, D., D. M. Siegel, and B. D. Metzger (2022). “Three-dimensional General-relativistic Simulations of Neutrino-driven Winds from Rotating Proto-neutron Stars”. *ApJ* 931, p. 104. DOI: 10.3847/1538-4357/ac69da. arXiv: 2203.16560 [astro-ph.HE].

Dessart, L. et al. (2009). “Neutrino Signatures and the Neutrino-Driven Wind in Binary Neutron Star Mergers”. *ApJ* 690, pp. 1681–1705. DOI: 10.1088/0004-637X/690/2/1681. arXiv: 0806.4380 [astro-ph].

Dessart, L. et al. (2009). “Neutrino Signatures and the Neutrino-Driven Wind in Binary Neutron Star Mergers”. *ApJ* 690, pp. 1681–1705. DOI: 10.1088/0004-637X/690/2/1681.

Dessart, L. et al. (2006). “Multi-Dimensional Radiation/Hydrodynamic Simulations of Protoneutron Star Convection”. *ApJ* 645, pp. 534–550.

Drout, M. R. et al. (2017). “Light Curves of the Neutron Star Merger GW170817/SSS17a: Implications for R-Process Nucleosynthesis”. *ArXiv e-prints*. arXiv: 1710.05443 [astro-ph.HE].

Duan, H. and Y. Qian (2004). “Neutrino processes in strong magnetic fields and implications for supernova dynamics”. *Phs. Rev. D* 69, pp. 123004–+. DOI: 10.1103/PhysRevD.69.123004. eprint: arXiv:astro-ph/0401634.

Duan, H. and Y.-Z. Qian (2004). “Neutrino processes in strong magnetic fields and implications for supernova dynamics”. *Phs. Rev. D* 69, pp. 123004–+. DOI: 10.1103/PhysRevD.69.123004.

Duan, H. and Y.-Z. Qian (2005). “Rates of neutrino absorption on nucleons and the reverse processes in strong magnetic fields”. *Phys. Rev. D.* 72, p. 023005. DOI: 10.1103/PhysRevD.72.023005.

Duflo, J. and A. P. Zuker (1995). “Microscopic mass formulas”. *PRC* 52, R23–R27. DOI: 10.1103/PhysRevC.52.R23. arXiv: nucl-th/9505011 [nucl-th].

Duncan, R. C., S. L. Shapiro, and I. Wasserman (1986). “Neutrino-driven winds from young, hot neutron stars”. *Astrophys. J.* 309, pp. 141–160. DOI: 10.1086/164587.

Duncan, R. C., S. L. Shapiro, and I. Wasserman (1986). “Neutrino-driven winds from young, hot neutron stars”. *ApJ* 309, pp. 141–160. DOI: 10.1086/164587.

Duncan, R. C. and C. Thompson (1992). "Formation of very strongly magnetized neutron stars - Implications for gamma-ray bursts". *ApJL* 392, pp. L9–L13. DOI: `10.1086/186413`.

Eichler, D. (2017). "Testing the Viewing Angle Hypothesis for Short GRBs with LIGO Events". *ApJL* 851, p. L32. DOI: `10.3847/2041-8213/aa9aec`. arXiv: `1710.05688 [astro-ph.HE]`.

Eichler, D., D. Guetta, and H. Manis (2009). "A Universal Central Engine Hypothesis for Short and Long Gamma-Ray Bursts". *ApJL* 690, pp. L61–L64. DOI: `10.1088/0004-637X/690/1/L61`. arXiv: `0810.3013`.

Eichler, D. et al. (1989). "Nucleosynthesis, neutrino bursts and gamma-rays from coalescing neutron stars". *Nature* 340, pp. 126–128. DOI: `10.1038/340126a0`.

Eichler, D. et al. (1989). "Nucleosynthesis, neutrino bursts and gamma-rays from coalescing neutron stars". *Nature* 340, pp. 126–128. DOI: `10.1038/340126a0`.

Eichler, M. et al. (2015). "The Role of Fission in Neutron Star Mergers and Its Impact on the r-Process Peaks". *ApJ* 808, p. 30. DOI: `10.1088/0004-637X/808/1/30`.

Eldridge, J. J. and E. R. Stanway (2022). "New Insights into the Evolution of Massive Stars and Their Effects on Our Understanding of Early Galaxies". *ARA&A* 60, pp. 455–494. DOI: `10.1146/annurev-astro-052920-100646`. arXiv: `2202.01413 [astro-ph.GA]`.

Eliseev, S. et al. (2013). "Phase-Imaging Ion-Cyclotron-Resonance Measurements for Short-Lived Nuclides". *Phys. Rev. Lett.* 110 (8), p. 082501. DOI: `10.1103/PhysRevLett.110.082501`.

Escher, J. E. and F. S. Dietrich (2006). "Determining (n,f) cross sections for actinide nuclei indirectly: Examination of the surrogate ratio method". *PRC* 74, p. 054601. DOI: `10.1103/PhysRevC.74.054601`.

Ezzeddine, R. et al. (2020). "The R-Process Alliance: First Magellan/MIKE Release from the Southern Search for R-process-enhanced Stars". *ApJ* 898, p. 150. DOI: `10.3847/1538-4357/ab9d1a`. arXiv: `2006.07731 [astro-ph.SR]`.

Faucher-Giguère, C.-A. and V. M. Kaspi (2006). "Birth and Evolution of Isolated Radio Pulsars". *ApJ* 643, pp. 332–355. DOI: `10.1086/501516`. arXiv: `astro-ph/0512585 [astro-ph]`.

Fernández, R. and B. D. Metzger (2013). "Delayed outflows from black hole accretion tori following neutron star binary coalescence". *MNRAS* 435, pp. 502–517. DOI: `10.1093/mnras/stt1312`. arXiv: `1304.6720 [astro-ph.HE]`.

Fernández, R. et al. (2022). “Fast flavor instability in hypermassive neutron star disk outflows”. *Phys. Rev. D* 106 (10), p. 103003. DOI: `10.1103/PhysRevD.106.103003`.

Ferrario, L. and D. Wickramasinghe (2006). “Modelling of isolated radio pulsars and magnetars on the fossil field hypothesis”. *MNRAS* 367, pp. 1323–1328. DOI: `10.1111/j.1365-2966.2006.10058.x`. arXiv: `astro-ph/0601258 [astro-ph]`.

Fischer, T. et al. (2010). “Protoneutron star evolution and the neutrino-driven wind in general relativistic neutrino radiation hydrodynamics simulations”. *Astron. Astrophys.* 517, A80. DOI: `10.1051/0004-6361/200913106`.

Fischer, T. et al. (2012). “Neutrino spectra evolution during protoneutron star deleptonization”. *Phys. Rev. D.* 85, p. 083003. DOI: `10.1103/PhysRevD.85.083003`. arXiv: `1112.3842 [astro-ph.HE]`.

Fong, W. and E. Berger (2013). “The Locations of Short Gamma-Ray Bursts as Evidence for Compact Object Binary Progenitors”. *Astrophys. J.* 776, p. 18. DOI: `10.1088/0004-637X/776/1/18`. arXiv: `1307.0819 [astro-ph.HE]`.

Fong, W. et al. (2016). “Radio Constraints on Long-Lived Magnetar Remnants in Short Gamma-Ray Bursts”. *Astrophys. J.* 831, p. 141. DOI: `10.3847/0004-637X/831/2/141`. arXiv: `1607.00416 [astro-ph.HE]`.

Foucart, F. (2012). “Black-hole-neutron-star mergers: Disk mass predictions”. *Phys. Rev. D* 86, p. 124007. DOI: `10.1103/PhysRevD.86.124007`. arXiv: `1207.6304 [astro-ph.HE]`.

Foucart, F. et al. (2012). “Black hole-neutron star mergers for 10 Msun black holes”. *Phys. Rev. D.* 85, p. 044015. DOI: `10.1103/PhysRevD.85.044015`.

Foucart, F. et al. (2013). “Black-hole-neutron-star mergers at realistic mass ratios: Equation of state and spin orientation effects”. *Phys. Rev. D.* 87, p. 084006. DOI: `10.1103/PhysRevD.87.084006`. arXiv: `1212.4810 [gr-qc]`.

Foucart, F. et al. (2014). “Neutron star-black hole mergers with a nuclear equation of state and neutrino cooling: Dependence in the binary parameters”. *Phys. Rev. D.* 90, p. 024026. DOI: `10.1103/PhysRevD.90.024026`. arXiv: `1405.1121 [astro-ph.HE]`.

Foucart, F. et al. (2015). “Post-merger evolution of a neutron star-black hole binary with neutrino transport”. *Phys. Rev. D* 91, p. 124021. DOI: `10.1103/PhysRevD.91.124021`. arXiv: `1502.04146 [astro-ph.HE]`.

Foucart, F. et al. (2016). “Impact of an improved neutrino energy estimate on outflows in neutron star merger simulations”. *Phys. Rev. D.* 94, p. 123016. DOI: `10.1103/PhysRevD.94.123016`. arXiv: `1607.07450 [astro-ph.HE]`.

Frankel, S. and N. Metropolis (1947). “Calculations in the Liquid-Drop Model of Fission”. *Physical Review* 72, pp. 914–925. DOI: `10.1103/PhysRev.72.914`.

Frebel, A. and A. P. Ji (2023). “Observations of R-Process Stars in the Milky Way and Dwarf Galaxies”. *arXiv e-prints*, arXiv:2302.09188. DOI: `10.48550/arXiv.2302.09188`. arXiv: `2302.09188 [astro-ph.SR]`.

Frebel, A. and J. E. Norris (2015). “Near-Field Cosmology with Extremely Metal-Poor Stars”. *ARA&A* 53, pp. 631–688. DOI: `10.1146/annurev-astro-082214-122423`. arXiv: `1501.06921 [astro-ph.SR]`.

Freiburghaus, C., S. Rosswog, and F. Thielemann (1999). “R-Process in Neutron Star Mergers”. *ApJ* 525, pp. L121–L124. DOI: `10.1086/312343`.

Freiburghaus, C., S. Rosswog, and F.-K. Thielemann (1999). “r-Process in Neutron Star Mergers”. *Astrophys. J.* 525, pp. L121–L124. DOI: `10.1086/312343`.

Freundlich, J. and D. Maoz (2021). “The delay time distribution of Type-Ia supernovae in galaxy clusters: the impact of extended star-formation histories”. *MNRAS* 502, pp. 5882–5895. DOI: `10.1093/mnras/stab493`. arXiv: `2012.00793 [astro-ph.GA]`.

Fröhlich, C. et al. (2006). “Composition of the Innermost Core-Collapse Supernova Ejecta”. *ApJ* 637, pp. 415–426. DOI: `10.1086/498224`. eprint: `astro-ph/0410208`.

Fryer, C. L., S. E. Woosley, and D. H. Hartmann (1999). “Formation Rates of Black Hole Accretion Disk Gamma-Ray Bursts”. *Astrophys. J.* 526, p. 152.

Fujibayashi, S. et al. (2017). “Properties of Neutrino-driven Ejecta from the Remnant of a Binary Neutron Star Merger: Pure Radiation Hydrodynamics Case”. *ApJ* 846, p. 114. DOI: `10.3847/1538-4357/aa8039`.

Fujibayashi, S. et al. (2022). “Collapse of rotating massive stars leading to black hole formation and energetic supernovae”. *arXiv e-prints*, arXiv:2212.03958. DOI: `10.48550/arXiv.2212.03958`. arXiv: `2212.03958 [astro-ph.HE]`.

Fujimoto, S.-i. et al. (2006). “Magnetohydrodynamic Simulations of a Rotating Massive Star Collapsing to a Black Hole”. *ApJ* 644, pp. 1040–1055. DOI: `10.1086/503624`.

Fujimoto, S.-i. et al. (2007). “Heavy-Element Nucleosynthesis in a Collapsar”. *ApJ* 656, pp. 382–392. DOI: `10.1086/509908`.

Fuller, J. and W. Lu (2022). “The spins of compact objects born from helium stars in binary systems”. *MNRAS* 511, pp. 3951–3964. DOI: `10.1093/mnras/stac317`. arXiv: `2201.08407 [astro-ph.HE]`.

Fuller, J., A. L. Piro, and A. S. Jermyn (2019). "Slowing the spins of stellar cores". *MNRAS* 485, pp. 3661–3680. DOI: `10.1093/mnras/stz514`. arXiv: `1902.08227 [astro-ph.SR]`.

Fuller, J. et al. (2015). "Asteroseismology can reveal strong internal magnetic fields in red giant stars". *Science* 350, pp. 423–426. DOI: `10.1126/science.aac6933`. arXiv: `1510.06960 [astro-ph.SR]`.

Galama, T. J. and others (1998). "An unusual supernova in the error box of the γ-ray burst of 25 April 1998". *Nature* 395, pp. 670–672. DOI: `10.1038/27150`.

Galeazzi, F. et al. (2013). "Implementation of a simplified approach to radiative transfer in general relativity". *Phys. Rev. D.* 88, p. 064009. DOI: `10.1103/PhysRevD.88.064009`.

Gao, H. et al. (2013). "Bright Broadband Afterglows of Gravitational Wave Bursts from Mergers of Binary Neutron Stars". *Astrophys. J.* 771, p. 86. DOI: `10.1088/0004-637X/771/2/86`. arXiv: `1301.0439 [astro-ph.HE]`.

Gehrels, N. and others (2006). "A new γ-ray burst classification scheme from GRB060614". *Nature* 444, pp. 1044–1046. DOI: `10.1038/nature05376`.

Gehrels, N. et al. (2006). "A new γ-ray burst classification scheme from GRB060614". *Nature* 444, pp. 1044–1046. DOI: `10.1038/nature05376`. eprint: `arXiv:astro-ph/0610635`.

Giacomazzo, B. and R. Perna (2013). "Formation of Stable Magnetars from Binary Neutron Star Mergers". *Astrophys. J. Lett.* 771, p. L26. DOI: `10.1088/2041-8205/771/2/L26`.

Gibson, S. L. et al. (2017). "Fallback accretion on to a newborn magnetar: short GRBs with extended emission". *MNRAS* 470, pp. 4925–4940. DOI: `10.1093/mnras/stx1531`. arXiv: `1706.04802 [astro-ph.HE]`.

Gill, R. and J. Heyl (2007). "The birthrate of magnetars". *MNRAS* 381, pp. 52–58. DOI: `10.1111/j.1365-2966.2007.12254.x`. arXiv: `astro-ph/0703346 [astro-ph]`.

Giuliani, S. A., G. Martínez-Pinedo, and L. M. Robledo (2018). "Fission properties of superheavy nuclei for r -process calculations". *PRC* 97, p. 034323. DOI: `10.1103/PhysRevC.97.034323`. arXiv: `1704.00554 [nucl-th]`.

Giuliani, S. A. et al. (2020). "Fission and the r-process nucleosynthesis of translead nuclei in neutron star mergers". *Phys. Rev. C* 102 (4), p. 045804. DOI: `10.1103/PhysRevC.102.045804`.

Goldschmidt, V. M. (1937). "Geochemische Verteilungsgesetze der Elemente. IX. Die Mengenverhältnisse der Elemente und der Atom-Arten." *Norske Vidensk.-Akad. i Oslo* 4.

Gompertz, B. P., P. T. O'Brien, and G. A. Wynn (2014). "Magnetar powered GRBs: explaining the extended emission and X-ray plateau of short GRB light curves". *MNRAS* 438, pp. 240–250. DOI: `10.1093/mnras/stt2165`. arXiv: `1311.1505 [astro-ph.HE]`.

Goodale, T. et al. (2003). "The Cactus Framework and Toolkit: Design and Applications". In: *Vector and Parallel Processing – VECPAR'2002, 5th International Conference, Lecture Notes in Computer Science*. Berlin: Springer.

Goodman, J. (1986). "Are gamma-ray bursts optically thick?" *ApJL* 308, pp. L47–L50. DOI: `10.1086/184741`.

Goriely, S (1999). "Uncertainties in the solar system r-abundance distribution". *A&A* 342, pp. 881–891.

Goriely, S., A. Bauswein, and H.-T. Janka (2011). "r-process Nucleosynthesis in Dynamically Ejected Matter of Neutron Star Mergers". *Astrophys. J. Lett.* 738, p. L32. DOI: `10.1088/2041-8205/738/2/L32`.

Goriely, S., S. Hilaire, and A. J. Koning (2008). "Improved predictions of nuclear reaction rates with the TALYS reaction code for astrophysical applications". *A&A* 487, pp. 767–774. DOI: `10.1051/0004-6361:20078825`. arXiv: `0806.2239 [astro-ph]`.

Goriely, S. et al. (2009). "Towards a prediction of fission cross sections on the basis of microscopic nuclear inputs". *PRC* 79, p. 024612. DOI: `10.1103/PhysRevC.79.024612`.

Goriely, S. et al. (2013). "New Fission Fragment Distributions and r-Process Origin of the Rare-Earth Elements". *Phys. Rev. Lett.* 111 (24), p. 242502. DOI: `10.1103/PhysRevLett.111.242502`.

Goriely, S. et al. (2015). "Impact of weak interactions of free nucleons on the r-process in dynamical ejecta from neutron star mergers". *Mon. Not. R. Astron. Soc.* 452, pp. 3894–3904. DOI: `10.1093/mnras/stv1526`.

Goriely, S. et al. (2015). "Impact of weak interactions of free nucleons on the r-process in dynamical ejecta from neutron star mergers". *MNRAS* 452, pp. 3894–3904. DOI: `10.1093/mnras/stv1526`. arXiv: `1504.04377 [astro-ph.SR]`.

Gossan, S. E., J. Fuller, and L. F. Roberts (2020). "Wave heating from proto-neutron star convection and the core-collapse supernova explosion mechanism". *MNRAS* 491, pp. 5376–5391. DOI: `10.1093/mnras/stz3243`. arXiv: `1910.07599 [astro-ph.HE]`.

Haensel, P., A. Y. Potekhin, and D. G Yakovlev (2007). *Neutron Stars 1*. 1st. New York: Springer-Verlag.

Haggard, D. et al. (2017). “XXX”. *ApJL*. DOI: `10.3847/2041-8213/aa8ede`. arXiv: `XXX [astro-ph.HE]`.

Halevi, G. and P. Mösta (2018). “r-Process nucleosynthesis from three-dimensional jet-driven core-collapse supernovae with magnetic misalignments”. *MNRAS* 477, pp. 2366–2375. DOI: `10.1093/mnras/sty797`.

Hallinan, G., A. Corsi, et al. (2017). “XXX”. *submitted*. DOI: `10.1038/ncomms12898`. arXiv: `XXX [astro-ph.HE]`.

Hansen, T. T. et al. (2015). “The role of binaries in the enrichment of the early Galactic halo. I. r-process-enhanced metal-poor stars”. *A&A* 583, A49. DOI: `10.1051/0004-6361/201526812`. arXiv: `1509.05344 [astro-ph.SR]`.

Hansen, T. T. et al. (2017). “An r-process Enhanced Star in the Dwarf Galaxy Tucana III”. *ApJ* 838, p. 44. DOI: `10.3847/1538-4357/aa634a`.

Harding, A. K. and D. Lai (2006). “Physics of strongly magnetized neutron stars”. *Rep. Prog. Phys.* 69, pp. 2631–2708. DOI: `10.1088/0034-4885/69/9/R03`.

Harten, A., P. D. Lax, and B. van Leer (1983). “On Upstream Differencing and Godunov-Type Schemes for Hyperbolic Conservation Laws”. *SIAM Review* 25, pp. 35–61. DOI: `http://dx.doi.org.subzero.lib.uoguelph.ca/10.1137/1025002`.

Hebeler, K. et al. (2010). “Constraints on Neutron Star Radii Based on Chiral Effective Field Theory Interactions”. *Physical Review Letters* 105, p. 161102. DOI: `10.1103/PhysRevLett.105.161102`.

Hempel, M. et al. (2012). “New Equations of State in Simulations of Core-collapse Supernovae”. *ApJ* 748, p. 70. DOI: `10.1088/0004-637X/748/1/70`. arXiv: `1108.0848 [astro-ph.HE]`.

Hempel, M. and J. Schaffner-Bielich (2010). “A statistical model for a complete supernova equation of state”. *Nuclear Physics A* 837, 210–254. DOI: `10.1016/j.nuclphysa.2010.02.010`.

Hirata, K. et al. (1987). “Observation of a neutrino burst from the supernova SN1987A”. *PRL* 58, pp. 1490–1493. DOI: `10.1103/PhysRevLett.58.1490`.

Hix, W. and F.-K. Thielemann (1999). “Computational methods for nucleosynthesis and nuclear energy generation”. *Journal of Computational and Applied Mathematics* 109, pp. 321–351. DOI: `10.1016/S0377-0427(99)00163-6`.

Hoffman, R. D., S. E. Woosley, and Y.-Z. Qian (1997). “Nucleosynthesis in Neutrino-driven Winds. II. Implications for Heavy Element Synthesis”. *ApJ* 482, p. 951. DOI: 10.1086/304181. eprint: astro-ph/9611097.

Holmbeck, E. M. et al. (2020). “The R-Process Alliance: Fourth Data Release from the Search for R-process-enhanced Stars in the Galactic Halo”. *ApJ Supplements* 249, p. 30. DOI: 10.3847/1538-4365/ab9c19. arXiv: 2007.00749 [astro-ph.SR].

Honda, S. et al. (2006a). “Neutron-Capture Elements in the Very Metal Poor Star HD 122563”. *ApJ* 643, pp. 1180–1189. DOI: 10.1086/503195. arXiv: astro-ph/0602107 [astro-ph].

Honda, S. et al. (2006b). “Neutron-Capture Elements in the Very Metal Poor Star HD 122563”. *ApJ* 643, pp. 1180–1189. DOI: 10.1086/503195. eprint: astro-ph/0602107.

Horesh, A. et al. (2016). “Testing the Magnetar Model via a Late-time Radio Observations of Two Macronova Candidates”. *Astrophys. J. Lett.* 819, p. L22. DOI: 10.3847/2041-8205/819/2/L22. arXiv: 1601.01692 [astro-ph.HE].

Horowitz, C. J. et al. (2018). “r-Process Nucleosynthesis: Connecting Rare-Isotope Beam Facilities with the Cosmos”. *arXiv e-prints*. arXiv: 1805.04637 [astro-ph.SR].

Hotokezaka, K., P. Beniamini, and T. Piran (2018). “Neutron star mergers as sites of r-process nucleosynthesis and short gamma-ray bursts”. *Int. J. Mod. Phys. D* 27, p. 1842005. DOI: 10.1142/S0218271818420051.

Hotokezaka, K., T. Piran, and M. Paul (2015). “Short-lived 244Pu points to compact binary mergers as sites for heavy r-process nucleosynthesis”. 11, pp. 1042–1042. DOI: 10.1038/nphys3574.

Howard, W. M. and P. Möller (1980). “Calculated Fission Barriers, Ground-State Masses, and Particle Separation Energies for Nuclei with 76 <= Z <= 100 and 140 <= N <= 184”. *Atomic Data and Nuclear Data Tables* 25, p. 219. DOI: 10.1016/0092-640X(80)90005-4.

Hoyle, F. et al. (1956). “Origin of the Elements in Stars”. *Science* 124, pp. 611–614. DOI: 10.1126/science.124.3223.611.

Hüdepohl, L. et al. (2010). “Neutrino Signal of Electron-Capture Supernovae from Core Collapse to Cooling”. *Phys. Rev. Lett.* 104, p. 251101. DOI: 10.1103/PhysRevLett.104.251101.

Hüdepohl, L. et al. (2010). “Neutrino Signal of Electron-Capture Supernovae from Core Collapse to Cooling”. *Phys. Rev. Lett.* 104 (25), p. 251101. DOI: 10.1103/PhysRevLett.104.251101.

Hulse, R. A. and J. H. Taylor (1975). “Discovery of a pulsar in a binary system”. *Astrophys. J. Lett.* 195, pp. L51–L53. DOI: `10.1086/181708`.

Igoshev, A. P., S. B. Popov, and R. Hollerbach (2021). “Evolution of Neutron Star Magnetic Fields”. *Universe* 7, p. 351. DOI: `10.3390/universe7090351`. arXiv: `2109.05584 [astro-ph.HE]`.

Jacobson, H. R. et al. (2015). “High-Resolution Spectroscopic Study of Extremely Metal-Poor Star Candidates from the SkyMapper Survey”. *ApJ* 807, p. 171. DOI: `10.1088/0004-637X/807/2/171`. arXiv: `1504.03344 [astro-ph.SR]`.

Janiuk, A. (2014). “Nucleosynthesis of elements in gamma-ray burst engines”. *Astronomy and Astrophysics* 568, A105. DOI: `10.1051/0004-6361/201423822`.

Janka, H.-T. (2012). “Explosion Mechanisms of Core-Collapse Supernovae”. *Annu. Rev. Nucl. Part. Sci.* 62, pp. 407–451. DOI: `10.1146/annurev-nucl-102711-094901`.

Janka, H.-T. et al. (2007). “Theory of core-collapse supernovae”. *Physics Reports* 442, pp. 38–74. DOI: `10.1016/j.physrep.2007.02.002`.

Jaura, O. et al. (2022). “Trapping of H II regions in Population III star formation”. *MNRAS* 512, pp. 116–136. DOI: `10.1093/mnras/stac487`. arXiv: `2202.09803 [astro-ph.SR]`.

Ji, A. P., M. R. Drout, and T. T. Hansen (2019). “The Lanthanide Fraction Distribution in Metal-poor Stars: A Test of Neutron Star Mergers as the Dominant r-process Site”. *ApJ* 882, p. 40. DOI: `10.3847/1538-4357/ab3291`.

Ji, A. P. et al. (2016). “R-process enrichment from a single event in an ancient dwarf galaxy”. *Nature* 531, pp. 610–613. DOI: `10.1038/nature17425`.

Ji, A. P. et al. (2023). “Metal Mixing in the r-process Enhanced Ultrafaint Dwarf Galaxy Reticulum II”. *AJ* 165, p. 100. DOI: `10.3847/1538-3881/acad84`. arXiv: `2207.03499 [astro-ph.GA]`.

Johnson, J. A. and M. Bolte (2002). “The r-Process in the Early Galaxy”. *ApJ* 579, pp. 616–625. DOI: `10.1086/342829`. arXiv: `astro-ph/0208375 [astro-ph]`.

Just, O. et al. (2022a). “Neutrino absorption and other physics dependencies in neutrino-cooled black hole accretion discs”. *MNRAS* 509, pp. 1377–1412. DOI: `10.1093/mnras/stab2861`. arXiv: `2102.08387 [astro-ph.HE]`.

Just, O. et al. (2022b). “r-process Viable Outflows are Suppressed in Global Alpha-viscosity Models of Collapsar Disks”. *ApJL* 934, p. L30. DOI: `10.3847/2041-8213/ac83a1`. arXiv: `2205.14158 [astro-ph.HE]`.

Just, O. et al. (2022c). “Fast neutrino conversion in hydrodynamic simulations of neutrino-cooled accretion disks”. *Phys. Rev. D.* 105, p. 083024. DOI: `10.1103/PhysRevD.105.083024`. arXiv: `2203.16559 [astro-ph.HE]`.

Kajino, T. et al. (2000). “Impact of A Few Body Reactions on Explosive Nucleosynthesis: Big-Bang and Supernovae”. In: *Few-Body Problems in Physics ’99*. Ed. by S. Oryu and S. Kamimura M. Ishikawa, p. 80. arXiv: `astro-ph/0006079 [astro-ph]`.

Kaneko, Y. et al. (2015). “Short gamma-ray bursts with extended emission observed with Swift/BAT and Fermi/GBM”. *MNRAS* 452, pp. 824–837. DOI: `10.1093/mnras/stv1286`. arXiv: `1506.05899 [astro-ph.HE]`.

Kaplan, J. D. et al. (2014). “The Influence of Thermal Pressure on Equilibrium Models of Hypermassive Neutron Star Merger Remnants”. *ApJ* 790, p. 19. DOI: `10.1088/0004-637X/790/1/19`. arXiv: `1306.4034 [astro-ph.HE]`.

Kappeler, F, H Beer, and K Wisshak (1989). “s-process nucleosynthesis-nuclear physics and the classical model”. *Reports on Progress in Physics* 52, p. 945. DOI: `10.1088/0034-4885/52/8/002`.

Kasen, D., N. R. Badnell, and J. Barnes (2013). “Opacities and Spectra of the *r*-process Ejecta from Neutron Star Mergers”. *ApJ, submitted, arXiv:1303.5788*. arXiv: `1303.5788 [astro-ph.HE]`.

Kasen, D. and L. Bildsten (2010). “Supernova Light Curves Powered by Young Magnetars”. *Astrophys. J.* 717, pp. 245–249. DOI: `10.1088/0004-637X/717/1/245`.

Kasen, D. and J. Barnes (2019). “Radioactive Heating and Late Time Kilonova Light Curves”. *ApJ* 876, p. 128. DOI: `10.3847/1538-4357/ab06c2`. arXiv: `1807.03319 [astro-ph.HE]`.

Kaspi, V. M. and A. M. Beloborodov (2017). “Magnetars”. *ARA&A* 55, pp. 261–301. DOI: `10.1146/annurev-astro-081915-023329`.

Kelic, A., M. Valentina Ricciardi, and K.-H. Schmidt (2009). “ABLA07 - towards a complete description of the decay channels of a nuclear system from spontaneous fission to multifragmentation”. *arXiv e-prints*, arXiv:0906.4193. DOI: `10.48550/arXiv.0906.4193`. arXiv: `0906.4193 [nucl-th]`.

Kidder, L. E. et al. (2000). “Black hole evolution by spectral methods”. *Phys. Rev. D.* 62, p. 084032. DOI: `10.1103/PhysRevD.62.084032`. eprint: `gr-qc/0005056`.

Kirby, E. N. et al. (2020). “The Stars in M15 Were Born with the r-process”. *ApJL* 891, p. L13. DOI: `10.3847/2041-8213/ab78a1`.

Kisaka, S. and K. Ioka (2015). “Long-lasting Black Hole Jets in Short Gamma-Ray Bursts”. *Astrophys. J. Lett.* 804, p. L16. DOI: `10.1088/2041-8205/804/1/L16`. arXiv: `1503.06791 [astro-ph.HE]`.

Kisaka, S., K. Ioka, and T. Sakamoto (2017). “Bimodal Long-lasting Components in Short Gamma-Ray Bursts: Promising Electromagnetic Counterparts to Neutron Star Binary Mergers”. *ApJ* 846, p. 142. DOI: `10.3847/1538-4357/aa8775`. arXiv: `1707.00675 [astro-ph.HE]`.

Kiuchi, K., K. Kyutoku, and M. Shibata (2012). “Three-dimensional evolution of differentially rotating magnetized neutron stars”. *Phys. Rev. D.* 86, p. 064008. DOI: `10.1103/PhysRevD.86.064008`.

Kiuchi, K. et al. (2018). “Global simulations of strongly magnetized remnant massive neutron stars formed in binary neutron star mergers”. *Phys. Rev. D.* 97, p. 124039. DOI: `10.1103/PhysRevD.97.124039`.

Klessen, R. S. and S. C. O. Glover (2023). “The first stars: formation, properties, and impact”. *arXiv e-prints*, arXiv:2303.12500. DOI: `10.48550/arXiv.2303.12500`. arXiv: `2303.12500 [astro-ph.CO]`.

Korobkin, O. et al. (2012). “On the astrophysical robustness of the neutron star merger r-process”. *MNRAS* 426, pp. 1940–1949. DOI: `10.1111/j.1365-2966.2012.21859.x`.

Korobkin, O. et al. (2012). “On the astrophysical robustness of the neutron star merger *r*-process”. *Mon. Not. R. Astron. Soc.* 426, pp. 1940–1949. DOI: `10.1111/j.1365-2966.2012.21859.x`. arXiv: `1206.2379 [astro-ph.SR]`.

Kouveliotou, C. et al. (1993). “Identification of two classes of gamma-ray bursts”. *ApJL* 413, pp. L101–L104. DOI: `10.1086/186969`.

Kouveliotou, C. et al. (1994). “The rarity of soft γ-ray repeaters deduced from reactivation of SGR1806 - 20”. *Nature* 368, pp. 125–127. DOI: `10.1038/368125a0`.

Kouveliotou, C. et al. (1998). “An X-ray pulsar with a superstrong magnetic field in the soft γ-ray repeater SGR1806 - 20”. *Nature* 393, pp. 235–237. DOI: `10.1038/30410`.

Kuroda, T. et al. (2020). “Magnetorotational Explosion of a Massive Star Supported by Neutrino Heating in General Relativistic Three-dimensional Simulations”. *ApJ* 896, p. 102. DOI: `10.3847/1538-4357/ab9308`. arXiv: `2003.02004 [astro-ph.HE]`.

Kyutoku, K. et al. (2015). “Dynamical mass ejection from black hole-neutron star binaries”. *Phys. Rev. D* 92, p. 044028. DOI: `10.1103/PhysRevD.92.044028`.

Kyutoku, K. et al. (2011). “Gravitational waves from spinning black hole-neutron star binaries: dependence on black hole spins and on neutron star equations of state”. *Phys. Rev. D.* 84, p. 064018. DOI: 10.1103/PhysRevD.84.064018. arXiv: 1108.1189 [astro-ph.HE].

Lai, D. and Y.-Z. Qian (1998). “Neutrino Transport in Strongly Magnetized Proto-Neutron Stars and the Origin of Pulsar Kicks: The Effect of Asymmetric Magnetic Field Topology”. *ApJ* 505, pp. 844–853. DOI: 10.1086/306203.

Lamers, H. J. G. L. M. and J. P. Cassinelli (1999). *Introduction to Stellar Winds*. Ed. by Lamers, H. J. G. L. M. & Cassinelli, J. P. Cambridge University Press.

Lattimer, J. M. and D. N. Schramm (1974). “Black-hole-neutron-star collisions”. *ApJL* 192, pp. L145–L147. DOI: 10.1086/181612.

Lattimer, J. M. et al. (1977). “The decompression of cold neutron star matter”. *ApJ* 213, pp. 225–233. DOI: 10.1086/155148.

Lattimer, J. M. and Y. Lim (2013). “Constraining the Symmetry Parameters of the Nuclear Interaction”. *ApJ* 771, p. 51. DOI: 10.1088/0004-637X/771/1/51. arXiv: 1203.4286 [nucl-th].

LeBlanc, J. M. and J. R. Wilson (1970). “A Numerical Example of the Collapse of a Rotating Magnetized Star”. *ApJ* 161, p. 541. DOI: 10.1086/150558.

Li, L.-X. and B. Paczyński (1998). “Transient Events from Neutron Star Mergers”. *Astrophys. J. Lett.* 507, pp. L59–L62. DOI: 10.1086/311680. eprint: astro-ph/9807272.

Li, X. and D. M. Siegel (2021). “Neutrino Fast Flavor Conversions in Neutron-Star Postmerger Accretion Disks”. *PRL* 126, p. 251101. DOI: 10.1103/PhysRevLett.126.251101. arXiv: 2103.02616 [astro-ph.HE].

Lippuner, J. and L. F. Roberts (2015). “r-process Lanthanide Production and Heating Rates in Kilonovae”. *Astrophys. J.* 815, p. 82. DOI: 10.1088/0004-637X/815/2/82.

Lippuner, J. et al. (2017). “Signatures of hypermassive neutron star lifetimes on r-process nucleosynthesis in the disc ejecta from neutron star mergers”. *MNRAS* 472, pp. 904–918. DOI: 10.1093/mnras/stx1987. arXiv: 1703.06216 [astro-ph.HE].

Lippuner, J. and L. F. Roberts (2017). “SkyNet: A Modular Nuclear Reaction Network Library”. *ApJ Supplements* 233, p. 18. DOI: 10.3847/1538-4365/aa94cb.

Lippuner, J. et al. (2017). “Signatures of hypermassive neutron star lifetimes on r-process nucleosynthesis in the disc ejecta from neutron star mergers”. *MNRAS* 472, pp. 904–918. DOI: 10.1093/mnras/stx1987.

Litvinov, Y. A. et al. (2004). “Precision experiments with time-resolved Schottky mass spectrometry”. 734, pp. 473–476. DOI: `10.1016/j.nuclphysa.2004.01.089`.

Lodders, K. (2003). “Solar System Abundances and Condensation Temperatures of the Elements”. *ApJ* 591, pp. 1220–1247. DOI: `10.1086/375492`.

Lorusso, G. et al. (2015). “β -Decay Half-Lives of 110 Neutron-Rich Nuclei across the N = 82 Shell Gap: Implications for the Mechanism and Universality of the Astrophysical r Process”. *PRL* 114, p. 192501. DOI: `10.1103/PhysRevLett.114.192501`.

Löffler, F. et al. (2012). “The Einstein Toolkit: a community computational infrastructure for relativistic astrophysics”. *Classical and Quantum Gravity* 29, p. 115001. DOI: `10.1088/0264-9381/29/11/115001`.

Ma, L. and J. Fuller (2019). “Angular momentum transport in massive stars and natal neutron star rotation rates”. *MNRAS* 488, pp. 4338–4355. DOI: `10.1093/mnras/stz2009`.

MacFadyen, A. I. and S. E. Woosley (1999). “Collapsars: Gamma-Ray Bursts and Explosions in “Failed Supernovae””. *ApJ* 524, pp. 262–289. DOI: `10.1086/307790`.

MacFadyen, A. I., S. E. Woosley, and A. Heger (2001). “Supernovae, Jets, and Collapsars”. *ApJ* 550, pp. 410–425. DOI: `10.1086/319698`.

Magg, M. et al. (2020). “A minimum dilution scenario for supernovae and consequences for extremely metal-poor stars”. *MNRAS* 498, pp. 3703–3712. DOI: `10.1093/mnras/staa2624`. arXiv: `2006.12517 [astro-ph.GA]`.

Mamdouh, A. et al. (2001). “Fission barriers of neutron-rich and superheavy nuclei calculated with the ETFSI method”. *Nuc. Phys. A* 679, pp. 337–358. DOI: `10.1016/S0375-9474(00)00358-4`. arXiv: `nucl-th/0010093`.

Manning, B. et al. (2019). “Informing direct neutron capture on tin isotopes near the N =82 shell closure”. *PRC* 99, p. 041302. DOI: `10.1103/PhysRevC.99.041302`.

Margutti, M. et al. (2017). “XXX”. *ApJL accepted.* DOI: `10.1038/ncomms12898`. arXiv: `XXX [astro-ph.HE]`.

Margutti, R. et al. (2018). “The Binary Neutron Star Event LIGO/Virgo GW170817 160 Days after Merger: Synchrotron Emission across the Electromagnetic Spectrum”. *ApJL* 856, p. L18. DOI: `10.3847/2041-8213/aab2ad`. arXiv: `1801.03531 [astro-ph.HE]`.

Martin, D. et al. (2015). “Neutrino-driven Winds in the Aftermath of a Neutron Star Merger: Nucleosynthesis and Electromagnetic Transients”. *Astrophys. J.* 813, p. 2. DOI: `10.1088/0004-637X/813/1/2`.

Martin, J. et al. (2014). "Comparing supernova remnants around strongly magnetized and canonical pulsars". *MNRAS* 444, pp. 2910–2924. DOI: `10.1093/mnras/stu1594`. arXiv: `1409.1027 [astro-ph.HE]`.

Martínez-Pinedo, G., T. Fischer, and L. Huther (2014). "Supernova neutrinos and nucleosynthesis". *Journal of Physics G Nuclear Physics* 41, p. 044008. DOI: `10.1088/0954-3899/41/4/044008`. arXiv: `1309.5477 [astro-ph.HE]`.

Martínez-Pinedo, G. et al. (2012). "Charged-Current Weak Interaction Processes in Hot and Dense Matter and its Impact on the Spectra of Neutrinos Emitted from Protoneutron Star Cooling". *PRL* 109, p. 251104. DOI: `10.1103/PhysRevLett.109.251104`.

Martínez-Pinedo, G. et al. (2012). "Charged-Current Weak Interaction Processes in Hot and Dense Matter and its Impact on the Spectra of Neutrinos Emitted from Protoneutron Star Cooling". *Physical Review Letters* 109, p. 251104. DOI: `10.1103/PhysRevLett.109.251104`. arXiv: `1205.2793 [astro-ph.HE]`.

Matteucci, F. et al. (2014). "Europium production: neutron star mergers versus core-collapse supernovae". *MNRAS* 438, pp. 2177–2185. DOI: `10.1093/mnras/stt2350`. arXiv: `1311.6980 [astro-ph.GA]`.

McKinney, J. C., A. Tchekhovskoy, and R. D. Blandford (2013). "Alignment of Magnetized Accretion Disks and Relativistic Jets with Spinning Black Holes". *Science* 339, pp. 49–. DOI: `10.1126/science.1230811`.

McLaughlin, G. C. and R. Surman (2005). "Prospects for obtaining an r process from Gamma Ray Burst Disk Winds". *Nuclear Physics A* 758, pp. 189–196. DOI: `10.1016/j.nuclphysa.2005.05.036`.

McMillan, P. J. (2011). "Mass models of the Milky Way". *MNRAS* 414, pp. 2446–2457. DOI: `10.1111/j.1365-2966.2011.18564.x`.

Meisel, Z. and S. George (2013). "Time-of-flight mass spectrometry of very exotic systems". *International Journal of Mass Spectrometry* 349-350, pp. 145–150. DOI: `10.1016/j.ijms.2013.03.022`.

Mendoza-Temis, J. J. et al. (2015). "Nuclear robustness of the r process in neutron-star mergers". *PRC* 92, p. 055805. DOI: `10.1103/PhysRevC.92.055805`.

Metzger, B. D. and E. Berger (2012). "What is the Most Promising Electromagnetic Counterpart of a Neutron Star Binary Merger?" *Astrophys. J.* 746, p. 48. DOI: `10.1088/0004-637X/746/1/48`. arXiv: `1108.6056 [astro-ph.HE]`.

Metzger, B. D. and G. C. Bower (2014). “Constraints on long-lived remnants of neutron star binary mergers from late-time radio observations of short duration gamma-ray bursts”. *Mon. Not. R. Astron. Soc.* 437, pp. 1821–1827. DOI: 10.1093/mnras/stt2010. arXiv: 1310.4506 [astro-ph.HE].

Metzger, B. D. and R. Fernández (2014). “Red or blue? A potential kilonova imprint of the delay until black hole formation following a neutron star merger”. *Mon. Not. R. Astron. Soc.* 441, pp. 3444–3453. DOI: 10.1093/mnras/stu802. arXiv: 1402.4803 [astro-ph.HE].

Metzger, B. D. and R. Fernández (2014). “Red or blue? A potential kilonova imprint of the delay until black hole formation following a neutron star merger”. *Mon. Not. R. Astron. Soc.* 441, pp. 3444–3453. DOI: 10.1093/mnras/stu802.

Metzger, B. D., D. Giannios, and S. Horiuchi (2011). “Heavy nuclei synthesized in gamma-ray burst outflows as the source of ultrahigh energy cosmic rays”. *MNRAS* 415, pp. 2495–2504. DOI: 10.1111/j.1365-2966.2011.18873.x. arXiv: 1101.4019 [astro-ph.HE].

Metzger, B. D., T. A. Thompson, and E. Quataert (2007). “Proto-Neutron Star Winds with Magnetic Fields and Rotation”. *Astrophys. J.* 659, pp. 561–579. DOI: 10.1086/512059.

Metzger, B. D., T. A. Thompson, and E. Quataert (2007). “Proto-Neutron Star Winds with Magnetic Fields and Rotation”. *ApJ* 659, pp. 561–579. DOI: 10.1086/512059. eprint: arXiv:astro-ph/0608682.

Metzger, B. D., T. A. Thompson, and E. Quataert (2008). “On the Conditions for Neutron-rich Gamma-Ray Burst Outflows”. *Astrophys. J.* 676, pp. 1130–1150. DOI: 10.1086/526418.

Metzger, B. D. et al. (2010b). “The effects of r-process heating on fallback accretion in compact object mergers”. *MNRAS* 402, pp. 2771–2777. DOI: 10.1111/j.1365-2966.2009.16107.x.

Metzger, B. D. et al. (2010a). “The effects of r-process heating on fallback accretion in compact object mergers”. *MNRAS* 402, pp. 2771–2777. DOI: 10.1111/j.1365-2966.2009.16107.x. arXiv: 0908.0530 [astro-ph.HE].

Metzger, B. D. et al. (2010b). “The effects of r-process heating on fallback accretion in compact object mergers”. *MNRAS* 402, pp. 2771–2777. DOI: 10.1111/j.1365-2966.2009.16107.x. arXiv: 0908.0530 [astro-ph.HE].

Metzger, B. D. et al. (2010a). “Electromagnetic counterparts of compact object mergers powered by the radioactive decay of r-process nuclei: Transients from compact object mergers”. *MNRAS* 406, pp. 2650–2662. DOI: 10.1111/j.1365-2966.2010.16864.x.

Metzger, B. D. et al. (2011). “The protomagnetar model for gamma-ray bursts”. *MNRAS* 413, pp. 2031–2056. DOI: 10.1111/j.1365-2966.2011.18280.x. arXiv: 1012.0001 [astro-ph.HE].

Metzger, B. D. et al. (2015). “Neutron-powered precursors of kilonovae”. *Mon. Not. R. Astron. Soc.* 446, pp. 1115–1120. DOI: 10.1093/mnras/stu2225.

Metzger, B. D., T. A. Thompson, and E. Quataert (2008). “On the Conditions for Neutron-rich Gamma-Ray Burst Outflows”. *ApJ* 676, pp. 1130–1150. DOI: 10.1086/526418. arXiv: 0708.3395 [astro-ph].

Metzger, B. D., T. A. Thompson, and E. Quataert (2018). “A Magnetar Origin for the Kilonova Ejecta in GW170817”. *ApJ* 856, p. 101. DOI: 10.3847/1538-4357/aab095.

Metzger, B. D., T. A. Thompson, and E. Quataert (2018). “A Magnetar Origin for the Kilonova Ejecta in GW170817”. *ApJ* 856, p. 101. DOI: 10.3847/1538-4357/aab095. arXiv: 1801.04286 [astro-ph.HE].

Meyer, B. S. and J. S. Brown (1997). “Survey of r-Process Models”. *ApJ Supplements* 112, pp. 199–220. DOI: 10.1086/313032.

Meyer, B. S. et al. (1992). “R-process nucleosynthesis in the high-entropy supernova bubble”. *ApJ* 399, pp. 656–664. DOI: 10.1086/171957.

Meyer, B. S. (1994). “The r-, s-, and p-Processes in Nucleosynthesis”. *ARA&A* 32, pp. 153–190. DOI: 10.1146/annurev.aa.32.090194.001101.

Meyer, B. S. (2002). “r-Process Nucleosynthesis without Excess Neutrons”. *PRL* 89, p. 231101. DOI: 10.1103/PhysRevLett.89.231101.

Miller, M. C. et al. (2019). “PSR J0030+0451 Mass and Radius from NICER Data and Implications for the Properties of Neutron Star Matter”. *ApJL*, p. L24.

Minaev, P. Y., A. S. Pozanenko, and V. M. Loznikov (2010). “Extended emission from short gamma-ray bursts detected with SPI-ACS/INTEGRAL”. *Astronomy Letters* 36, pp. 707–720. DOI: 10.1134/S1063773710100026. arXiv: 1009.2685 [astro-ph.HE].

Möller, P. et al. (2016). “Nuclear ground-state masses and deformations: FRDM(2012)”. *Atomic Data and Nuclear Data Tables* 109-110, pp. 1–204. DOI: 10.1016/j.adt.2015.10.002.

Montes, F. et al. (2007). “Nucleosynthesis in the Early Galaxy”. *ApJ* 671, pp. 1685–1695. DOI: 10.1086/523084. arXiv: 0709.0417 [astro-ph].

Mösta, P. et al. (2014). "Magnetorotational Core-collapse Supernovae in Three Dimensions". *ApJL* 785, p. L29. DOI: 10.1088/2041-8205/785/2/L29.

Mösta, P. et al. (2014). "Magnetorotational Core-collapse Supernovae in Three Dimensions". *ApJL* 785, p. L29. DOI: 10.1088/2041-8205/785/2/L29. arXiv: 1403.1230 [astro-ph.HE].

Mösta, P. et al. (2014). "GRHydro: a new open-source general-relativistic magnetohydrodynamics code for the Einstein toolkit". *CQG* 31, p. 015005. DOI: 10.1088/0264-9381/31/1/015005.

Mösta, P. et al. (2015). "A large-scale dynamo and magnetoturbulence in rapidly rotating core-collapse supernovae". *Nature* 528, pp. 376–379. DOI: 10.1038/nature15755. arXiv: 1512.00838 [astro-ph.HE].

Mösta, P. et al. (2018). "r-process Nucleosynthesis from Three-dimensional Magnetorotational Core-collapse Supernovae". *ApJ* 864, p. 171. DOI: 10.3847/1538-4357/aad6ec.

Mösta, P. et al. (2020). "A Magnetar Engine for Short GRBs and Kilonovae". *ApJL* 901, p. L37. DOI: 10.3847/2041-8213/abb6ef.

Mumpower, M. R. et al. (2017). "Estimation of M 1 scissors mode strength for deformed nuclei in the medium- to heavy-mass region by statistical Hauser-Feshbach model calculations". *PRC* 96, p. 024612. DOI: 10.1103/PhysRevC.96.024612. arXiv: 1706.07504 [nucl-th].

Mumpower, M. et al. (2016). "The impact of individual nuclear properties on r -process nucleosynthesis". *Progress in Particle and Nuclear Physics* 86, pp. 86–126. DOI: 10.1016/j.ppnp.2015.09.001.

Munson, J. M. et al. (2018). "Recoil-ion detection efficiency for complex β decays studied using the Beta-decay Paul Trap". *Nuclear Instruments and Methods in Physics Research A* 898, pp. 60–66. DOI: 10.1016/j.nima.2018.04.063.

Nagakura, H., A. Burrows, and D. Vartanyan (2021). "Supernova neutrino signals based on long-term axisymmetric simulations". *MNRAS* 506, pp. 1462–1479. DOI: 10.1093/mnras/stab1785. arXiv: 2102.11283 [astro-ph.HE].

Nagataki, S. et al. (2007). "Numerical Study of Gamma-Ray Burst Jet Formation in Collapsars". *ApJ* 659, pp. 512–529. DOI: 10.1086/512057.

Nakamura, K. et al. (2015). "r-process nucleosynthesis in the MHD+neutrino-heated collapsar jet". *A&A* 582, A34. DOI: 10.1051/0004-6361/201526110.

Nakazato, K. et al. (2013). “Supernova Neutrino Light Curves and Spectra for Various Progenitor Stars: From Core Collapse to Proto-neutron Star Cooling”. *ApJ Supplements* 205, p. 2. doi: 10.1088/0067-0049/205/1/2. arXiv: 1210.6841 [astro-ph.HE].

Narayan, R., B. Paczynski, and T. Piran (1992). “Gamma-ray bursts as the death throes of massive binary stars”. *Astrophys. J. Lett.* 395, pp. L83–L86. doi: 10.1086/186493.

Narayan, R., B. Paczynski, and T. Piran (1992). “Gamma-ray bursts as the death throes of massive binary stars”. *Astrophys. J. Lett.* 395, pp. L83–L86. doi: 10.1086/186493. eprint: arXiv:astro-ph/9204001.

Neilsen, D. et al. (2014). “Magnetized neutron stars with realistic equations of state and neutrino cooling”. *Phys. Rev. D.* 89, p. 104029. doi: 10.1103/PhysRevD.89.104029.

Nevins, B. and L. F. Roberts (2023). “Proto-neutron star convection and the neutrino-driven wind: implications for the r-process”. *MNRAS* 520, pp. 3986–3999. doi: 10.1093/mnras/stad372. arXiv: 2302.01249 [astro-ph.HE].

Nicholl, M. et al. (2017). “The superluminous supernova SN 2017egm in the nearby galaxy NGC 3191: a metal-rich environment can support a typical SLSN evolution”. *ArXiv e-prints.*

Nishimura, S. et al. (2006). “r-Process Nucleosynthesis in Magnetohydrodynamic Jet Explosions of Core-Collapse Supernovae”. *ApJ* 642, pp. 410–419. doi: 10.1086/500786. arXiv: astro-ph/0504100 [astro-ph].

Nomoto, K., C. Kobayashi, and N. Tominaga (2013). “Nucleosynthesis in Stars and the Chemical Enrichment of Galaxies”. *ARA&A* 51, pp. 457–509. doi: 10.1146/annurev-astro-082812-140956.

Norris, J. P. and J. T. Bonnell (2006). “Short Gamma-Ray Bursts with Extended Emission”. *ApJ* 643, pp. 266–275. doi: 10.1086/502796. eprint: arXiv:astro-ph/0601190.

Norris, J. P., N. Gehrels, and J. D. Scargle (2010). “Threshold for Extended Emission in Short Gamma-ray Bursts”. *ApJ* 717, pp. 411–419. doi: 10.1088/0004-637X/717/1/411. arXiv: 0910.2456 [astro-ph.HE].

Obergaulinger, M. and M. Á. Aloy (2021). “Magnetorotational core collapse of possible GRB progenitors - III. Three-dimensional models”. *MNRAS* 503, pp. 4942–4963. doi: 10.1093/mnras/stab295. arXiv: 2008.07205 [astro-ph.HE].

Obergaulinger, M., O. Just, and M. A. Aloy (2018). “Core collapse with magnetic fields and rotation”. *Journal of Physics G Nuclear Physics* 45, p. 084001. doi: 10.1088/1361-6471/aac982. arXiv: 1806.00393 [astro-ph.HE].

O'Connor, E. and C. D. Ott (2010). "A new open-source code for spherically symmetric stellar collapse to neutron stars and black holes". *CQG* 27, p. 114103. DOI: `10.1088/0264-9381/27/11/114103`.

Olausen, S. A. and V. M. Kaspi (2014). "The McGill Magnetar Catalog". *ApJ Supplements* 212, p. 6. DOI: `10.1088/0067-0049/212/1/6`. arXiv: `1309.4167 [astro-ph.HE]`.

Olson, P. and U. R. Christensen (2006). "Dipole moment scaling for convection-driven planetary dynamos". *Earth and Planetary Science Letters* 250, pp. 561–571. DOI: `10.1016/j.epsl.2006.08.008`.

Otsuki, K. et al. (2000). "General Relativistic Effects on Neutrino-driven Winds from Young, Hot Neutron Stars and r-Process Nucleosynthesis". *ApJ* 533, pp. 424–439. DOI: `10.1086/308632`. eprint: `astro-ph/9911164`.

Paczynski, B. (1986). "Gamma-ray bursters at cosmological distances". *Astrophys. J. Lett.* 308, pp. L43–L46. DOI: `10.1086/184740`.

Paczynski, B. (1986). "Gamma-ray bursters at cosmological distances". *Astrophys. J. Lett.* 308, pp. L43–L46. DOI: `10.1086/184740`.

Panov, I. V., I. Y. Korneev, and F. K. Thielemann (2008). "The r-Process in the region of transuranium elements and the contribution of fission products to the nucleosynthesis of nuclei with A $\leq$ 130". *Astronomy Letters* 34, pp. 189–197. DOI: `10.1007/s11443-008-3006-1`.

Panov, I. V. et al. (2005). "Calculations of fission rates for r-process nucleosynthesis". 747, pp. 633–654. DOI: `10.1016/j.nuclphysa.2004.09.115`. arXiv: `astro-ph/0412654 [astro-ph]`.

Panov, I. V. et al. (2010). "Neutron-induced astrophysical reaction rates for translead nuclei". *å* 513, A61. DOI: `10.1051/0004-6361/200911967`.

Parfrey, K., D. Giannios, and A. M. Beloborodov (2015). "Black hole jets without large-scale net magnetic flux". *MNRAS* 446, pp. L61–L65. DOI: `10.1093/mnrasl/slu162`. arXiv: `1410.0374 [astro-ph.HE]`.

Pascal, A., J. Novak, and M. Oertel (2022). "Proto-neutron star evolution with improved charged-current neutrino-nucleon interactions". *MNRAS* 511, pp. 356–370. DOI: `10.1093/mnras/stac016`. arXiv: `2201.01955 [nucl-th]`.

Paschalidis, V., M. Ruiz, and S. L. Shapiro (2015). "Relativistic Simulations of Black Hole-Neutron Star Coalescence: The Jet Emerges". *ApJ* 806, p. L14. DOI: `10.1088/2041-8205/806/1/L14`. arXiv: `1410.7392 [astro-ph.HE]`.

Perego, A. et al. (2014). “Neutrino-driven winds from neutron star merger remnants”. *Mon. Not. R. Astron. Soc.* 443, pp. 3134–3156. doi: `10.1093/mnras/stu1352`.

Perley, D. A. et al. (2009). “GRB 080503: Implications of a Naked Short Gamma-Ray Burst Dominated by Extended Emission”. *ApJ* 696, pp. 1871–1885. doi: `10.1088/0004-637X/696/2/1871`. arXiv: `0811.1044`.

Perley, D. A. et al. (2009). “GRB 080503: Implications of a Naked Short Gamma-Ray Burst Dominated by Extended Emission”. *ApJ* 696, pp. 1871–1885. doi: `10.1088/0004-637X/696/2/1871`.

Perley, D. A. et al. (2020). “The Zwicky Transient Facility Bright Transient Survey. II. A Public Statistical Sample for Exploring Supernova Demographics”. *ApJ* 904, p. 35. doi: `10.3847/1538-4357/abbd98`. arXiv: `2009.01242 [astro-ph.HE]`.

Perna, R. et al. (2008). “How rapidly do neutron stars spin at birth? Constraints from archival X-ray observations of extragalactic supernovae”. *MNRAS* 384, pp. 1638–1648. doi: `10.1111/j.1365-2966.2007.12821.x`. arXiv: `0712.1040 [astro-ph]`.

Petermann, I. et al. (2012). “Have superheavy elements been produced in nature?” *European Physical Journal A* 48, p. 122. doi: `10.1140/epja/i2012-12122-6`. arXiv: `1207.3432 [nucl-th]`.

Peters, P. C. (1964). “Gravitational Radiation and the Motion of Two Point Masses”. *Phys. Rev.* 136, B1224–B1232.

Pons, J. A. et al. (1999). “Evolution of Proto-Neutron Stars”. *ApJ* 513, pp. 780–804. doi: `10.1086/306889`.

Pons, J. A. et al. (1999). “Evolution of Proto-Neutron Stars”. *ApJ* 513, pp. 780–804. doi: `10.1086/306889`. eprint: `arXiv:astro-ph/9807040`.

Pooley, D. et al. (2018). “GW170817 Most Likely Made a Black Hole”. *ApJL* 859, p. L23. doi: `10.3847/2041-8213/aac3d6`. arXiv: `1712.03240 [astro-ph.HE]`.

Portegies Zwart, S. F. and L. R. Yungelson (1998). “Formation and evolution of binary neutron stars”. *A&A* 332, pp. 173–188. doi: `10.48550/arXiv.astro-ph/9710347`. arXiv: `astro-ph/9710347 [astro-ph]`.

Potel, G., F. M. Nunes, and I. J. Thompson (2015). “Establishing a theory for deuteron-induced surrogate reactions”. *PRC* 92, p. 034611. doi: `10.1103/PhysRevC.92.034611`.

Prantzos, N. et al. (2020). “Chemical evolution with rotating massive star yields II. A new assessment of the solar s- and r-process components”. *MNRAS* 491, pp. 1832–1850. DOI: `10.1093/mnras/stz3154`. arXiv: `1911.02545 [astro-ph.GA]`.

Prasanna, T. et al. (2022). “The early evolution of magnetar rotation - I. Slowly rotating 'normal' magnetars”. *MNRAS* 517, pp. 3008–3023. DOI: `10.1093/mnras/stac2651`. arXiv: `2208.09042 [astro-ph.HE]`.

Prasanna, T. et al. (2023). “The early evolution of magnetar rotation – II. Rapidly rotating magnetars: Implications for Gamma-Ray Bursts and Super Luminous Supernovae”. *arXiv e-prints*, arXiv:2305.16412. DOI: `10.48550/arXiv.2305.16412`. arXiv: `2305.16412 [astro-ph.HE]`.

Pretorius, F. (2005). “Evolution of binary black hole spacetimes”. *Phys. Rev. Lett.* 95, p. 121101.

Price, D. J. and S. Rosswog (2006). “Producing Ultrastrong Magnetic Fields in Neutron Star Mergers”. *Science* 312, pp. 719–722. DOI: `10.1126/science.1125201`. arXiv: `astro-ph/0603845 [astro-ph]`.

Pruet, J., T. A. Thompson, and R. D. Hoffman (2004). “Nucleosynthesis in Outflows from the Inner Regions of Collapsars”. *ApJ* 606, pp. 1006–1018. DOI: `10.1086/382036`.

Qian, Y. Z. and G. J. Wasserburg (2001). “A Model for Abundances in Metal-poor Stars”. *ApJ* 559, pp. 925–941. DOI: `10.1086/322367`. arXiv: `astro-ph/0106085 [astro-ph]`.

Qian, Y.-Z. and G. J. Wasserburg (2007). “Where, oh where has the r-process gone?” *Phys. Rep.* 442, pp. 237–268. DOI: `10.1016/j.physrep.2007.02.006`.

Qian, Y.-Z. and G. J. Wasserburg (2007). “Where, oh where has the r-process gone?” 442, pp. 237–268. DOI: `10.1016/j.physrep.2007.02.006`. arXiv: `0708.1767`.

Qian, Y.-Z. and S. E. Woosley (1996). “Nucleosynthesis in Neutrino-driven Winds. I. The Physical Conditions”. *ApJ* 471, pp. 331–351. DOI: `10.1086/177973`.

Qian, Y. and S. E. Woosley (1996). “Nucleosynthesis in Neutrino-driven Winds. I. The Physical Conditions”. *ApJ* 471, pp. 331–+. DOI: `10.1086/177973`. eprint: `arXiv:astro-ph/9611094`.

Qian, Y.-Z. et al. (1993). “Connection between flavor-mixing of cosmologically significant neutrinos and heavy element nucleosynthesis in supernovae”. *Phys. Rev. Lett.* 71 (13), pp. 1965–1968. DOI: `10.1103/PhysRevLett.71.1965`.

Radice, D. et al. (2016). “Dynamical mass ejection from binary neutron star mergers”. *MNRAS* 460, pp. 3255–3271. DOI: `10.1093/mnras/stw1227`.

Radice, D. et al. (2018). “Binary Neutron Star Mergers: Mass Ejection, Electromagnetic Counterparts, and Nucleosynthesis”. *ApJ* 869, p. 130. DOI: `10.3847/1538-4357/aaf054`.

Raives, M. J., M. S. B. Coleman, and T. A. Thompson (2023). “Magnetized Rotating Isothermal Winds”. *arXiv e-prints*, arXiv:2302.05462. DOI: `10.48550/arXiv.2302.05462`. arXiv: `2302.05462 [astro-ph.SR]`.

Raynaud, R. et al. (2020). “Magnetar formation through a convective dynamo in protoneutron stars”. *Science Advances* 6, eaay2732. DOI: `10.1126/sciadv.aay2732`. arXiv: `2003.06662 [astro-ph.HE]`.

Reboul-Salze, A. et al. (2022). “MRI-driven $\alpha\Omega$ dynamos in protoneutron stars”. *A&A* 667, A94. DOI: `10.1051/0004-6361/202142368`. arXiv: `2111.02148 [astro-ph.HE]`.

Rees, M. J. (1988). “Tidal disruption of stars by black holes of 10 to the 6th-10 to the 8th solar masses in nearby galaxies”. *Nature* 333, pp. 523–528. DOI: `10.1038/333523a0`.

Reichert, M. et al. (2023). “Magnetorotational supernovae: a nucleosynthetic analysis of sophisticated 3D models”. *MNRAS* 518, pp. 1557–1583. DOI: `10.1093/mnras/stac3185`. arXiv: `2206.11914 [astro-ph.HE]`.

Reichert, M. et al. (2020). “Neutron-capture elements in dwarf galaxies III: A homogenized analysis of 13 dwarf spheroidal and ultra-faint galaxies”. *arXiv:2004.01195 [astro-ph]*. arXiv: 2004.01195.

Reifarth, R. et al. (2017). “Spallation-based neutron target for direct studies of neutron-induced reactions in inverse kinematics”. *Physical Review Accelerators and Beams* 20, p. 044701. DOI: `10.1103/PhysRevAccelBeams.20.044701`. arXiv: `1704.08689 [physics.ins-det]`.

Reiter, M. P. et al. (2020). “Mass measurements of neutron-rich gallium isotopes refine production of nuclei of the first r-process abundance peak in neutron-star merger calculations”. *Phys. Rev. C* 101 (2), p. 025803. DOI: `10.1103/PhysRevC.101.025803`.

Richers, S. et al. (2021). “Particle-in-cell simulation of the neutrino fast flavor instability”. *Phys. Rev. D.* 103, p. 083013. DOI: `10.1103/PhysRevD.103.083013`.

Roberts, L. F. (2012). “A New Code for Proto-neutron Star Evolution”. *ApJ* 755, p. 126. DOI: `10.1088/0004-637X/755/2/126`. arXiv: `1205.3228 [astro-ph.HE]`.

Roberts, L. F., S. Reddy, and G. Shen (2012). “Medium modification of the charged-current neutrino opacity and its implications”. *PRC* 86, p. 065803. DOI: `10.1103/PhysRevC.86.065803`.

Roberts, L. F., S. E. Woosley, and R. D. Hoffman (2010). "INTEGRATED NUCLEOSYNTHESIS IN NEUTRINO-DRIVEN WINDS". *ApJ* 722, pp. 954–967. DOI: `10.1088/0004-637X/722/1/954`.

Roberts, L. F., S. E. Woosley, and R. D. Hoffman (2010). "Integrated Nucleosynthesis in Neutrino-driven Winds". *ApJ* 722, pp. 954–967. DOI: `10.1088/0004-637X/722/1/954`. arXiv: `1004.4916 [astro-ph.HE]`.

Roberts, L. F. et al. (2012). "Protoneutron Star Cooling with Convection: The Effect of the Symmetry Energy". *PRL* 108, p. 061103. DOI: `10.1103/PhysRevLett.108.061103`.

Roberts, L. F. et al. (2012a). "Protoneutron Star Cooling with Convection: The Effect of the Symmetry Energy". *PRL* 108, p. 061103. DOI: `10.1103/PhysRevLett.108.061103`. arXiv: `1112.0335 [astro-ph.HE]`.

Roberts, L. F. et al. (2012b). "Protoneutron Star Cooling with Convection: The Effect of the Symmetry Energy". *Physical Review Letters* 108, p. 061103. DOI: `10.1103/PhysRevLett.108.061103`. arXiv: `1112.0335 [astro-ph.HE]`.

Roberts, L. F. et al. (2017). "The influence of neutrinos on r-process nucleosynthesis in the ejecta of black hole-neutron star mergers". *MNRAS* 464, pp. 3907–3919. DOI: `10.1093/mnras/stw2622`.

Roberts, L. F. and S. Reddy (2017). "Neutrino Signatures from Young Neutron Stars". In: *Handbook of Supernovae*. Ed. by A. W. Alsabti and P. Murdin. Springer International Publishing AG, p. 1605. DOI: `10.1007/978-3-319-21846-5\_5`.

Roederer, I. U. et al. (2014). "Detection of Neutral Phosphorus in the Near-ultraviolet Spectra of Late-type Stars". *ApJ* 797, p. 69. DOI: `10.1088/0004-637X/797/1/69`. arXiv: `1410.8539 [astro-ph.SR]`.

Roederer, I. U. et al. (2022). "The R-process Alliance: A Nearly Complete R-process Abundance Template Derived from Ultraviolet Spectroscopy of the R-process-enhanced Metal-poor Star HD 222925". *ApJ Supplements* 260, p. 27. DOI: `10.3847/1538-4365/ac5cbc`. arXiv: `2205.03426 [astro-ph.SR]`.

Röpke, F. K. and O. De Marco (2023). "Simulations of common-envelope evolution in binary stellar systems: physical models and numerical techniques". *Living Reviews in Computational Astrophysics* 9, p. 2. DOI: `10.1007/s41115-023-00017-x`. arXiv: `2212.07308 [astro-ph.SR]`.

Rosswog, S. (2005). "Mergers of Neutron Star-Black Hole Binaries with Small Mass Ratios: Nucleosynthesis, Gamma-Ray Bursts, and Electromagnetic Transients". *Astrophys. J.* 634, pp. 1202–1213. DOI: `10.1086/497062`. eprint: `arXiv:astro-ph/0508138`.

Rosswog, S. (2007). “Fallback accretion in the aftermath of a compact binary merger”. *Mon. Not. R. Astron. Soc.* 376, pp. L48–L51. DOI: 10.1111/j.1745-3933.2007.00284.x.

Rosswog, S. (2007). “Fallback accretion in the aftermath of a compact binary merger”. *Mon. Not. R. Astron. Soc.* 376, pp. L48–L51. DOI: 10.1111/j.1745-3933.2007.00284.x. eprint: arXiv:astro-ph/0611440.

Rosswog, S. (2015). “The multi-messenger picture of compact binary mergers”. *Int. J. Mod. Phys. D* 24, p. 30012. DOI: 10.1142/S0218271815300128.

Rosswog, S. and M. Liebendörfer (2003). “High-resolution calculations of merging neutron stars - II. Neutrino emission”. *MNRAS* 342, pp. 673–689. DOI: 10.1046/j.1365-8711.2003.06579.x.

Rosswog, S. et al. (1999). “Mass ejection in neutron star mergers”. *A&A* 341, pp. 499–526.

Rosswog, S. et al. (2014). “The long-term evolution of neutron star merger remnants – I. The impact of *r*-process nucleosynthesis”. *Mon. Not. R. Astron. Soc.* 439, pp. 744–756. DOI: 10.1093/mnras/stt2502. arXiv: 1307.2939 [astro-ph.HE].

Rosswog, S. et al. (2014). “The long-term evolution of neutron star merger remnants - I. The impact of r-process nucleosynthesis”. *Monthly Notices of the Royal Astronomical Society* 439, pp. 744–756. DOI: 10.1093/mnras/stt2502.

Rosswog, S. et al. (2017). “The first direct double neutron star merger detection: implications for cosmic nucleosynthesis”. *ArXiv e-prints*.

Rowlinson, A. et al. (2013). “Signatures of magnetar central engines in short GRB light curves”. *MNRAS* 430, pp. 1061–1087. DOI: 10.1093/mnras/sts683.

Rowlinson, A. et al. (2013). “Signatures of magnetar central engines in short GRB light curves”. *Mon. Not. R. Astron. Soc.* 430, pp. 1061–1087. DOI: 10.1093/mnras/sts683. arXiv: 1301.0629 [astro-ph.HE].

Ruderman, M. (1972). “Pulsars: Structure and Dynamics”. *ARA&A* 10, p. 427. DOI: 10.1146/annurev.aa.10.090172.002235.

Ruffert, M., H.-T. Janka, and G. Schaefer (1996). “Coalescing neutron stars - a step towards physical models. I. Hydrodynamic evolution and gravitational-wave emission.” *A&A* 311, pp. 532–566.

Sarin, N. et al. (2022). “Linking the rates of neutron star binaries and short gamma-ray bursts”. *Phys. Rev. D.* 105, p. 083004. DOI: 10.1103/PhysRevD.105.083004. arXiv: 2201.08491 [astro-ph.HE].

Scheck, L. et al. (2006). "Multidimensional supernova simulations with approximative neutrino transport. I. Neutron star kicks and the anisotropy of neutrino-driven explosions in two spatial dimensions". *A&A* 457, pp. 963–986. DOI: `10.1051/0004-6361:20064855`.

Schnetter, E., S. H. Hawley, and I. Hawke (2004). "Evolutions in 3D numerical relativity using fixed mesh refinement". *CQG* 21, pp. 1465–1488.

Sekiguchi, Y. et al. (2011). "Effects of Hyperons in Binary Neutron Star Mergers". *PRL* 107, p. 211101. DOI: `10.1103/PhysRevLett.107.211101`.

Sekiguchi, Y. et al. (2016). "Dynamical mass ejection from the merger of asymmetric binary neutron stars: Radiation-hydrodynamics study in general relativity". *Phys. Rev. D.* 93, p. 124046. DOI: `10.1103/PhysRevD.93.124046`. arXiv: `1603.01918 [astro-ph.HE]`.

Shibata, M. and K. Taniguchi (2006). "Merger of binary neutron stars to a black hole: Disk mass, short gamma-ray bursts, and quasinormal mode ringing". *Phys. Rev. D* 73, p. 064027. DOI: `10.1103/PhysRevD.73.064027`.

Shibata, M. et al. (2011). "Afterglow of a Binary Neutron Star Merger". *ApJL* 734, p. L36. DOI: `10.1088/2041-8205/734/2/L36`.

Siegel, D. M. and R. Ciolfi (2016). "Electromagnetic Emission from Long-lived Binary Neutron Star Merger Remnants. II. Lightcurves and Spectra". *ApJ* 819, p. 15. DOI: `10.3847/0004-637X/819/1/15`.

Siegel, D. M., R. Ciolfi, and L. Rezzolla (2014). "Magnetically Driven Winds from Differentially Rotating Neutron Stars and X-Ray Afterglows of Short Gamma-Ray Bursts". *ApJL* 785, p. L6. DOI: `10.1088/2041-8205/785/1/L6`.

Siegel, D. M. and B. D. Metzger (2017). "Three-dimensional GRMHD simulations of the remnant accretion disks from neutron star mergers: outflows and r-process nucleosynthesis". *ArXiv e-prints.* arXiv: `1705.05473 [astro-ph.HE]`.

Siegel, D. M. and P. Mösta (2018). *GRMHD_ con2prim: a framework for the recovery of primitive variables in general-relativistic magnetohydrodynamics.* Zenodo. DOI: `10.5281/zenodo.1213306`.

Siegel, D. M. (2019). "GW170817 -the first observed neutron star merger and its kilonova: Implications for the astrophysical site of the r-process". 55, p. 203. DOI: `10.1140/epja/i2019-12888-9`.

Siegel, D. M. (2022). "r-Process nucleosynthesis in gravitational-wave and other explosive astrophysical events". *Nature Reviews Physics* 4, pp. 306–318. DOI: `10.1038/s42254-022-00439-1`.

Siegel, D. M., J. Barnes, and B. D. Metzger (2019). "Collapsars as a major source of r-process elements". *Nature* 569, pp. 241–244. DOI: `10.1038/s41586-019-1136-0`.

Siegel, D. M. and B. D. Metzger (2017). "Three-Dimensional General-Relativistic Magnetohydrodynamic Simulations of Remnant Accretion Disks from Neutron Star Mergers: Outflows and r -Process Nucleosynthesis". *PRL* 119, p. 231102. DOI: `10.1103/PhysRevLett.119.231102`.

Siegel, D. M. and B. D. Metzger (2018a). "Three-dimensional GRMHD Simulations of Neutrino-cooled Accretion Disks from Neutron Star Mergers". *ApJ* 858, p. 52. DOI: `10.3847/1538-4357/aabaec`.

Siegel, D. M. and B. D. Metzger (2018b). "Three-dimensional GRMHD Simulations of Neutrino-cooled Accretion Disks from Neutron Star Mergers". *ApJ* 858, p. 52. DOI: `10.3847/1538-4357/aabaec`.

Siegel, D. M. et al. (2013). "Magnetorotational instability in relativistic hypermassive neutron stars". *Phys. Rev. D.* 87, 121302(R). DOI: `10.1103/PhysRevD.87.121302`.

Siegel, D. M. et al. (2018). "Recovery Schemes for Primitive Variables in General-relativistic Magnetohydrodynamics". *ApJ* 859, p. 71. DOI: `10.3847/1538-4357/aabcc5`.

Siegl, K. et al. (2018). "Recoil ions from the β decay of ^{134}Sb confined in a Paul trap". *PRC* 97, p. 035504. DOI: `10.1103/PhysRevC.97.035504`.

Simon, J. D. (2019). "The Faintest Dwarf Galaxies". *ARA&A* 57, pp. 375–415. DOI: `10.1146/annurev-astro-091918-104453`. arXiv: `1901.05465 [astro-ph.GA]`.

Skinner, M. A., A. Burrows, and J. C. Dolence (2016). "Should One Use the Ray-by-Ray Approximation in Core-collapse Supernova Simulations?" *ApJ* 831, p. 81. DOI: `10.3847/0004-637X/831/1/81`. arXiv: `1512.00113 [astro-ph.SR]`.

Sneden, C., J. J. Cowan, and R. Gallino (2008). "Neutron-Capture Elements in the Early Galaxy". *Annu. Rev. Astron. Astrophys.* 46, pp. 241–288. DOI: `10.1146/annurev.astro.46.060407.145207`.

Sneden, C. et al. (1994). "Ultra–Metal-poor Halo Stars: The Remarkable Spectrum of CS 22892-052". *ApJL* 431, p. L27. DOI: `10.1086/187464`.

Soares-Santos, M. et al. (2017). "The Electromagnetic Counterpart of the Binary Neutron Star Merger LIGO/Virgo GW170817. I. Discovery of the Optical Counterpart Using the Dark Energy Camera". *ApJL* 848, p. L16. DOI: `10.3847/2041-8213/aa9059`. arXiv: `1710.05459 [astro-ph.HE]`.

Spite, F. et al. (2018). “Abundance patterns of the light neutron-capture elements in very and extremely metal-poor stars”. *A&A* 611, A30. DOI: `10.1051/0004-6361/201732096`. arXiv: `1801.01304 [astro-ph.SR]`.

Spruit, H. C. (2008b). “Theory of magnetically powered jets”. *arXiv:0804.3096*.

Spruit, H. C. (2008a). “Origin of neutron star magnetic fields”. In: *40 Years of Pulsars: Millisecond Pulsars, Magnetars and More*. Ed. by C. Bassa, Z. Wang, A. Cumming, & V. M. Kaspi. Vol. 983. American Institute of Physics Conference Series, pp. 391–398. DOI: `10.1063/1.2900262`.

Steiner, A. W., M. Hempel, and T. Fischer (2013). “Core-collapse supernova equations of state based on neutron star observations”. *ApJ* 774, p. 17. DOI: `10.1088/0004-637x/774/1/17`.

Stergioulas, N. and J. L. Friedman (1995). “Comparing models of rapidly rotating relativistic stars constructed by two numerical methods”. *ApJ* 444, p. 306. DOI: `10.1086/175605`.

Suess, H. E. (1988). “V. M. Goldschmidt and the origin of the elements”. *Applied Geochemistry* 3, pp. 385–391. DOI: `https://doi.org/10.1016/0883-2927(88)90119-9`.

Sumiyoshi, K. et al. (2000). “Hydrodynamical Study of Neutrino-Driven Wind as an r-Process Site”. *PASJ* 52, pp. 601–611. DOI: `10.1093/pasj/52.4.601`. eprint: `astro-ph/9912156`.

Sun, B. et al. (2008). “Nuclear structure studies of short-lived neutron-rich nuclei with the novel large-scale isochronous mass spectrometry at the FRS-ESR facility”. 812, pp. 1–12. DOI: `10.1016/j.nuclphysa.2008.08.013`.

Sun, B.-H. and J. Meng (2008). “NUCLEAR PHYSICS: Challenge on the Astrophysical R-Process Calculation with Nuclear Mass Models”. *Chinese Physics Letters* 25, pp. 2429–2431. DOI: `10.1088/0256-307X/25/7/027`. arXiv: `0807.2509 [nucl-th]`.

Suzuki, T. K. and S. Nagataki (2005). “Alfvén Wave-driven Proto-Neutron Star Winds and r-Process Nucleosynthesis”. *ApJ* 628, pp. 914–922. DOI: `10.1086/430847`. eprint: `astro-ph/0412362`.

Symbalisty, E. and D. N. Schramm (1982). “Neutron star collisions and the r-process”. *Astrophys. J. Lett.* 22, pp. 143–145.

Symbalisty, E. M. D. (1984). “Magnetorotational iron core collapse”. *ApJ* 285, pp. 729–746. DOI: `10.1086/162551`.

Takahashi, K., J. Witti, and H.-T. Janka (1994). "Nucleosynthesis in neutrino-driven winds from protoneutron stars II. The r-process". *A&A* 286, pp. 857–869.

Takahashi, K., J. Witti, and H.-T. Janka (1994). "Nucleosynthesis in neutrino-driven winds from protoneutron stars II. The r-process". *Astron. Astrophys.* 286, pp. 857–869.

Tchekhovskoy, A. and D. Giannios (2015). "Magnetic flux of progenitor stars sets gamma-ray burst luminosity and variability". *MNRAS* 447, pp. 327–344. DOI: `10.1093/mnras/stu2229`. arXiv: `1409.4414 [astro-ph.HE]`.

Thielemann, F. K. et al. (2017). "Neutron Star Mergers and Nucleosynthesis of Heavy Elements". *Annual Review of Nuclear and Particle Science* 67, pp. 253–274. DOI: `10.1146/annurev-nucl-101916-123246`. arXiv: `1710.02142 [astro-ph.HE]`.

Thompson, C. and R. C. Duncan (1993). "Neutron star dynamos and the origins of pulsar magnetism". *ApJ* 408, pp. 194–217. DOI: `10.1086/172580`.

Thompson, T. A. (2003). "Magnetic Protoneutron Star Winds and r-Process Nucleosynthesis". *Astrophys. J. Lett.* 585, pp. L33–L36. DOI: `10.1086/374261`.

Thompson, T. A., A. Burrows, and B. S. Meyer (2001). "The Physics of Proto-Neutron Star Winds: Implications for r-Process Nucleosynthesis". *ApJ* 562, pp. 887–908. DOI: `10.1086/323861`. eprint: `astro-ph/0105004`.

Thompson, T. A., P. Chang, and E. Quataert (2004). "Magnetar Spin-Down, Hyperenergetic Supernovae, and Gamma-Ray Bursts". *ApJ* 611, pp. 380–393. DOI: `10.1086/421969`. eprint: `astro-ph/0401555`.

Thompson, T. A., P. Chang, and E. Quataert (2004). "Magnetar Spin-Down, Hyperenergetic Supernovae, and Gamma-Ray Bursts". *Astrophys. J.* 611, pp. 380–393. DOI: `10.1086/421969`.

Thompson, T. A. (2003). "Magnetic Protoneutron Star Winds and r-Process Nucleosynthesis". *ApJL* 585, pp. L33–L36. DOI: `10.1086/374261`. arXiv: `astro-ph/0302132 [astro-ph]`.

Thompson, T. A. and A. ud Doula (2018). "High-entropy ejections from magnetized proto-neutron star winds: implications for heavy element nucleosynthesis". *MNRAS* 476, pp. 5502–5515. DOI: `10.1093/mnras/sty480`.

Thompson, T. A. and A. ud-Doula (2018). "High-entropy ejections from magnetized proto-neutron star winds: implications for heavy element nucleosynthesis". *MNRAS* 476, pp. 5502–5515. DOI: `10.1093/mnras/sty480`. arXiv: `1709.03997 [astro-ph.HE]`.

Thornburg, J. (2004). “Black-hole excision with multiple grid patches”. *CQG* 21, pp. 3665–3691. DOI: 10.1088/0264-9381/21/15/004.

Tóth, G. (2000). “The
$\nabla \cdot B = 0ConstraintinShock - CapturingMagnetohydrodynamicsCodes$”. *JCPH* 161, pp. 605–652. DOI: 10.1006/jcph.2000.6519.

Troja, E., L. Piro, H. van Eerten, et al. (2017). “XXX”. *Nature*. DOI: 10.1038/nature24290. arXiv: XXX [astro-ph.HE].

Troja, E. et al. (2008). “Different progenitors of short hard gamma-ray bursts”. *MNRAS* 385, pp. L10–L14. DOI: 10.1111/j.1745-3933.2007.00421.x. arXiv: 0711.3034.

Truran, J. W. et al. (1968). “Rapid Neutron Capture in Supernova Explosions”. *APSS* 1, pp. 129–146. DOI: 10.1007/BF00653851.

Tsang, M. B. et al. (2012). “Constraints on the symmetry energy and neutron skins from experiments and theory”. *PRC* 86, p. 015803. DOI: 10.1103/PhysRevC.86.015803. arXiv: 1204.0466 [nucl-ex].

Usov, V. V. (1992a). “Millisecond pulsars with extremely strong magnetic fields as a cosmological source of gamma-ray bursts”. *Nature* 357, pp. 472–474. DOI: 10.1038/357472a0.

Usov, V. V. (1992b). “Millisecond pulsars with extremely strong magnetic fields as a cosmological source of gamma-ray bursts”. *Nature* 357, pp. 472–474. DOI: 10.1038/357472a0.

Vilen, M. et al. (2018). “Precision Mass Measurements on Neutron-Rich Rare-Earth Isotopes at JYFLTRAP: Reduced Neutron Pairing and Implications for r -Process Calculations”. *PRL* 120, p. 262701. DOI: 10.1103/PhysRevLett.120.262701.

Villar, V. A. et al. (2017). “The Combined Ultraviolet, Optical, and Near-infrared Light Curves of the Kilonova Associated with the Binary Neutron Star Merger GW170817: Unified Data Set, Analytic Models, and Physical Implications”. *ApJL* 851, p. L21. DOI: 10.3847/2041-8213/aa9c84. arXiv: 1710.11576 [astro-ph.HE].

Vink, J. and L. Kuiper (2006). “Supernova remnant energetics and magnetars: no evidence in favour of millisecond proto-neutron stars”. *MNRAS* 370, pp. L14–L18. DOI: 10.1111/j.1745-3933.2006.00178.x.

Vink, J. and L. Kuiper (2006). “Supernova remnant energetics and magnetars: no evidence in favour of millisecond proto-neutron stars”. *MNRAS* 370, pp. L14–L18. DOI: 10.1111/j.1745-3933.2006.00178.x. eprint: arXiv:astro-ph/0604187.

Vlasov, A. D., B. D. Metzger, and T. A. Thompson (2014). “Neutrino-heated winds from rotating protomagnetars”. *MNRAS* 444, pp. 3537–3558. DOI: 10.1093/mnras/stu1667. arXiv: 1405.7043 [astro-ph.HE].

Vlasov, A. D. et al. (2017). “Neutrino-heated winds from millisecond protomagnetars as sources of the weak r-process”. *MNRAS* 468, pp. 1522–1533. DOI: 10.1093/mnras/stx478. arXiv: 1701.03123 [astro-ph.HE].

Wallner, A. et al. (2015). “Abundance of live 244Pu in deep-sea reservoirs on Earth points to rarity of actinide nucleosynthesis”. *Nature Communications* 6, p. 5956. DOI: 10.1038/ncomms6956.

Wallner, A. et al. (2021). “60Fe and 244Pu deposited on Earth constrain the r-process yields of recent nearby supernovae”. 372, pp. 742–745. DOI: 10.1126/science.aax3972.

Wanajo, S. (2013). “The r-process in Proto-neutron-star Wind Revisited”. *ApJL* 770, p. L22. DOI: 10.1088/2041-8205/770/2/L22. arXiv: 1305.0371 [astro-ph.SR].

Wanajo, S. et al. (2014). “Production of All the r-process Nuclides in the Dynamical Ejecta of Neutron Star Mergers”. *ApJL* 789, p. L39. DOI: 10.1088/2041-8205/789/2/L39.

Wanajo, S. et al. (2014). “Production of All the r-process Nuclides in the Dynamical Ejecta of Neutron Star Mergers”. *ApJL* 789, p. L39. DOI: 10.1088/2041-8205/789/2/L39. arXiv: 1402.7317 [astro-ph.SR].

Wanajo, S. (2018). “Physical Conditions for the r-process. I. Radioactive Energy Sources of Kilonovae”. *ApJ* 868, p. 65. DOI: 10.3847/1538-4357/aae0f2. arXiv: 1808.03763 [astro-ph.HE].

Wanajo, S., H.-T. Janka, and S. Kubono (2011). “Uncertainties in the νp-process: Supernova Dynamics Versus Nuclear Physics”. *ApJ* 729, p. 46. DOI: 10.1088/0004-637X/729/1/46. arXiv: 1004.4487 [astro-ph.SR].

Wang, L. et al. (2001). “Bipolar Supernova Explosions”. *ApJ* 550, pp. 1030–1035. DOI: 10.1086/319822.

Wang, T. and A. Burrows (2023). “Neutrino-Driven Winds in Three-Dimensional Core-Collapse Supernova Simulations”. *arXiv e-prints*, arXiv:2306.13712. DOI: 10.48550/arXiv.2306.13712. arXiv: 2306.13712 [astro-ph.SR].

Wasserburg, G. J., M. Busso, and R. Gallino (1996). “Abundances of Actinides and Short-lived Nonactinides in the Interstellar Medium: Diverse Supernova Sources for the r-Processes”. *ApJL* 466, p. L109. DOI: 10.1086/310177.

Weber, E. J. and J. Davis Leverett (1967). “The Angular Momentum of the Solar Wind”. *ApJ* 148, pp. 217–227. DOI: 10.1086/149138.

Wehmeyer, B., M. Pignatari, and F.-K. Thielemann (2015). “Galactic evolution of rapid neutron capture process abundances: the inhomogeneous approach”. *MNRAS* 452, pp. 1970–1981. DOI: 10.1093/mnras/stv1352.

White, C. J. et al. (2022). “On the Origin of Pulsar and Magnetar Magnetic Fields”. *ApJ* 926, p. 111. DOI: 10.3847/1538-4357/ac4507. arXiv: 2111.01814 [astro-ph.HE].

Wilson, J. R. et al. (1986). “Stellar core collapse and supernova.” *Annals of the New York Academy of Sciences* 470, pp. 267–293. DOI: 10.1111/j.1749-6632.1986.tb47980.x.

Winteler, C. et al. (2012). “Magnetorotationally Driven Supernovae as the Origin of Early Galaxy r-process Elements?” *ApJL* 750, p. L22. DOI: 10.1088/2041-8205/750/1/L22.

Winteler, C. et al. (2012). “Magnetorotationally Driven Supernovae as the Origin of Early Galaxy r-process Elements?” *ApJL* 750, p. L22. DOI: 10.1088/2041-8205/750/1/L22. arXiv: 1203.0616 [astro-ph.SR].

Winteler, C. (2014). “Light element production in the big bang and the synthesis of heavy elements in 3D MHD jets from core-collapse supernovae”. PhD thesis. University of Basel, Switzerland.

Witti, J., H. T. Janka, and K. Takahashi (1994). “Nucleosynthesis in neutrino-driven winds from protoneutron stars I. The α-process”. *A&A* 286, pp. 841–856.

Woltjer, L. (1964). “X-Rays and Type I Supernova Remnants.” *ApJ* 140, pp. 1309–1313. DOI: 10.1086/148028.

Woods, P. M. and C. Thompson (2006). “Soft gamma repeaters and anomalous X-ray pulsars: magnetar candidates”. *Compact stellar X-ray sources.* Ed. by Lewin, W. H. G. & van der Klis, M., pp. 547–586.

Woosley, S. E. (1993). “Gamma-ray bursts from stellar mass accretion disks around black holes”. *Astrophys. J.* 405, p. 273. DOI: 10.1086/172359.

Woosley, S. E. and R. D. Hoffman (1992). “The alpha-process and the r-process”. *ApJ* 395, pp. 202–239. DOI: 10.1086/171644.

Woosley, S. E. et al. (1994). “The r-process and neutrino-heated supernova ejecta”. *ApJ* 433, pp. 229–246. DOI: 10.1086/174638.

Woosley, S. E. et al. (1994). “The \$r\$-process and neutrino-heated supernova ejecta”. *Astrophys. J.* 433, pp. 229–246. DOI: 10.1086/174638.

Yan, X. L. et al. (2016). "Recent results on mass measurements of exotic nuclides in storage rings". In: *Journal of Physics Conference Series*. Vol. 665. Journal of Physics Conference Series, p. 012053. DOI: `10.1088/1742-6596/665/1/012053`.

Yee, R. M. et al. (2013). "β-Delayed Neutron Spectroscopy Using Trapped Radioactive Ions". *PRL* 110, p. 092501. DOI: `10.1103/PhysRevLett.110.092501`.

Yoon, S.-C. and N. Langer (2005). "On the evolution of rapidly rotating massive white dwarfs towards supernovae or collapses". *Astron. Astrophys.* 435, pp. 967–985. DOI: `10.1051/0004-6361:20042542`.

Zeipel, H. von (1924). "The radiative equilibrium of a rotating system of gaseous masses". *Mon. Not. Roy. Soc.* 84, pp. 665–683.

Zevin, M. et al. (2019). "Can Neutron-star Mergers Explain the r-process Enrichment in Globular Clusters?" *ApJ* 886, p. 4. DOI: `10.3847/1538-4357/ab498b`.

Zhou, P. et al. (2019). "Spatially resolved X-ray study of supernova remnants that host magnetars: Implication of their fossil field origin". *A&A* 629, A51. DOI: `10.1051/0004-6361/201936002`. arXiv: `1909.01922 [astro-ph.HE]`.

Appendix A: Appendix

A.1 Numerical Tests

This Appendix presents a number of tests we have performed on the simulation results, which justify simplifications made in the grid setup and assumptions regarding the microphysics we have included.

A.1.1 Spatial Resolution

Figure A.1 shows the vertical scale-height of the magnetic field strength B and neutrino optical depth $\tau_{\bar{\nu}_e}$ as a function of radius for the strongly magnetized model `hi-B`. We resolve the magnetic field by at least 10 grid points throughout the entire simulation domain. The same conclusion holds for model `lo-B`.

Although we only marginally resolve the neutrinosphere with ≈ 1 grid point per scale height at radii where $\tau_{\bar{\nu}_e} \sim 1$, the main effect of this deficiency is on the properties (luminosity, mean energy) of the escaping neutrino flux (Paper I). Although the asymptotic electron fraction of the wind is very sensitive to these properties, the main focus of this study is on the effects of a strong magnetic field for an otherwise fixed neutrino radiation field (and the neutrino properties do not depend strongly on the magnetic field; see Tab. **??**). Furthermore, at larger radii, specifically in the gain region where net neutrino heating launches the wind, we do sufficiently resolve the optical depth scale height. For the purposes of this study, the resolution of our simulations is therefore sufficient to capture magnetic field effects and bulk wind dynamics.

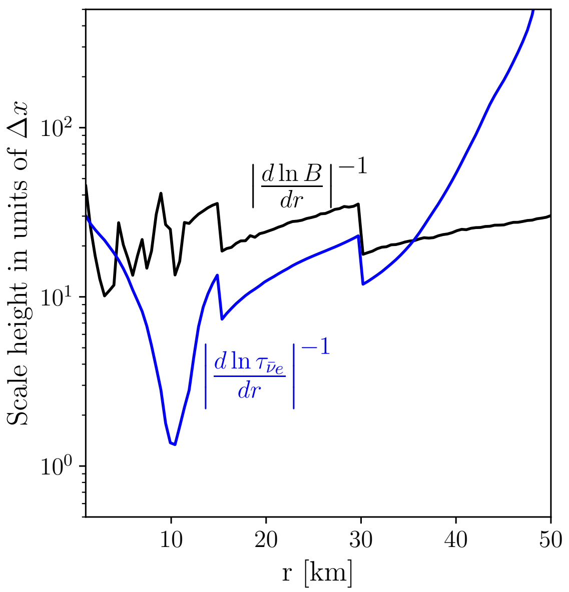

Figure A.1: Vertical scale-height as a function of radius of the magnetic field $\boldsymbol{B}$ (black) and neutrino optical depth $\tau_{\bar{\nu}_e}$ (blue) for model `hi-B`, normalized by the grid step size Δx. The radial profiles correspond to the slice through the magnetic dipole axis ($y = 0$ plane), averaged over polar angle between $\theta = 0°$ and $\theta = 45°$, and time-averaged over the first 4 ms after the magnetic field is initialized. Discontinuities at 15 km and 30 km reflect refinement level boundaries.

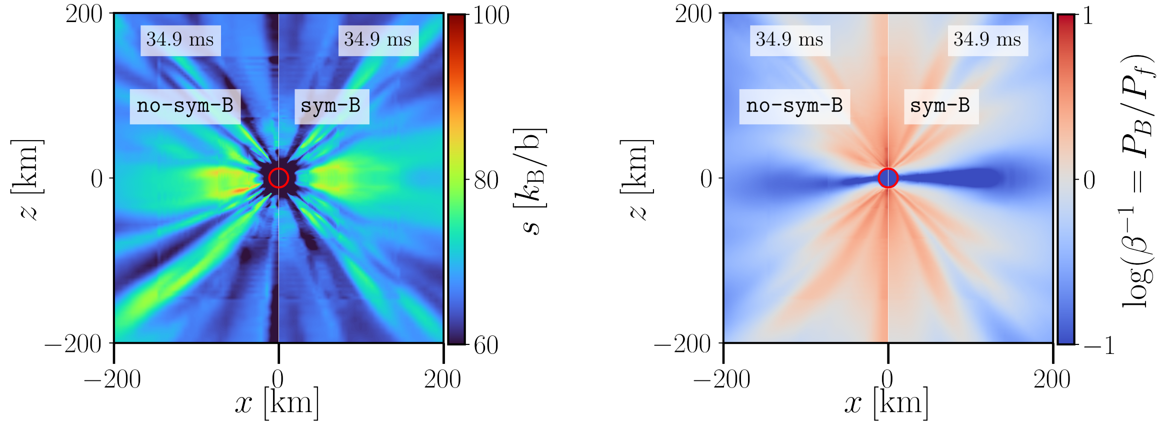

Figure A.2: Comparison of wind properties with and without imposing reflection symmetry across the equatorial plane. Shown are wind cross-sections in the plane of the magnetic dipole axis for specific entropy (left panel) and magnetic-to-fluid pressure ratio (right panel) time-averaged over the interval $t \simeq 30 - 35$ ms after the B-field is initialized. For each panel: the simulation is run across the full $\theta \in [0, \pi]$ domain (left; model `no-sym-B`); reflection symmetry across the $z = 0$ plane is employed (right; model `sym-B`).

A.1.2 Hemisphere Symmetry Assumption

We perform two otherwise identical simulations, with and without imposing reflection symmetry across the equatorial ($z = 0$) plane, to check that the results of the half-hemisphere simulations presented in this paper are independent of the use of this assumption (`no-sym-B` and `sym-B`, Tab. **??**). The two simulations use the same refinement level box sizes as those of our fiducial models, but with the resolution of the smallest refinement level being 450 m rather than 150 m, for reasons of computational expense associated with the full-domain simulations. The set-up of the two models is similar to the fiducial magnetized models: after reaching roughly steady-state wind properties with zero magnetic field, we initialize the dipole magnetic field of strength $B_{\rm S} \approx 2.2 \times 10^{15}$ G and further evolve the models for $\simeq 40$ ms.

Broadly, the temporal evolution of the two simulations are qualitatively similar to those of the `hi-B` model ($B_{\rm S} = 2.5 \times 10^{15}$ G): a thin reconnection layer with low magnetic-to-fluid pressure ratio β^{-1} forms in the equatorial plane, and high β^{-1} in the polar region due to magnetic field lines being torn open and approaching a split monopole-like solution in that region. The half and full-domain simulations are even more similar to each other. Figure A.2 shows a snapshot comparing the magnetic-to-fluid pressure ratio roughly 35 ms after the magnetic field has been initialized. Although the low β^{-1} equatorial current sheet/reconnection layer becomes slightly warped in the full-domain simulation (perhaps due to reconnection related-instabilities), the reconnection layer appears nearly symmetric and similar to the half-domain simulation when time-averaged over a 20 ms interval. We conclude that while our half-domain simulation may miss some features of the dynamics near the equatorial plane, the time-averaged wind properties will not be greatly effected by this simplification.

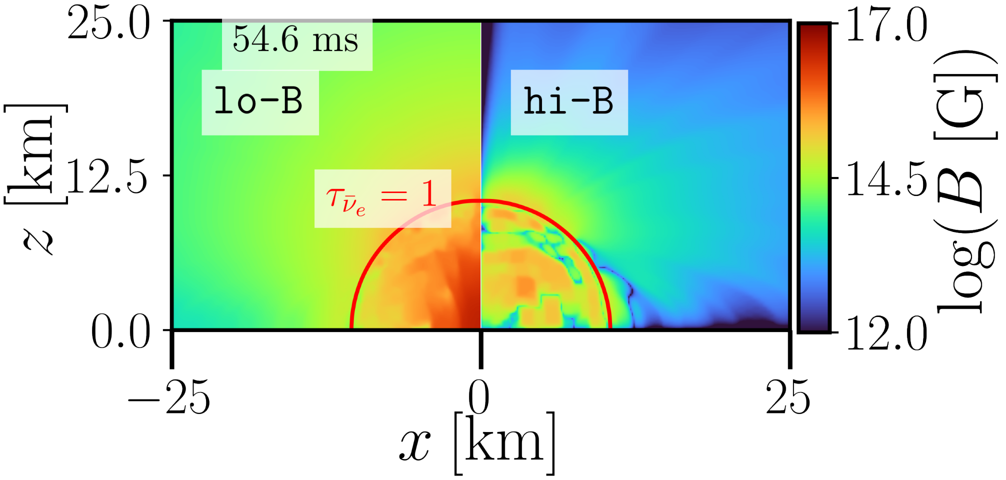

Figure A.3: Strength of the poloidal (left) and toroidal (right) magnetic field components for model `hi-B` approximately 55 ms after initialization of the magnetic field. The red contour indicates the location of the neutrinosphere.

A.1.3 Toroidal Field

Absent any large-scale non-radial motions (due, e.g., to rotation), or the presence of other non-axisymmetric instabilities such as convection, we should expect the strength of the toroidal component of the magnetic field, $B_{\rm T}$, to remain highly subdominant compared to the poloidal field, $B_{\rm P}$. We check this expectation in Fig. A.3 by showing B_T and $B_{\rm P}$ from a snapshot of our `hi-B` model at 60 ms. The ratio $B_{\rm T}/B_{\rm P}$ achieves a maximum value 10^{-1} inside the PNS, but has typical values $\lesssim 10^{-2}$ outside the neutrinosphere everywhere else on the grid. As expected, the toroidal field should thus have no appreciable impact on the wind dynamics in the case of a non-rotating PNS.

A.1.4 Landau Level Effects

Strong magnetic fields modify neutrino absorption and emission rates as well as the EOS via quantization of electron and positron energy levels resulting from the quantization into Landau levels of $e^{\pm}$ motion transverse to the magnetic field (Lai and Qian, 1998; Duan and Qian, 2004, 2005). Such modifications become irrelevant for temperatures $T \gtrsim T_B$ or $\rho \gg \rho_B$, where T_B is a critical temperature

$$T_B = \begin{cases} \frac{m_e c^2}{k_B}\left(\sqrt{\frac{2B}{B_{\rm Q}}+1}-1\right) & \text{for } \rho \le \rho_B \\ \frac{\hbar\omega_c}{k_B}(1+x_F^2)^{-1/2} & \text{for } \rho \gg \rho_B \end{cases} \tag{A.1}$$

and ρ_B is a critical density

$$\rho_B = 2.23 \times 10^9 \left(\frac{Y_e}{0.1}\right)^{-1} \left(\frac{B}{10^{15}\ {\rm G}}\right)^{3/2} {\rm g\ cm^{-3}}, \tag{A.2}$$

defined as the density below which only the ground Landau level is populated by electrons (Harding and Lai, 2006; Haensel, Potekhin, and Yakovlev, 2007). Here, m_e is the electron mass, c is the speed of light, $\omega_c = eB/(m_e c)$ is the cyclotron frequency, $x_F = (\hbar/m_e c)(3\pi^2 Y_e \rho/m_{\rm u})^{1/3}$ is the normalized relativistic Fermi momentum, $m_{\rm u}$ the atomic mass

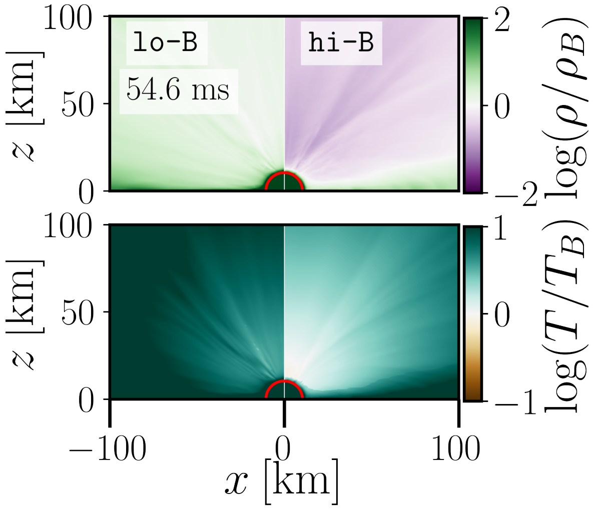

Figure A.4: Cross-section of the $y = 0$ magnetic dipole axis plane for the `lo-B` (left) and `hi-B` run (right) ≈ 55 ms after the magnetic field is initialized, showing the ratio of temperature T (top) and density ρ (bottom) to their respective critical values T_B and ρ_B below which quantizing effects of the magnetic field on the EOS and weak interactions are expected (Eqs. A.1 and A.2). Since $T/T_B > 1$ everywhere, electrons and positrons populate many Landau levels, even in the regime where $\rho < \rho_B$. The magnetic winds are thus in the non-quantizing regime, justifying our negligence of magnetic-field effects onto the EOS and weak interactions. The red contour indicates the $\tau_{\bar{\nu}_e} = 1$ neutrinosphere surface.

unit, and $B_{\rm Q} = 4.414 \times 10^{13}$ G is the critical QED magnetic field strength (obtained by equating the cyclotron energy of an electron to $m_e c^2$). If either the density or temperature is larger than their respective critical values, the $e^{\pm}$ distributions extend over many Landau levels and the magnetic field does not have a quantizing effect. Figure A.4 shows the ratios T/T_B and ρ/ρ_B of our magnetized runs once a stationary PNS wind has emerged. Since $T > T_B$ everywhere, the magnetic field is non-quantizing, even in the polar regions where $\rho < \rho_B$, justifying our assumptions regarding the impact of magnetic fields on the EOS and weak interactions.

A.1.5 Divergence-free Constraint Violations

The magnetic field in our simulations is evolved using the FluxCT method (Tóth, 2000) to maintain the solenoidal constraint $\nabla \cdot \mathbf{B} = 0$ during evolution. While interior to refinement level boundaries this constrained transport algorithm preserves $\nabla \cdot \mathbf{B}$ to machine precision, spurious violations are introduced over time at refinement level boundaries due to interpolation during prolongation and restriction operations, which do not preserve $\nabla \cdot \mathbf{B}$ to machine precision. Although we use additional overlap zones at refinement boundaries to minimize the impact of spurious violations on the evolution of the system, significant violations in ghost zones may impact the solution quantitatively beyond a certain timescale, which depends on the exact grid setup and the physical system. In the current case, spurious violations introduced during the first $\sim 150\,\mathrm{ms}$ of 'pre-evolution' to establish a stationary, essentially non-magnetized wind (cf. Sec. **??**), as well as violations introduced during magnetic field initialization and subsequent strongly magnetized evolution give rise to spurious accumulation of errors at refinement boundaries to the $\sim$ 1% level by $\gtrsim 60\,\mathrm{ms}$ after the large-scale dipole magnetic field is initialized. Figure A.5 illustrates the spurious growth of $\nabla \cdot \mathbf{B}$ at refinement boundaries as a function of time after initialization of the dipole field. At $\approx 64\,\mathrm{ms}$ and onward, we consider the accumulated errors at refinement level boundaries in the wind zone ($\sim 60\,\mathrm{km}$) prohibitive to fully trusting results from subsequent evolution and thus choose not to include subsequent simulation data into our analyses. In order to prevent effects of spurious $\nabla \cdot \mathbf{B}$ violations on the closed zone material while maintaining the resolution requirements at the neutrinosphere (Appendix A.1.1) would require increasing the innermost box to $\approx 100\,\mathrm{km}$. The associated increase in computational cost by a factor of $\sim (100/15)^3 \approx 300$ would render these simulations computationally infeasible.

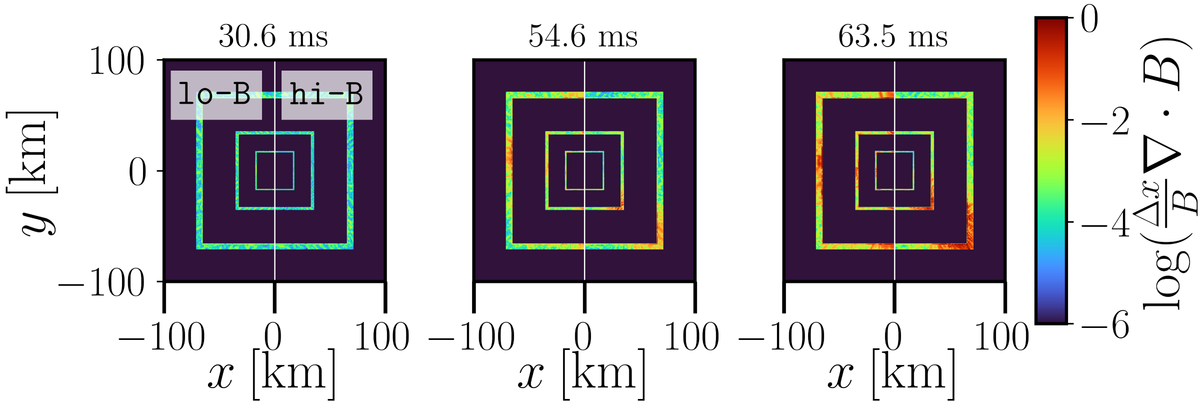

Figure A.5: Equatorial plane ($z = 0$) cross-section at 3 snapshots in time (≈ 31 ms, 55 ms, 64 ms after dipole magnetic field initialization) for models `lo-B` (shown in the $x < 0$ domain) and `hi-B` (shown in the $x > 0$ domain). The color represents the relative level of $\nabla \cdot \mathbf{B}$ violations, where Δx is the grid spacing, and B is the overall strength of the magnetic field. While the constraint transport scheme maintains $\nabla \cdot \mathbf{B}$ to machine precision interior to refinement level boundaries, spurious violations are introduced at refinement boundaries due to interpolation operations.